The Geochronology of Plutonism Associated with the Great Glen Fault, Northern Scottish Highlands

Careen MacRae
BSc (Hons) University of Glasgow

Submitted in fulfilment of the requirements of the degree
Master of Science (Research)

School of Geographical and Earth Sciences,
College of Science and Engineering,
University of Glasgow

Abstract

The Northern Highlands of Scotland contain Palaeozoic intrusions emplaced during collision of continents Baltica and Laurentia of the late Caledonian Scandian Orogeny. However, uncertainties remain regarding the accuracy of existing isotope dilution geochronology and understanding of the geodynamic history in relation to spatial and temporal distribution of intrusions. This study obtained emplacement dates by zircon U-Pb LA-ICP-MS (laser ablation-inductively coupled plasma-mass spectrometry) for the Strontian intrusion Sunart facies (423.5 ± 2.1 Ma), Strontian Sanda facies (418.2 ± 6.3 Ma), Helmsdale intrusion (417.0 ± 4.0 Ma) and Abriachan intrusion (418.2 ± 5.6 Ma). These dates provide confidence in existing literature, and a new date for the Abriachan intrusion. Further, use of in situ analysis produced evidence of antecrystic zircon and thus pre-emplacement magmatism in each sample up to a maximum age of c. 450 Ma, supportive of the lower crustal hot zone model for late Caledonian magmatism in the Northern Highlands. LA-ICP-MS zircon trace element data obtained for the Strontian Sunart facies similarly support open system magma evolution and homogenisation within a lower crustal hot zone prior to emplacement.

Spatially limited mid – upper crustal emplacement and thus limited mobilisation of hot zone material from c. 450 – c. 432 Ma is attributed to compression in the Laurentian margin induced by the initial stages of continental collision. Widespread mid – upper crustal emplacement from c. 432 – c. 423 Ma typically associated with regional transpression is interpreted as comprising new mantle derived melt and remobilised hot zone material. This widespread emplacement may have been triggered by lithospheric delamination, particularly the peak in emplacement at c. 425 Ma. A final phase of emplacement of evolved magmas is defined at c. 418 – c. 417 Ma and is highly spatially limited to the Great Glen Fault and related faults. This phase is interpreted to comprise remobilised hot zone material emplaced during a phase of strike slip displacement and may be related to continued uplift and the accretion of peri-Gondwanan terranes to Laurentia further southwest.

Table of Contents

List of Tables

List of Figures

Acknowledgements

Thanks go firstly to my supervisor, Iain Neill. His motivation for forward-looking research with a view to tangible community benefit has been nothing short of inspirational, and has been a privilege and a pleasure to learn from. This degree has been a thoroughly enriching experience despite significant ups and downs, and I sincerely thank Iain for his compassion and (often cake-based) support throughout. Thank you also to my second supervisor, Joshua Einsle. While this strain of work didn't make it as far as this thesis, he has, with unabated enthusiasm, enabled my introduction to the world of Data Science which brings with it a new perspective and skills I will take forward with me.

Thank you to Mark Wildman for his invaluable support and training throughout this project in the lab and in understanding geochronological data, and for conducting the apatite and trace element analysis and processing of trace element data. Thanks also go to Matt Divers for their assistance with all things code related, Liene Spruženiece for her guidance and training during SEM analysis and for carbon coating of zircon samples, Connor Brolly for cutting and polishing of the thin sections, and Eilidh Milne for prior collection of the Abriachan granite sample.

Thank you also to Bailey Lathrop for their abundant energy and passion on field trips, and for being a delight to bump into in the department.

Thank you to my family for their ongoing support and belief, and for entertaining my insistence on pursuing research despite not always quite understanding what I'm up to. Particular mention goes to Katerina Braun for her support and encouragement during my final year of undergraduate study. I would like to thank all of the GES PGRs, especially those in room 414, for their camaraderie and shenanigans which made day to day research life that bit brighter. Thank you also to all those at GU Salsa and Latin Dance Society for their warmth and vibrance over the last two and a half years.

Finally, Chloe Gemmell, Neve Norris, Shona Swan, Gopikaa Vijayakumar and Puja Jadav cannot be thanked enough. They have been an amazing support network and their daily presence will be greatly missed as this chapter draws to a close. Special thanks also to Neve for being a top-notch flatmate, and Chloe for helping to keep each other sane during our many (many) hours of zircon related kerfuffle.

Author's declaration

I declare that, except where explicit reference is made to the contribution of others, that this dissertation is the result of my own work and has not been submitted for any other degree at the University of Glasgow or any other institution.

Careen MacRae

Chapter 1 Introduction

Collision magmatism and post-subduction magmatism (sensu Pearce *et al.* 1990; Richards 2009; Guo and Wilson 2019) are key components of the continental collision phase of the Wilson cycle. They are arguably a net contributor to continental crustal growth and its chemistry, and have implications for resource distribution and our understanding of collision dynamics and modern volcanic hazards (e.g., Annen *et al.* 2006; Richards 2009; Neill *et al.* 2015; Couzinié *et al.* 2016; Lebedev *et al.* 2021; Gómez Frutos and Castro 2023).

Current understanding of collision and post-subduction magmatism posits derivation from a mix of sources, including (a) the asthenosphere, due to upwelling and decompression melting, (b) the mantle lithosphere, due to heat advection from the upwelling asthenosphere, and (c) the crust, due to assimilation into existing magmas during storage and ascent and direct crustal melts (e.g., Annen et al., 2006; England and Thompson, 1984; Kaislaniemi et al., 2014). Their mechanisms, however, remain equivocal. Asthenospheric upwelling and mantle melting is suggested to be triggered by slab break off following collision (Davies and von Blanckenburg 1995; Keskin 2003), large scale lithospheric delamination (Pearce *et al.* 1990; Turner *et al.* 1992; Kay and Kay 1993), small scale delamination (Elkins-Tanton 2007; Kaislaniemi *et al.* 2014), and asthenospheric convection around topographic gradients at the base of the lithosphere (Missenard and Cadoux 2012). Crustal melts have been attributed to compression melting of hydrous phases (Allen *et al.* 2013), crustal thickening and radiogenic heating (England and Thompson 1984, 1986), and deep subduction of crustal material (Zhao *et al.* 2013).

The Caledonian-Appalachian orogenic belt is an example of a Lower Palaeozoic collisional setting in which Baltica, Laurentia, and peri-Gondwanan continental masses came together during subduction and closure of the Iapetus Ocean (Bird et al., 2013; Dewey et al., 2015; Dewey and Strachan, 2003). The Caledonian Orogeny (*sensu lato*) was marked by extensive magmatic activity during active subduction, island arc accretion and continental collision (Van Staal *et al.* 1998; Fowler *et al.* 2008; Oliver *et al.* 2008).

Plutons broadly associated with continental collision are expressed in the northern Scottish Highlands as the inconsistently defined “Newer Granites” (Fig. 1.1; Read, 1961; Soper, 1986; Stephens and Halliday, 1984). These have traditionally been associated with subduction processes, but also slab breakoff and upwelling of the asthenosphere following continental collision of Baltica and Laurentia (Atherton and Ghani 2002). Their petrogenesis has been ascribed to melting of the subduction-modified sub-continental lithospheric mantle (SCLM), with varying degrees of crustal input (e.g., Fowler et al., 2008; Neilson et al., 2009). However, traditional explanations do not sufficiently account for the spatial-temporal distribution of plutons, their petrogenesis in relation to associated mafic intrusions, or genesis of the Trans-Suture Suite intrusions across the Southern Uplands and Northern England (Fowler *et al.* 2008; Miles 2013; Searle 2021; Archibald *et al.* 2022).

Many of these intrusions are also spatially associated with the major orogen-parallel Great Glen strike-slip fault system (Hutton 1988; Hutton and McErlean 1991; Stewart *et al.* 2001; Milne *et al.* 2023). Intrusion ages of plutons have frequently been used to constrain the nature and timing of its displacement (Hutton 1988; Hutton and McErlean 1991; Rogers and Dunning 1991; Stewart *et al.* 2001). However, despite decades of research, there are still uncertainties regarding the absolute age and tectonic significance of some plutons (e.g., Ratagain, Lawrence et al., 2023, 2022). The largest plutonic complex, at Strontian (Fig. 1.1), has long been argued to have been emplaced during Great Glen Fault motion (Watson 1984; Hutton 1988), but several phases of intrusion at the complex are undated or existing data have never been peer reviewed (e.g., Paterson et al., 1993). Others, such as Helmsdale and Abriachan (Fig. 1.1) lack any robust geochronological, geochemical, and structural analysis. Additionally, published geochronology of Northern Highlands plutons is dominated by a single study, that of Rogers and Dunning (1991), whose emplacement ages have recently been challenged in the literature (Lawrence et al., 2022; Milne et al., 2023). As such, before delving deeper into the petrogenesis and geodynamic setting of these plutons, it is already apparent that there are significant data gaps and therefore an incomplete understanding of emplacement timing and mechanisms (Archibald et al., 2022; Milne et al., 2023).

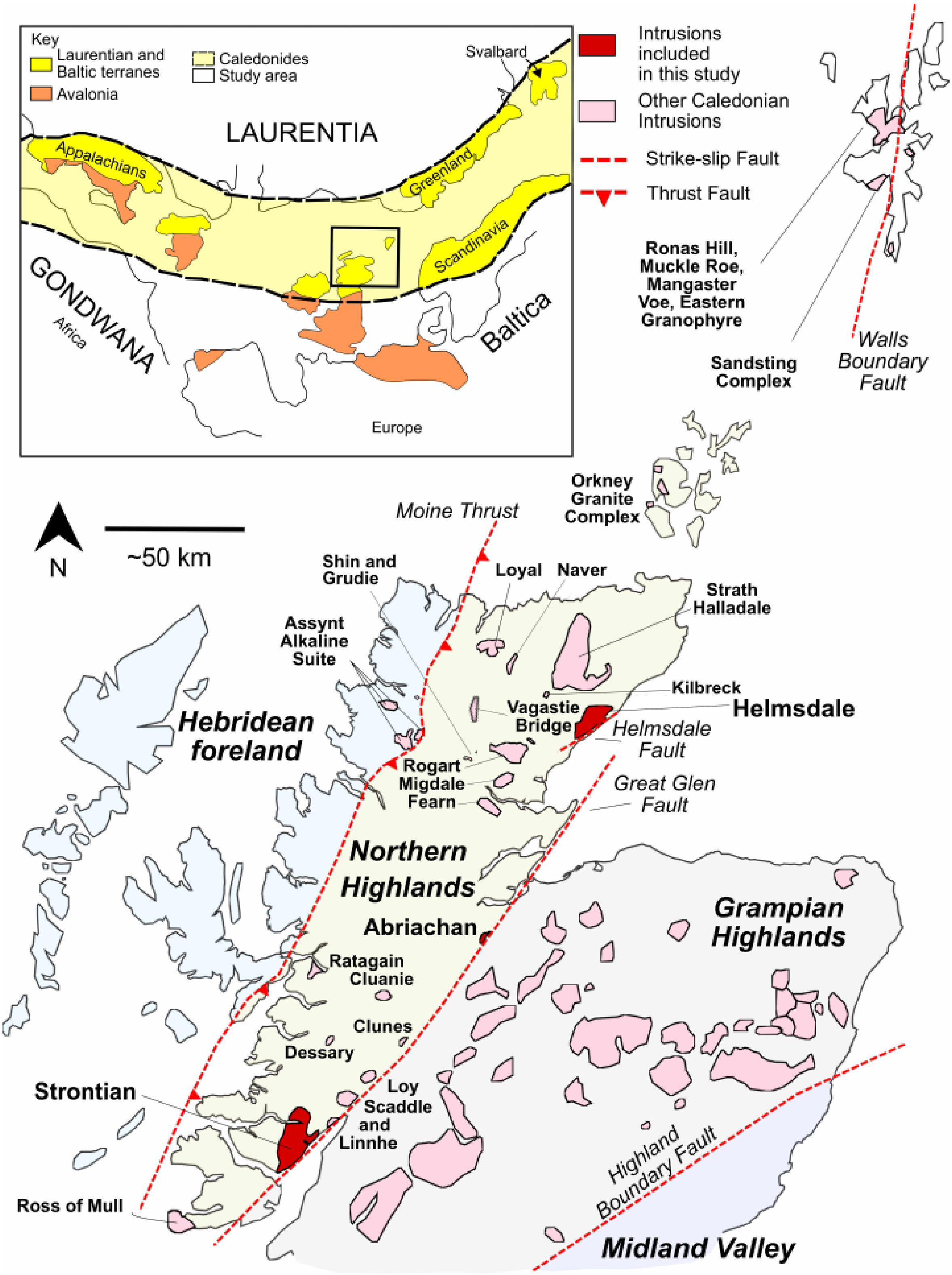

Figure 1.1 Map of Northern Scotland highlighting major faults and the distribution of Caledonian intrusions. Inset shows a Palaeozoic reconstruction highlighting the extent of the Caledonian mountain belt and terrane affinities. Map adapted from British Geological Survey (2016), Fowler et al. (2008), Lancaster et al. (2017), McKerrow et al. (2000), Searle (2021), Strachan et al. (2020a).

Recent studies have begun to review Caledonian “Newer Granite” paradigms and address these data gaps, applying internationally recognised petrogenetic and geodynamic models to the Caledonian Orogeny (Searle 2021; Archibald *et al.* 2022; Milne *et al.* 2023). Of particular relevance to this study is the Lower Crustal Hot Zone (LCHZ) model, also referred to as a Deep Crustal Hot Zone (DCHZ) or Trans-crustal Magmatic System, whereby magmas may undergo protracted crustal storage and processing by fractional crystallisation, assimilation and mixing (Hildreth and Moorbath 1988; Annen *et al.* 2006; Liu and Lee 2020; Lim *et al.* 2023). New in-situ U-Pb zircon geochronology data has enabled the discernment of a more prolonged zircon growth record and crustal processing of magma than previously recognised, allowing application of the LCHZ model to the Scottish and Irish Caledonides (Miles *et al.* 2014; Lancaster *et al.* 2017; Fritschle *et al.* 2018; Hines *et al.* 2018; Archibald *et al.* 2021, 2022; Milne *et al.* 2023).

The LCHZ model is yet to be tested across the Scottish Caledonides and has only been inferred in individual plutons in a few scattered recent U-Pb zircon studies as above, and older in situ mineral chemistry approaches (Oliver *et al.* 2008; Steinhoefel *et al.* 2008; Clemens *et al.* 2009; Bruand *et al.* 2014). Elsewhere, the evolution of magmas in the context of a LCHZ has relevance to system-scale resource distribution (e.g., Chiaradia, 2022, 2020), a point that has never been tackled in Scotland. This knowledge gap comes in spite of known occurrences of mineralisation, such as at Strontian (Pb, Zn, barite), Helmsdale (U, geothermal energy potential) and Abriachan (carbonatite-related fenitisation, geothermal energy potential) (Tweedie 1979; Garson *et al.* 1984; Kimbell 1986; Gillespie *et al.* 2013). Developing a more robust understanding of the Caledonian post-subduction magmatic system and its mineral occurrences will further both scientific understanding and address whether there is presently unknown potential for a UK supply of critical metals, in line with UK government Net Zero targets and British Geological Survey aims (UK Government 2022; Deady *et al.* 2023). In particular as most of our understanding and quantification of UK mineral resources comes from the British Geological Survey’s Mineral Reconnaissance Programme (1979-1995). Hence data are a generation old, and often lacking information on metals, and the derivation of metals, which have since become ‘critical’ (European Commission 2020; UK Government 2022).

The overarching purpose of this research is therefore to tackle some of the knowledge gaps which remain despite an upsurge in interest in Caledonian magmatism in recent years. In particular gaps relating to plutons of tectonic importance within the Great Glen Fault System of the Northern Highlands. My aims are to:

1) build on the recent body of work on Caledonian intrusions, by testing further intrusions across a wider geographical area for evidence of the operation of an LCHZ beneath the Northern Highlands and apply findings to our understanding of petrogenesis and geodynamics.

2) provide updated emplacement ages for intrusions of the Northern Highlands and discuss implications for the construction of large plutonic systems during the Caledonian Orogeny, and their relationship to geodynamics and the development of the Great Glen Fault System. These aims shall be fulfilled by the following objectives:

Objective a) Sample the Helmsdale, Abriachan and Strontian plutons; at Strontian sample both major phases and a suspected Caledonian minor intrusion.

Objective b) Laser Ablation – Inductively Coupled Plasma – Mass Spectrometry (LA-ICP-MS) U-Pb dating of zircons for each sample, and identify xenocrystic, antecrystic and emplacement populations of zircon.

Objective c) LA-ICP-MS U-Pb apatite dating to constrain emplacement timing for the minor intrusion which may lack a zircon record of emplacement.

Objective d) age constrained LA-ICP-MS trace element analysis of zircon to identify chemical evolution of magma and distinguish zircon populations.

Objective e) Synthesize geochronology results with existing data from the Northern Highlands to suggest an updated potential framework for late Caledonian magmatism and its geodynamic implications.

Chapter 2 Background

2.1 Geology of the Northern Highlands

The nature of basement rock in the Northern Highlands is evidenced only by orthogneiss-dominant inliers (Fig. 2.1). Unconformable and depositional field relationships identify these as the basement on which the Wester Ross and Loch Ness supergroups were deposited atop (Holdsworth 1989; Krabbendam *et al.* 2014). Some inliers also display fault-bounded contacts with the surrounding metasediment (Fig. 2.1; Holdsworth, 1989; Tanner, 1970). All were uplifted to their current structural level during Caledonian orogenesis (Bird *et al.* 2023). These inliers are typically believed to be Laurentian in origin and represent a part of its margin based on lithology and comparable Archaean protolith ages (e.g., Friend et al., 2008), though recent work has identified potential derivation from Baltica for some (Bird *et al.* 2023; Strachan *et al.* 2020b).

The Northern Highlands are dominated by psammite and semi-pelite of the Morar Group (Wester Ross Supergroup), and Glenfinnan and Loch Eil Groups (Loch Ness Supergroup) (Fig. 2.1). Sediments were deposited in a Neoproterozoic basin in mostly shallow marine environments, though the Morar Group also contains fluvial deposits (Krabbendam *et al.* 2008, 2022). Metamorphism affected these groups during multiple orogenic events: the Renlandian, 950 – 940 Ma (Morar Group only) (Bird *et al.* 2018); Knoydartian, 840 – 725 Ma (Rogers *et al.* 1998; Cawood *et al.* 2015); and Caledonian (see section 2.2). The Morar Group is divided from the overlying Loch Ness Supergroup by the Sgurr Beag thrust, while the Glenfinnan and Loch Eil Groups are stratigraphically conformable (Fig. 2.1; Krabbendam et al., 2022). Additionally, the Knoydartian age West Highland Granite Gneiss suite outcrops approximately along the Glenfinnan-Loch Eil Group boundary and were also affected by Caledonian deformation (Johnstone 1975; Barr *et al.* 1985; Rogers *et al.* 2001).

The Northern Highlands are bounded to the north-west by the Moine Thrust, a Knoydartian age structure reworked as the Caledonian orogenic front (Krabbendam *et al.* 2018, 2022) and to the south-east by the Great Glen Fault (GGF), developed during late Caledonian strike slip faulting (Stewart *et al.* 1999). Though the GGF has been previously interpreted as a terrane boundary,

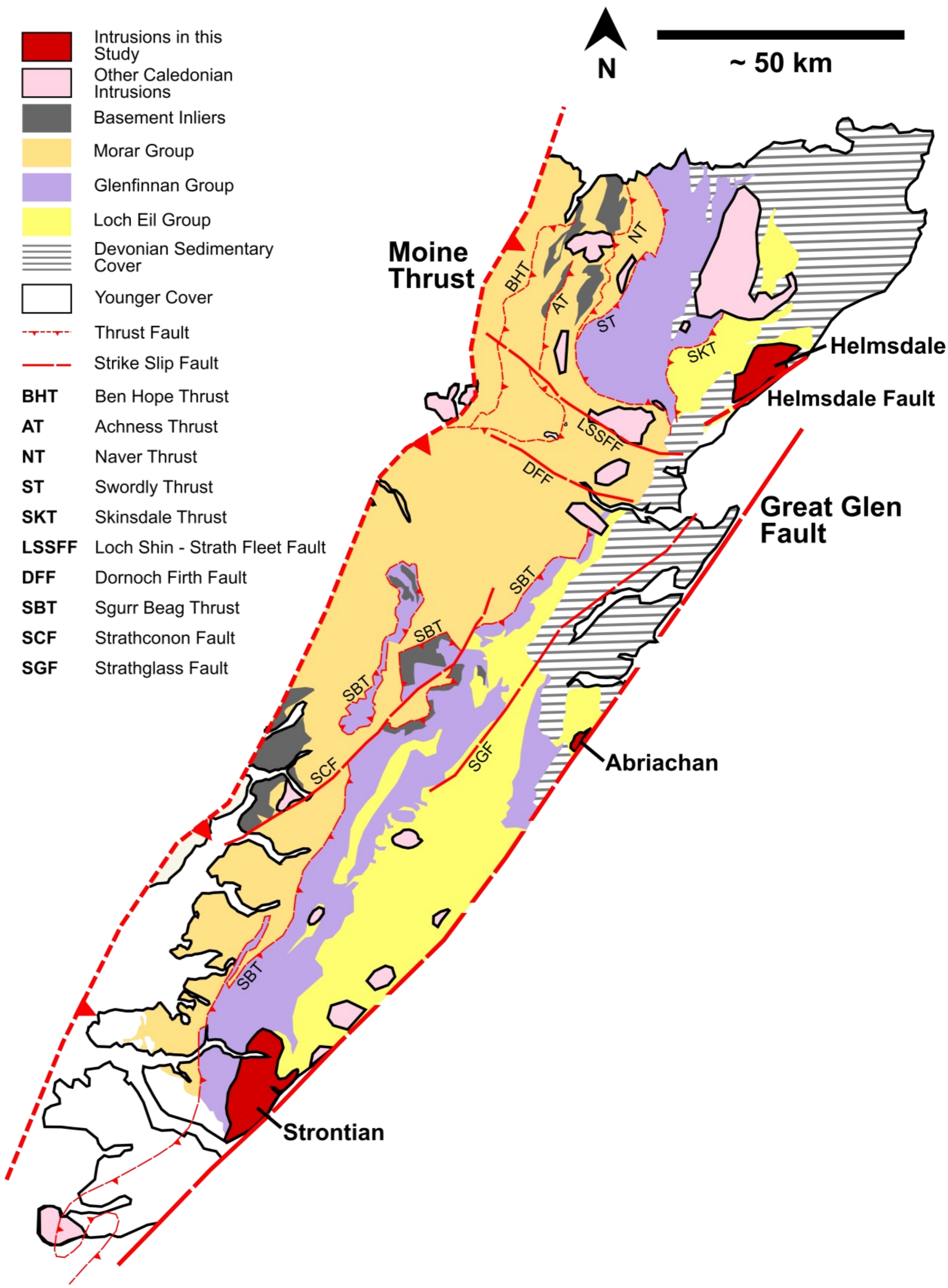

Figure 2.1 Map of the Northern Highlands of mainland Scotland highlighting key thrust and strike slip faults active during the Caledonian Orogeny, Proterozoic basement units and Archaean inliers, Caledonian intrusions and younger cover. Map adapted from British Geological Survey (2016), Fowler et al. (2008), Holdsworth et al. (2015), Krabbendam et al. (2022), Mazza et al. (2018), Milne (2019), Neill and Stephens (2009), Searle (2021), Strachan et al. (2020a, 2010).

correlation of Knoydartian deformation between the Wester Ross and Loch Ness supergroups, and the Dava and Glen Banchor successions in the Grampian Highlands refutes this (Noble *et al.* 1996; Highton *et al.* 1999; Oliver *et al.* 2000; Strachan *et al.* 2002).

Syn- and post- Caledonian orogenic collapse Devonian sediments of the Old Red Sandstone (ORS) cover much of coast of Caithness and the Moray Firth, Orkney, and extends offshore (Fig. 2.1; P. F. Friend et al., 2000). The ORS in this region comprises the Orcadian Basin, and grades upwards from dominantly alluvial fan deposits in fault-bounded basins, to dominantly alluvial, fluvial and lacustrine deposits with limited marine and aeolian deposits (Rogers *et al.* 1989; P. F. Friend *et al.* 2000; Woodcock and Strachan 2012). Carboniferous intrusions, Paleogene intrusions and lavas and Jurassic sedimentary cover also occur but are not discussed further in this study (e.g., Thomson et al., 1999; Upton et al., 2004).

2.2 Tectonic Framework and the Caledonian Orogeny

The Iapetus ocean developed during rifting of supercontinent Rodinia c. 590 – 550 Ma (Oliver *et al.* 2008; Robert *et al.* 2021), separating the continents Laurentia (modern Greenland, North America, Scotland and Ireland), Baltica (Scandinavia and central Europe), and Gondwana (Africa and South America) (Fig. 1.1 inset). Development of basin wide sedimentation accompanied Iapetus rifting (e.g., Krabbendam et al., 2022). Further rifting of peri-Gondwanan terranes led to the development of the Rheic ocean. Rifted terranes include Avalonia (modern England, Wales, and northern Europe), and Ganderia (Appalachians, North America) (Domeier 2016).

Onset of subduction within Iapetus and thus its closure began c. 515 – 505 Ma, though understanding of the number and orientation of subduction zones and associated sedimentary basins during closure is limited (van Staal and Zagorevski 2023; Gasser *et al.* 2024). Closure of the Iapetus terminated with the amalgamation of aforementioned continents and development of the Caledonian Orogenic Belt stretching from the Appalachians, east Greenland and the British Isles to Scandinavia (Fig. 1.1). In the Scottish and Irish geological literature, the Caledonian Orogeny is typically described as a series of discrete orogenic events, discussed below.

2.2.1 The Grampian Orogeny

The Grampian Orogeny followed a period of south directed subduction (Dewey 2005) and subsequent north-west directed obduction of the Unst and Highland Boundary ophiolites onto the Laurentian margin c. 488 - 484 Ma (Chew *et al.* 2010; Crowley and Strachan 2015). Orogenesis was driven by collision of an intra-oceanic arc with the eastern Laurentian margin and caused regional metamorphism until c. 465 Ma (Oliver *et al.* 2000; Stewart *et al.* 2017). It is postulated that the orogenic front to this event is buried within the Northern Highlands (Dallmeyer *et al.* 2001; Dunk *et al.* 2019). The arc is considered to have accreted to Laurentia due to its buoyancy and so is thought to constitute the basement of Scotland's Midland Valley, although this is uncertain due to the extent of younger sedimentary cover (Badenszki *et al.* 2019) (Fig. 1.1). The Ballantrae ophiolite was obducted south of the Midland Valley c. 478 – 464 Ma during the latter stages of the Grampian Orogeny (Stone and Rushton 2018), and orogenesis was then followed by rapid exhumation (Oliver *et al.* 2000). The Grampian Orogeny is suggested to be broadly equivalent to arc accretion identified in the Appalachian mountains and Newfoundland (e.g., C. R. L. Friend et al., 2000; van Staal et al., 2009).

Large scale deformation, including nappe formation, developed throughout the Dalradian metasediments of the Grampian Highlands (Chew and Strachan 2014; Tanner 2014). In the Northern Highlands, preserved Grampian deformation is mostly limited to the eastern parts of the Sgurr Beag and Naver nappes, bound to the west by the Sgurr Beag and Naver thrusts respectively (Fig. 2.1). Deformation is recorded by syn-kinematic pegmatites (Cutts *et al.* 2010), regional migmatisation synchronous with folding (Kinny et al., 1999; Strachan et al., 2020a), and possible Grampian age fabrics and mineral lineations (Holdsworth and Roberts 1984; Rogers *et al.* 2001; Law *et al.* 2021). However, fabrics and lineations may have been overprinted or re-orientated by later deformation, and their assignation to Grampian deformation is less equivocal (Law *et al.* 2021). Grampian folding in the Naver and Sgurr Beag nappes is suggested by Strachan et al., (2020) to be composite, deformed also by Scandian orogenesis (section 2.2.3). As such, the nature and extent of Grampian deformation in the Northern Highlands is uncertain (Krabbendam *et al.* 2011). Peak metamorphic conditions of ~650 – 700 ^{0}C at c. 471 – 467 Ma in mainland Scotland, and c. 485 Ma in Shetland (Fig. 1.1) are recorded by zircon U-Pb, monazite U-Pb and garnet Lu-Hf, Sm-Nd and in situ geochemical analyses (C. R. L. Friend *et al.* 2000; Oliver *et al.* 2000; Baxter *et al.* 2002; Cutts *et al.* 2010; Walker *et al.* 2021). The Grampian Orogeny may have involved collision and re-accretion of rifted peri-Laurentian masses, including a further intra-oceanic arc, onto the Laurentian passive margin, highlighting the uncertainty surrounding Iapetus subduction systems (Dunk *et al.* 2019; Gasser *et al.* 2024).

Magmatism associated with the Grampian orogeny comprises foliated mantle-derived gabbros (with mantle-like $^{87}Sr/^{86}Sr_i$ ratios) and crust-derived S-type granitoids (with upper-crustal $^{87}Sr/^{86}Sr_i$, $^{206}Pb/^{204}Pb$ and $\delta^{18}O$) located in the Grampian Highlands (Pankhurst 1969; Harmon *et al.* 1984; Oliver *et al.* 2008). This magmatism has been variably attributed to e.g., crustal thickening and heat advection from the asthenosphere (Oliver *et al.* 2008), decompression melting of the asthenosphere and resulting heat advection from the mantle and gabbroic magmas to the crust, driven by slab breakoff (Mark *et al.* 2020), lithospheric thinning due to extension-driven orogenic collapse (Viete *et al.* 2010), and lithospheric thinning due to slab rollback (Johnson *et al.* 2017). These intrusions are typically associated with contact metamorphism (Pattison and Goldsmith 2022).

While some authors suggest subduction maintained a single direction throughout the Caledonian Orogeny (Johnson *et al.* 2017; Dunk *et al.* 2019; Mark *et al.* 2020; Searle 2021), the end of accretion is typically associated with a reversal in subduction polarity from south dipping to north/north-west dipping beneath Laurentia (Bird et al., 2013; Dewey and Shackleton, 1984; Ryan and Dewey, 2004).

2.2.2 The Grampian-II Event

Ages of prograde metamorphism at c. 450 Ma in the Northern Highlands were first identified by Bird et al., (2013). The metamorphic ages were recorded in garnets within the Morar and Glenfinnan Groups (Fig. 2.1), and thrusting in a proto Sgurr Beag-Naver Nappe was inferred to explain metamorphism (Bird et al., 2013). Further ages spanning c. 458 – 446 Ma within the Morar Group have been identified by U-Pb zircon, U-Pb monazite and ^{40}Ar-^{39}Ar muscovite analyses of pegmatites and reworked of gneisses and metasediments (Cawood *et al.* 2015). In Shetland (Fig.

1.1), similar ages of c. 451 - 462 Ma, c. 450 Ma, and c. 458 – 442 Ma have been identified by U-Pb monazite, Rb-Sr mica, and Lu-Hf and Sm-Nd garnet analyses respectively (Cutts *et al.* 2011; Walker *et al.* 2016, 2021). Although not formally ascribed to the Grampian–II phase, monazite U-Pb ages of c. 445 Ma were identified by Mako et al. (2019).

These ages were initially interpreted as the result of collision of a micro-continental fragment with the Laurentian margin c. 450 Ma and suggested to be analogous to the Appalachian Taconic-II Orogeny (Bird et al., 2013). However this is not conclusive as no remnants of a continental fragment or arc have been found in Scotland, and possible associated fragments in the Scandinavian Caledonides are only loosely suggested (Bird et al., 2013; Cawood et al., 2015).

More recent work postulates that these ages are part of a more continuous period of metamorphism due to the initial collision of uneven Laurentia and Baltica continental margins, prior to orogen-wide hard collision and attempted subduction of continental material (Slagstad and Kirkland 2018; Milne *et al.* 2023). This is supported by monazite-xenotime thermometry which indicates that the Northern Highlands experienced temperatures of at least 400 – 500 ^{0}C at 445 – 440 Ma (Mako *et al.* 2024).

Magmatism at this time is discussed in section 2.2.3.

2.2.3 The Scandian Orogeny

Final closure of Iapetus occurred via sinistrally oblique collision of Laurentia and (Avalonia-)Baltica, i.e. the Scandian Orogeny, and subduction of the Baltic margin (Barnes et al., 2023; Möller et al., 2024; Soper et al., 1992; Strachan et al., 2020a). This was followed by collision with peri-Gondwanan terranes and closure of the Rheic ocean, though this is now more typically defined as Acadian than end-Caledonian orogenesis (e.g., van Staal et al., 2021). Onset of the Scandian Orogeny in Scotland is dated at c. 437 Ma (Freeman et al., 1998; Strachan et al., 2020a). However, Slagstad and Kirkland (2018) identified onset of metamorphism in the Scandinavian Caledonides up to ~ 10 Myr earlier than had previously been recognised due to initial arrival of promontories along the Baltica margin. Milne et al. (2023) interpreted this proposal, with their identified magmatic ages and metamorphic ages in the literature spanning c. 450 – 440 Ma (see section 2.2.2), as evidence for a similar scenario in in the Northern Highlands. Milne et al. (2023) conclude that a period of crustal thickening occurred from c. 450 Ma onwards before hard continental collision with subduction of continental material began c. 437 Ma (Strachan et al., 2020a).

Regardless of when the Scandian Orogeny began, widespread regional metamorphism occurred up to sillimanite-migmatite grade, with a peak temperature of 650 – 700 ^{0}C at c. 425 Ma within the Naver nappe (Kinny *et al.* 1999; Mako 2019). It is suggested that this metamorphic peak is representative of peak temperature but not peak crustal thickness, as it followed decompression from 8 – 9 kbar to 6 – 7 kbar, and that heating was driven by advection from intruding magma (Mako 2019; Mako *et al.* 2024). Temperatures over 600 ^{0}C, and ductile deformation along the Moine thrust zone persisted until c. 420 – 415 Ma indicating a protracted Scandian deformation history (Freeman *et al.* 1998; Dallmeyer *et al.* 2001; Mako *et al.* 2024; Strachan *et al.* 2020a).

Crustal shortening was accommodated by nappe formation and ductile thrust development. The Moine thrust defines the Orogenic front, and has total movement of > 100 km, possibly accompanied by intra-nappe shortening of > 50 km (Elliott and Johnson 1980; Krabbendam *et al.* 2008, 2022). Significant thrust development included the inversion of metamorphic gradients after peak metamorphism and temperature was reached (Thigpen et al., 2021). Shortening and inversion was accommodated by folding on the stacked (from structurally highest to lowest) Skinsdale, Naver, Sgurr Beag, Ben Hope and Moine nappes and shearing on the associated thrusts (Fig. 2.1; Ashley et al., 2015; Mako, 2019). Further southwest, shortening was accommodated by motion on the Sgurr Beag thrust and upright folding within the Moine and Sgurr Beag nappes (Fig. 2.1, 2.2; Strachan and Evans, 2008).

Final out of sequence thrust deformation at c. 425 Ma in the structurally higher nappes is suggested to have been enabled by weakening of the hinterland crust due to magmatic intrusions (Mako 2019; Mako *et al.* 2024). Current understanding of the transition from a thrust-dominant to transpression-dominant environment is that early strike slip faulting overlapped in time with thrusting on a basal detachment, with strike slip motion and the Great Glen Fault System (Fig. 1.1,

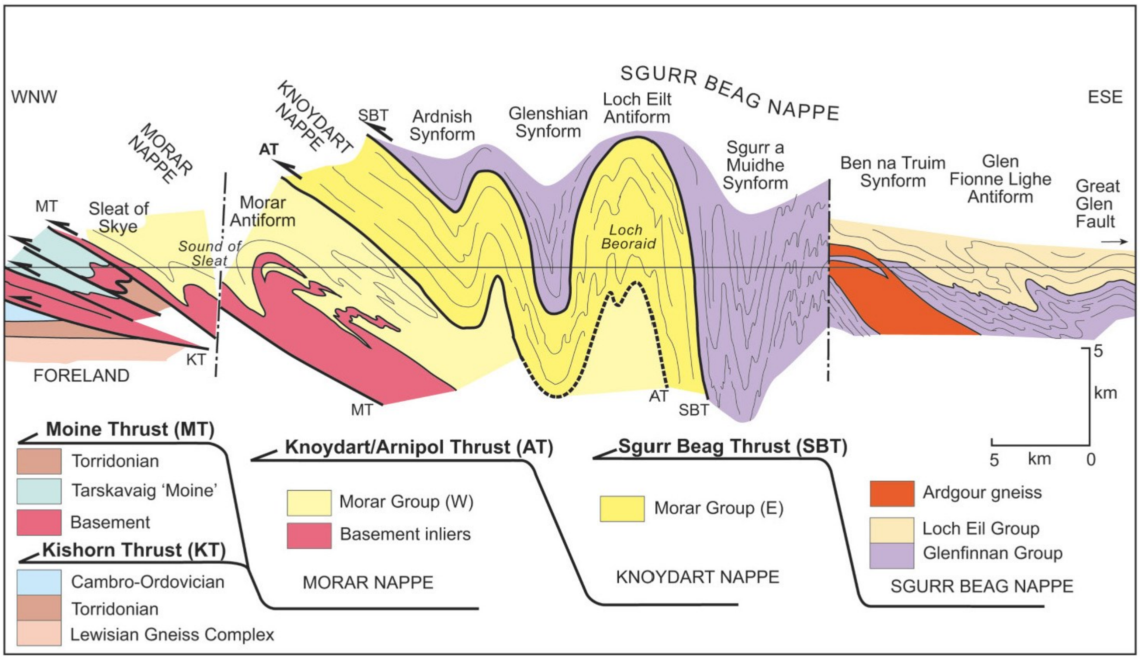

Figure 2.3 From Powell and Friend (2010), schematic cross section of the Northen Highlands from Glenfinnan (ESE) to Morar (WNW). Highlights where the Morar and Glenfinnan Groups, and Sgurr Beag and Knoydart/Arnipol thrusts have been affected by Scandian upright folding (Highland 'Steep belt', west of and including the Sgurr a Muidhe Synform) compared with where the Glenfinnan and Loch Eil Groups to the ESE (Highland 'flat belt'). Groups structurally below the Moine thrust shown (Torridonian, Tarskavaig, Cambro-Ordovician) are those now considered part of the Morar Group (Krabbendam *et al.* 2022).

2.1) becoming dominant by 420 - 415 Ma (Kocks *et al.* 2014; Holdsworth *et al.* 2015; Strachan *et al.* 2020a). See section 2.3.3 for further comments. This was also accompanied by strike slip motion on the Highland Boundary Fault further south and west along the Laurentian margin (Fig. 1.1; e.g., McKay et al., 2024).

Deformation and thickening were followed by rapid uplift and erosion, with total exhumation in the hinterland estimated at around 32 – 38 km (Ashley *et al.* 2015; Mako *et al.* 2019; Spencer *et al.* 2020). Cooling rates based on ^{40}Ar-^{39}Ar thermochronological analyses are estimated at 9 – 31 ^{0}C Myr^{-1} from c. 425 to 414.4 Ma, increasing to ~ 45 ^{0}C Myr^{-1} from 414.4 to c. 411 Ma, and then maintaining 45 ^{0}C Myr^{-1} or increasing to as much as 90 ^{0}C Myr^{-1} to reach surface temperatures by 407 – 403 Ma at the onset of sedimentation (Spencer *et al.* 2020). Exhumation may have been enhanced by lower crustal flow and gravitational collapse, and may also be related to the onset of transpressional faulting (Spencer *et al.* 2021; Mako *et al.* 2024). The duration of the Scandian Orogeny described above is consistent with a location for the Northern Highlands on the periphery of the orogen at this time, with the orogen core further northeast (Strachan *et al.* 2020a).

Previous literature has suggested the period from ~450 - ~430 Ma is one of magmatic quiescence (Oliver *et al.* 2008; Miles *et al.* 2016; Archibald *et al.* 2022). This is now refuted by a range of data indicating arc magmatism was active during his time, including emplacement of the Muckle Roe (438 Ma), Glen Loy and Linnhe (441 Ma) intrusions, and Cluanie pluton antecrysts dating c. 438 – c. 447 Ma (Lancaster *et al.* 2017; Milne 2019; Milne *et al.* 2023) (Table 2.1, Fig. 1.1). Milne et al. (2023) interpret this period as one of active arc magmatism and development of a lower crustal hot zone, but limited escape and emplacement of magma due to Scandian collision from c. 450 Ma. Emplacement that does occur during this time is limited by the availability of structural ascent pathways (Neill and Stephens 2009; Goodenough *et al.* 2011; Milne *et al.* 2023). See sections 2.3.2 and 2.3.3 for further discussion.

2.3 Caledonian Intrusions in the Northern Highlands

Magmatic intrusions in the Northern Highlands, (as described in section 2.2) and particularly those aged 435 Ma or younger, are often termed the ‘Newer Granites’ (Fig. 1.1, 2.1; Read, 1961). However, this term is no longer fit for purpose as its classification is demonstrably inaccurate. Many plutons deemed by Read (1961) to have been emplaced ‘forcefully’ are shown to have been emplaced via structural pathways (e.g., Stewart et al., 2001), and emplacement along ring faults is now regarded as incorrect (Muir and Vaughan 2017). The updated intrusion age-based definition of Pankhurst and Sutherland (1982) is also no longer applicable following the greater age range of intrusions now identified (e.g., Lancaster et al., 2017; Milne et al., 2023). Furthermore, geochemical work has identified that the intrusions do not all share the same melting, evolution and emplacement history and so are not necessarily a cohesive group (e.g., Brown et al., 2008; Fowler et al., 2008; Stephens and Halliday, 1984). Thus, they will be referred to as Caledonian Intrusions throughout, as per Milne et al. (2023).

2.3.1 Caledonian Intrusions: Petrogenesis and Geochronology

Caledonian Intrusions in the Northern Highlands are summarised in Table 2.1 and Fig. 1.1. Intrusions are dominantly comprised of granodiorite, with some granite, diorite, tonalite and syenite (Fowler *et al.* 2008), though some contain more significant mafic components e.g., Glen Loy (Johnstone and Mykura, 1989) and Glen Dessarry (Richardson, 1968). Additionally some are composite and comprise multiple lithologies e.g., Strontian, (Hutton, 1988; Sabine, 1963), Rogart (Kocks et al., 2014) and Ratagain (Lawrence et al., 2022;). Associated mafic to felsic minor intrusions also occur, including vein complexes (Fettes and Macdonald 1978; Smith 1979).

Northern Highlands Caledonian intrusions are commonly associated with lamprophyres and appinites. Appinites (hornblende diorite, pyroxene-hornblende diorite to gabbro or hornblendite cumulate) typically occur at pluton peripheries and are younger than or coeval with the felsic intrusions (Rock and Hunter 1987; Fowler 1988; Rock *et al.* 1988; Fowler and Henney 1996). The occurrence of appinites, frequent occurrence of mafic enclaves and a dominantly calc-alkaline, I-type chemistry of intrusions are key indicators of the mantle derivation and water-rich nature of magmas (Halliday *et al.* 1987; Holden *et al.* 1987; Fowler *et al.* 2008). Intrusions are characteristically high in Ba, Sr and other Large Ion Lithophile Elements (LILE), and light Rare Earth Element (REE)-enriched. In addition to Sr-Nd-O isotopic data this chemistry has constrained the mantle source character to subduction-modified sub-continental lithospheric mantle (SCLM), with variable input from subducted pelagic sediments (Stephens and Halliday 1984; Fowler *et al.* 2001, 2008; Neilson *et al.* 2009).

A limited number of Northern Highlands intrusions have adakite-like La/Yb and Sr/Y signatures, including the Cluanie and Clunes plutons (Neill and Stephens 2009; Archibald *et al.* 2022; Milne *et al.* 2023). This signature is favoured by Milne et al. (2023) to derive from fractionation of hornblende amphibole ± garnet during magma storage and processing within a Lower Crustal Hot Zone (LCHZ) prior to magma ascent and emplacement. The broadly homogenised chemistry of intrusions is also consistent with LCHZ genesis of magmas (Milne *et al.* 2023).

Table 2.1 Geochronology of Northern Highlands intrusions west of the Great Glen Fault and Walls Boundary Fault systems, adapted from Milne et al. (2023). Methodology is U-Pb unless otherwise stated. Z = zircon, MB = molybdenite, M = monazite, B = baddeleyite, T = titanite; ID-TIMS = isotope dilution - thermal ionisation mass spectrometry, LA-ICP-MS = laser ablation – inductively coupled plasma – mass spectrometry, SHRIMP = sensitive high resolution ion microprobe. *Unpublished MSc thesis.

Granitoid	Types	Emplacement timing (Ma)	Methodology	Antecrystic zircon growth (Ma)	Reference
Glen Dessarry	Syenite; stock	447.9 ± 2.9	Z ID-TIMS	Not identified	Goodenough *et al.* (2011)
Glen Loy*	Gabbro to granite; stock	441.6 ± 2.3	Z LA-ICP-MS	~457 - 447	Milne (2019)
Linnhe*	Granite; pluton dissected by Great Glen Fault	441.3 ± 2.3	Z LA-ICP-MS	~462 - 450	Milne (2019)
Muckle Roe, Shetland	Granophyre; stock	438.0 ± 7.6	Z LA-ICP-MS	Not identified	Lancaster *et al.* (2017)
Naver Suite incl. Vagastie, Creag nan Suibheag, Creag Mhor	Granite to monzo-diorite; sheets	432.4 ± 0.5 to 425.7 ± 0.2	Z ID-TIMS Z SHRIMP	*Up to ~455 Ma*	Strachan *et al.* (2020a), Kinny *et al.* (2003)
Orkney granite complex	Granite, pegmatite, aplite; sheets	431.9 ± 0.5 to 428.5 ± 0.3	Z ID-TIMS	Not identified	Lundmark *et al.* (2019)
Cluanie	Trondhjemite; stock	431.9 ± 1.7	Z LA-ICP-MS	~447 - 438	Milne et al. (2023)
Assynt Alkaline Suite	Syenite and other alkaline rocks; small plutons, sheets, stocks	431.1 ± 1.2 to 429.2 ± 0.5	Z ID-TIMS	Not identified	Goodenough *et al.* (2011)
Grudie Bridge and Loch Shin	Monzogranite; stock and minor intrusions	429.9 ± 5.2 to 427.9 ± 2.8	MB Re-Os TIMS	Not identified	Holdsworth *et al.* (2015)
Clunes	Tonalite; sheet	427.8 ± 1.9	Z ID-TIMS	Not identified	Stewart *et al.* (2001)

Ronas Hill, Shetland	Granophyre, minor gabbro and diorite; stock, sheets	427.5 ± 5.1	Z LA-ICP-MS	Not identified	Lancaster *et al.* (2017)
Loch Loyal	Syenite and associated rocks; pluton	426 ± 9	Z ID-TIMS	Not identified	Halliday *et al.* (1987)
Strath Halladale	Ultramafic to granite; pluton	426 ± 2	M ID-TIMS	Not identified	Kocks *et al.* (2006)
Glen Scaddle	Mafic to granite; stock	426 ± 3	Z ID-TIMS	Not identified	Strachan & Evans (2008)
Rogart	Ultramafic to granite; pluton	425 ± 1.5	Z ID-TIMS	Not identified	Kocks *et al.* (2014)
Ratagain	Ultramafic to granite; stock	425 ± 3	Z+B ID-TIMS	Not identified	Rogers & Dunning (1991)
Strontian	**Appinite to granodiorite (Sunart); pluton**	**425 ± 3**	**Z+T ID-TIMS**	***Possible ~440 - 436***	**Rogers & Dunning (1991)**
	Biotite granite (Sanda)	**418 ± 1**	**M unknown**	**Not identified**	**Paterson *et al.* (1993)**
Abriachan	**Granite; stock**	**n/a**	**n/a**	**n/a**	**n/a**
Helmsdale	**Granite; pluton**	**c. 420**	**Z ID-TIMS**	**Not identified**	**Pidgeon and Aftalion (1978)**
Ross of Mull	Appinite to granite; pluton	418 ± 5	Z SHRIMP	~432 - 430	Oliver *et al.* (2008)
Rosemarkie	Leucogranite veins	400.8 ± 2.6	Z+M ID-TIMS	Not identified	Mendum & Noble (2010)

Evolution of magmas prior to final emplacement is constrained by REE patterns and Sr-Nd isotope data, and shown to be controlled by fractionation and varying degrees of crustal contamination (Fowler *et al.* 2008). Crustal contamination is by assimilation of either Wester Ross and Loch Ness supergroup metasediments, or Archaean basement, and additionally evidenced by the occurrence of zircon xenocryst inheritance (Pidgeon and Aftalion 1978; Halliday *et al.* 1979; Fowler *et al.* 2008; Paterson *et al.* 1992a).

In situ chemical analysis is consistent with assembly of plutons in batches from a pre-existing mush, consistent with the multiple phases within plutons seen in the field (McLeod *et al.* 2011; Bruand *et al.* 2014). This is also supported by study of magnetic fabrics in the Ratagain pluton, indicative of incremental batch assembly over time (Lawrence *et al.* 2022). Emplacement is typically understood to be at mid to upper crustal levels (e.g., Holdsworth et al., 1999; Lawrence et al., 2023) though quantitative geobarometry is limited (Tyler and Ashworth 1982; Neill and Stephens 2009; Matthews *et al.* 2023).

Existing geochronology of Caledonian intrusions is summarised in Table 2.1. The record is dominated by U-Pb zircon analyses as Rb-Sr mica-whole rock dating, previously commonly used to date Caledonian intrusions elsewhere in Scotland, have been largely determined to date cooling histories instead of emplacement ages due to lower closure temperatures (e.g., Rogers and Dunning, 1991; Thirlwall, 1988). ^{40}Ar-^{39}Ar mineral ages also aid constraint of rapid cooling and uplift following peak Scandian orogenesis (Torsvik *et al.* 2003). Furthermore, the record is dominated by a single U-Pb zircon Air Abrasion – Isotope Dilution-Thermal Ionisation Mass Spectrometry (AA-ID-TIMS) study by Rogers and Dunning (1991), following similar regional zircon study by Pidgeon and Aftalion (1978). AA-ID-TIMS data still provides the most recent or robust dates available for some intrusions (Table 2.1; e.g., Halliday et al., 1979; Stewart et al., 2001; Strachan and Evans, 2008).

A concern common to many AA-ID-TIMS ages is the use of small numbers of grains when some aliquots failed to produce satisfactory concordant ages, which at times has led to reliance on discordant analyses or those which show Pb loss concordia trends (e.g., Strontian, Rogers and Dunning, 1991). The technique's limited capacity to account for zircon growth zones of a potential range of ages compared to more recent Chemical Abrasion – Isotope Dilution – Thermal Ionisation Mass Spectrometry (CA-ID-TIMS) is also a concern (Mattinson 2005; Gaynor *et al.* 2022). Often, no cathodoluminescence imaging was conducted to provide textural control of zircon despite previously known evidence for inheritance (Pidgeon and Aftalion 1978; Halliday *et al.* 1979). Recent studies have therefore begun to question to validity of these dates, highlighting where studies involving limited aliquots may not capture the full story recorded by zircon ages (Milne *et al.* 2023), and where geochronology is inconsistent with interpretations drawn from structural data (Lawrence *et al.* 2022).

Some Northern Highlands intrusions have updated U-Pb zircon CA-ID-TIMS ages (Goodenough et al., 2011; Lundmark et al., 2019; Strachan et al., 2020a; Table 2.1). While these ages are typically more precise than AA-ID-TIMS studies, they are often still reliant on a small number of grains (e.g., Loch Loyal, Goodenough et al., 2011). Granites, including some in the Caledonides, have been shown to have been assembled in batches and experienced prior processing and storage, thus reliance on limited grain numbers risks bias towards antecrystic ages (Fritschle *et al.* 2018; Archibald and Murphy 2021; Lim *et al.* 2023).

On top of the lack of robustness of some past studies, the geochronological record of Caledonian intrusion is incomplete. Only a small number of in situ geochronology studies of Caledonian Intrusions exist (Kinny *et al.* 2003; Oliver *et al.* 2008; Lancaster *et al.* 2017; Archibald and Murphy 2021; Milne *et al.* 2023). Of these, only Milne et al. (2023) consider the evidence for and role of an LCHZ, though extended ranges of magmatic zircon U-Pb ages are also identified by the data of Kinny et al. (2003). Many intrusions still rely on an AA-ID-TIMS age (e.g., Ratagain, Rogers and Dunning, 1991), or on limited analyses or discordia ages (Pidgeon and Aftalion 1978), as noted above. Others are limited to unpublished ages (Paterson *et al.* 1993), or lack any geochronological analysis (e.g., Abriachan, the Glen Garry vein complex). Composite intrusions often have only one of their phases dated, without high precision modern CA-ID-TIMS dating to definitively determine emplacement history (e.g., Rogart, Kocks et al., 2014).

2.3.2 Caledonian Intrusions: Geodynamics

The dominant model used to explain Caledonian magma genesis In the Northern Highlands is as follows: magmatic quiescence from ~450 to ~430 Ma, continental collision at c. 430 Ma, slab break off beneath the Laurentia at c. 428 Ma, followed by upwelling of the asthenosphere into the gap and resultant melting of subduction-modified SCLM (Atherton and Ghani 2002; Fowler *et al.* 2008; Neilson *et al.* 2009). Further suggestions and adjustments have since been made to this model and include a) slab breakoff instead beneath the Grampian Highlands, possibly continuing from an initial tear closer to Baltica (Neilson *et al.* 2009); b) diachronous breakoff due to oblique convergence starting beneath Shetland and propagating through the Northern Highlands (at c. 430 Ma), Grampian Highlands and then Southern Uplands, with lateral asthenospheric flow and melting of SCLM and(or) the slab (Hildebrand *et al.* 2018; Archibald *et al.* 2022); and c) breakoff at c. 426 Ma to coincide with peak temperatures (Mako *et al.* 2019; Milne *et al.* 2023). An additional model by Oliver et al. (2008) implies the post-collisional development of a mantle wedge and arc magmatism. This is not observed elsewhere in the world and the model does not allow sufficient time between collision at c. 430 Ma and peak emplacement at c. 425 Ma to account for all of mantle wedge development, slab dewatering, melting and emplacement into the mid to upper crust.

However, there are remaining issues with the above break off model and adjustments. The distribution of Caledonian intrusions does not match the linear distribution expected from slab breakoff magmatism as emplacement is known to be strongly controlled by the availability of structural pathways (e.g., Kocks et al., 2014; Stewart et al., 2001). The suggested timing of diachronous breakoff is inconsistent with collision dynamics as it would require breakoff pre- or at a similar time to peak metamorphism and collision in the Northern Highlands (Mako 2019; Archibald *et al.* 2022; Milne *et al.* 2023; Strachan *et al.* 2020a). There is also no further evidence for a propagating slab tear (Neilson *et al.* 2009). The addition of dates for Glen Dessarry and Muckle Roe since the 2002 model of Atherton and Ghani was proposed (c. 448 and c. 438 Ma) extends the range of magmatism in the Northern Highlands and Shetland to 448 – 418 Ma (Table 2.1, Fig. 1.1). It is unclear whether slab breakoff would drive magmatism for this extended period of time (Garzanti *et al.* 2018). Furthermore, slab breakoff is recognised elsewhere to have limited direct impact on magmatism, particularly on upper crustal magmatic processes such as emplacement, and suggests reassessment of Northern Highlands ideas is now necessary (Neill *et al.* 2015; Freeburn *et al.* 2017).

A period of limited emplacement c. 450 – c.430 Ma prior to breakoff is often cited (Atherton and Ghani 2002; Oliver *et al.* 2008; Archibald *et al.* 2022). This has been attributed to a period of magmatic quiescence due to a flat slab scenario or an over steepened slab, or that existing arc material was removed by erosion (Glazner 1991; Oliver *et al.* 2008; Dewey *et al.* 2015; Miles *et al.* 2016; Archibald *et al.* 2022). The Shetland and Glen Dessarry ages mentioned above, Cluanie antecrysts with ages spanning c. 450 – 438 Ma (Table 2.1) and petrogenesis of these intrusions indicate that subduction-derived mantle melting and magmatism did occur during this time (Fowler 1992; Goodenough *et al.* 2011; Lancaster *et al.* 2017; Milne *et al.* 2023; Strachan *et al.* 2020a). This age range, in particular of antecrystic ages, has been interpreted by Milne et al. (2023) as evidence for the presence of an LCHZ beneath the Northern Highlands and adds geochronology to existing evidence for the existence of magmas in the crust prior to final emplacement of plutons (McLeod *et al.* 2011; Bruand *et al.* 2014).

Milne et al. (2023) thus updated the Northern Highlands geodynamic model to include continued arc magmatism and LCHZ development enabled by initial collision with Baltica promontories from c. 450 Ma (Slagstad and Kirkland 2018). Milne et al. (2023) interpreted the genesis of adakite-like magmas to be the result of protracted fractionation of amphibole ± garnet in the lower crust and limited magma escape from the LCHZ during ongoing collision. Following the onset of orogen wide hard collision at c. 437 Ma (Strachan *et al.* 2020a), slab breakoff occurred c. 426 Ma, dated by peak heat advection, and driving disturbance of the LCHZ and subsequent upper crustal magmatism and emplacement (Mako 2019; Milne *et al.* 2023). However, this model still suffers from the issue that breakoff is not shown to have significant impact on magmatism (Freeburn *et al.* 2017). A lack of recognition more widely in the Northern Highlands of the existence of an LCHZ, upper plate dynamics and stress states, and other possible geodynamic occurrences such as lithospheric delamination or slab rollback also remain an issue and warrants further investigation of what the temporal and geologic record of the various intrusions can tell us.

2.3.3 The Great Glen Fault

The Great Glen Fault System (Fig. 1.1, 2.1) developed during late Caledonian strike slip deformation driven by sinistrally oblique collision, and has a net sinistral transpressive displacement with a south-east component of downthrow (Soper *et al*. 1992; Stewart *et al*. 1999). The fault has since undergone multiple, dominantly dextral, reactivations with a total displacement of ~ 30 to ~ 40 km (Le Breton *et al*. 2013; Dichiarante *et al*. 2016). The main fault trace has limited exposure along its length, and comprises a 3 km wide damage zone with a 300 m wide core (Stewart *et al*. 1999). Mylonite situated at present exposure levels initially formed at ~ 9 – 16 km depth and is overprinted by cataclasite (Stewart *et al*. 1999). The main GGF trace is associated with numerous other strike slip faults including the Strathconon and Strathglass faults (Fig. 2.1; Stewart et al., 1999). Geophysical studies have identified the GGF as a transcurrent fault which truncates Caledonian thrust structures at depth (Hall *et al*. 1984; Snyder and Flack 1990).

A minimum age of sinistral strike slip deformation is constrained by emplacement of the Cluanie intrusion c. 432 Ma, associated with the Strathglass fault (Neill and Stephens 2009; Milne *et al*. 2023). Sinistral displacement is also evidenced by emplacement at c. 430 Ma on the dextral anti-Reidel Loch Shin Line, and likely on a GGF associated strike slip fault in Orkney (Holdsworth *et al*. 2015; Lundmark *et al*. 2019; Milne *et al*. 2023a). A possible phase of dextral motion involving emplacement of the Strontian Sanda facies (c. 418 Ma; Paterson *et al*. 1993) was proposed by Hutton (1988) but has not been investigated since. A switch from regional transpression to transtension is proposed to have occurred at c. 410 Ma at the onset of ORS basin development (Dewey and Strachan 2003), c. 425 Ma on the basis of emplacement of the Rogart intrusion associated with dextral Loch Shin Line motion (Table 2.1, Fig. 1.1; Holdsworth *et al*. 2015), or c. 415 Ma at the end of Moine thrust motion and contractional deformation (Strachan *et al*. 2020a). Caledonian displacement occurred until at least c. 406 – 399 Ma, with high temperature deformation noted at c. 406 – 403 Ma (Mendum and Noble 2010; Law *et al*. 2023). Law et al. (2023) suggest the high temperature deformation noted at 406 – 403 Ma in basement inliers exposed at Rosemarkie on the GGF may relate to the switch from dominant transpression to transtension. As such the range of dates suggested for this switch mean its age is somewhat equivocal.

The magnitude of net sinistral displacement has invoked significant debate. An initial estimate of c. 100 km by Kennedy (1946) based on matching of the Strontian and Foyers intrusions is shown to not be the case due to differences between the intrusions in palaeomagnetic history, structure and nature of the contacts with country rock (Marston 1967; Pidgeon and Aftalion 1978; Torsvik 1984). Palaeomagnetic data has variably assigned displacements of a few 100 km (e.g., Smith and Watson, 1983; Torsvik, 1984), though offset of at least 500 km is suggested to be necessary to account for the lack of identified Scandian deformation in the Grampian Highlands (Dewey and Strachan 2003; Dewey *et al.* 2015). Such a large offset leaves the question of what material would have occurred between the Northern and Grampian Highlands, and is not seen in other orogens (Searle 2021). The most recent estimation of displacement, 250 – 300 km, has been proposed based on reconciling immature sandstone units either side of the GGF with their proximal basement source, matching of metamorphic belts and structurally similar granitoid complexes (e.g., Galway and Argyll), and similar xenocryst records preserved in Caledonian intrusions proximal to the GGF (Prave *et al.* 2024). Indeed, a smaller displacement is more consistent with the fault's demoted status from a terrane boundary and with non-continuity with the Walls Boundary Fault in Shetland (Fig. 1.1; Armitage et al., 2021; Strachan et al., 2002).

Understanding of the timing and nature of slip is strongly tied to intrusion ages, emplacement models and imposed tectonic fabrics where magma was emplaced via releasing bends, fault splays, and antithetic faults (Hutton 1988; Stewart *et al.* 2001; Kocks *et al.* 2006, 2014; Neill and Stephens 2009; Holdsworth *et al.* 2015; Lawrence *et al.* 2022). This understanding includes possible timing of a switch from transpression to transtension with orogenic collapse as discussed above (Holdsworth *et al.* 2015). Therefore accurate dating and emplacement models of plutons are critical for accurate interpretation of fault movement and understanding of regional geodynamics, of which the age and emplacement of some has come under question (e.g., Lawrence et al., 2022; Milne et al., 2023). Additionally, the timing of the proposed dextral phase thus far has only an unpublished age (Hutton 1988; Paterson *et al.* 1993), and other fault-associated intrusions lack robust geochronology, geochemistry and structural analysis (e.g., Helmsdale, Abriachan, Fearn and Migdale; Table 2.1, Fig. 1.1). As such, particular reassessment of intrusions in the context of understanding fault motion is warranted.

2.3.4 Summary of Key Issues Explored in this Thesis

A summary of existing issues with Northern Highlands geochronology, as discussed above, which this thesis attempts to address are given below.

1) **Insufficient coverage in space and time of existing geochronology.** Many Northern Highlands intrusions lack recognition of their complete magmatic history, have emplacement ages based only on outdated techniques, and(or) are undated. In situ U-Pb zircon datasets obtained in this study provide emplacement ages and extended magmatic history for intrusion phases with unreliable, unpublished or no emplacement age (Helmsdale, Abriachan, Strontian Sunart and Sanda facies; see section 2.3).

2) **Driver of the c. 428 to c. 423 Ma increase in magmatism and emplacement.** Slab breakoff is not sufficient as a solution to late Caledonian magmatism. Discussion in this thesis will utilise zircon U-Pb data obtained to explore the possible roles of an LCHZ, lithospheric delamination and slab rollback, and crustal stress in late Caledonian magmatism and geodynamic processes.

3) **Nature and timing of phases of Great Glen Fault motion.** Current understanding of GGF motion relies on an incomplete geochronological record. The spatial-temporal distribution of magmatism and its driving geodynamic mechanisms are discussed with respect to possible associated phases of strike slip deformation.

2.4 Intrusions Studied Here

2.4.1 Strontian

The Strontian intrusion outcrops over an area of ~ 200 km^2, is truncated to its southeast by the Great Glen Fault and was emplaced into the Glenfinnan Group of the Loch Ness Supergroup metasediments (Fig. 2.3; Krabbendam et al., 2022;

Sabine, 1963). The intrusion consists of two main phases, the outer Sunart and inner Sanda facies as termed by Paterson et al. (1992b) (Fig. 2.3). The outer Sunart facies comprises granodiorite which grades inwards from a non-porphyritic to a porphyritic variety and contains abundant mafic enclaves of hornblende diorite, sometimes described as appinite (Munro 1965; Holden *et al.* 1987, 1991; Castro and Stephens 1992; Fowler *et al.* 2008). The Sanda facies consists of biotite granodiorite and makes up the south and east of the intrusion, cross-cutting the Sunart facies. At its northern margin the Sanda facies intrudes the Sunart facies and surrounding country rock in a series of veins and narrow sheets (Fig. 2.3; Munro, 1965). Both phases are cut by aplite and pegmatite veins, appinites, and lamprophyres presumed to be Caledonian in age. Further alkaline minor intrusions, including lamprophyres, of approximately Permian to Carboniferous age and a WNW–ESE trending Pb-Zn-carbonate vein cross-cut the pluton and surrounding country rock (Fig. 2.3; Castro and Stephens, 1992; Fowler et al., 2008; Gallagher, 1963, 1958; Munro, 1965; Sabine, 1963). The Sanda facies is interpreted to have been emplaced via a dextral shear zone associated with the GGF, with extensional splays at its terminus (Hutton 1988). This model requires dextral motion on the GGF at the time of emplacement, thus constraining the emplacement age of the Sanda facies may constrain GGF history. Emplacement of the intrusion as a whole has been implied to be due to local extension developed during sinistral motion on the GGF related to associated block movement (Watson 1984).

Whole rock Sr-Nd and $\delta^{18}O$ isotope data indicates derivation from an isotopically depleted source and minimal contamination by Glenfinnan Group sediments on emplacement for the Sunart facies (Fowler *et al.* 2008). It should be noted that geochemical and geochronological studies have dominantly sampled the Sunart facies, and similar isotopic data is not available for the Sanda facies (Fowler *et al.* 2008; Bruand *et al.* 2014; Paterson *et al.* 1992b). A recent study by Matthews et al. (2023) did however sample both the Sunart and Sanda phases and identified some differences: greater aluminium saturation and lower total Rare Earth Element (REE) content in the Sanda facies than Sunart.

ID-TIMS zircon and titanite analyses by Rogers and Dunning (1991) provide the most up to date geochronology for the Sunart facies. Two zircon fractions, which were not subject to air abrasion pre-treatment, gave a $^{206}Pb/^{238}U$ vs $^{207}Pb/^{235}U$ concordia

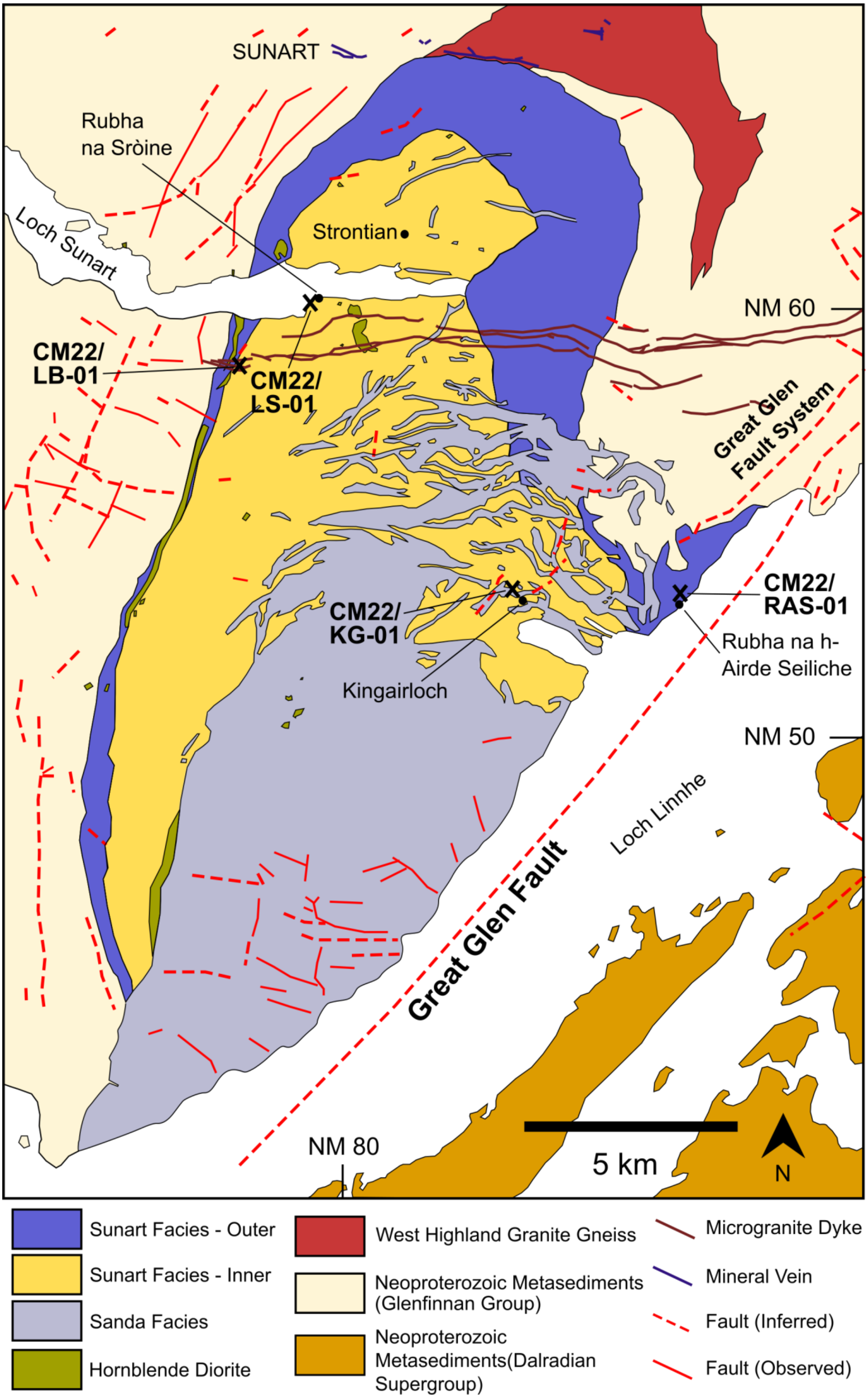

Figure 2.4 Summary map of the Strontian pluton and surrounding area with sample locations marked. Map data from British Geological Survey (2016), and Sabine, (1963).

upper intercept age of 425 ± 3 Ma. A titanite fraction, subjected to air abrasion pre-treatment, gave a 206Pb/238U age of 423 ± 3 Ma (Table 2.1). The Sunart granodiorite is not typically considered to contain inherited zircon (Pidgeon and Aftalion 1978; Halliday et al. 1979), although two discordant zircon analyses by Rogers and Dunning (1991) gave $^{206}Pb/^{238}U$ ages of 436 Ma and 440 Ma, and were interpreted as such and extrapolated to an upper intercept age of c. 1713 Ma. Identification of zircon zonation and growth over multiple stages by Pidgeon and Aftalion (1978) may give further confidence that zircon growth occurred prior to emplacement during LCHZ storage of magma. Conversely, the Sanda facies contain a significant inherited component. Backscattered electron images obtained by (Paterson et al. 1992a) showed that Sanda facies zircon often contain older cores, sometimes with magmatic zoning. Discordant zircon analyses c. 500 Ma were also previously extrapolated to an age of c. 1462 Ma and interpreted as an inherited component (Halliday et al. 1979). A U-Pb monazite age of 418 ± 1 Ma (Paterson et al. 1993) has been previously obtained for the Sanda granodiorite but has never been peer-reviewed and no further details were published. Subsequent conversation with Drs Bruce Paterson and Ed Stephens in July 2024 resulted in the retrieval of the original dataset and confirmation of a $^{207}Pb/^{235}U$ ID-TIMS age of 418.0 ± 0.7 Ma. $^{207}Pb/^{235}U$ ages are preferred for monazite data due to uncertainty regarding excess ^{206}Pb production due to incorporation of Th during crystallisation (Schärer 1984; Parrish 1990).

2.4.2 Helmsdale

The Helmsdale granite (~ 100 km^2) consists of an outer porphyritic alkali-feldspar granite with occasional appinitic enclaves which grades into an inner non-porphyritic microgranite (Fig. 2.4; Fowler et al., 2008; Kocks, 2002; Tweedie, 1979). The pluton is situated adjacent to the Helmsdale Fault, intrudes the Loch Eil Group of the Loch Ness Supergroup and is uncomfortably overlain by Devonian Lower Old Red Sandstone (Fig. 2.4; Krabbendam et al., 2022; Trewin and Thirlwall, 2002). It is suggested to have been emplaced via the fault, however, this interpretation is based on decades old magnetic and gravity data and a presumed Carboniferous age of the intrusion (Smith and Briden 1977; Tulstrup 1980). Whole rock isotopic data indicates an isotopically enriched source for the Helmsdale intrusion and minimal assimilation on emplacement, the latter somewhat contrasting the with evidence for an inherited zircon component

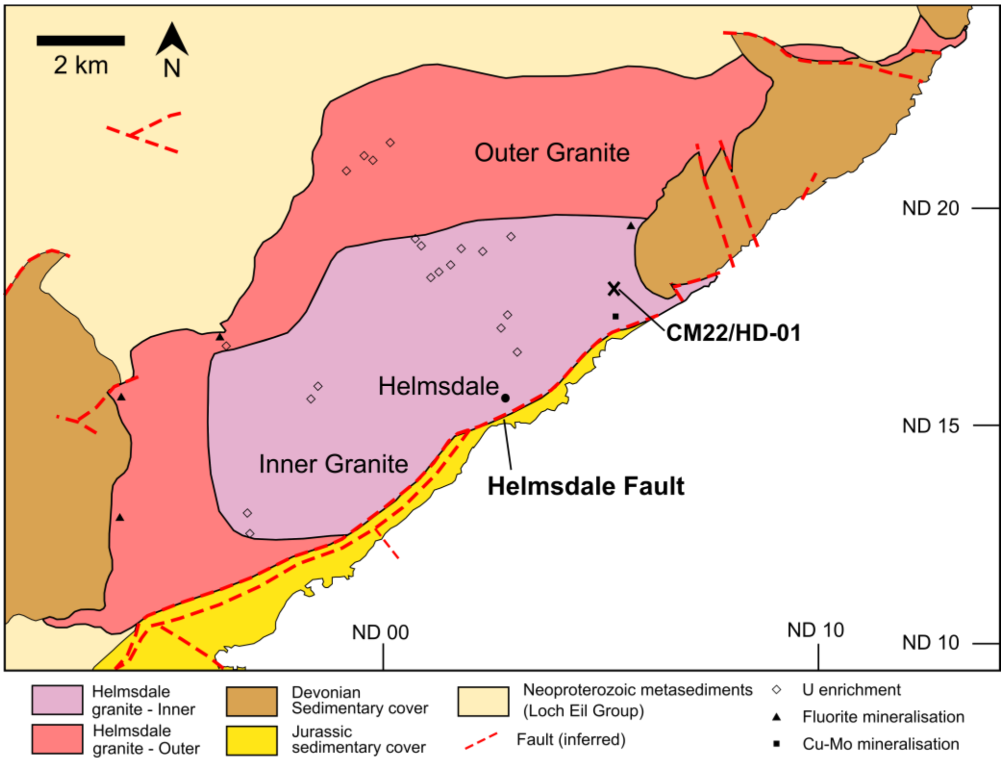

Figure 2.5 Summary map of the Helmsdale pluton and surrounding area with sample location marked. Map data from British Geological Survey (2016) and Tweedie, (1979).

(Fowler et al., 2008; Pidgeon and Aftalion, 1978; this study). The Helmsdale intrusion and overlying sediments also contain elevated U concentration and are associated with U mineralisation, and the intrusion is noted as high heat producing (Tweedie 1979; Gillespie *et al.* 2013). Further, elevated Te, Se, Cu and Mo contents are known within the overlying sediments and Helmsdale Fault network (Tweedie 1979; Parnell 1988; Pointer *et al.* 1989; Simpson *et al.* 1997; Bullock *et al.* 2017).

An age of c. 420 Ma for the inner granite was determined by Pidgeon and Aftalion (1978) using ID-TIMS. However, this age was determined using a $^{206}Pb/^{238}U$ vs $^{207}Pb/^{235}U$ concordia lower intercept of three strongly discordant inherited grains with an upper intercept age of c. 2 Ga (Pidgeon and Aftalion 1978). Biotite K-Ar cooling ages of 410 ± 15 Ma and 397 ± 14 Ma were also obtained by (Miller and Brown 1965). Field relationships indicate the granite may have re-deformed Scandian regional fabrics in the country rock on emplacement while the granite itself is suggested to lack tectonic fabric (Kocks 2002). Emplacement therefore occurred towards the end of the Scandian Orogeny, which lasted until c. 415 Ma, likely < c. 426 Ma following the end of upright folding (Kocks 2002; Strachan and Evans 2008; Strachan *et al.* 2020a).

2.4.3 Abriachan

The Abriachan intrusion (~ 2.7 km^2) consists of medium to coarse grained, alkali-feldspar rich biotite to monzogranite emplaced into the Glenfinnan Group metasediments adjacent to the GGF (Fig. 2.5; Ansberque et al., 2019; Garson et al., 1984; Krabbendam et al., 2022). There has been limited petrogenetic investigation into the intrusion but REE concentrations suggest it is similar to other late Caledonian intrusions (Ryder and Gillis 1994), while apatite geochemistry indicates a slightly higher degree of magma differentiation (Ansberque *et al.* 2019). The intrusion is noted as high heat producing, and is associated with carbonatite metasomatism and U-F mineralisation (Garson *et al.* 1984; Simpson *et al.* 1997; Gillespie *et al.* 2013; Heptinstall *et al.* 2023). Fenitisation affects the northern end of the intrusion and extends north into the Loch Ness Supergroup, as well as affects further areas of the Loch Ness supergroup and overlying ORS to the north and northeast respectively (Fig. 2.5; Garson et al., 1984; Heptinstall et al., 2023). Similar metasomatism and calcite veining occurs at Foyers, Moniack, Dochfour and Rosemarkie in the region of the GGF fault. Recent geochemical study of fenitisation suggests that fenitisation may have derived from a sodic-alkaline carbonatite pluton at shallow depth in the region, affected by hydrothermal alteration following GGF shearing (Deans et al. 1971; Garson et al. 1984; Heptinstall et al. 2023). The Abriachan intrusion may have been affected by faulting shortly after emplacement, though an emplacement model and structural data are not available (Watson and Plant 1997).

Geochronological data for the intrusion is similarly lacking. The intrusion was sampled for apatite geochemistry as part of a regional provenance study, but produced a low apatite yield and was therefore found unsuitable for apatite U-Pb geochronology (Ansberque et al. 2019). A K-Ar date of 394 ± 15 Ma was obtained by Deans et al. (1971) for metasomatic crocidolite from Learnie Quarry, northeast of Rosemarkie, providing a minimum age constraint for the granite.

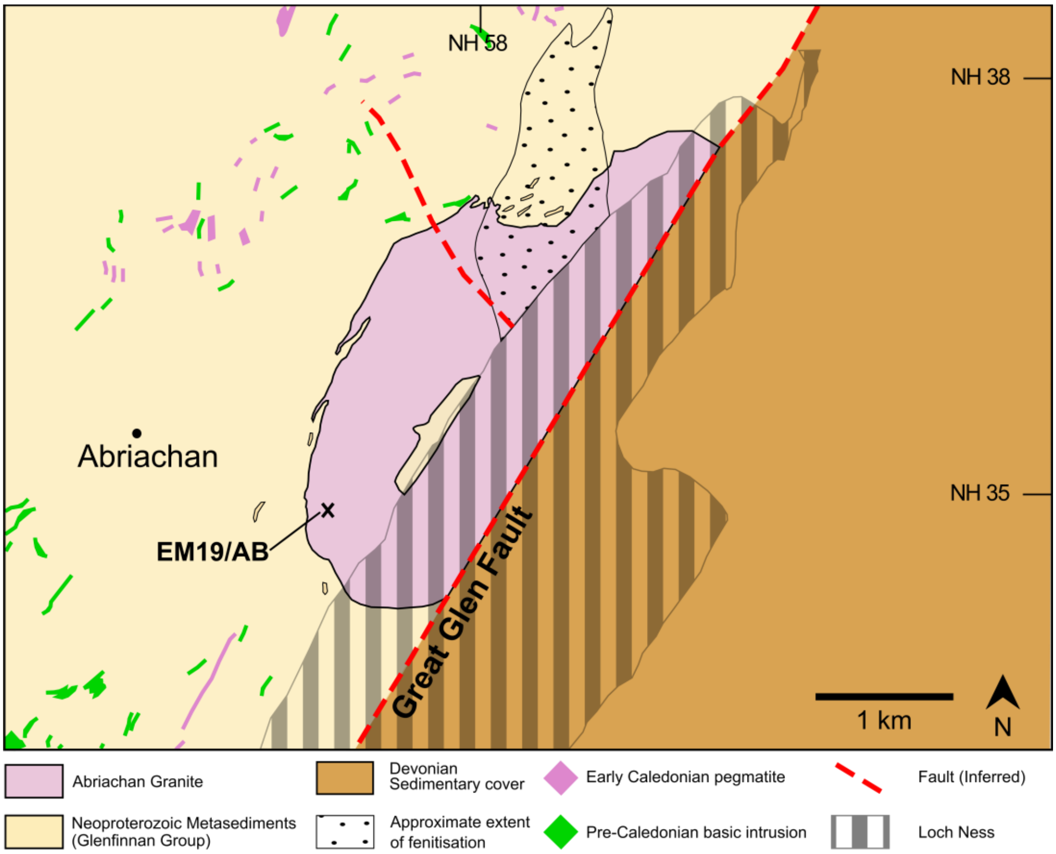

Figure 2.6 Summary map of the Abriachan intrusion and surrounding area with sample location marked. Map data from British Geological Survey (2016) and Garson et al. (1984).

Chapter 3 Methods

3.1 Sample Collection

Sampling locations were selected for (a) accessibility of exposures during day trips from Glasgow, and (b) to ensure the different facies of the Strontian pluton were sampled. Sample locations and materials are summarised in Table 3.1, and Fig. 2.3 - 2.5, and are discussed below.

Table 3.1 Summary of sample locations.

Sample ID	Location: British National Grid Reference	Material Sampled
CM22/RAS-01	Rubha na h-Airde Seiliche: NM 8789 5327	Strontian - Sunart Granodiorite, Outer
CM22/LS-01	Rubha na Sròine, Loch Sunart south shore: NM 7925 6000	Strontian - Sunart Granodiorite, Inner
CM22/KG-01	Kingairloch: NM 8395 5337	Strontian - Sanda Granodiorite
CM22/HD-01	Helmsdale: ND 0530 1812	Helmsdale - Inner Granite
EM19/AB	Abriachan: NH 5689 3487	Abriachan Granite
CM22/LB-01	Liddesdale Burn: NM 7763 5866	Strontian - Microgranite dyke

Sample CM22/RAS-01 was collected from the roadside of the B8043 between Kilmalieu and Glengalmadale, from a large boulder which was identical to those around it. In-situ rock faces were generally fractured but difficult to extract samples from, with extensive reddening in in-situ rock and boulders likely due to proximity to the Great Glen Fault. This sample will enable comparison of the outer Sunart granodiorite, from an under-sampled location, with the inner Sunart Granodiorite further north (CM22/LS-01) which has been sampled extensively for past geochronology and geochemistry (Rogers and Dunning 1991; Fowler *et al.* 2008; Matthews *et al.* 2023). Sample CM22/LS-01 was collected in situ from the shore of Loch Sunart east of Liddesdale just off the A884. Sample CM22/KG-01 was collected from an intrusive sheet at the northern end of the Sanda granodiorite identified along a forestry track off the north side of the B8043 northwest of the Kingairloch power station, close to the Sanda-Sunart contact. The microgranite sample, CM22/LB-01, was collected in-situ in Liddesdale burn at Liddesdale Bridge. This sample came from a substantial microgranite dyke which is prominent on published maps, cross-cutting the outer Strontian granodiorite and surrounding country rock (Fig. 2.3; British Geological Survey, 2016).

The Helmsdale sample, CM22/HD-01, was collected by Iain Neill in 2023. This sample was collected from a heavily fractured portion of the Helmsdale Inner Granite on a road cutting beyond a prominent U-bend in the A9 road at Navidale (Fig. 2.4).

Sample EM19/AB was collected from the Abriachan granite by Eilidh Milne in 2019 from north of the minor road between the A82 on Loch Ness-side and the hamlet of Abriachan. This location is at the south end of the Abriachan granite avoiding regions of the intrusion affected by fenitisation (Fig. 2.5; Garson et al., 1984).

3.2 Crushing and Mineral Separation

Weathered edges of samples were sawn off and 30 μm thin sections cut prior to crushing and separation. Samples were processed via standard crushing, milling and magnetic and heavy liquid separation procedures as outlined below. At each stage rigorous cleaning of equipment was carried out between processing of each sample. All sample preparation and analysis were conducted at the University of Glasgow.

3.2.1 Crushing and Initial Density Separation

Samples were each crushed using a steel Retsch jaw crusher and steel disc mill to obtain the <500 μm fraction. Sample CM22/LB-01 was not processed with the disc mill to avoid over-crushing of the already fine-grained sample, and fragmentation of apatite grains due to shearing.

The < 500 μm fraction obtained for each sample was then passed over a Gemini shaking table to distribute material into four density fractions to remove the clay and dust fraction and concentrate zircon. Effectiveness of separation was uncertain as there was little observable difference between the densest two fractions, and so these were processed as one fraction during subsequent separation stages to minimise possible omission of zircon.

3.2.2 Mineral Separation

Once dried, the densest two fractions of each sample were passed through vertical magnetic separation to remove the most crudely magnetic material. First at a current of 1.0 A, and the resulting non-magnetic fraction passed through a second time with a current of 2.0 A to remove any remaining para-magnetic material.

A portion of the non-magnetic fraction was added to a 2 l separation funnel with heavy liquid lithium heteropolytungstate (LST) of density 2.8 gcm^{-3}. Sufficient LST was used to coat the grains and allow them to mix and move freely. The LST and sample material was stirred for a few minutes with a motorised stirrer and left to settle. Once separated the dense fraction of samples (> 2.8 gcm^{-3}) settled at the funnel base was released into filter paper and washed with deionised water. Similarly, the LST and remaining material (< 2.8 gcm^{-3}) was released from the funnel and filtered, the material washed with deionised water and the LST reused.

The > 2.8 gcm^{-3} fraction of each sample was then passed through horizontal magnetic separation. The magnet was set at a 20^0 angle, and the samples passed through at currents of 0.45 A, with subsequent non-magnetic fractions passed through at 0.8 A and then 1.2 A.

The resulting non-magnetic fraction of each sample was further separated using diiodomethane (DIM) heavy liquid of density 3.3 gcm^{-3}. The sample and DIM were added to a 100 ml separation flask and agitated with a stirrer to break the surface tension and allow separation. After a few minutes the settled, > 3.3 gcm^{-3} fraction and remaining < 3.3 gcm^{-3} float fraction were released separately into filter paper, cleaned with acetone and stored in vials once dry.

3.2.3 Mineral Picking and Mounting

The final non-magnetic, > 3.3 gcm^{-3} fraction of each sample was scattered onto a glass slide from which ≤ 100 zircon grains per sample were picked onto double sided tape. Grains were picked as soon as they were identified as zircon to aim to reduce bias towards larger zircons. Apatite grains of sample CM22/LB-01 were picked from the < 3.3 gcm^{-3} faction obtained by DIM separation.

Resin moulds were placed over the tape and 2-3 ml of epo-thin resin poured into the mould and left to cure. Once cured the resin pucks and grains were abraded to expose zircon surfaces first with 15 µm metallographic paper by hand, then with 8 µm metallographic paper by hand on a rotating stage. They were then polished with 3 µm water-based diamond polish on an automatic rotating stage, and finally with 1 µm aluminium oxide powder ($Al_2 0_3$) suspended in water by hand on a rotating stage.

3.3 Cathodoluminescence Imaging

Once polished, zircon mounts were coated with carbon and secondary electron (SE) and cathodoluminescence (CL) images were obtained manually for each grain using a Quanta 200F environmental scanning electron microscope. Images were obtained with a working distance of 15 mm, an electron accelerating voltage of 15 ekV, and a scan speed of 20 - 30s per grain. Magnification, brightness and contrast was adjusted per grain to optimise clarity of grain structures. Once imaged the carbon coat was removed using Al_2O_3 polish as described in section 3.2.3.

The CL and SE images were used to select and label locations for zircon U-Pb LA-ICP-MS analysis. Sites were selected to avoid fractures, growth zone boundaries and inclusions, and to maximise coverage of zircon growth history and return of concordant data points. Where possible, a second spot within the same growth layer was labelled on grains with a view to measuring age-controlled trace element concentrations once geochronological data were collected.

3.4 LA-ICP-MS and Data Processing

Copper reference markers were fixed to the zircon and apatite mounts, and the relative locations of selected laser spots and markers was recorded using an Axio Imager.M2m microscope and associated ZenCore software with the CL images as a guide. The locations were then imported into the GeoStar LA-ICP-MS software and spot locations corrected as necessary, again using the labelled CL images as a guide. Apatite grains were not imaged and one spot per grain was analysed.

Zircon and apatite grains were ablated using an Australian Scientific Instruments RESOlution laser and ablated material carried in Ar to a Thermo iCAP-RQ single collector mass spectrometer. Zircon U-Pb analyses were conducted over three sessions and interspersed with analyses of the NIST610 glass, and 91500, Plešovice and Temora-2 zircon reference materials (Wiedenbeck *et al.* 1995; Black *et al.* 2004; Sláma *et al.* 2008). Apatite U-Pb analyses were conducted over one session and samples interspersed with analysis of the NIST612 glass and Mt McClure, Madagascar, Durango and Mt Dromedary apatite reference materials (Schoene and Bowring 2006; Paul *et al.* 2021; Apen *et al.* 2024). Laser settings for each session are summarised in Table 3.2, and weighted mean ages of zircon reference materials and discordia ages of apatite reference materials are summarised in Tables 3.3 and 3.4, with the full data presented in Appendix D).

Table 3.2 Summary of LA-ICP-MS analysis settings. Internal isotope standards are highlighted in bold.

<table>
<tr><th>Session</th><th>Samples</th><th>Spot Diameter;
Ablation time;
On Sample Fluence;
Laser Frequency</th><th>Isotopes measured</th></tr>
<tr><td>Zircon U-Pb 1</td><td>CM22/RAS-01</td><td rowspan="3">30 µm
30 s
3 Jcm^{-2}
10 Hz</td><td rowspan="3">^{29}Si, ^{200}Hg, ^{204}Pb, ^{206}Pb, ^{207}Pb, ^{208}Pb, ^{232}Th, ^{235}U, ^{238}U</td></tr>
<tr><td>Zircon U-Pb 3</td><td>CM22/KG-01
EM19/AB
CM22/LB-01</td></tr>
<tr><td>Zircon U-Pb 4</td><td>CM22/LS-01
CM22/HD-01</td></tr>
<tr><td>Apatite U-Pb 1</td><td>CM22/LB-01</td><td>38 µm
30 s
3 Jcm^{-2}
5 Hz</td><td>^{43}Ca, ^{200}Hg, ^{204}Pb, ^{206}Pb, ^{207}Pb, ^{208}Pb, ^{232}Th, ^{235}U, ^{238}U</td></tr>
<tr><td>Zircon Trace Elements</td><td>CM22/RAS-01
CM22/LS-01</td><td>30 µm
30 s
3.5 Jcm^{-2}
10 Hz</td><td>^{91}Zr, ^{49}Ti, ^{51}V, ^{57}Fe, ^{63}Cu, ^{66}Zn, ^{88}Sr, ^{93}Nb, ^{109}Ag, ^{118}Sn, ^{139}La, ^{140}Ce, ^{141}Pr, ^{146}Nd, ^{147}Sm, ^{153}Eu, ^{157}Gd, ^{89}Y, ^{159}Tb, ^{163}Dy, ^{165}Ho, ^{166}Er, ^{169}Tm, ^{172}Yb, ^{175}Lu, ^{178}Hf, ^{181}Ta, ^{182}W</td></tr>
</table>

The uncertainty for the Mt McClure discordia age is large (± 25 Ma, Table 3.4), which may be due to the limited number of analyses. The effects of n numbers on precision are shown by Mt McClure apatite U-Pb LA-ICP-MS data by Cogné et al. (2024) for which sessions with a greater number of analyses (≤ 40) and larger spot sizes (40 x 40 μm square) produced more precise ages (their Table 2). Use of higher laser fluence (3.9 J cm^{-2}) by Cogné et al. (2024) may have further contributed to the overall more precise ages than were obtained in this study. Regardless of the cause, the large uncertainty is of limited effect given (i) the Mt McClure reference material was not used as the primary calibration standard, and (ii) the apatite data from sample CM22/LB-01 is presented only for completeness and was not used to inform discussion (see page 38).

Table 3.3 Summary of LA-ICP-MS zircon reference material ages, spots ages were corrected for common Pb using the Stacey-Kramers model as provided by IsoplotR prior to weighted mean calculations (Stacey and Kramers 1975). Accepted ages sourced from Black et al. (2004), Sláma et al. (2008), and Wiedenbeck et al. (1995).

		Reference Material		
		91500	**Plešovice**	**Temora 2**
Accepted Age (Ma)		1065	337.13±0.37	418.1±2.2
Weighted Mean $^{206}Pb/^{238}U$ Age by session (Ma)	Zircon U-Pb 1	**1062.4 ± 4.5** *n = 24* *MSWD = 0.48*	**342.9 ± 1.7** *n = 24* *MSWD = 0.84*	**418.2 ± 2.0** *n = 22* *MSWD = 2.0*
	Zircon U-Pb 3	**1062.5 ± 4.2** *n = 27* *MSWD = 0.5*	**338.2 ± 1.6** *n = 27* *MSWD = 0.95*	**414.3 ± 1.9** *n = 24* *MSWD = 1.3*
	Zircon U-Pb 4	**1062.3 ± 3.8** *n = 27* *MSWD = 0.64*	**340.1 ± 1.5** *n = 27* *MSWD = 0.71*	**415.0 ± 1.7** *n = 22* *MSWD = 2.0*

Table 3.4 Summary of LA-ICP-MS apatite reference material discordia ages, as calculated by IsoplotR discordia model 1. Accepted ages sourced from Apen et al. (2024), Paul et al. (2021), and Schoene and Bowring (2006).

	Reference Material		
	Mt McClure	**Durango**	**Mt Dromedary**
Accepted Age (Ma)	523.51 ± 2.09	32.716 ± 0.072	98.4 ± 0.5
Discordia Age (Ma)	**517.0 ± 25.0** *n = 21* *MSWD = 0.79*	**33.0 ± 5.9** *n = 16* *MSWD = 0.93*	**87.0 ± 17.0** *n = 18* *MSWD = 0.94*

Zircon U-Pb data reduction was carried out using Iolite v.4 U-Pb Geochronology Data Reduction Scheme (Paton *et al*. 2011), with the 91500 zircon as the primary standard. During this stage analyses were thoroughly checked for evidence of Pb loss, common Pb, or where analysis had crossed multiple zones of zircon growth or mineral inclusions. This process was carried out using Iolite's VizualAge live concordia plot tool to check the age and concordance of integrations which encompassed different proportions of the total analysis time (Petrus and Kamber 2012). Careful visual inspection of integrations was carried out at the same time. Where it improved accuracy of age results, or enabled a concordant age to be extracted, the integration was reduced to include only a portion of the total analysis time, removing sections where the age was affected by factors mentioned above. This ensures validity of results and maximises data points available for analysis. Reduction of the integration was only carried out where it was viable to include the initial portion of the ablation, corresponding to the polished and imaged grain surface, to maintain a valid link to the CL image for textural control. Spots which appeared concordant but showed evidence of Pb loss at this stage, were rejected from weighted mean age calculations.

Given the low precision of single collector mass spectrometry, no systematic correction for common Pb could be applied. Isotopes ^{204}Pb and ^{200}Hg were measured during analysis (Table 3.2) and monitored during inspection of integrations. The ^{204}Pb measurement is considered to encompass ICP-MS counts of both ^{204}Pb, and isobaric interference by ^{204}Hg. Where ^{204}(Pb + Hg) levels of an integration spike above that of ^{200}Hg, points tended to plot horizontally to the right of the concordia towards infinite ^{207}Pb/^{235}U. Spots with such characteristics were interpreted as containing increased quantities of ^{204}Pb (and thus common Pb) above background ^{204}Pb, ^{204}Hg and ^{200}Hg levels and were omitted from weighted mean calculations (Horstwood *et al*. 2003). Those without ^{204}(Pb + Hg) spikes and which overlapped with the concordia line or were very close to it were later corrected using the Stacey-Kramers model (see below).

Zircon data were then presented using IsoplotR software version 6.2.1 (https://isoplotr.es.ucl.ac.uk, Vermeesch, 2018). The full data set for each sample was presented on a Wetherill concordia plot with 2σ error ellipses. The following steps were then undertaken for each sample to determine an age which may be representative of emplacement. Spots with ages older than 470 Ma or which showed a clear Pb loss concordia trend were omitted. Remaining concordant and near-concordant grains were presented on a $^{206}Pb/^{238}U$ age weighted mean plot, and corrected for common Pb using the Stacey-Kramers model as provided by IsoplotR (Stacey and Kramers 1975; Vermeesch 2018). Corrected spots significantly younger than the anticipated emplacement age were omitted and attributed to Pb loss. Spots which appear to have more subtly affected by Pb loss, with younger ages now more apparent once corrected, were omitted. All spots for which the respective grain produced a core or inner rim age younger than the corresponding rim or outermost rim age, or where a core age exhibited signs of Pb loss, were omitted (some exceptions are discussed in chapter 5). Spots of cores and inner portions of magmatic rims, where there was substantive further rim growth, were omitted from the weighted mean age of emplacement as these were likely to represent antecrystic growth. Spots of magmatic rims for which the age was outwith error of younger and more likely emplacement related rims were also omitted as likely representing antecrystic growth. The mean standard weighted deviation (MSWD) statistic (Wendt and Carl, 1991) was monitored during this process using figure 3 of Spencer et al. (2016) to ensure the final selection of spots comprise a statistically valid population. A $^{206}Pb/^{238}U$ weighted mean age was calculated for each sample using the final selection of spots.

Apatite data were processed using the Iolite v.4 VizualAge UcomPbine Data Reduction Scheme with the Madagascar apatite as the primary reference material (Paton *et al.* 2010, 2011; Chew *et al.* 2014). Processed data was then plotted on a Tera-Wasserberg plot using IsoplotR version 6.2.1 (https://isoplotr.es.ucl.ac.uk, Vermeesch, 2018). Analyses which did not lie along the discordia line were omitted and a discordia age calculated using discordia model 1 (Vermeesch 2018). Due to limited apatite and zircon recovery, and limited range of $^{238}U/^{206}Pb$ and $^{207}Pb/^{206}Pb$ ratios of apatite analyses along the discordia line, age results for sample CM22/LB-01 are broadly Caledonian but deemed insufficient to be of use to understand magmatism at Strontian and as such are not discussed further. Complete data and a summary of results for CM22/LB-01 are given in Appendices D and F.

As samples CM22/RAS-01 and CM22/LS-01 provided abundant geochronological data, zircon growth zones with concordant emplacement or antecrystic ages and sufficient space for a second LA-ICP-MS spot were selected for further trace element analysis. Trace element analysis was similarly carried out using an Australian Scientific Instruments RESOlution laser and ablated material carried in Ar to a Thermo iCAP-RQ single collector mass spectrometer. Analyses were conducted over one session and interspersed with analyses of the NIST610 glass, 91500, My Dromedary and Plešovice zircon reference materials, and an in-house reference material (Wiedenbeck *et al.* 1995; Sláma *et al.* 2008; Allen and Campbell 2012). Trace element analysis LA-ICP-MS settings are given in Table 3.2. Trace element data reduction was carried out using the Iolite v.4 3D Elements data reduction scheme (Paton *et al.* 2011; Paul *et al.* 2023). The 91500 (matrix matched) and NIST610 (contains all elements of interest) reference materials were used as the primary standards for data reduction. Trace element data was then filtered to remove analyses for which mass ICP-MS counts were below baseline counts at the data reduction stage, and for which the 1σ % error was > 50 % (i.e., 2σ error > 100%). Measured REE concentrations were normalised to chondrite values of McDonough and Sun (1995) for inspection. Ti-in-zircon temperature for each spot was calculated using the titanium concentration measured and titanium-temperature-zircon relationship of Watson et al. (2006). Out of economic geology interest, bivariate plots were constructed of transition metal concentration against Gd concentration (as a medium rare earth element proxy), Yb concentration (as a heavy rare earth element proxy) and corresponding uncorrected spot age. No trends were apparent and transition metal concentrations were highly variable (c.f. Gardiner et al., 2021). Transition metal analyses are therefore not discussed further within the main body of this thesis. Full trace element data including transition metals, REE and Ti-in-zircon calculations, is presented in Appendix E.

Chapter 4 Results

4.1 Petrography

Samples collected are dominantly granodiorite comprising anhedral to subhedral crystals of plagioclase, K-feldspar, quartz, and biotite. Sample CM22/LS-01 also contains amphibole. Samples collected from closer to the GGF and associated faults typically show more features of potentially fault related deformation and alteration such as undulose extinction and haematite veins. Mineralogical composition and key features observed in thin section for each sample are summarised in Table 4.1. Representative photomicrographs are presented in Appendix A.

4.2 Geochronology

Zircon texture and U-Pb geochronology results for each intrusive phase sampled are given below. The full data sets, CL images and zircon textural descriptions are presented in Appendices B – D. Core-rim boundaries are defined where there is a clear change in zircon texture, CL brightness or significant cross cutting relationships are observed between regions of oscillatory zoning. Textural definitions are otherwise as per (Corfu *et al*. 2003).

4.3 Strontian Sunart Granodiorite: CM22/LS-01 and CM22/RAS-01

Zircons from sample CM22/LS-01 are subhedral to euhedral, and range from c. 70 – 400 μm, though dominantly measure within c. 125 – 250 μm (Appendix B). Of the 99 grains imaged, 82 were analysed with 122 spots, 41 of which (34 %) are concordant or near concordant (Table 4.2). One spot is concordant but rejected due to evidence of Pb loss (008.1), and the remaining spots deemed to be affected by significant common Pb or Pb loss (Appendix C). Analysed grains are dominated by oscillatory zoning, often complex and well-developed, and sometimes convolute (Fig. 4.1a-c,e, 4.2a-c,f-h). Inclusions are common within both cores and rim sometimes overlapping both, as are cross-cutting homogeneous zones, sometimes orientated sub-parallel to zonation and sometimes with convolute boundaries (Fig.4.1a-c,e-g, 4.2a-f). Rims are typically narrow with respect to cores, although grains often consist of complex oscillatory zoning throughout

Table 4.1 Summary of mineralogy and key features of samples observed in thin section. Percentage mineral compositions and grain sizes given are estimates. For sample EM19/AB primary mineralogical composition varied between two thin sections and ranges of mineral percentages are given where appropriate. Quartz-Alkali Feldspar-Plagioclase-Feldspathoid (QAPF) classifications given follow the classification scheme of Le Bas and Streckeisen (1991).

Sample	QAPF Classification	Grain Size (mm)	Primary Mineralogy	Alteration Assemblage	Additional Features
CM22/LS-01	Granodiorite	0.1 - 6	Plagioclase (25 %), K-feldspar (10%), quartz (40 %), biotite (15 %), hornblende (10 %). Accessory zircon and titanite.	Sericite (micro veins, alteration of feldspars), chlorite (replaces hornblende).	K-feldspar megacrysts ≤ 6 mm, often perthitic. Occasional myrmekitic textures. Curved biotite cleavages. Amphibole typically occurs in clusters with no preferred orientation.
CM22/RAS-01	Granodiorite	0.1 - 5	Plagioclase (35 %), K-feldspar (18 %), biotite (7 %), quartz (~40 %). Accessory zircon and titanite.	Sericite (alteration of feldspars), haematite (veining in biotite, infill of micro-cataclasite zones).	K-feldspar megacrysts ~ 5 mm. Biotite often in clusters with curved cleavages and undulose extinction. Quartz extinction is typically undulose. A quartz-dominant micro-cataclasite zone cross-cuts much of the thin section.
CM22/KG-01	Granodiorite	0.2 - 5	Plagioclase (33 %), K-feldspar (10 %), quartz (43 %), biotite (14 %), Accessory zircon.	Sericite (alteration of feldspars), haematite (along grain boundaries), oxides (discrete patch).	K-feldspar megacrysts, ~ 3.5 – 5 mm, sometimes perthitic. Some myrmekitic texture in smaller K-feldspar grains. Quartz extinction is typically undulose.
CM22/HD-01	Monzogranite - Granodiorite	0.2 - 6	Plagioclase (35 %), K-feldspar (20 %), quartz (35 %), biotite (10 %). Accessory zircon.	Sericite (veinlets and microfracture fill, replaces plagioclase), haematite (veinlets and microfracture fill), chlorite (replaces biotite), oxides (discrete grains and patches).	Plagioclase megacrysts ~1.5 x 5 mm. K-feldspar megacrysts ~ 5 – 6mm, often strongly perthitic with inclusions of euhedral plagioclase. Quartz shows weakly undulose extinction.
EM19/AB	Monzogranite	0.2 - 6	Plagioclase (25 %), K-feldspar (25 – 35 %), quartz (40 %), biotite (0 - 10 %). Accessory oxides and titanite.	Chlorite and sericite (alteration of feldspars), haematite (intra-grain microcracks, along grain boundaries, veinlets).	Plagioclase albite twin lamellae sometimes displaced by up to ~ 0.1 mm. K-feldspar often strongly perthitic. Quartz extinction frequently undulose. Quartz-dominant micro-cataclasite zones up to ~ 0.5 mm wide occur infrequently.

Table 4.2 Summary of the number of grains imaged and analysed for each sample. *Grains imaged* indicates the number of grains imaged by CL and SE; *grains analysed* is the number of those imaged selected for LA-ICP-MS analysis; *spots analysed* is the total number of LA-ICP-MS spots analysed; *rejected at data reduction stage* is the number of spots which are concordant but showed evidence of Pb loss effects during data reduction; *spots concordant* is the number of concordant or near concordant spots not deemed to have been affected by significant Pb loss or common Pb expressed in absolute number and as a percentage of spots analysed.

Sample	Grains Imaged	Grain Analysed	Spots Analysed	Rejected at Data Reduction Stage (Pb loss)	Spots concordant
CM22/LS-01	99	82	122	1	41 (34 %)
CM22/RAS-01	87	63	88	3	39 (44 %)
CM22/KG-01	100	69	100	3	28 (28 %)
CM22/HD-01	91	61	87	5	32 (37 %)
EM19/AB	91	50	62	2	29 (47 %)

(Fig. 4.1c, 4.2, Appendix B). Open fractures are common, but dominantly < 50 μm long and often spatially limited to grain margins or the vicinity of a larger fracture or damaged zone (Fig.4.1h). Occasionally fractures cross-cut the length of grains, and they are sometimes distributed radially about the core (Fig.4.1h, Appendix B). Grains which were not analysed often consist of highly convolute or patchy zoning, oscillatory zoning which is very narrow or complex, or are more heavily fractured (Appendix B, C).

Zircons from sample CM22/RAS-01 are predominantly subhedral, and range in size from c. 80 – 250 μm, though dominantly measure c. 125 – 200 μm (Appendix B). Of the 87 grains imaged, 63 were analysed with 88 spots, 39 of which (44%) are concordant or near concordant (Table 4.2). Three are concordant but rejected due to evidence of Pb loss (48.1, 70.1, 75.1) and remaining spots are deemed to be affected by significant common Pb or Pb loss (Appendix C). Analysed grains are dominantly comprised of well developed, often complex, oscillatory zoning, with homogeneous or patchy cores (Fig. 4.3, 4.4). Where they occur, rims are typically narrow and dark with respect to cores, though many consist of complex oscillatory zoning throughout (Fig. 4.3a,b,d, 4.4, Appendix B). Zoning is often locally cross-cut by relatively CL-bright patches with convolute boundaries (4.2c,h, Appendix B, C). Inclusions occur commonly in both cores and rims, sometimes overlapping

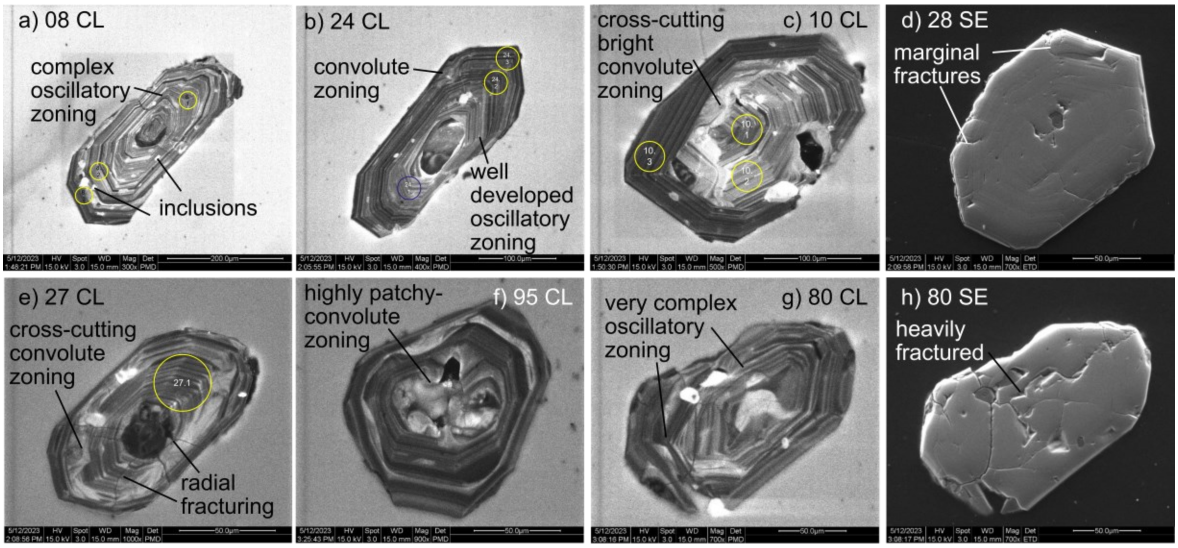

Figure 4.1 CM22/LS-01, selection of CL and SE zircon images of grain numbers (a) 08, (b) 24, (c) 10, (d) 28, (e) 27, (f) 95 and (g, h) 80. Analysed spots highlighted were rejected due to evidence of Pb loss or common Pb (yellow, a-c, e).

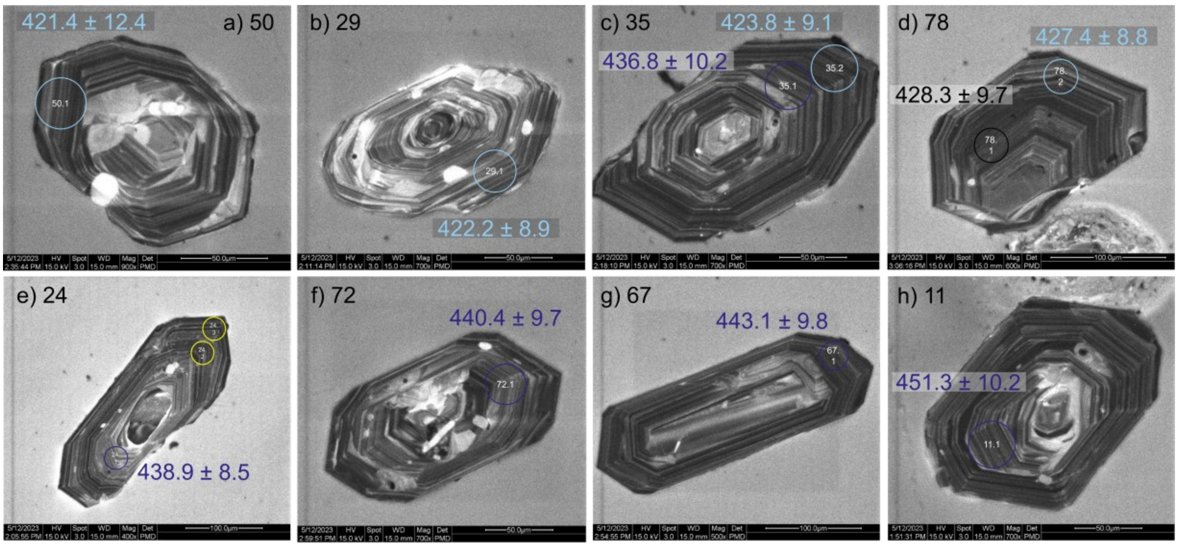

Figure 4.2 CM22/LS-01, representative selection of CL images of emplacement related or antecrystic zircon. Grains shown are numbers (a) 50, (b) 29, (c) 35, (d) 78, (e) 24, (f) 72, (g) 67 and (h) 11. Analysed spots are labelled with corresponding ages prior to common Pb correction with 2σ uncertainties for those interpreted as emplacement related (light blue) or antecrysts (dark blue). Spots without annotated ages were rejected due to evidence of Pb loss or common Pb (yellow, e).

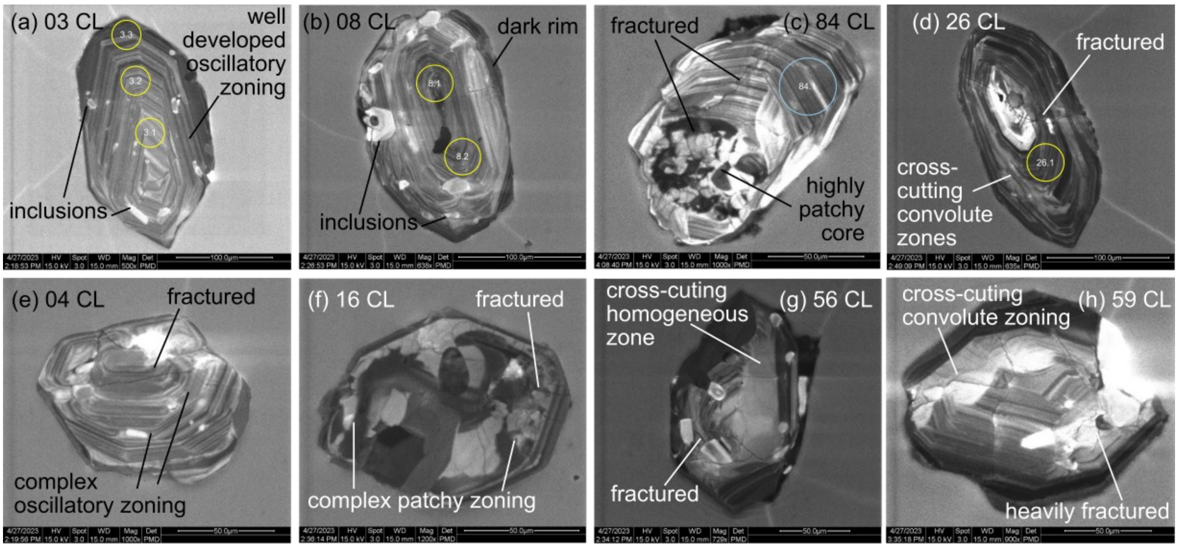

Figure 4.3 CM22/RAS-01, selection of CL and SE zircon images of grain numbers (a) 03, (b) 08, (c) 84, (d) 26, (e) 04, (f) 16 and (g) 56 and h) 59. Analysed spots highlighted were rejected due to evidence of Pb loss or common Pb (yellow, a, b, c) or represent emplacement growth (light blue, c).

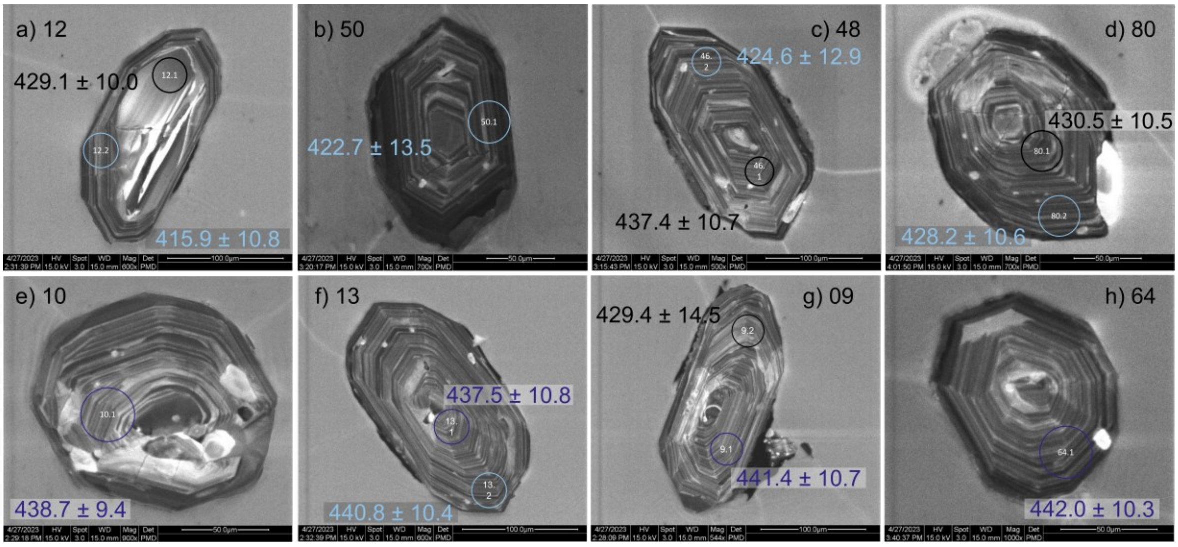

Figure 4.4 CM22/RAS-01, representative selection of CL images CL images of emplacement related or antecrystic zircon. Grains shown are numbers (a) 12, (b) 50, (c) 48, (d) 80, (e) 10, (f) 13, (g) 09 and (h) 64. Analysed spots are labelled with corresponding ages prior to common Pb correction for those interpreted as emplacement related (light blue), antecrysts (dark blue), and spots not texturally justifiable as emplacement related (black).

both, and are up to ~40 μm in length (fig. 4.3a,b,g,h, 4.4b-f, h). Many are fractured (Fig. 4.3a-h, 4.4a,b,d,e). Grains which were not analysed comprise one or more of: complex patchy zoning; oscillatory zoning which is too narrow or complex for a 30 μm laser spot; zoning more extensively cross-cut by homogeneous zones, or heavy fracturing (Fig. 4.3e-g, Appendix B).

Neither sample shows evidence of xenocrystic grains older than Caledonian age (Fig. 4.5a,b,d,e). A limited number of discordant grains in each sample show an approximate trend towards 0 Ma likely indicative of Pb loss, and many discordant grains which show approximately horizontal trends where zircon or other material containing common Pb may have been ablated (Fig.4.5a,d). Final remaining concordant and near concordant spots consist of oscillatory zoned cores and rims, or grains with continuous oscillatory zoning and three semi-homogenous cores (RAS_57.1, RAS_12.1, RAS_79.1, Appendix B).

Following the methodology to identify an age which may be consistent with emplacement of the Sunart granodiorite, spots of sample CM22/LS-01 from oscillatory zoned rims or the outermost portion of oscillatory zoning give a weighted mean $^{206}Pb/^{238}U$ age of 423.5 ± 2.8 Ma (n = 11, MSWD = 1.6) (Table 4.3, Fig. 4.2, 4.5c, Appendix B). Spots older than the potential emplacement population range in $^{206}Pb/^{238}U$ age (uncorrected for common Pb, see chapter 3) from 435.1 ± 9.3 to 451.3 ± 10.2 Ma (Table 4.3, Fig. 4.5b,c). Similarly, spots of CM22/RAS-01 of oscillatory zoned rims give a weighted mean $^{206}Pb/^{238}U$ age of 423.6 ± 3.1 Ma (n = 13, MSWD = 1.4) (Table 4.3, Fig. 4.4, 4.5f). Spots older than the potential emplacement population range in uncorrected $^{206}Pb/^{238}U$ age from 438.4 ± 11.5 to 442.0 ± 10.3 Ma (Table 4.3, Fig. 4.5e,f, Appendix B). Spots older than the emplacement populations may be considered antecrystic. Spots interspersed among the emplacement populations reflect zircon which was not texturally justifiable as emplacement related and may represent (i) an inner portion of a grain with an outermost rim emplacement age or (ii) zircon which underwent partial or full Pb loss and age resetting at emplacement (see chapter 5 for further discussion).

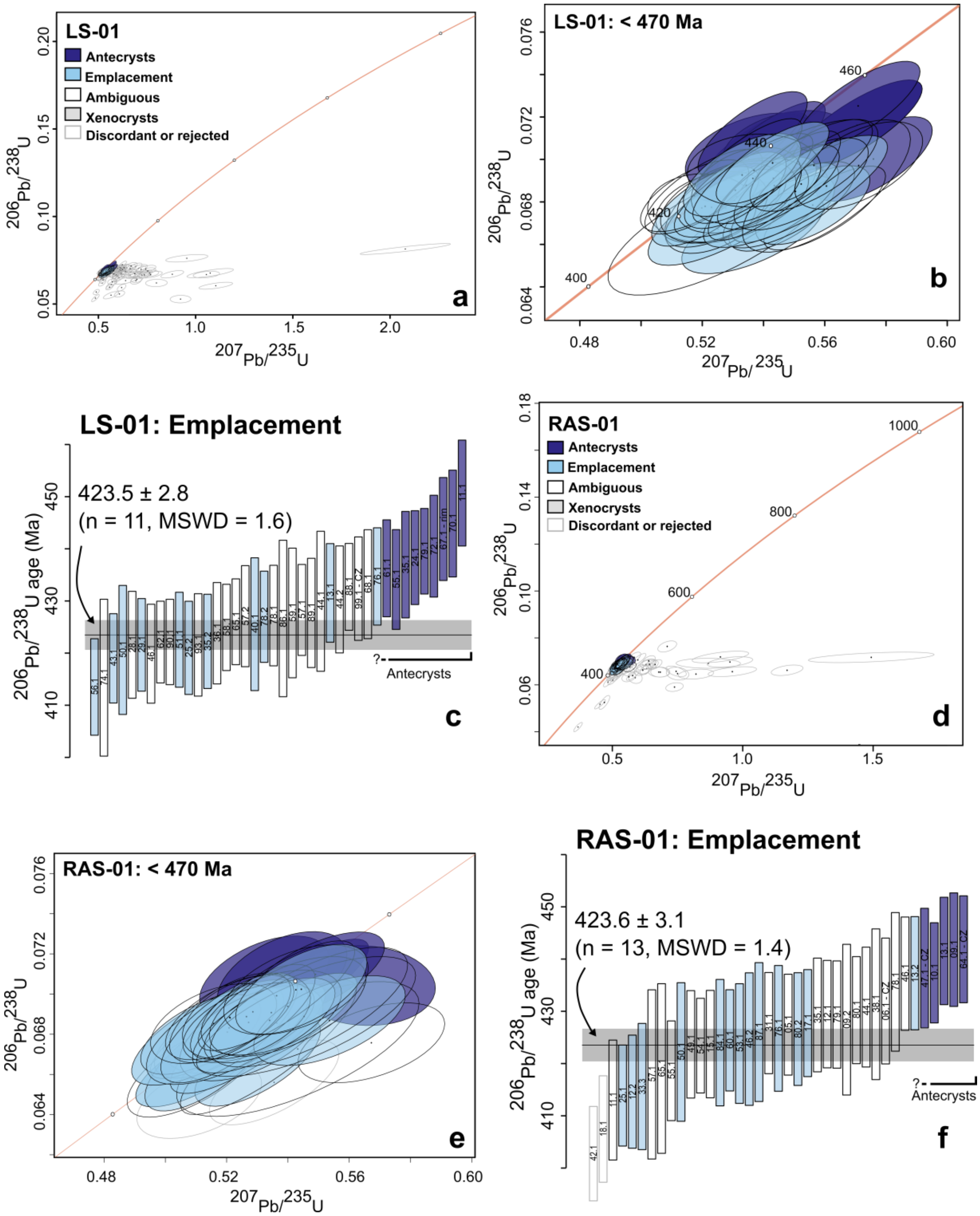

Figure 4.5 Summary of U-Pb geochronology results for samples CM22/LS-01 (a-c) and CM22/RAS-01 (d-f). Concordia plots show the full data sets (a, d) and concordant and near concordant spots < 470 Ma (b, e) prior to common Pb correction. Weighted mean plots show common Pb corrected ages with the final weighted mean emplacement ages (c, f). Shaded points represent spots interpreted as emplacement growth (light blue) or antecrystic growth (dark blue). Clear points represent spots interpreted as rims affected by Pb loss (grey outline) and spots which couldn't be texturally justified as emplacement related (black outline). All emplacement spots are rims and all antecrystic spots are cores unless otherwise labelled. CZ = a whole grain with continuous oscillatory zoning.

As samples CM22/LS-01 and CM22/RAS-01 give ages within error of each other and show similar magmatic Th/U values ranging 0.35 – 1.09 with a mean of 0.67, and 0.53 – 0.90 with a mean of 0.73 respectively (Fig. 4.6, Appendix D), the data from both samples was collated to obtain a more precise Sunart granodiorite facies age. The spots from both samples previously interpreted as emplacement growth were collated in IsoplotR and a weighted mean $^{206}Pb/^{238}U$ age of 423.5 ± 2.1 Ma (n = 24, MSWD = 1.4) was obtained (Table 4.3, Fig. 4.7). Spots of cores or inner portions of magmatic rims with substantive further rim growth remain omitted from the weighted mean age as these were considered unlikely to represent growth during final emplacement (Archibald *et al*. 2021; Miller *et al*. 2007). Spots older than the oldest texturally-identified emplacement related growth may be considered antecrystic (Fig. 4.7).

Table 4.3 Summary of preferred emplacement ages. Maximum antecryst ages given are the individual $^{206}Pb/^{238}U$ point age prior to common Pb correction.

	Weighted mean $^{206}Pb/^{238}U$ Age (Ma)	n	MSWD	Maximum antecryst age (Ma)
CM22/LS-01	423.5 ± 2.8	11	1.6	451.3 ± 10.2
CM22/RAS-01	423.6 ± 3.1	13	1.4	442.0 ± 10.3
Sunart combined age	423.5 ± 2.1	24	1.4	451.3 ± 10.2
CM22/KG-01	418.2 ± 6.3	3	0.29	443.1 ± 11.3
CM22/HD-01	417.0 ± 4.0	6	0.63	439.0 ± 9.0
EM19/AB	418.2 ± 5.6	4	1.9	428.8 ± 11.3

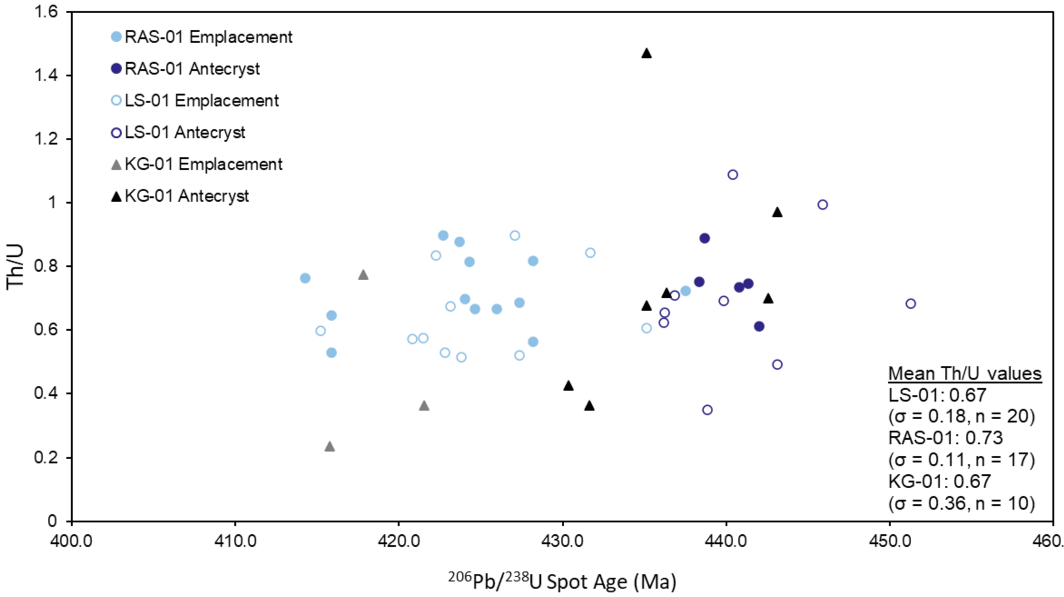

Figure 4.6 Th/U of emplacement related and antecrystic spots of Strontian samples against uncorrected $^{206}Pb/^{238}U$ spot age. Mean Th/U values with corresponding standard deviation and number of analyses are shown.

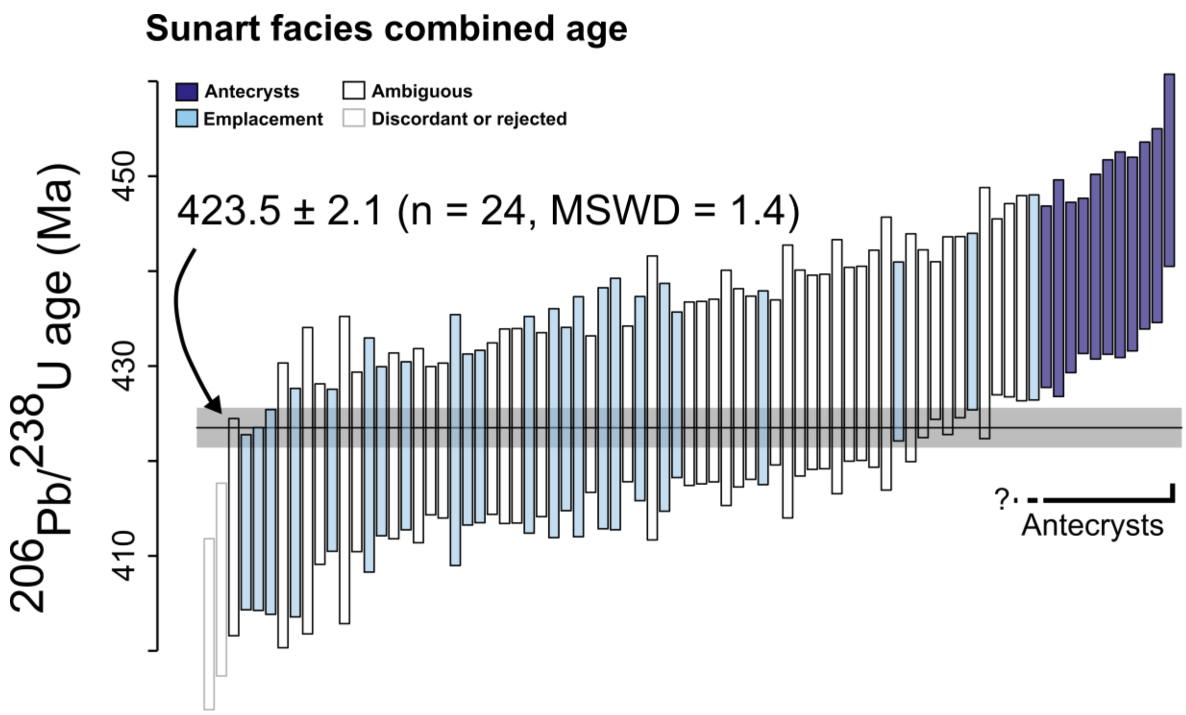

Figure 4.7 Combined weighted mean age of samples CM22/LS-01 and CM22/RAS-01. Clear points represent spots interpreted as rims affected by Pb loss (grey outline) and spots which couldn't be texturally justified as emplacement related (black outline).

4.4 Strontian Sanda Granodiorite: CM22/KG-01

Grains are dominantly subhedral, with size ranging c. 80 – 300 μm, though dominantly in the range c. 100 – 200 μm. Those picked on to mount 2 are of smaller average size than mount 1, ranging from c. 80 – 200 μm, though are dominantly in the range c. 100 – 150 μm. Compared with zircons on mount 1 which range 100 – 300 μm and are dominantly 100-200 μm. Analysed grains frequently contain homogeneous to patchy zoned cores, often partially resorbed (Fig. 4.8a-d, 4.9b-f, i), and magmatic rims with poorly- to well-developed oscillatory zoning (Fig. 4.9a-d, 4.9a-i). Oscillatory zoning is finely to moderately spaced and often complex (Fig. 4.8a-e, 4.9). Core to rim proportions are variable (Appendix B).

Unanalysed grains contain cores with highly patchy and(or) convolute zoning; regions of oscillatory zoning are too narrow to fit a 30 μm spot analysis, or sometimes are fractured (Fig. 4.8e-h; Appendix B). Of the 100 grains imaged, 69 were analysed with 100 spots. Of these, 28 are concordant or near concordant, and three were concordant or near concordant but rejected due to evidence of Pb loss (29.1, 43.2, 2_12.2, Table 4.2, Appendix C). The remaining spots were deemed to be affected by significant common Pb or Pb loss.

Concordant spots older than Caledonian age are from oscillatory zoned cores and rims, and semi-homogeneous cores often with hints of oscillatory zoning. Older spots form a range of dominantly isolated spots, some within error of each other, from c. 1825 – 1317 Ma and c. 808 – 830 Ma (Appendix C, Fig. 4.10a). Caledonian age concordant spots range in $^{206}Pb/^{238}U$ age from c. 415 – c. 443 Ma (Fig. 4.10a,b). Discordant grains older than Caledonian age approximate Pb loss trends towards 0 Ma likely stemming from xenocrystic spots aged 1317 – 1825 Ma (Fig. 4.10a).

A spread of discordant grains with approximately horizontal trends stem from concordant Caledonian ages towards infinite $^{207}Pb/^{235}U$ may be due to analysis of zircon or other material containing common Pb such as resin (Fig. 4.10a). The remaining concordant and near concordant spots are from oscillatory zoning and six semi-homogenous cores, with magmatic Th/U values in the range 0.23 – 1.6 (Fig. 4.6, 4.9; Yakymchuk et al., 2018). Following the methodology to identify an

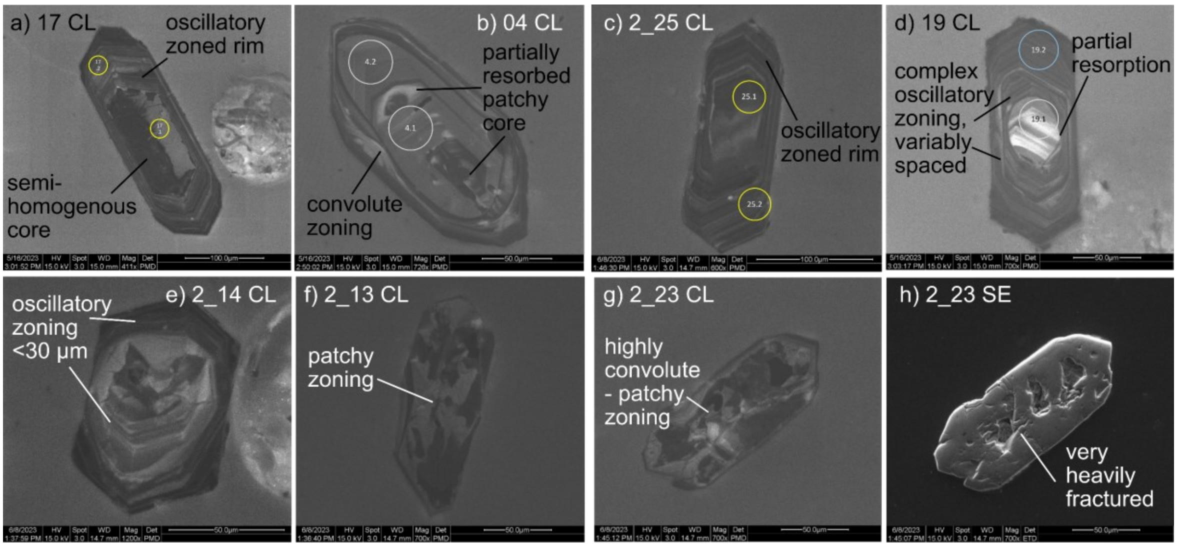

Figure 4.8 CM22/KG-01, representative selection of CL and SE zircon images of grain numbers (a) 17, (b) 04, (c) 2_25, (d) 19, (e) 2_14, (f) 2_13, and (g, h) 2_23. Analysed spots highlighted were rejected due to evidence of Pb loss or common Pb (yellow, a, c), or represent xenocrystic growth (grey, b, d) or emplacement growth (light blue, d).

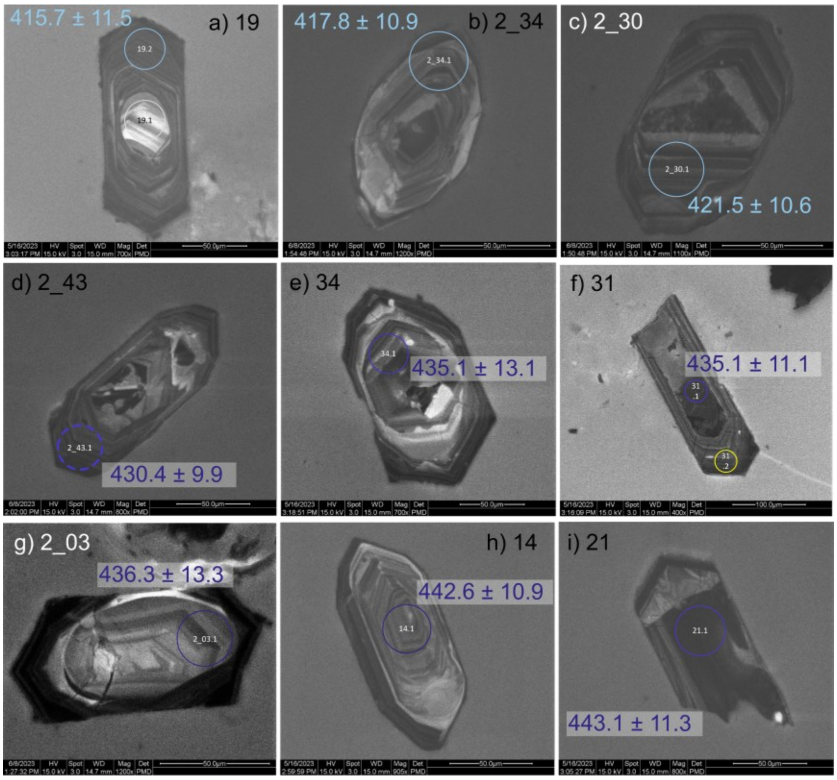

Figure 4.9 CM22/KG-01, CL images of all grains for which analyses gave emplacement or antecrystic ages, (a) 19, (b) 2_34, (c) 2_30, (d) 2_43, (e) 34, (f) 31, (g) 2_03, (h) 14 and (i) 21. Analysed spots are labelled with corresponding ages prior to common Pb correction for those interpreted as emplacement related (light blue), antecrysts (dark blue), and for spots not texturally justifiable as emplacement related (black).

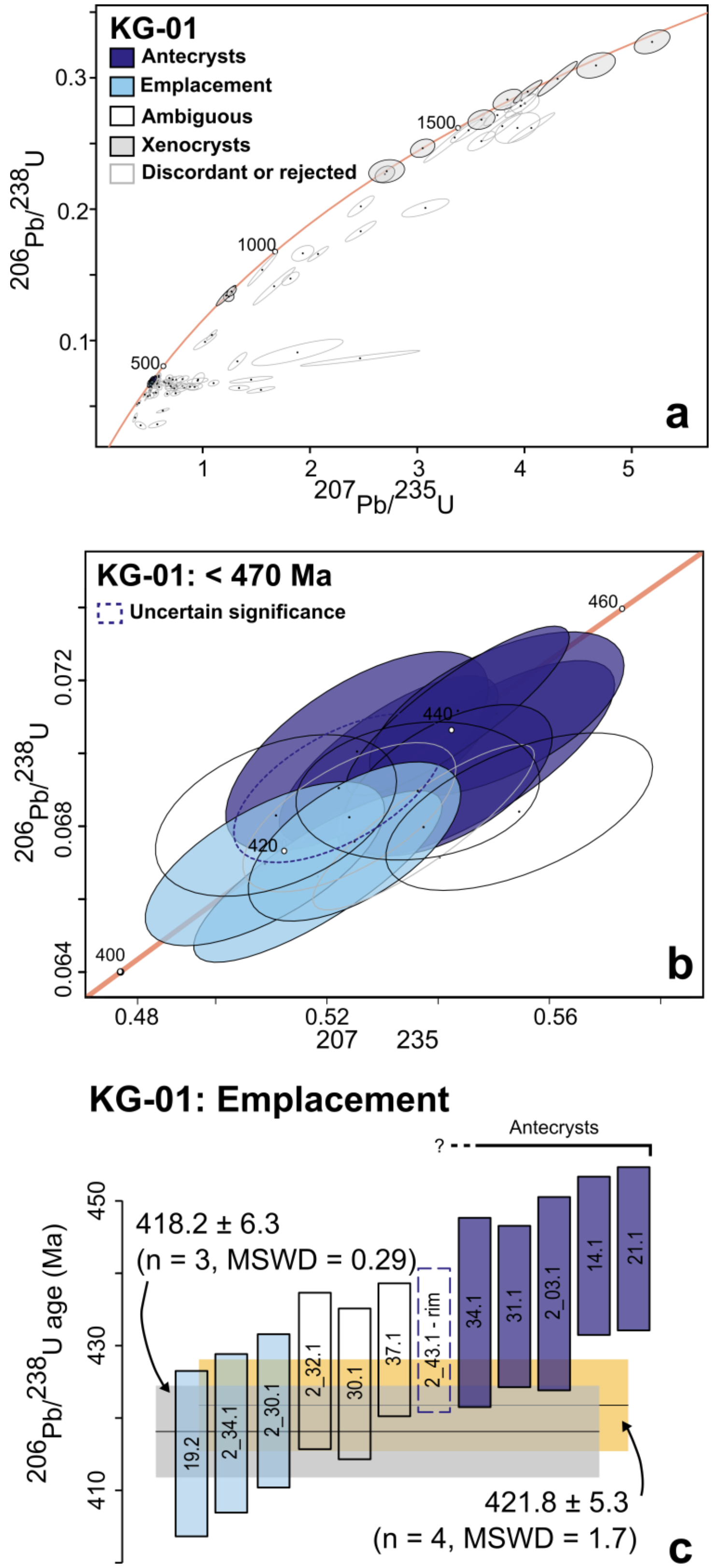

Figure 4.10 Summary of U-Pb geochronology results for sample CM22/KG-01; Concordia plots show the full dataset (a) and concordant and near concordant spots < 470 Ma (b) prior to common Pb correction. The weighted mean plot (c) shows common Pb corrected $^{206}Pb/^{238}U$ ages and the possible weighted mean emplacement ages. Shaded points represent spots interpreted as emplacement growth (light blue) or antecrystic growth (dark blue). Spot 2_43.1 with uncertain emplacement or antecrystic affinity is highlighted with a dashed outline. Clear points represent spots which couldn't be texturally justified as emplacement related (black outline). All emplacement spots are rims and all antecrystic spots are cores unless otherwise labelled.

age which may be consistent with emplacement of the Sanda granodiorite (see chapter 3), a weighted mean $^{206}Pb/^{238}U$ age of 421.8 ± 5.3 (n = 4, MSWD = 1.7) was determined (Fig. 4.10c). However, this age is very close to and well within error of samples CM22/LS-01 and CM22/RAS-01 and may conflict with geochemical evidence that these are different phases (e.g., Matthews et al., 2023). Removing the oldest of these four spots gives a weighted mean $^{206}Pb/^{238}U$ age of 418.2 ± 6.3 (n = 3, MSWD = 0.29), consistent with the previously determined monazite U-Pb age of 418 ± 1 Ma (Table 4.3, Fig. 4.10c; Paterson et al., 1993). Detailed discussion on selection of the 418.2 ± 6.3 Ma zircon age is presented in section 5.1.2. Spots older than both possible emplacement populations range in uncorrected $^{206}Pb/^{238}U$ age from 435.1 ± 13.1 to 443.1 ± 11.3 Ma and may be considered antecrysts. Spots with ages between that of the emplacement and antecryst populations are cores (Appendix B, D) and likely represent antecrystic or xenocrystic zircon which underwent partial or full Pb loss and age resetting at emplacement (Fig. 4.10b,c; discussed further in chapter 5).

4.5 Helmsdale Inner Monzogranite-Granodiorite: CM22/HD-01

Zircons are dominantly subhedral, and range in size between 70 and 240 μm, though dominantly range between 100 and 175 μm. Analysed grains often contain patchy zoned, oscillatory zoned, heterogeneous and homogeneous cores with partially resorbed to resorbed boundaries (Fig. 4.11a,c,e, 4.12a,c,f,g). Bright narrow zones around core margins also occur (Fig.4.11a,c; Appendix B). Rims are commonly dark, homogeneous to oscillatory zoned and narrow with respect to cores though some grains have more equal core-rim proportions (Fig.4.11a,c, 4.12c,g; Appendix B). Other analysed grains are more strongly euhedral with fine oscillatory zoning throughout, often with no clear core-rim distinction though sometimes contain a very small homogeneous core (Fig. 4.11e, 4.12a,b,d-f; Appendix B). Open fractures are also common, particularly around grain margins approximately parallel to grain edges, though some grains contain fractures throughout (Fig.4.11b,d,h; Appendix B). Occasional large open fractures which cross-cut the length or width of grains occur (Fig.4.11f, Appendix B). Grains which were too small, very heterogeneous or very heavily fractured were not analysed (Fig. 4.11b,d,f-h; Appendix B). Of the 91 grains imaged, 61 were analysed with 87

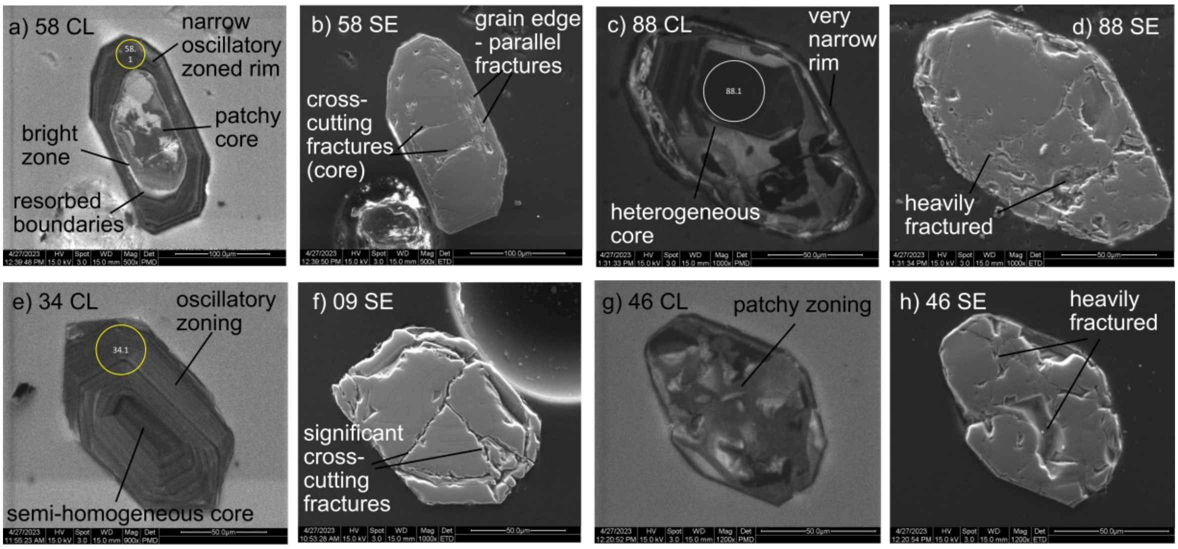

Figure 4.11 CM22/HD-01, representative selection of CL and SE zircon images of grain numbers (a, b) 58, (c, d) 88, (e) 34, (f) 09, and (g, h) 46. Analysed spots highlighted were rejected due to evidence of Pb loss or common Pb (yellow, a, e), or represent xenocrystic zircon (grey, c).

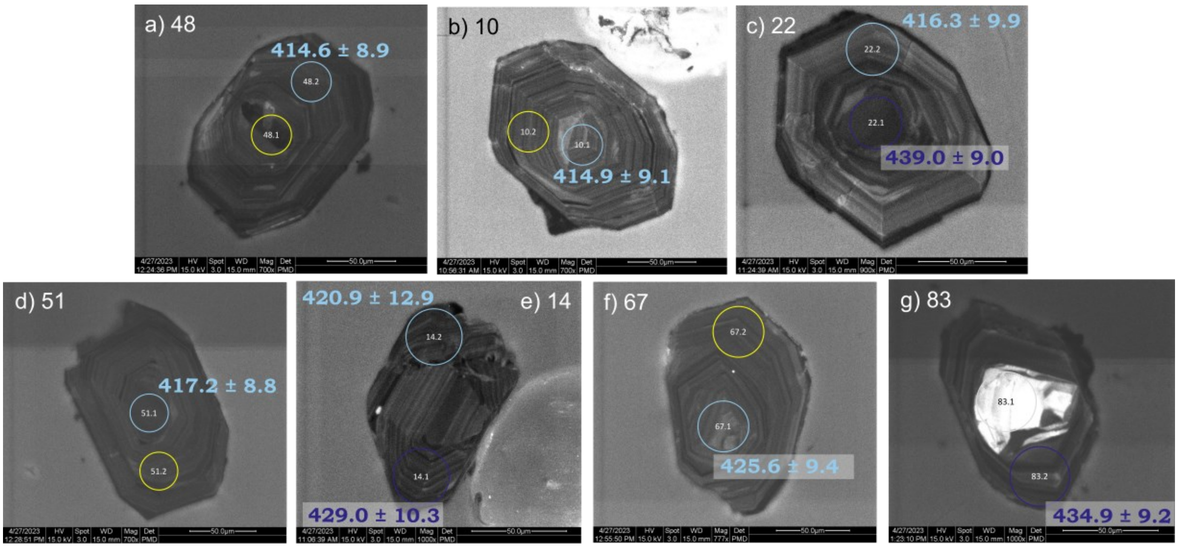

Figure 4.12 CM22/HD-01, CL images of all grains for which analyses gave emplacement or antecrystic ages, (a) 48, (b) 10, (c) 22, (d) 51, (e) 14, (f) 67, and (g) 83. Analysed spots are labelled with corresponding ages prior to common Pb correction for those interpreted as emplacement related (light blue) and antecrysts (dark blue). Further spots highlighted are attributed to Pb loss (yellow, a, b, d, f) or xenocrystic (grey, g).

spots, of which 32 (37 %) of which are concordant or near concordant. Five were concordant but rejected due to evidence of Pb loss (01.2, 34.1, 44.2, 51.2, 79.1; Table 4.2).

Older concordant spots include an isolated spot at c. 1780 Ma, and spreads of ages from c. 1600 to 1720 Ma and 1460 to 1540 Ma. Further isolated points occur at c. 1260 Ma, 1000 Ma, 930 Ma, and two points within error at c. 1100 Ma (Fig4.14a; Appendix C). Three spots within error occur between c. 470 to 480 Ma (Fig4.14a; Appendix C). The youngest spread of ages occurs between c. 390 to 450 Ma, the youngest of which was rejected for evidence of Pb loss (Fig. 4.14b). Discordant spots, likely affected by Pb loss, approximately trend from both the older and younger concordant spots towards 0 Ma (Fig. 4.14a). Concordant spots aged 470 Ma and older, are from oscillatory zoned zircon rims and cores, and three homogeneous to semi-homogeneous core zones (Appendix B) and may be considered xenocrystic (see chapter 5 for further discussion).

Remaining concordant and near concordant spots < 470 Ma consist of spots of oscillatory zoned rims and grains comprising continuous oscillatory zoning with magmatic Th/U values (Fig. 4.13; Appendix D; Yakymchuk et al., 2018). Following the methodology to identify an age that may be consistent with emplacement of the Helmsdale inner granite, these spots give a weighted mean $^{206}Pb/^{238}U$ age of 417.0 ± 4.0 Ma (n = 6, MSWD = 0.63) (Table 4.3; Fig. 4.14b,c). Spots older than the potential emplacement population range in uncorrected $^{206}Pb/^{238}U$ age from 425.1 ± 10.8 to 439.0 ± 9.0 Ma may be considered antecrystic (Fig. 4.12, 4.14c; see chapter 5 for further discussion).

4.6 Abriachan Granite: EM19/AB

Zircons from sample EM19/AB are dominantly subhedral, and range in size from 60 to 200 μm, though dominantly measure 130 – 175 μm (Appendix B). Analysed grains contain complex oscillatory zoned, heterogenous or homogeneous cores with partially resorbed to resorbed boundaries, with oscillatory zoned or homogeneous rims (Fig.4.15a-e, 4.16; Appendix B). Core diameter is often larger than the rim width, though the core-rim ratio is variable, and some analysed grains

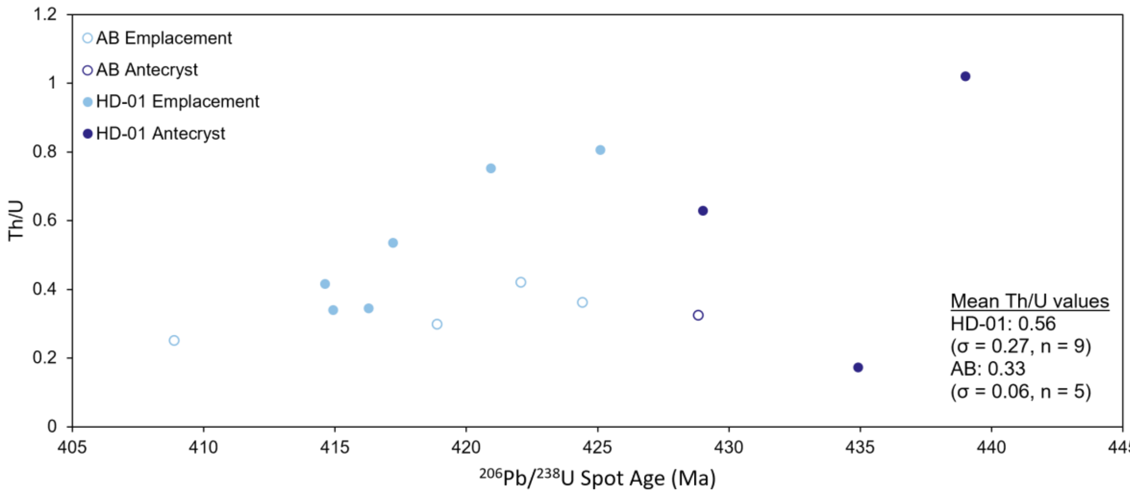

Figure 4.13 Th/U values for emplacement related and antecrystic spots of Helmsdale and Abriachan samples against uncorrected $^{206}Pb/^{238}U$ spot age. Mean Th/U values with corresponding standard deviation and number of analyses are shown.

are oscillatory zoned throughout with no distinct core and rim (Fig. 4.15f, 4.16; Appendix B). Very bright, narrow, homogeneous zones are common at core-rim boundaries (Fig.4.16a-c; Appendix B). Minor bright homogeneous zones which cross-cut oscillatory zoning occur, and occasionally small inclusions occur within rims (Fig.4.15c,f,; Appendix B). Grains which were not analysed are commonly highly heterogeneous or patchy, very complex, contained zones too small for a 30 µm laser spot, or are heavily fractured (Fig.4.15g,h; Appendix B). Of the 91 grains imaged, 50 were analysed with 62 spots, 29 (47 %) of which are concordant or near concordant (Table 4.2; Appendix C). Two spots are concordant but were rejected due to evidence of Pb loss (50.2, 58.1).

Older concordant spots from broad to oscillatory zoned cores and rims give two clusters of three spots at c. 1750 Ma and at c. 1630 Ma, and a spread of spots between c. 1530 to 1365 Ma mostly within error of each other (Fig. 4.14d; Appendix B). Older spots from homogeneous to semi-homogeneous cores give a cluster of spots at c. 1020 Ma and a grain aged c. 980 Ma within error of these, and an isolated spot at 477 Ma (Fig. 4.14; Appendix B). These spots may be considered xenocrystic (see chapter 5 for further discussion).

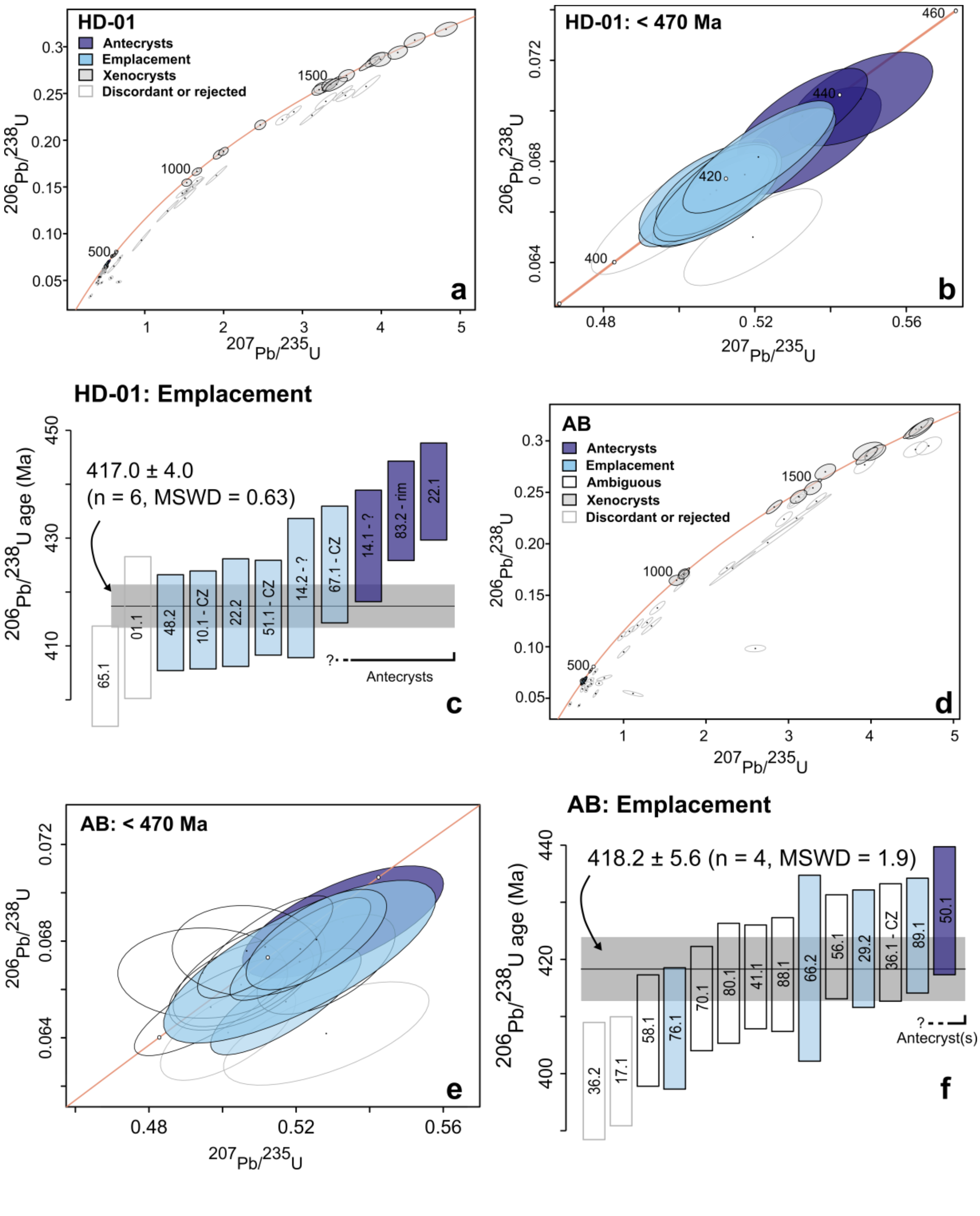

Figure 4.14 Summary of U-Pb geochronology results for samples CM22/HD-01 (a-c) and EM19/AB (d-f). Concordia plots show the full data sets (a, d) and concordant and near concordant spots < 470 Ma (b, e) prior to common Pb correction. Weighted mean plots show common Pb corrected ages with the final weighted mean emplacement ages (c, f). Shaded points represent spots interpreted as emplacement growth (light blue) or antecrystic growth (dark blue). Clear points represent spots interpreted as rims affected by Pb loss (grey outline) and spots which couldn't be texturally justified as emplacement related (black outline). All emplacement spots are rims and all antecrystic spots are cores unless otherwise labelled. CZ = a whole grain with continuous oscillatory zoning. It should be noted that the texture of grain 14 of sample CM22/HD-01 does not show clear relative timing of growth zones.

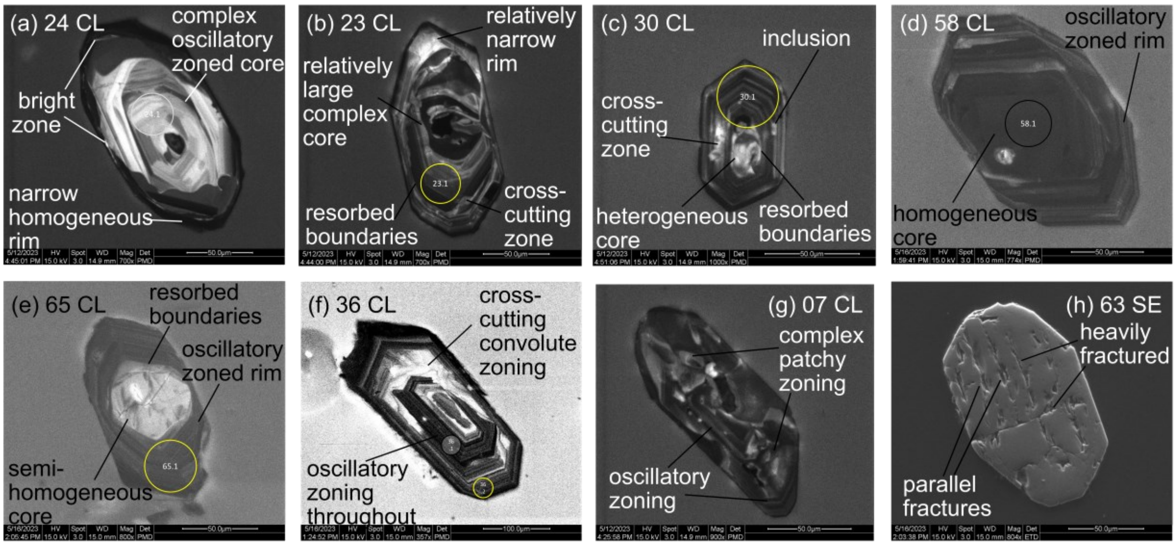

Figure 4.15 EM19/AB, representative selection of CL and SE zircon images of grain numbers (a) 24, (b) 23, (c) 30, (d) 58, (e) 65, (f) 36, (g) 07, and (h) 63. Analysed spots highlighted were rejected due to evidence of Pb loss or common Pb (yellow, b, c, e), or were concordant or near concordant but not texturally justifiable as emplacement related (black, d).

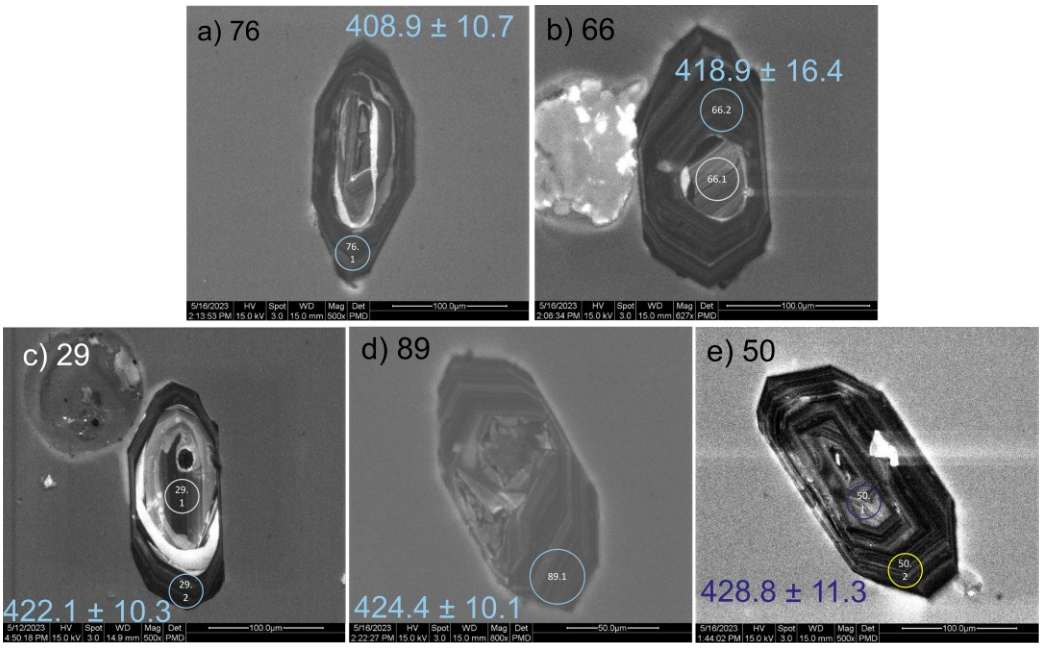

Figure 4.16 EM19/AB, CL images of all grains for which analyses gave emplacement and antecrystic ages, (a) 76, (b) 66, (c) 29, (d) 89, and (e) 50. Analysed spots are labelled with corresponding ages prior to common Pb correction for those interpreted as emplacement related (light blue), and antecrysts (dark blue). Further analysed spots highlighted are interpreted as having been affected by Pb loss (yellow, e) or as xenocrystic (grey, b, c).

Remaining concordant and near concordant spots < 470 Ma consist of spots of oscillatory zoned rims and homogenous to semi-homogenous cores with magmatic Th/U values (Fig. 4.13, 4.16, Appendix B; Yakymchuk et al., 2018). Following the method for identification of an age that may be consistent with emplacement of the Abriachan granite these spots produce a mean weighted $^{206}Pb/^{238}U$ age of 418.2 ± 5.6 Ma (n = 4, MSWD = 1.9) (Table 4.3; Fig. 4.14f). One spot older than the possible emplacement population has an uncorrected $^{206}Pb/^{238}U$ of 428.8 ± 11.3 Ma and may be considered antecrystic. Spots of emplacement age but not texturally justifiable as emplacement related are typically cores and may be interpreted as antecrystic or xenocrystic zircon which underwent partial or full Pb loss at emplacement (Fig. 4.14e,f; see chapter 5 for further discussion).

4.7 Zircon Geochemistry of the Sunart Granodiorite

As set out in Chapter 2, transition metals are not discussed further, and data is given in Appendix E. REE and Ti-in-zircon temperature results for samples CM22/LS-01 and CM22/RAS-01 obtained by LA-ICP-MS are presented below. REE_N in text refers to measured REE concentrations normalised to chondrite meteorite concentration using the values of McDonough and Sun (1995).

4.9.1 Rare Earth Elements

Both samples show steep overall trends highly enriched in heavy REE and typically limited enrichment or depletion in light REE (Fig. 4.17). Light REE depletion to enrichment with respect to chondrite values shows a range of 0.17 – 2.00 for CM22/LS-01 and 0.11 – 8.81 for CM22/RAS-01. Two spots have light REE content significantly above this range, with La_N chondrite normalised values of 98 and 317 (Fig. 4.17; Appendix E). Analyses of both samples typically show strong positive Ce anomalies. Minimum Ce_N for sample CM22/LS-01 is 63.76 compared to minimum La_N and Pr_N values of 0.17 and 0.83 respectively (Fig. 4.17). For sample CM22/RAS-01 minimum Ce_N observed is 76.64 compared with La_N and Pr_N minimum values of 0.11 and 0.86 respectively (Fig. 4.17). Ce anomalies are less distinct or absent in the analyses with elevated light REE content. Weak to very weak negative Eu anomalies are also typically present in analyses of both samples, with the exception of those with elevated light REE (Fig. 4.17).

Medium to heavy REE define a clear trend of increasing enrichment with increasing atomic number, with Dy_N and Lu_N values ranging 105.49 – 227.52 and 1402.82 – 2594.50 respectively for sample CM22/LS-01 and 200.04 – 484.63 and 1831.10 – 4247.26 respectively for sample CM22/RAS-01 (Fig. 4.17). There is no discernible distinction between chondrite normalised REE values of emplacement related and antecrystic zircon growth in either sample, with significant overlap in values. (Fig. 4.17).

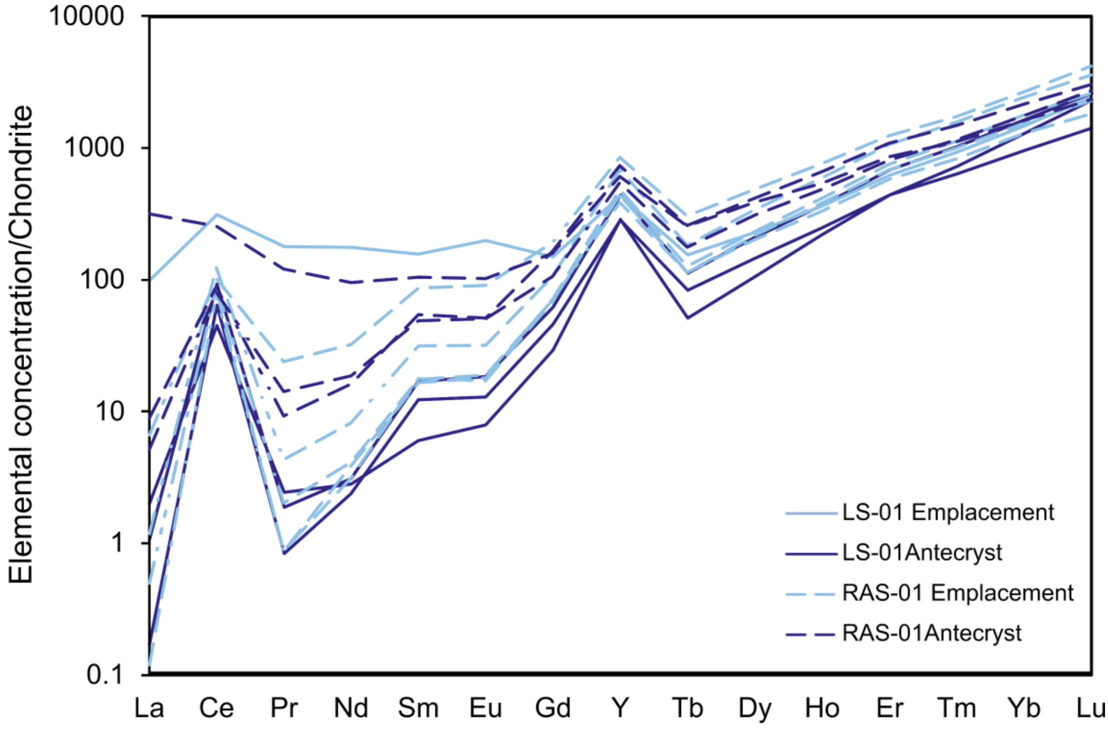

Figure 4.17 Chondrite normalised zircon LA-ICP-MS REE + yttrium data for Strontian Sunart granodiorite samples CM22/LS-01 and CM22/RAS-01. Emplacement and antecryst spot classifications are as per individual sample age determinations.

4.9.2 Ti-in-Zircon Thermometry

Calculated Ti-in-zircon temperature for LA-ICP-MS analyses of sample CM22/LS-01 dominantly range between 637 and 683 ºC, with an outlier at 792 ºC (Fig. 4.18). Temperatures for sample CM22/RAS-01 range dominantly between 647 and 700 ºC, with an outlier producing a temperature of 849 ºC (Fig. 4.18). Outliers with elevated Ti-in-zircon temperature correspond to those with elevated light REE content (Fig. 4.17, 4.18; Appendix E). Excluding outliers, emplacement related spots appear to have higher average Ti-in-zircon temperature than antecrystic spots. However, there is overlap in temperature results between antecrystic and emplacement spots, and a difference between the populations is not confidently discernible (Fig. 4.18).

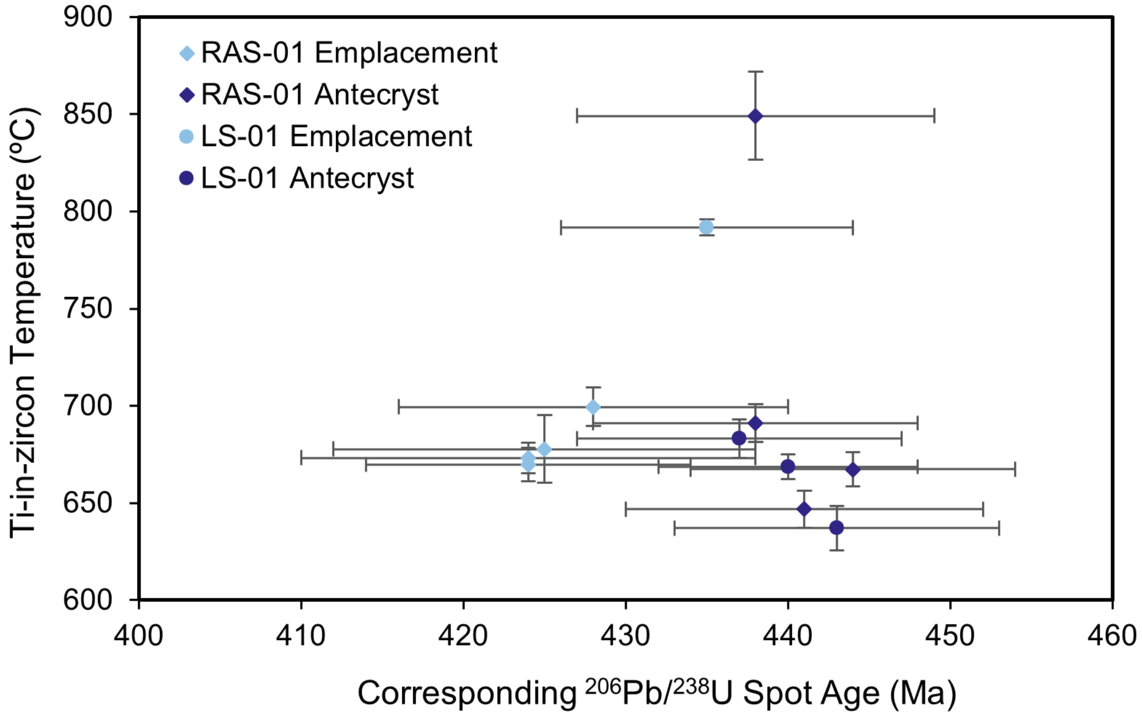

Figure 4.18 Ti-in-zircon temperature for Strontian Sunart granodiorite samples. Errors shown are 2σ (spot ages prior to common Pb correction), and 1σ (Ti-in-zircon temperature). Temperature errors include that of the LA-ICP-MS measurement of Ti content, and that induced by the calculation (Watson *et al.* 2006). Emplacement and antecryst spot classifications are as per individual sample age determinations.

Chapter 5 Discussion

5.1 What's in an age? From Antecrysts to Final Emplacement

5.1.1 Strontian Sunart Facies: CM22/LS-01 and CM22/RAS-01

Sunart facies samples CM/LS-01 and CM22/RAS-01 produced individual emplacement ages with low errors of c. 0.7 %, of 423.5 ± 2.8 Ma (n = 11, MSWD = 1.6) and 423.6 ± 3.1 Ma (n = 13, MSWD = 1.4) respectively (Table 4.3, Fig. 4.5). These ages give a range of antecrystic uncorrected spot ages (i.e., spot ages prior to Stacey-Kramers correction, see section 3.4) of ~437 Ma to 451.3 ± 10.2 Ma (Table 4.3, Fig.4.5). A combined final emplacement age of 423.5 ± 2.1 Ma (n = 24, MSWD = 1.4) was obtained given individual ages are statistically indistinguishable from each other (Fig. 4.7). Each of these ages produce MSWD values within the acceptable range of Spencer et al. (2016). As zircon from each of these samples have textures indicative of magmatic growth (see section 4.2.1), exceptions were made as per the method set out in chapter 3 to exercise caution and ensure confidence that spots selected for weighted mean calculations represent emplacement related growth. Notable spots omitted from the weighted mean include 47.1, 64.1, and 6.1 of sample CM22/RAS-01, and spot 99.1 of sample CM22/LS-01 as these grains are small with irregular shapes that may be a result of resorption and were interpreted as the cores of partially resorbed antecrysts (Fig. 4.5, Appendix B). CM22/LS-01 spot 67.1 was omitted despite being on a well-formed rim as it is significantly older than, and outwith error of, many of the younger emplacement related rims and is interpreted as antecrystic growth (Fig. 4.5c, Appendix B). Further, including these spots in the weighted mean calculation causes MSWD to increase above the acceptable range of Spencer et al. (2016) providing additional confidence in their omission. Additional omitted spots represent the inner portion of continuous growth for which only the outermost growth was included in the weighted mean age. Spot 33.3 of CM22/RAS-01 remains included in the weighted mean despite a younger age for (and thus omission of) the corresponding core spot 33.1, as 33.1 is adjacent to small fracture attributed as a probable cause of Pb loss. Relative ages of spots 33.3 (outer rim) and 33.2 (inner rim) are as anticipated (Appendix B, C).

The presence of an antecrystic rim, and grains comprising continuous magmatic growth emplacement age and pre-emplacement age (e.g., CM22/LS-01 grain 35, Fig. 4.2c, 4.5c) highlights the uncertainty associated with texturally distinguishing between emplacement and antecrystic populations. As such it is possible that the antecrystic population may stretch younger than is interpreted here. Unclassified core and inner rim ages interspersed among the emplacement population may represent i) antecrystic growth affected by total or partial Pb loss at the time of emplacement which produce emplacement ages, ii) genuine antecrystic growth unaffected by Pb loss but which was not classed as such due to uncertainty in the emplacement-antecryst boundary, or iii) aforementioned inner portions of continuous zircon growth (Fig. 4.5b,c,e,f).

Despite some uncertainty over exactly how many dated zircon zones are definitively antecrystic, such zones are almost certainly present. The range of ages obtained extends beyond that expected for zircon growth during final cooling following emplacement (Fig. 4.7, 4.10, 4.14). This extensive and complex zircon history is also showcased within individual grains which show a large time span between inner and outer grain portions (e.g., CM22/LS-01 grain 35, Fig. 4.2c). Such differences within grains are suggested to be caused by transportation of antecrystic zircon to emplacement depth prior to final growth (e.g., Archibald *et al*. 2021, their figure 12D). Similarity between the oldest zones and emplacement related zones in Th/U values (Fig. 4.6, 4.13), REE contents (Fig. 4.17) and magmatic oscillatory zoning textures (Fig. 4.2, 4.4, 4.9, 4.12, 4.16) support derivation from a homogenised source and thus that zones not formed on emplacement are antecrystic, not xenocrystic.

This evidence for antecrysts supports the hypothesis that an existing LCHZ within the Northern Highlands crust produced a homogenised, evolved mush available for remobilisation and emplacement of magma (Milne *et al*. 2023). The lack of trend in Th/U ratios with age similarly supports this interpretation (Fig. 4.6), and is consistent with the minimal amount of crustal assimilation determined for the Sunart facies by Fowler et al. (2008). The magmatic zoning at spot locations and Th/U values > 0.1 (Fig. 4.6) give further confidence that these are emplacement and LCHZ-related antecrysts, and not xenocrysts (Yakymchuk *et al*. 2018). Similarity in textures and Th/U values between Sunart facies samples and individual ages within error (Fig. 4.1-4.6) also support that the porphyritic and non-porphyritic Sunart facies zones consist of one magmatic phase within the precision of LA-ICP-MS analysis completed here.

The final age of 423.5 ± 2.1 Ma is somewhat younger, though within error of, the zircon ID-TIMS age obtained by Rogers and Dunning (1991) of 425 ± 3 Ma. Although, direct comparison is precluded given differences in analytical technique. The data of Rogers and Dunning (1991) has lower individual point errors of only a few Myr, much lower than the ~10 Myr obtained here. Although, their data gives an overall error of ± 3 Ma similar to that of the individual ages and greater than that of the final age obtained in this study. It has been noted that use of weighted mean and MSWD statistics can produce overly precise ages such that the error obtained for the Sunart facies ages, particularly the combined age, may also be inaccurate (Condon et al., 2024 and references therein). The data presented by Rogers and Dunning (1991) no longer meets reporting standards as individual age errors are not given, and the final age determination relies on an upper concordia intercept (Geological Society of London 2015; Condon *et al.* 2024).

Further uncertainty derives from the likely Pb loss recorded by grains analysed by Rogers and Dunning (1991) seen in the shape of the error ellipses (Fig. 5.1, zircon fractions 8 and 9). Pb loss in these grains is further evidenced by the older $^{206}Pb/^{238}U$ and $^{207}Pb/^{235}U$ ages obtained for their titanite analysis despite the lower U-Pb closure temperature of this mineral (e.g., Cherniak and Watson, 2001; Kohn, 2017). Pb loss in these zircon fractions may be explained by the lack of air abrasion pre-treatment despite evident fracturing (Rogers and Dunning 1991, p. 20). $^{206}Pb/^{238}U$ and $^{207}Pb/^{235}U$ ages obtained for these zircons are thus likely too young, hence the reporting of an upper intercept age by Rogers and Dunning (1991). There is also no data to show that the zircon fractions included in the final age determination of Rogers and Dunning (1991) are not antecrystic. This uncertainty in whether the fractions represent emplacement related growth is a key limitation on confidence in the age of Rogers and Dunning (1991). In particular, given the presence of older, if discordant, air-abraded zircon fractions with $^{206}Pb/^{238}U$ ages of 436 and 440 Ma presented in their work (Fig. 5.1, zircon fractions 10 and 11). This limitation is further emphasised by the evidence for antecrysts and difficulty in determining emplacement related growth presented in this thesis.

The c. 423 Ma ages obtained in this study are instead consistent with the 423 ± 3 Ma titanite age obtained by Rogers and Dunning (1991) (Fig. 5.1). There may be some uncertainty in the accuracy of the titanite age as it lies slightly above the Wetherill concordia line (Fig. 5.1), and could be representative of cooling through the titanite U-Pb closure temperature some few Myr after cooling through zircon closure on emplacement (e.g., Cherniak and Watson, 2001; Kohn, 2017). Ages of 423.5 ± 2.1 and 423 ± 3 Ma are similarly consistent with yet unpublished CA-ID-TIMS zircon U-Pb data indicating Sunart facies emplacement at c. 423 Ma (Nick M.W. Roberts, pers. comm. 2023). Consistency in age across techniques and geochronometers therefore provides confidence that the Sunart facies of Strontian was emplaced at c. 423 Ma. Regardless of the uncertainties discussed above, the LA-ICP-MS data and CL images obtained in this work provide a justifiable emplacement age, with a fuller magmatic history and detailed textural evidence of zircon growth identified.

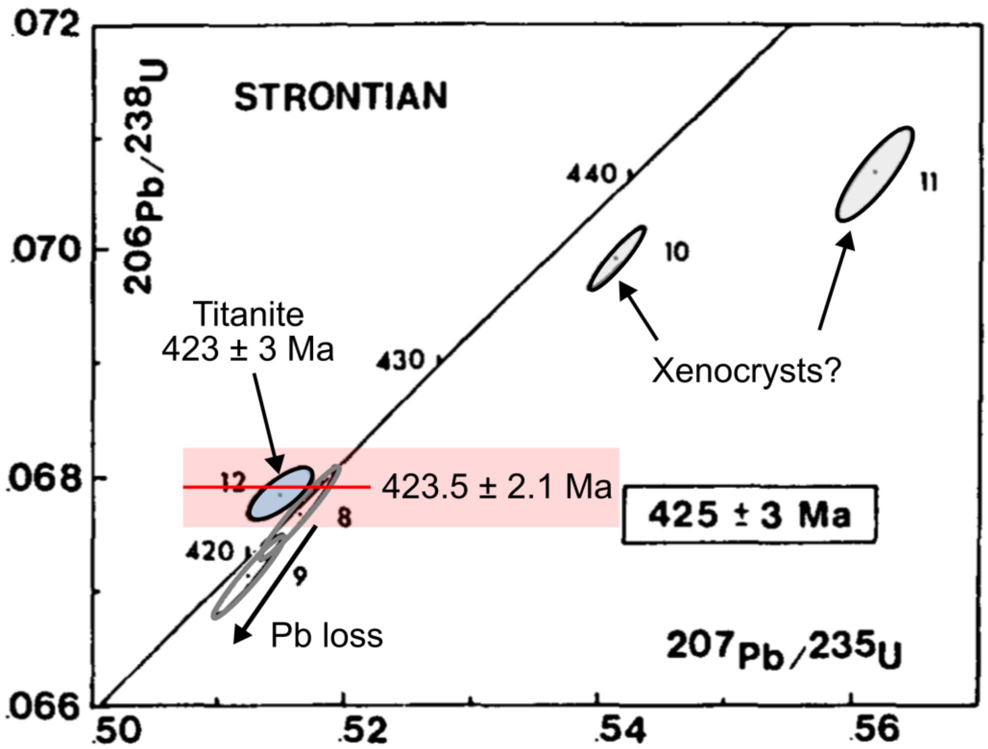

Figure 5.1 After Rogers and Dunning (1991), shows existing ID-TIMS zircon and titanite ages with the combined Sunart facies weighted mean age of 423.5 ± 2.1 Ma obtained in this study highlighted in red.

No xenocrystic ages were identified in either Sunart facies sample. This is consistent with the lack of homogenous or patchy zoned cores in CL images (Section 4.2.1) and with previous studies (Rogers and Dunning 1991). A lack of inheritance contrasts somewhat with evidence for crustal assimilation, though assimilation is notably minimal (Fowler *et al.* 2008). This lack of xenocrystsalso contrasts with the inner Strontian Sanda facies in which xenocrysts are abundant (Paterson *et al.* 1992a). The reason for the lack of xenocrysts could be due to its protracted emplacement and cooling history (emplacement related zircon age ranges c. 415 – c. 437 Ma; Fig. 4.5), as the magma remaining hotter for longer may enable the dissolution of inherited zircon. Additionally, the Sanda facies sample of Paterson et al. (1992) was collected from a sheet at the facies margin, where more significant inheritance may be expected than from the central intrusion (e.g., Wang et al., 2017). As such it is not certain whether this contrast in inheritance pattern will remain valid if compared with Sanda facies material collected from a location more central to the facies.

5.1.2 Strontian Sanda Facies: CM22/KG-01

Sample CM22/KG-01 produced an emplacement age of 421.8 ± 5.3 (n = 4, MSWD = 1.7) (Fig. 4.10). However, as set out briefly in section 4.2.2, this age is close to and well within error of the ages obtained for the Sunart facies, and may conflict with geochemical evidence that the Sanda and Sunart phases are distinct phases (Matthews *et al.* 2023). Similarly, greater variability in Th/U values, differing textures seen in CL with fewer inclusions and significant presence of xenocrystic cores appear to support that these are distinct phases (Fig. 4.1-4.4, 4.6, 4.8, 4.9, Appendix B). This result is also somewhat in contrast with, though still within error of, the 418 ± 1 Ma monazite U-Pb age obtained by Paterson et al. (1993). Removing the oldest of the spots included in the weighted mean calculation gives an age of 418.2 ± 6.3 (n = 3, MSWD = 0.29) (Table 4.3, Fig. 4.10). This alternative age is in much stronger agreement with the existing monazite age. While the 418.2 ± 6.3 Ma age has a low MSWD of 0.29 which may indicate under dispersed data and has a large error which still leaves it within error of the Sunart facies ages, this could be attributed to the lack of data and large individual point errors than inaccuracy of the age. Further, the monazite age of Paterson et al. (1993) is likely to represent emplacement age and not an antecrystic or xenocrystic age given the rarity of monazite inheritance (e.g., Crowley et al., 2008 and references therein)

As such, 418.2 ± 6.3 Ma is tentatively taken as the preferred age of the Sanda facies intrusion based on zircon methods. Further zircon dating work with greater precision is now being carried out at the British Geological Survey to confidently constrain emplacement of the Sanda facies outwith error of the Sunart facies.

An emplacement age of 418.2 ± 6.3 Ma thus reclasses spot 2_43.1 of sample CM22/KG-01, a rim spot, as an antecryst (Fig. 4.9d, 4.10) and highlights the difficulty in discerning emplacement related from antecrystic grains and the complexity of zircon growth history. The range of antecryst ages for sample CM22/KG-01 is therefore c. 420 to c. 443 Ma, with the caution that some spots classed as antecrysts may represent antecrysts or xenocrystic cores which have experienced partial Pb loss. The presence of antecrysts and consistency in Th/U values across emplacement related and antecrystic zircon (Fig. 4.6) supports the hypothesis that Northern Highlands magmas developed in a homogenised LCHZ prior to final emplacement (Milne *et al*. 2023).

This sample produced a younger maximum antecryst age than Sunart facies samples (Fig. 4.5c,f, 4.10c). While this could represent a genuine shorter antecryst history, it is also possible that (a) an older antecryst population exists but has not been sampled, and(or) (b) an older antecryst population had existed but were dissolved during longer storage. It is also possible that some of these antecrysts were scavenged from magma which crystallised at the time of Sunart facies emplacement. Further, the maximum uncorrected antecryst age of 443.1 ± 11.3 Ma (Table 4.3, Fig. 4.10) is still within error of the maximum Sunart facies uncorrected antecryst age 451.3 ± 10.2 Ma, and similar to the maximum uncorrected antecryst age for sample CM22/RAS-01 of 442.0 ± 10.3 Ma (Fig. 4.5, 4.10). Sample CM22/KG-01 therefore does not alter the range of antecryst ages present in Strontian intrusion phases and supports an onset of semi-continuous magmatism associated with Baltica-Laurentia convergence at c. 450 Ma.

The suggestion of Matthews et al. (2023) that the Sanda facies are only ‘slightly younger’ than the Sunart facies does not negate the ~5 Myr gap between the precise age for the Sanda facies of Paterson et al. (1993) and the combined Sunart facies age found here. Field relationships suggested by Matthews et al. (2023) to be indicative ofsuch a gap are not described by the authors, and chemical similarity of phases referred to is unsurprising given the regional chemical similarity of Caledonian intrusions (Fowler *et al*. 2008).

Xenocrysts aged c. 1737 Ma and c. 1825 Ma (Fig. 4.10a) were likely incorporated during assimilation of Laurentian basement affected by Laxfordian deformation (Storey *et al*. 2010). Xenocrysts ages spanning c. 1608 – c. 1686 Ma may be derived from Northern Highlands basement of Laurentian or Baltic affinity (Strachan *et al*. 2020b), or Palaeoproterozoic basement (Prave *et al*. 2024). Xenocrysts aged c. 1531 – c. 1317 Ma and c. 808 – c. 830 Ma were likely incorporated during assimilation of Glenfinnan and Loch Eil Group sediments, encompassing detrital zircons and Knoydartian aged metamorphic zircons respectively (Cawood *et al*. 2004, 2015; Kirkland *et al*. 2008; Spencer *et al*. 2015; Krabbendam *et al*. 2022).

5.1.3 Helmsdale: CM22/HD-01

Sample CM22/HD-01 produced an emplacement age of 417.0 ± 4.0 (n = 6, MSWD = 0.63). This age confirms the c. 420 Ma estimate of Pidgeon and Aftalion (1978) and gives a range of uncorrected antecryst ages of 429.0 ± 10.3 to 439.0 ± 9.0 Ma (Table 4.3, Fig. 4.14c). Notable considerations concerning spots included in this emplacement age are as follows. Spot 48.1, a grain core, is younger than the corresponding rim spot 48.2. However, this was attributed to a hairline fracture visible in the CL image enabling Pb loss to occur in this region of the grain and so a younger age for 48.1 (Fig. 4.12a). Spot 48.2 does not appear to be reached by the fracture and showed no evidence of Pb loss at the data reduction stage. Spot 48.2 was therefore not rejected in this instance and was included in the final weighted mean calculation. Spots 10.1, 51.1, and 67.1 are all located on the centre of grains with continuous oscillatory zoning and were thus included on the assumption that these relatively small grains grew entirely during emplacement (Fig. 4.12b,d,f, 4.14c). These spots should thus be considered with caution as it is not possible to definitively determine emplacement or antecrystic affinity. Omitting these spots however does not alter the weighted mean result significantly producing an age of 416.4 ± 5.9 Ma (n = 3, MSWD = 0.34) so they remain included to improve error and confidence in statistical acceptability.

Grain 14 is also entirely comprised of oscillatory zoning but is not consistently zoned from centre to rim (Fig. 4.12e). Spots 14.1 (older) and 14.2 (younger) were thus interpreted as antecrystic and emplacement related respectively. Spot 83.2 is located on an oscillatory zoned rim. However, it is outwith or only just within error of the youngest four emplacement related spots and its inclusion in the weighted mean calculation results in an unacceptable MSWD statistic. Spot 83.2 is therefore omitted and considered antecrystic. Grain 22 (Fig. 4.12c) produces core and rim ages outwith error of one another, providing confident evidence of a prior phase of antecrystic growth within an LCHZ and later growth during emplacement. The presence of oscillatory zoned emplacement related and antecrystic growth, including an antecrystic rim, highlights the complexity of zircon growth history.

Antecrysts therefore range in age from c. 429 – c. 439 Ma (Fig. 4.14c). As discussed in section 5.1.2 for sample CM22/KG-01, while this may represent a shorter antecryst history than that identified in the Sunart intrusive phase, it is possible that an older antecryst population was either not sampled, or existed but was later dissolved. Accounting for error, the oldest analysis for this sample gives a maximum uncorrected antecryst age of 448.0 Ma. This maximum age is similar to the c. 451 Ma age obtained from CM22/LS-01 and is within error of this analysis (Fig. 4.5, Appendix C), and so likely supports c. 450 as the age of onset of antecryst crystallisation. Sampling was of the inner Helmsdale granite. As such it could be that the less evolved outer granite contains a longer antecrystic record.

Xenocrysts aged c. 1726 and c. 1782 (Fig. 4.14a) are likely to have been incorporated during assimilation of Laurentian basement (Storey *et al.* 2010). Those aged c. 1600 – c. 1660 Ma (Fig. 4.14a) may be derived from basement of Laurentian or Baltic origin (Strachan *et al.* 2020b), or possibly Loch Eil group detritus (Cawood *et al.* 2004; Spencer *et al.* 2015; Krabbendam *et al.* 2022). Xenocrysts aged c. 1262 Ma and c. 1469 – c. 1492 Ma (Fig. 4.14a) were likely incorporated during assimilation of Loch Eil metasediments (Cawood *et al.* 2004; Spencer *et al.* 2015; Krabbendam *et al.* 2022). Xenocrysts aged c. 992 – c. 1093 Ma are ages associated with the Grenville orogen, and may have been incorporated directly from Northern Highlands basement affected by Grenvillian orogenesis (Bird et al., 2023; Strachan et al., 2020b), or from Loch Eil metasediments as detrital zircons (Cawood *et al.* 2004; Spencer *et al.* 2015; Krabbendam *et al.* 2022).

A xenocryst age of 926 ± 17 Ma (Fig 4.14a, Appendix C) is younger than recognised Grenvillian events (e.g., Brewer et al., 2003), though is difficult to ascribe to Renlandian orogenesis. This age is outwith recognised Renlandian ages in Scotland and this event did not affect the < 885 Ma Loch Eil Group into which the Helmsdale intrusion is emplaced (Cawood *et al.* 2004; Bird *et al.* 2018). This age may be attributed to minor Renlandian detritus in the Loch Eil Group as it is within error of the youngest Loch Eil Group detrital zircon identified by Cawood et al. (2004) of 962 ± 32 Ma. Xenocryst ages from c. 471 – c. 486 Ma are Grampian in age and have Th/U values and textures indicative of a magmatic origin (Fig. 4.14a, Appendix B, C). As such they may have been incorporated as primary magmatic or detrital zircons but are not likely to represent primary metamorphic growth. The greater proportion of xenocrysts likely sourced from the Loch Eil Group than basement is consistent with findings of Fowler et al. (2008) that the Helmsdale granite underwent minor assimilation of Loch Ness Supergroup material.

5.1.4 Abriachan: EM19/AB

Sample EM19/AB produced an age of 418.2 ± 5.6 Ma (n = 4, MSWD = 1.9) consisting only of spots on oscillatory zoned rims (Table 4.3, Fig. 4.14f, 4.16). Spots with ages interspersed among emplacement related rim ages are typically from homogenous cores, sometimes with marginal oscillatory zoning, and are interpreted as antecrystic or xenocrystic cores which experienced total Pb loss and U-Pb system resetting on emplacement (spots 58.1, 70.1, 80.1, 41.1, 56.1, Fig. 4.14f, Appendix B). Remaining spots omitted are from oscillatory zoning of grains which display a dark band of younger growth (88.1), substantial younger growth (36.1), or clear differences in CL brightness and cross cutting of oscillatory zoning between core and rim growth (50.1) (Fig. 4.16e, Appendix B). Of these omitted spots, only 50.1 can be confidently interpreted as antecrystic core growth as it is older than all emplacement spots and has clearer core-rim definition. Spots 36.1 and 88.1 could be interpreted as either (i) antecrystic growth which has experienced partial Pb loss undetectable at the precision level of LA-ICP-MS, or (ii) legitimate antecrystic growth ages. However, the latter would implicate at least spot 89.1 as antecrystic as it is older than both spots 36.1 and 88.1, despite clearly being located on rim growth (Fig. 4.14f, 4.16d). Accepting the latter would therefore induce uncertainty in the assignation of emplacement or antecrystic affinity of spots and thus also in the final weighted mean age.

The only identified antecrystic spot, 50.1 has an uncorrected age of 428.8 ± 11.3 Ma (Fig. 4.16e, Appendix C). Accounting for error, this gives a maximum possible antecryst age of 440.1 Ma. As discussed above for samples CM22/KG-01 and CM22/HD-01, while this may represent a shorter antecryst history than that identified in the Sunart intrusive phase, it is possible that an older antecryst population was not sampled, or, existed but was later dissolved in unfavourable magmatic conditions. This result thus neither negates or provides clear evidence in support of the onset of LCHZ development at c. 450 Ma.

Xenocrysts aged c. 1746 – c. 1756 Ma (Fig. 4.14d) are likely derived from Laurentian basement affected by Laxfordian metamorphism (Storey *et al.* 2010). Those aged c. 1617 – c. 1640 Ma may be derived from Northern Highlands basement of Laurentian or Baltic origin (Strachan *et al.* 2020b), or possibly Loch Eil detritus (Cawood *et al.* 2004; Spencer *et al.* 2015; Krabbendam *et al.* 2022), while those aged c. 1364 – c. 1540 Ma have likely been incorporated via assimilation of Loch Eil Group material (Cawood *et al.* 2004; Spencer *et al.* 2015; Krabbendam *et al.* 2022). Xenocryst ages from c. 982 – c. 1019 Ma are likely associated with Grenvillian events (Bird et al., 2023; Strachan et al., 2020b), and may have derived from affected basement or been incorporated as Loch Eil Group detritus (Cawood *et al.* 2004; Spencer *et al.* 2015; Krabbendam *et al.* 2022). A semi-homogenous xenocrystic core aged 477 Ma is Grampian in age, with a Th/U ratio of 0.02 and may therefore represent a primary metamorphic growth or metamorphic age resetting (Fig. 4.14d, Appendix B, C). Sample EM19/AB has a very similar pattern of inheritance to sample CM22/HD-01, which in addition to similar age and therefore likely similar structural level of emplacement and possibly temperature, suggests the Abriachan and inner Helmsdale magmas passed through similar basement and structural pathways during final ascent.

5.2 Tectonic Implications 1: Distribution and Character of Late Caledonian Magmatic Phases

As discussed in Chapter 2, previous studies have identified antecrystic zircon growth during times associated with very limited upper to mid crustal magma emplacement from c. 450 – c. 430 Ma, interpreted to evidence the development of an LCHZ within the Northern Highlands (Table 2.1; Milne et al., 2023). From c. 430 - c. 425 Ma is identified as a period of widespread emplacement of significant volumes of magma, typically granodiorite with abundant mafic material and often associated with thrust and strike slip fault emplacement pathways (Table 2.1; (Stewart *et al.* 2001; Goodenough *et al.* 2011; Milne *et al.* 2023). As discussed below, existing data and data obtained here provides additional geochemical and geochronological evidence for the development of a widespread LCHZ which was mobilised between c. 430 - c. 423 Ma, and a further pulse of evolved magmatism at c. 420 – c. 417 Ma, the latter localised to locations directly abutting the GGF or associated faults.

5.2.1 Trace Element Geochemistry: Evidence for a Hot Zone

Zircon trace element geochemistry of samples CM22/LS-01 and CM22/RAS-01 supports the LCHZ hypothesis of Milne et al. (2023) in addition to geochronology. Trends indicative of magmatic evolution may be expected to show in zircon-compatible heavy REE (Hanchar and Van Westrenen 2007; Barth and Wooden 2010), though neither sample CM22/LS-01 or CM22/RAS-01 show clear trends in heavy REE or difference between emplacement and antecryst populations (Fig. 4.17). This overlap in heavy REE values, as well as in Ti-in-zircon temperatures (Fig. 4.18) and Th/U values (Fig. 4.6, 4.13, section 5.1), supports that the magma underwent homogenisation prior to zircon saturation, likely within an LCHZ (Hildreth and Moorbath 1988; Annen *et al.* 2006; Milne *et al.* 2023).

Varied light REE values are likely due to contamination of analyses by light REE-rich sub-micron scale phosphate inclusions such as monazite during ablations (Fig. 4.17, Appendix E; e.g., Burnham, 2020; Claiborne et al., 2018; Whitehouse and Kamber, 2002; Zhong et al., 2018). Spots with light REE chondrite normalised values > 100 are likely particularly affected by such inclusions. While inclusions seen in CL images were avoided where possible, inclusions are abundant in zircons of samples analysed for trace elements and sub-micron scale inclusions may go undetected by CL. As such, light REE do not give significant indication of zircon growth history, though along with abundant inclusions in CL images, may evidence a period of rapid zircon growth within locally REE-enriched magma.

Analyses with low light REE and low La concentration may be more representative of genuine zircon light REE concentrations (Zhong et al., 2019; Zou et al., 2019). Analyses with La_N < ~10 for samples CM22/LS-01 and CM22/RAS-01 show strong positive Ce anomalies typical of zircon and attributed to oxidised magmatic conditions (Fig. 4.17; e.g., Loader et al., 2022). These low La_N analyses also show a very weak or no Eu anomaly which may be attributed to suppression of plagioclase fractionation with possible garnet fractionation, and(or) oxidised magmatic conditions (Fig. 4.17; Tang et al., 2020; Trail et al., 2012; Yakymchuk et al., 2023). These indications of plagioclase suppression and possible garnet fractionation are in line with evidence for adakite-like Caledonian intrusions and consistent with a thickened crust under compression during zircon growth (Alonso-Perez *et al.* 2009; Neill and Stephens 2009; Chiaradia 2015; Milne *et al.* 2023). Evidence for an oxidised magma is consistent with a subduction affinity of magmas (Fowler *et al.* 2008; Padrón-Navarta *et al.* 2023).

Titanium-in-zircon temperature may provide evidence for the existence of an LCHZ comprised of crystal mush and little change to magmas during emplacement. Temperatures for both samples CM22/LS-01 and CM22/RAS-01 are typically < 700 ºC, with little to no clear difference between emplacement related and antecrystic spots (Fig. 4.18). Higher temperatures outwith typical range at ~ 790 and ~ 850 ºC correspond to spots with elevated light REE concentration. As such these temperature results are likely due to contamination of analysis by Ti-rich inclusions such as rutile or ilmenite, and are likely not representative of legitimate zircon crystallisation temperature (Siégel *et al.* 2018). However, the Ti in zircon thermometer is known to underestimate magma temperature. Temperature may be underestimated by ~ 70 ºC at pressures < 1 GPa, and is increasingly underestimated at greater pressure (Ferriss *et al.* 2008; Schiller and Finger 2019; Crisp *et al.* 2023). Adjusting results accordingly gives typical temperatures for emplacement related spots of ~ 740 – 770 ºC. This is an approximation, however, due to low resolution constraint of the pressure dependence of Ti substitution (Ferriss *et al.* 2008), and uncertainty of pressure conditions at the time of Sunart facies emplacement (0.225 GPa, Matthews et al., 2023; cf. 0.41 GPa Tyler and Ashworth, 1982). An appropriate correction for LCHZ related spots is also uncertain as pressure conditions are unknown. However, crustal thickness of the Laurentian margin of ~ 45 km and so pressures of > 1 GPa are plausible given the evidence for garnet fractionation and similar crustal thickness of modern collision zones (Annen *et al.* 2006; Pamukçu *et al.* 2007; Chiaradia 2015; Milne *et al.* 2023). Calculated temperatures would thus need to be corrected by a greater amount for

LCHZ related spots than emplacement related spots (Ferriss *et al.* 2008). It is not clear whether corrections would remove the slight decreasing trend seen in uncorrected results and level out emplacement and LCHZ related temperatures, or reverse the trend seen. These possibilities would imply little change in temperature on emplacement, or a degree of cooling on emplacement respectively.

Overall corrected Ti-in-zircon temperature estimates for LCHZ zircon crystallisation are therefore in the region of ~ 740 - ~ 800 ºC and within the expected range for crystallisation of evolved, hydrous magmas (Scaillet and MacDonald 2001; Scaillet *et al.* 2016). Aforementioned strong Ce anomalies (Fig. 4.17) could also indicate low magma temperatures (Loader *et al.* 2022). Temperatures in this range and a lack of clear trend may suggest magmas were in a partially crystallised state throughout their history. The presence of zircon antecrysts also support that magmas were partially crystallised, as their survival map imply antecrysts were physically and chemically shielded from dissolution by new magmas during phases of recharge and homogenisation (e.g., Miller et al., 2007). It could be argued that Ti-in-zircon temperatures are oscillatory (Fig, 4.18). If so, oscillating temperature may represent cyclical recharge with hotter, mafic magma and subsequent fractionation, mixing and cooling within an LCHZ.

The above evidence for homogenised mushy magma with subduction-like chemical characteristics situated in thickened crust is consistent with magma evolution within an LCHZ as per the hypothesis of Milne et al. (2023). The spatio-temporal distribution of magmatism in relation to the LCHZ is henceforth discussed.

5.2.2 Phase 1: c. 450 – c. 430 Ma

This period has been previously identified as a ‘magmatic gap’ (Oliver *et al.* 2008; Dewey *et al.* 2015) due to recognition only of emplacement of the Glen Dessarry intrusion at this time (Table 2.1; Goodenough et al., 2011). However there has since been identification of significant magmatism at this time, including emplacement of the Glen Loy, Linnhe, and Muckle Roe intrusions (Table 2.1; Lancaster et al., 2017; Milne, 2019). Following the contributions from this study, evidence for the formation of antecrysts and therefore existence of an LCHZ, as discussed above, now extends ~ 200 km from Strontian, Linnhe, Cluanie and Glen Loy to Helmsdale (Milne, 2019; Milne et al., 2023).

Magma emplaced during this phase is highly variable in composition, from alkaline mafic (Glen Dessarry, Glen Loy) to granitic (Linnhe) (Richardson 1968; Fowler *et al.* 2008; Milne 2019). The Glen Dessarry and Glen Loy intrusions in particular display this variation. The Glen Dessarry intrusion comprises an outer melasyenite and inner K-feldspar-rich leucosyenite, both of which are alkaline, quartz-bearing and contain portions of ultramafic cumulate (Richardson 1968; Fowler 1992; Fowler *et al.* 2008). The Glen Loy intrusion is alkaline to sub-alkaline, and comprises hornblende gabbro which grades into diorite, with granitic pegmatites and minor lamprophyre intrusions (Milne 2019). This may reflect earlier stages of LCHZ development prior to widespread magma evolution and homogenisation seen in granodiorites from c. 430 Ma onwards (see section 5.2.3).

The occurrence of mafic facies and enclaves at Glen Loy (Johnstone and Mykura 1989) and Glen Dessarry (Richardson 1968) also indicates mantle input to magma sources, consistent with previously determined subduction related magma origins (Fowler *et al.* 2008). Mantle derived input to an LCHZ may have occurred just prior to ascent and emplacement of these bodies. Given the above evidence for the occurrence of magmatism and LCHZ activity, the period c. 450 – c. 430 Ma does not represent a magmatic gap, only that magma escape from an LCHZ and subsequent emplacement in the mid to upper crust was limited to stocks (Fig. 5.2a). Additionally, intrusions emplaced during this time are typically proximal to the Great Glen and Walls Boundary Faults, with the exception of Glen Dessarry adjacent to the Sgurr Beag Thrust. This distribution suggests emplacement was limited to structurally accessible locations (Fig. 5.2a). Limited emplacement along with continued magmatic addition to an LCHZ may be related to compressive crustal stress, discussed further in section 5.3.

Additionally, in situ U-Pb zircon analyses by Kinny et al. (2003) of the Vagastie Bridge and Naver Granites identified ages up to c. 455 Ma, which may represent antecrystic zircon growth and would extend the spatial extent of the LCHZ further northwest (Fig. 5.2a). In-situ U-Pb zircon study of Shetland intrusions has not identified antecrysts, though this may be due to focused analysis of zircon rims in order to hone in on emplacement related zircon growth (Lancaster *et al.* 2017).

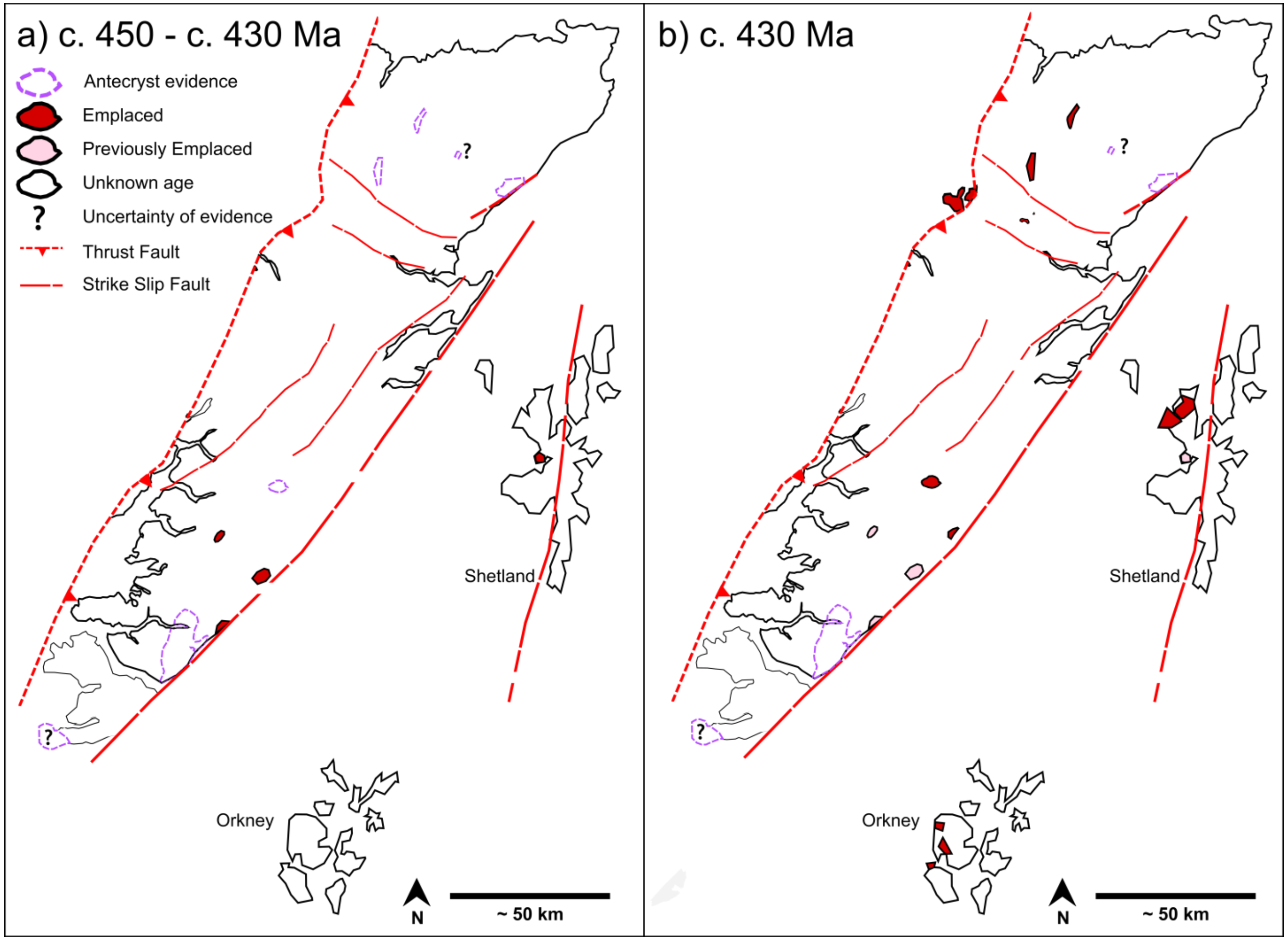

Figure 5.2 Summary maps of magmatic emplacement in the mainland Northern Highlands, Orkney and Shetland for time slices a) c. 450 – c. 430 Ma, b) c. 430 Ma, c) c. 428 – c. 423 Ma and d) c. 418 – c. 417 Ma. Preferred emplacement ages obtained from zircon U-Pb methods in this study are highlighted, though it should be noted the monazite U-Pb age of Paterson et al. (1993) provides a more precise emplacement age for the Strontian Sanda facies. Orkney and Shetland are not shown in their true locations.

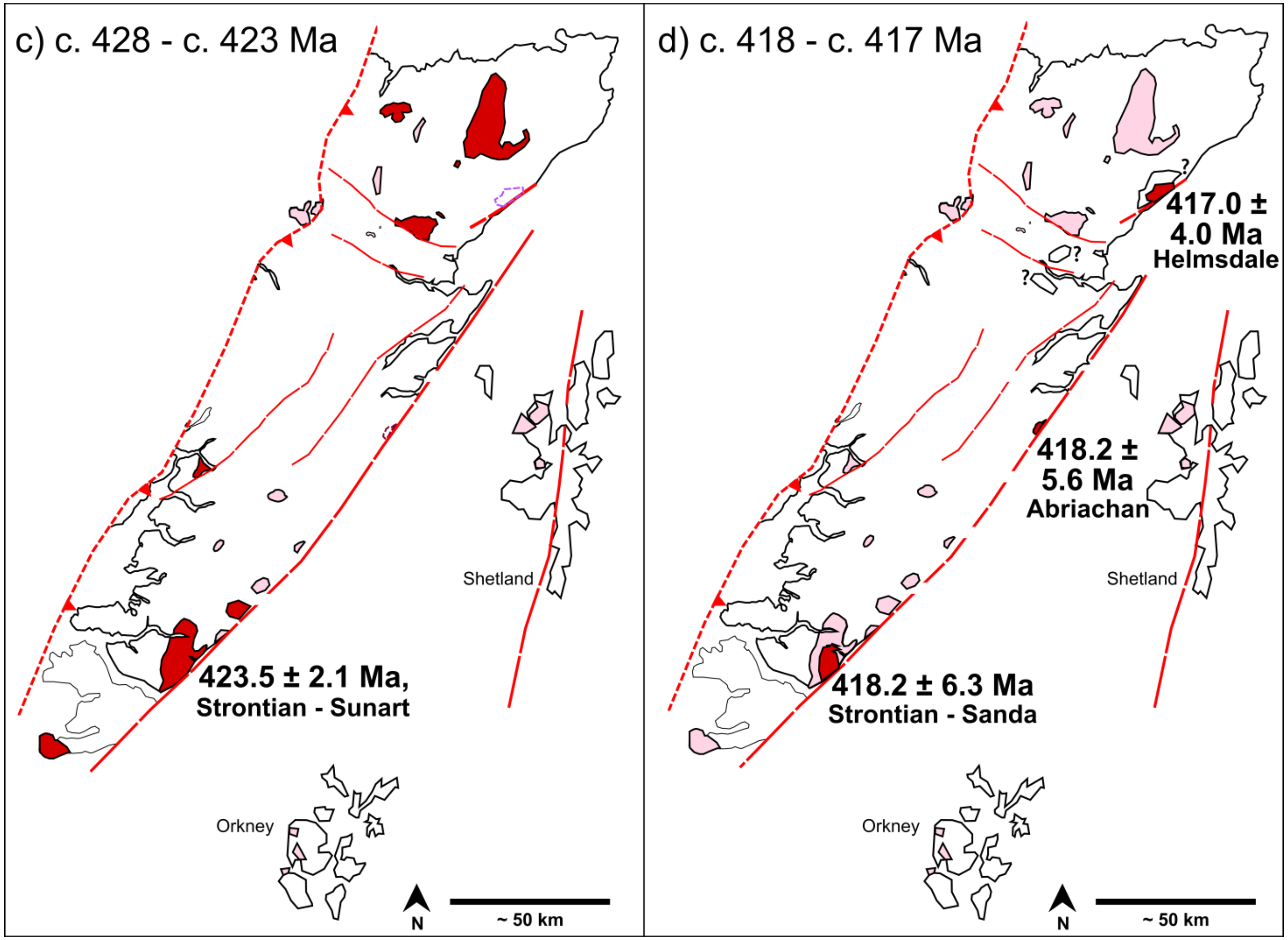

Figure 5.2 (continued).

As such the occurrence of magmatism at c. 440 Ma in this location likely implies the presence of the LCHZ beneath Shetland, and this is not precluded by a lack of evidence for antecrysts (Lancaster *et al.* 2017). Two ion microprobe U-Pb zircon analyses obtained by Oliver et al. (2008) for the Ross of Mull Granite (ROMG) produced $^{206}Pb/^{238}U$ ages of c. 430 Ma. The full ROMG dataset of Oliver et al. (2008) gives an MSWD of 1.5, outside the acceptable range for n = 12 and errors of 1σ (Spencer *et al.* 2016). In contrast, omitting the oldest two analyses at c. 430 Ma gives a much more acceptable MSWD of 0.95, implying the older analyses are not statistically part of the emplacement related zircon population and thus may represent antecrystic growth. The workflow of Oliver et al. (2008) similarly focused analysis on magmatic zircon rims and data does not preclude the existence of older antecrystic zircon growth. A further ion microprobe analysis obtained by McAteer et al. (2014) gave a $^{206}Pb/^{238}U$ age of c. 427 Ma which could also represent zircon growth earlier than emplacement. The CA-ID-TIMS emplacement age of the ROMG by the British Geological Survey provisionally suggested to be c. 423 Ma may further support that ages of c. 427 and c. 430 Ma represent antecrystic growth (Nick M.W. Roberts, pers. comm. 2023). If LCHZ activity did occur beneath both Mull and Shetland, this would extent the LCHZ system across a distance of approximately 500 km (Fig. 1.1, 5.2a).

5.2.3 Phase 2: c. 430 – c. 423 Ma

This period saw an upsurge in mid - upper crustal pluton emplacement across the Northern Highlands, including plutons with significant areal extent and thus potentially volume, such as the Sunart phase at Strontian, Strath Halladale (~ 175 km^2) and Rogart intrusions (Table 2.1; Fig. 5.2b; Kocks *et al.* 2006, 2014; Fowler *et al.* 2008). Previous understanding of the spatio-temporal distribution of magmatism at this time posits a magmatic peak at c. 425 – c. 426Ma (Archibald et al., 2022; Atherton and Ghani, 2002). While a peak at this time remains valid, the magmatism associated with this time slice may be extended to encompass c. 430 – c. 423 Ma given new CA-ID-TIMS data from the ROMG indicates it was emplaced at c. 423 Ma. This new age extends the spatio-temporal distribution of emplacement associated with the magmatic upsurge younger in time and to the far southwest of the Northern Highlands (Nick M.W. Roberts, pers. comm., 2024; Fig. 5.2b). Similar to those emplaced prior to 430 Ma, emplacement at this time is structurally controlled. Emplacement may switch from being controlled by thrust faulting c. 430 Ma, to controlled by strike slip faulting thereafter (e.g., Loch Shin and Grudie, Holdsworth et al., 2015; Rogart, Kocks et al., 2014; Naver Suite, Strachan et al., 2020a). The timing of this switch is constrained firstly by the emplacement of the Assynt Alkaline Suite, interpreted to have been emplaced at the end of significant motion on the Moine thrust (Table 2.1; Goodenough et al., 2011). Emplacement of the Clunes tonalite c. 428 Ma is interpreted as concurrent with sinistral strike slip faulting associated with the main GGF (Stewart *et al.* 2001), though there is some concern over the validity of this age. A weighted mean calculation of the Clunes $^{206}Pb/^{238}U$ data produces an age of 425.68 ± 1.00 Ma (MSWD = 0.36, n= 4), younger than the accepted upper intercept age of 427.8 ± 1.9 Ma (Fig. 5.3). Though Pb loss trends in the grains analysed may indicate that the $^{206}Pb/^{238}U$ ages (and thus the weighted mean age) are younger than their true growth age, it is also possible that the ~428 Ma age comes from antecrystic zircons.

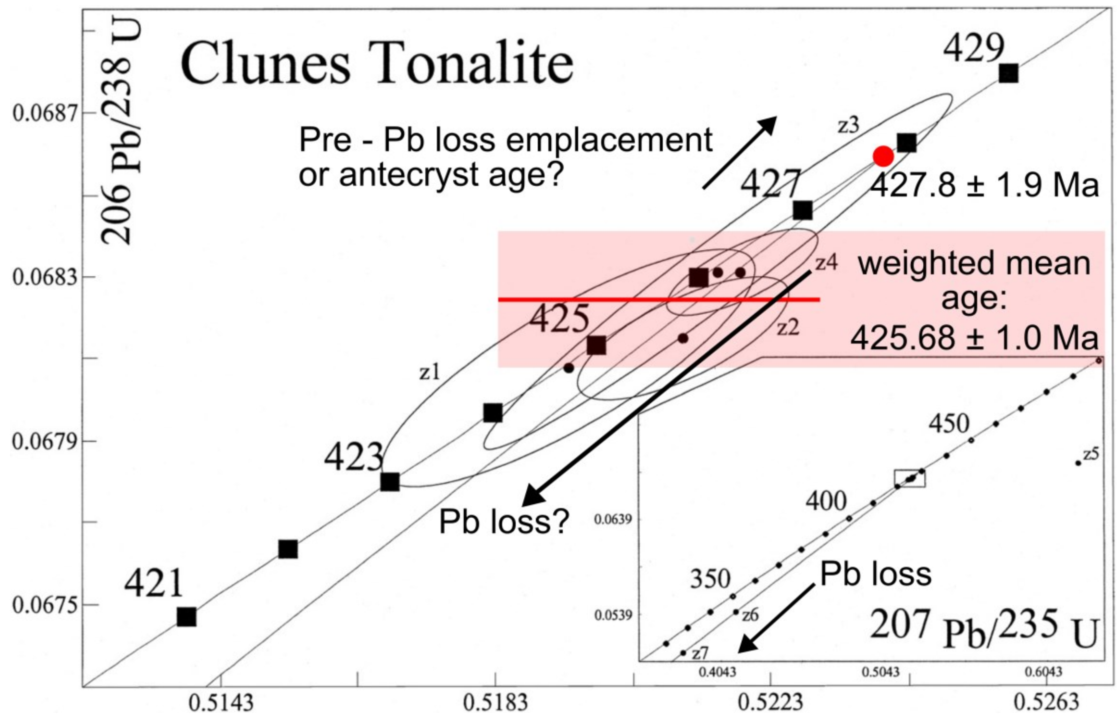

Figure 5.3 After Stewart et al. (2001), shows existing ID-TIMS zircon data with the existing upper intercept age marked with a red circle, and $^{206}Pb/^{238}U$ weighted mean age of zircon fractions z1 – z4 highlighted in red.

Therefore, a more detailed analysis is merited. Emplacement of the Cluanie pluton at c. 432 Ma has also been interpreted as related to strike slip activity, presenting an open question about the extent of concurrence of thrusting and strike-slip faulting (Neill and Stephens 2009; Milne *et al.* 2023). Temporal overlap in late ductile thrusting with significant strike slip motion is interpreted as broadly representing mid - upper crustal strike slip above a basal decollement (Strachan *et al.* 2020a). However, remaining uncertainties in available geochronology, such as that of Clunes, yet leaves uncertainty in the relative timing of thrust vs strike slip faulting and their association with Scandian upright folding in the mid - upper crust (Strachan and Evans 2008). Understanding of timing is further hindered by limited coverage of structural and fault plane or deformation geochronology data in the southwest Northern Highlands where thrust-, strike slip- and upright folding-related features are more easily delineated (Strachan et al., 2002 and references therein).

Intrusions of this time period are dominantly calc-alkaline granodiorite enriched in Sr and Ba concentration, and are often associated with hydrous gabbro to diorite facies, mafic enclaves and minor intrusions often described as appinites (Castro and Stephens 1992; Fowler *et al.* 2008). Notable outliers to this otherwise fairly consistent group include, alkaline syenite intrusions (Assynt Alkaline Suite, Loch loyal, some phases of the Ratagain pluton), and the adakite-like nature of the Cluanie pluton (Thompson and Fowler 1986; Fowler *et al.* 2008; Lawrence *et al.* 2023; Milne *et al.* 2023).

In contrast to plutons emplaced prior to c. 430 Ma, intrusions emplaced between c. 430 – c. 423 Ma are spread much more widely across the Northern Highlands (Fig. 5.2c). Though plutons emplaced during this period are still emplaced in relation to structures such as the Strathconon Fault (Lawrence *et al.* 2022) and Loch Shin Line (Holdsworth *et al.* 2015) (Fig. 5.2c). The occurrence of abundant mafic facies and enclaves within these plutons is consistent with the addition of new mantle derived melt into the homogenised silicic magmas of LCHZ (e.g., Castro and Stephens, 1992; Kocks et al., 2014). Input of mantle derived magma may have helped drive remobilisation of the resulting granitic mush with mafic components.

Evidence for antecrystic zircon growth (Milne et al., 2023; this study) and for extensive magma escape from the LCHZ (Fig. 5.2c), is coupled to an abundance of less-evolved facies and an increased spatial extent of mid to upper crustal emplacement (Fig. 2.5c). Together these observations suggest that the LCHZ beneath the Northern Highlands was being substantively disrupted – with significant new magmatic addition and extensive remobilisation of melt and mush towards higher crustal levels. Potential changes in geodynamics which may explain these features, are discussed in section 5.3.

5.2.4 Phase 3: c. 418 - c. 417 Ma

Emplacement during this period was spatially limited to structures associated with the GGF or related faults, including the inner Helmsdale and Sanda intrusive phases (Table 2.1, Fig. 5.2d). These intrusions are of lower combined total area and fewer in number than those emplaced over c. 428 – c. 423 Ma, implying a lower overall magma volume was emplaced into the mid - upper crust during this time (Fig. 5.2d; Digimap, 2024). These intrusions typically comprise less metaluminous to weakly peraluminous biotite granite - granodiorite with no noted tectonic fabric imposed (Kocks 2002; Matthews *et al.* 2023). Mafic facies are considerably less common during this time. Limited enclaves occur within the Sanda facies at Strontian (Holden *et al.* 1987, 1991), and only occasional appinite inclusions are identified at Helmsdale (Fowler *et al.* 2008). No mafic material has been identified within the Abriachan granite. Additionally, no geochronological study of mafic magmatic enclaves has been undertaken. It may be that enclaves which do occur in these later plutons can be explained by earlier crystallisation within a hot zone and then entrainment during a final pulse of emplacement.

The lack of mafic material in these intrusions imply little to no new mantle-derived input of mafic magmas to the hot zone. In addition, the typically highly evolved and red alkali feldspar-rich nature suggests these magmas are the result of long-term evolution and homogenisation. Each of these features indicates that final magma remobilisation and emplacement were likely not driven by changes in mantle dynamics, and instead by change in crustal tectonics. In particular, the (limited) difference in phases emplaced at Strontian highlights that these are magmas tapped from a common LCHZ source. These phases are chemically similar though the later Sanda facies is more evolved, and are of different ages and zircon

Th/U ratios, (this study; Matthews et al., 2023), indicating they have likely been sourced from the same reservoir along the same structural pathway at different times.

A final small volume biotite granite phase identified within the Rogart pluton contains no tectonic fabric. This late phase and further additional biotite granites Orrin, Fearn, and Migdale may also be part of this late pulse of emplacement and worth obtaining geochronology data to find out (Fig. 5.2d; British Geological Survey, 2016; Kocks et al., 2014). Effort to obtain further LA-ICP-MS zircon U-Pb ages for these intrusions is underway (I. Neill, pers. comm. 2024).

5.3 Tectonic Implications 2: Regional Scandian Tectonics

5.3.1 Arc Magmatism and Lower Crustal Hot Zone Development

The evidence for antecrysts and mush state of magmas discussed in sections 5.1 and 5.2 as well as geochemical and field evidence of homogenisation, magma mingling and incremental growth of plutons (Holden *et al.* 1987; Fowler *et al.* 2001, 2008; Lawrence *et al.* 2022), are all consistent with protracted magma storage and evolution in an LCHZ (Hildreth and Moorbath 1988; Annen *et al.* 2006; Cashman *et al.* 2017). Evidence for the presence of an LCHZ within the Northern Highlands crust is now identified from Strontian to Helmsdale (Fig. 5.2; this study; Archibald and Murphy, 2021; Lancaster et al., 2017; Milne et al., 2023; Oliver et al., 2008). This hot zone lasted in time from c. 450 Ma to at least c. 417 Ma when the last remobilisations of magma from the LCHZ to the mid – upper crust occurred (Table 2.1; section 5.2; Milne et al., 2023).

Lower crustal hot zones are known to develop during arc magmatism (e.g., Bardelli et al., 2023; Cashman et al., 2017). In comparison, purely collision derived crustal melts have typically less total volume and a shorter history of occurrence than that observed in the Northern Highlands, as they segregate from migmatites during peak collision (e.g., Nabelek, 2020). Migmatites did not form in the Northern Highlands until c. 425 Ma and are only identified closer to the orogenic core in the far northeast of the Northern Highlands (Kinny *et al.* 1999). Purely collision derived magma therefore cannot account for the distribution of plutons across the Northern Highlands, their range of mafic facies or the range of antecryst ages up to c. 450 Ma. The most likely geodynamic step following the completion of Grampian arc accretion is a return to subduction and continued closure of the Iapetus Ocean. A return to 'normal' Iapetus subduction processes is consistent with the relatively short gap of ~15 Myr between the end of Grampian-I orogenesis and the onset of magmatism and a reasonable explanation for the onset of arc magmatism and LCHZ development c. 450 Ma. LCHZ development is associated with arcs experiencing compressive stress in the upper plate (e.g., Chiaradia et al., 2020, 2009). Thrust dominated compression and deformation is thought to inhibit magma ascent and force magma to intrude along approximately horizontal fractures and develop sills, thus leading to the development of a lower crustal sill complex as per Hildreth and Moorbath (1988) (Tibaldi 2008; Chaussard and Amelung 2014; Richards 2021).

The suggestion of Milne et al. (2023) that LCHZ development was enabled by compression in the upper plate induced by the initial arrival of Baltic promontories c. 450 Ma is consistent with these factors and antecryst ages obtained in this study (Fig. 5.4a). The suggestion is also consistent with the timing of the prograde Grampian–II event (Bird *et al*. 2013; Cawood *et al*. 2015). Additionally, mid - upper crustal emplacement which does occur prior to c. 430 Ma is dominantly older than c. 438 Ma. The youngest pre ~ 430 Ma intrusion in Shetland is the c. 438 Ma Muckle Roe Granophyre, the Linnhe and Glen Loy intrusions are c. 441 Ma and Glen Dessarry c. 447 Ma (Table 2.1; Goodenough et al., 2011; Lancaster et al., 2017; Milne, 2019). This restriction in ages may be consistent with the hard docking of Baltica against Laurentia at c. 437 Ma further inhibiting magma escape from the hot zoneuntil the onset of strike slip tectonics at c. 432 Ma (Fit. 5.3b; Neill and Stephens 2009; Holdsworth *et al*. 2015; Lundmark *et al*. 2019; Milne *et al*. 2023a; Strachan *et al*. 2020a). The above discussed relationship between LCHZ development, magma ascent, and upper plate stress regime strongly highlights the importance of obtaining full magmatic histories over overtly focusing emplacement ages. That said, the cause of a compressive upper plate regime prior to the onset of hard collision at c. 437 Ma may be difficult to prove due to the sparse range of radiometric ages and structural data of Grampian–II deformation, particularly as data is sparse compared to that of potentially correlative deformation in the Scandinavian Caledonides (Cawood *et al*. 2015; Walker *et al*. 2016, 2021; Slagstad and Kirkland 2018).

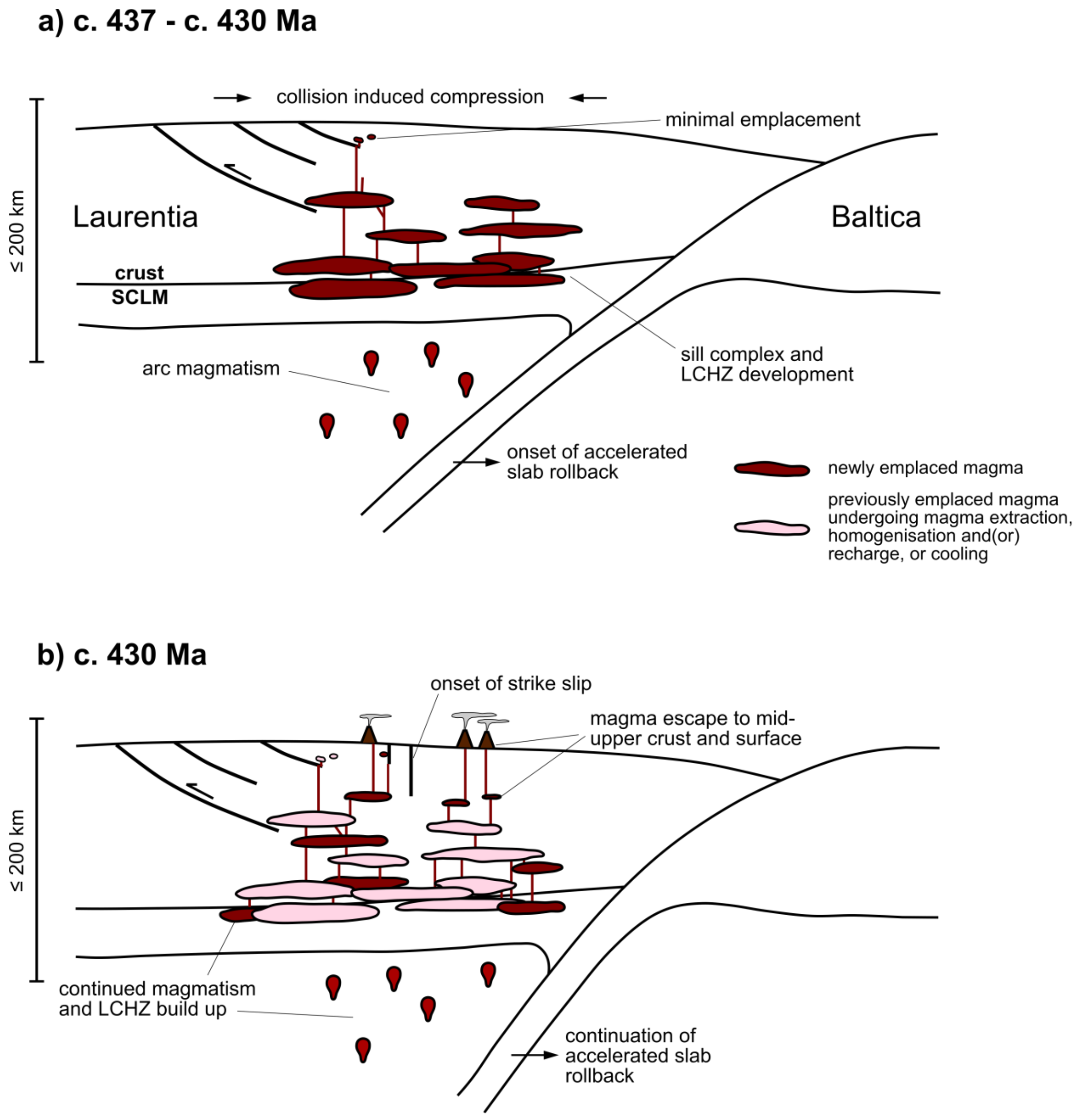

Figure 5.4 Schematic diagrams showing the evolution of the Scandian Orogenesis and magmatism from a) hard collision of Laurentia with Baltica and the latter stages of subduction, b) the onset of strike slip faulting, c) the occurrence of drip delamination and lithospheric thinning following the attainment of peak crustal thickness, to d) post-orogenic uplift and erosion with extensive strike slip faulting. Scale and lithospheric thickness estimate based on a similar geodynamic setting in Anatolia (Artemieva and Shulgin 2019).

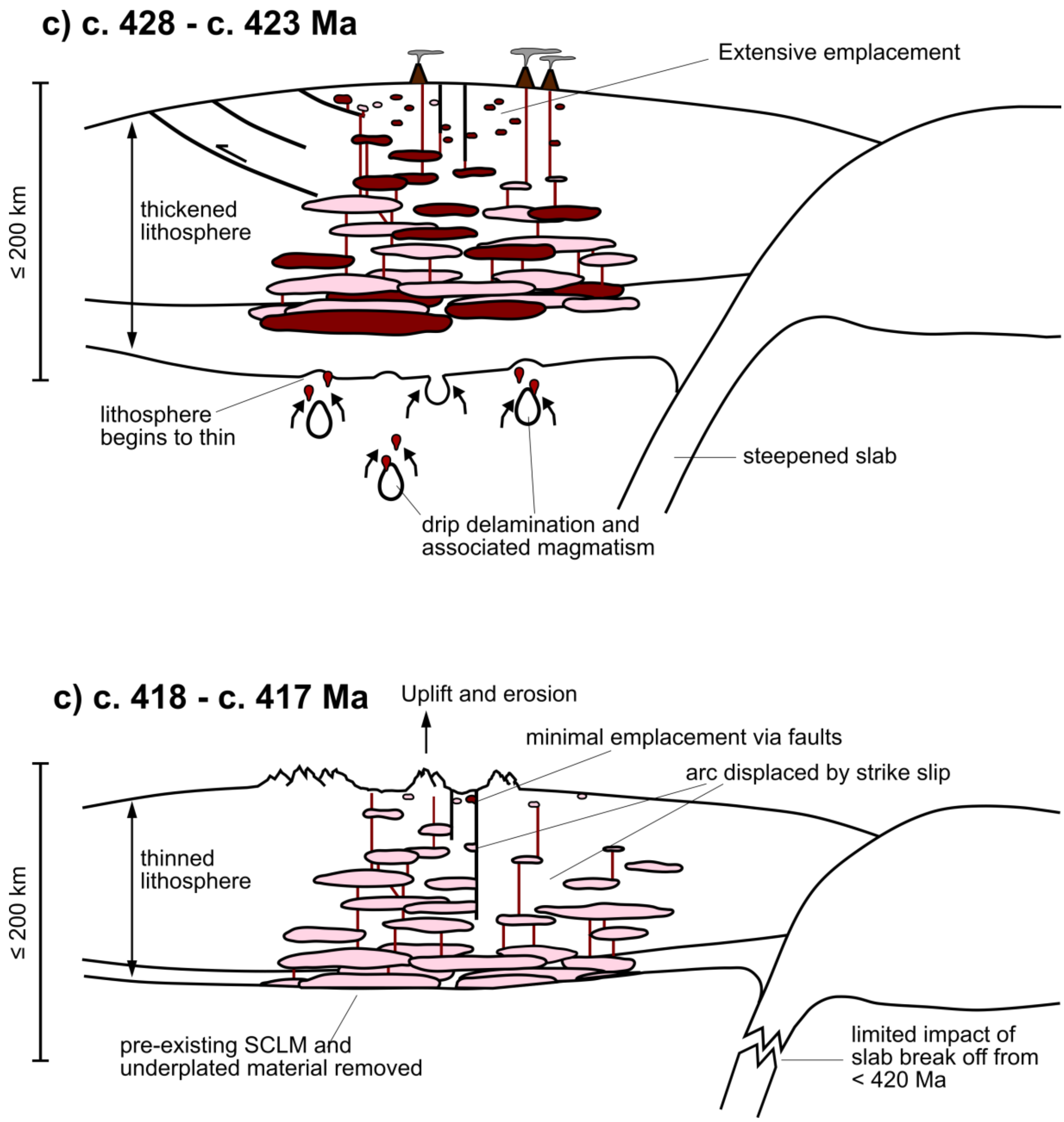

Figure 5.4 (continued).

The biggest limitation to understanding upper crustal dynamics of this period may be that the location of the Northern Highlands within the orogenic belt is unconstrained. Lack of constraint on the Northern Highlands' location relative to the trench, arc axis, and the Scandinavian Caledonides leaves considerable uncertainty over the likely strength of influence of occurrences such as accelerated slab rollback and the arrival of Baltica promontories (Stewart *et al.* 2001; Stone 2014; Armitage *et al.* 2024; McKay *et al.* 2024). It is therefore difficult to conclude much in the way of geodynamics besides that the Laurentian margin was likely under compression from c. 450 Ma, with extensive magmatic addition to the lower crust but only minor volumes of magma emplaced in the mid - upper crust.

5.3.2 Increase in Magmatic Output c. 428 – c. 423 Ma

As discussed in Chapter 2, various authors have suggested that slab breakoff during collision is a key driver of magmatism at this time. However, it is now known that breakoff has a limited direct overall effect on magmatism via mantle upwelling and is only of significance close to the suture (e.g., Freeburn et al 2018). The Northern Highlands were most likely situated in the arc or back arc region of the Caledonides, meaning we require an alternative mechanism for enhanced magmatism during orogenesis. Magmatic emplacement, as discussed above, is likely to be strongly related to a change in upper plate crustal stresses associated with thrust and strike slip faulting. However, the abundance of mafic facies at this time must also be considered reflective of contemporaneous melting of the upper mantle, driven by alternative deep geodynamic processes. Lithospheric delamination is suggested here as an alternative and complementary model to explain magmatism and orogenic uplift. Delamination has not previously been considered for the Northern Highlands despite its prevalence in current collision and continental arc settings (e.g., Pearce *et al.* 1990; Ducea *et al.* 2013; Kaislaniemi *et al.* 2014; Magni and Király 2020; He and Kapp 2023).

Delamination provides a more suitable spatial pattern of magmatism than slab breakoff to explain the distribution of Northern Highlands plutons, particularly 'drip' style delamination or 'convective thinning' (Elkins-Tanton 2007; Ducea *et al.* 2013). In this scenario, drip delamination is conventionally thought to occur following compression and shortening of the lithosphere until the mantle lithosphere becomes gravitationally unstable. Rayleigh-Taylor instabilities develop and mantle lithospheric material delaminates in approximately circular plumes (Houseman and Molnar 1997; Gorczyk *et al.* 2012; Beall *et al.* 2017; Stein *et al.* 2022). Densification of the mantle lithosphere via shortening and metamorphism or magmatic underplating, or existing heterogeneity in mantle lithosphere density may promote gravitational instability but is not necessary for delamination to occur (Houseman *et al.* 1981; Gorczyk *et al.* 2012). Instabilities and thus delamination at the mantle lithosphere - asthenosphere boundary may also occur where mantle lithosphere material has weak rheological and low negative buoyancy properties. These properties may occur due to increased temperature of the mantle lithosphere following lithospheric shortening and forcing of mantle lithosphere to greater depth and(or) the presence of melt or fluid components introduced by prior subduction (Kaislaniemi *et al.* 2014). Asthenospheric convection encouraged by ongoing convergence can also cause instabilities and delamination to develop at the asthenosphere-lithosphere boundary (Kaislaniemi *et al.* 2014; Magni and Király 2020). Drip delamination is shown to be slower to initiate than large scale 'peel-off' delamination (Beall *et al.* 2017). Once initiated however, the upward motion of hot asthenosphere into the space above delaminated material and(or) lateral migration of asthenospheric convection cells exposes further SCLM to convection and drives further delamination events (Fig. 5.5; Kaislaniemi et al., 2014; Stein et al., 2022).

Melting associated with delamination may occur via (i) decompression melting of metasomatised asthenosphere induced by convection, or (ii) melting of the asthenosphere, and down going and remaining mantle lithosphere triggered by devolatisation of the down going drip material as it reaches greater depths (Fig. 5.5; Elkins-Tanton, 2007; Elkins-Tanton and Grove, 2003; Harig et al., 2010; Kaislaniemi et al., 2014). Delamination and associated melting may thus produce a seemingly random distribution of magmatism and emplacement on regional scales (Kaislaniemi *et al.* 2014; Magni and Király 2020).

A drip delamination scenario therefore better explains the distribution of pluton emplacement across the Northern Highlands than slab breakoff, slab delamination, or peel-off delamination which produce asymmetric and(or) linear emplacement patterns, the former only affecting an area close to the suture (Magni and Király 2020). The full extent of the area affected by delamination is difficult to determine due to later strike slip offsets (Fig. 5.4c,d; e.g., Stewart et al., 2001). This scenario still accounts for observed lithologies and chemistries of intrusions. As melt is likely to be generated from subduction-modified delaminated or remaining SCLM (Fig. 5.5), the resulting melt carries the enriched light REE, large ion lithophile element (LILE) and SCLM related isotopic signatures of late Caledonian intrusions and is consistent with petrogenetic findings of Fowler et al. (2008). This melting will input new mantle melt into the hot zone, of contrasting temperature and chemistry than existing more evolved and homogenised magmas. This input likely disturbed the LCHZ leading to the ascent of reawakened earlier mushes, now containing mafic enclaves, as well as more substantive batched if mafic magmas (including those of appinitic affinity) as seen in the field (e.g., Castro and Stephens, 1992). Accelerated slab rollback and slab steepening from c. 437 Ma, expected with ongoing collision and evidenced in the Scandinavian Caledonides (Slagstad and Kirkland 2018), may have encouraged more vigorous asthenospheric convection (Fig. 5.4). In turn, convection may enhance melting by both exposing the upper plate mantle lithosphere to more vigorous convection and asthenospheric heat, and encouraging asthenosphere decompression melting (Kaislaniemi *et al.* 2014). More vigorous convection may also enhance asthenosphere-lithosphere boundary instability and convection cell migration thus inducing further delamination and melting, and so may help to explain the large volume of magma emplaced in the Northern Highlands at this time (Fig. 5.2c, 5.3c).

Delamination driven or aided by crustal thickening to the point of gravitational instability is consistent with the coincidence of peak metamorphism c. 425 Ma, ~ 12 Myr into hard collision, as peak crustal thickness may be expected to occur at this time (Kinny *et al.* 1999; Mako *et al.* 2019; Strachan *et al.* 2020a). Geobarometric and geothermometric data by (Mako *et al.* 2019) appears to support this. The decompression from 8 – 9 kbar to 6 – 7 kbar identified between 426 ± 2 Ma and 425 Ma may be consistent with uplift via isostatic compensation and asthenosphere upwelling due to accelerated rollback and delamination, with

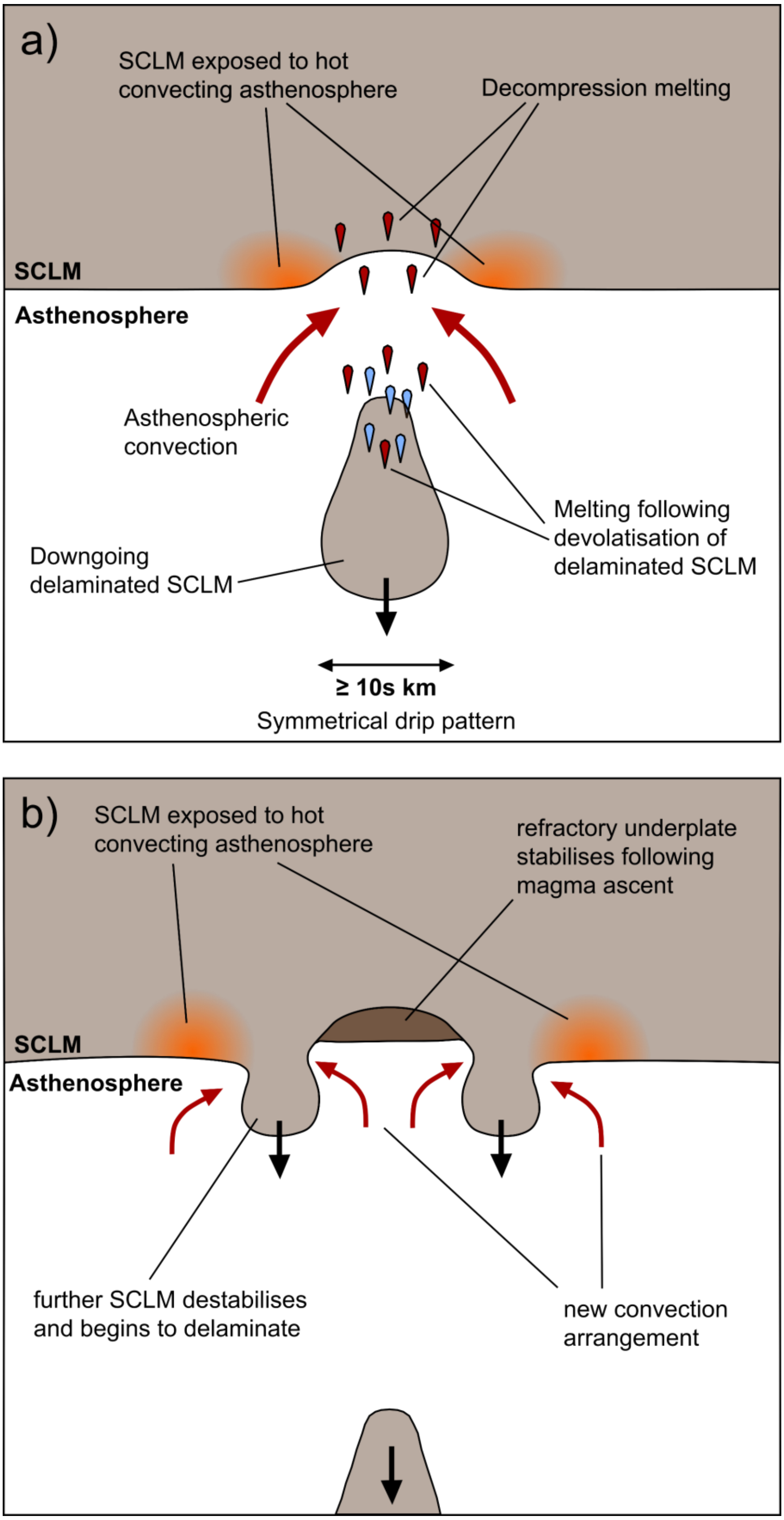

Figure 5.5 Schematic diagram of a) mantle melting associated with drip delamination and b) migration of mantle convection and development of further delamination once delamination has begun. Mechanisms depicted as outlined by Elkins-Tanton (2007) and Kaislaniemi et al. (2018, 2014).

of regional peak kyanite-sillimanite grade assemblages and of lower pressure cordierite overprinting associated with the Strontian intrusion aureole c. 423 Ma. The uncertainty in the monazite U-Pb age of 426 ± 2 Ma (Mako *et al.* 2019) gives a maximum age for peak crustal thickness of 428 Ma. Peak thickness at 428 Ma gives sufficient time for instabilities, delamination and melting to develop and produce a peak in emplacement at c. 426 – c. 425 Ma given the short lived duration of drip delamination events of ~ 1 Myr (Archibald *et al.* 2022; Stein *et al.* 2022).

While peak crustal thickness is consistent with broadly coeval delamination at c. 426 Ma, it is not certain whether the maximum measured pressure of 8 – 9 kbar coincides with peak crustal thickness due to limited geobarometry across the Northern Highlands. If peak crustal thickness is typically expected a few Myr before peak temperature, peak temperature and metamorphism at c. 425 Ma identified by Kinny et al. (1999) may yet be due to both advection of magmatic heat and radiogenic heating due to thickening (Mako *et al.* 2019, 2024). Mantle lithosphere instabilities and delamination may therefore be aided or otherwise explained by weakening and lowered viscosity of the lower crust due to increased temperature and magmatic component. A weakened lower crust has been shown to enable delamination in the absence of a dense mantle lithosphere or eclogitic root (Stein *et al.* 2022).

One drawback in confirming a delamination scenario is the lack of contemporary geophysical evidence for active delamination, or of the thickness and density of the mantle lithosphere at the time of magmatism. Limited spatial extent of geobarometric work also hinders confidence in this interpretation. Resultant patterns of uplift due to delamination may also be difficult to disentangle from that due to exhumation and associated with strike slip faulting (Spencer *et al.* 2020).

Regardless of deep geodynamic processes, the final emplacement of magmas during this period is controlled by structural pathways, dominantly by sinistral strike slip faults (Stewart *et al.* 2001; Neill and Stephens 2009). Concurrence of the upsurge in plutonism and the switch from thrust dominant to transpression dominant deformation may be expected, as transpressional faults are known to enable vertical ascent and escape of magmas from LCHZs (de Saint Blanquat *et al.* 1998; Chaussard and Amelung 2014; Richards 2021). Weakening of the crust due to magmatism may also have enabled localisation of strike slip deformation thus devising its own escape (D'Lemos *et al.* 1992). Timing of delamination, uplift and subsequent strike slip deformation and mid - crustal emplacement may also be consistent with the Spencer et al. (2021) model of gravitational collapse of the Northern Highlands. This scenario may similarly be consistent with the possibility that transpression contributed to rapid exhumation (Mako *et al.* 2024). Uplift and decompression during collapse likely also helped facilitate magma ascent, and may have encouraged any final crustal melting (Brown, 2007 and references therein).

5.3.3 Nature of Great Glen Fault Motion c. 418 – c. 417 Ma

Intrusions known to have emplaced over c. 418 – c. 417 Ma are the inner Helmsdale granite (417.0 ± 4.0 Ma), Abriachan granite (418.2 ± 5.6 Ma), and the Sanda facies of the Strontian intrusion (418 ± 1 Ma, Paterson et al., 1993) (Table 2.1, Fig. 5.2d). These intrusions have similar chemistries to those emplaced at c. 428 - c. 423 Ma though are somewhat more evolved (Fowler *et al.* 2008; Ansberque *et al.* 2019; Matthews *et al.* 2023). Their antecryst cargo (Fig. 4.10, 4.14) indicates remobilisation of evolved, granitic mush from the LCHZ. A further episode of strike slip motion concurrent with the end of the Scandian episode c. 418 – c. 417 Ma may have enabled this final small batch of evolved magmas to escape the LCHZ.

The limited occurrence of mafic facies and enclaves within the inner Helmsdale and Sanda phases (Castro and Stephens 1992; Fowler *et al.* 2008) and the lack of identified mafic material in the Abriachan intrusion further indicates that little to no new mantle melt was added to the crust at this time. A lack of addition of mafic material may indicate that these intrusions were more likely sourced from the LCHZ and remobilised by changes to crustal stress than from new mantle melts generated by slab or mantle dynamics (Fig. 5.4d). A crustal melt component in these late biotite-bearing intrusions may also be possible given the ongoing decompression and uplift at the time (Spencer *et al.* 2020). The less metaluminous to more peraluminous character of the Helmsdale and Sanda facies intrusions, and a similarly weakly metaluminous late biotite granite noted at the Rogart intrusion, in comparison with earlier more metaluminous intrusions may also support a crustal melt component (Fig. 5.6; Fowler *et al.* 2001; Chappell et al., 2012). Extensive inheritance may also support a more significant crustal melt component

(Fig. 4.10a, 4.14a,d, Paterson *et al.* 1992a). Further granitoid samples in the literature with similar Aluminium Saturation Index (ASI) > 1 were collected from relatively marginal locations within the Rogart and Strath Halladale plutons and may instead reflect assimilation during emplacement (Fig. 5.6; Appendix G). This interpretation is consistent with isotopic data obtained by Fowler et al. (2008) of the Rogart quartz-monzodiorite and Strath Halladale samples and so does not negate that a crustal source melt component is unique to the late intrusions.

Further, it is not clear why magmatism appears to end c. at 417 Ma despite the occurrence of transtension, uplift and orogenic collapse from c. 415 Ma, typically associated with decompression melting (Hollister and Andronicos 2006; Mako *et al.* 2019; Spencer *et al.* 2020; Goscombe *et al.* 2022; Strachan *et al.* 2020a) and continued magmatism further south (Oliver *et al.* 2008; Hines *et al.* 2018). It may be that decompression magmatism is represented only by minor intrusion suites at the crustal level currently exposed. Minor intrusions of presumed Caledonian age are widespread across the Northern Highlands, including evolved minor intrusions which cross-cut granitoid plutons and earlier minor intrusions (e.g., Fettes and Macdonald, 1978; Fowler and Henney, 1996; Goodenough et al., 2004; Smith, 1979). However, the minor intrusions are without radiometric ages and this suggestion remains speculative.

All intrusions from this period are intruded along the GGF or thought to be intruded along associated proximal structures (Tulstrup 1980; Hutton 1988). Of these intrusions the Sanda facies is the only one with a detailed emplacement model available, that of Hutton (1988). The model invokes local extension at the termination of a splay fault off the GGF system, with dextral overall GGF motion. However, this model has not been reviewed or advanced since its publication, and its interpretations were based on the geochronological data available at the time. The age of 435 ± 10 Ma (Halliday *et al.* 1979) for the outer Strontian Sunart facies is no longer applicable and the model and its implications should be revisited. Structural, geochronological and geothermometric data from Rosemarkie at the far northeast of the main GGF trace indicate sinistral GGF movement at c. 400 Ma (Mendum and Noble 2010; Law *et al.* 2023). The only concrete magmatic evidence of sinistral motion is associated with the Clunes tonalite, c. 428 Ma (Stewart *et al.* 2001). Hutton's (1988) model therefore challenges the implication that this was a

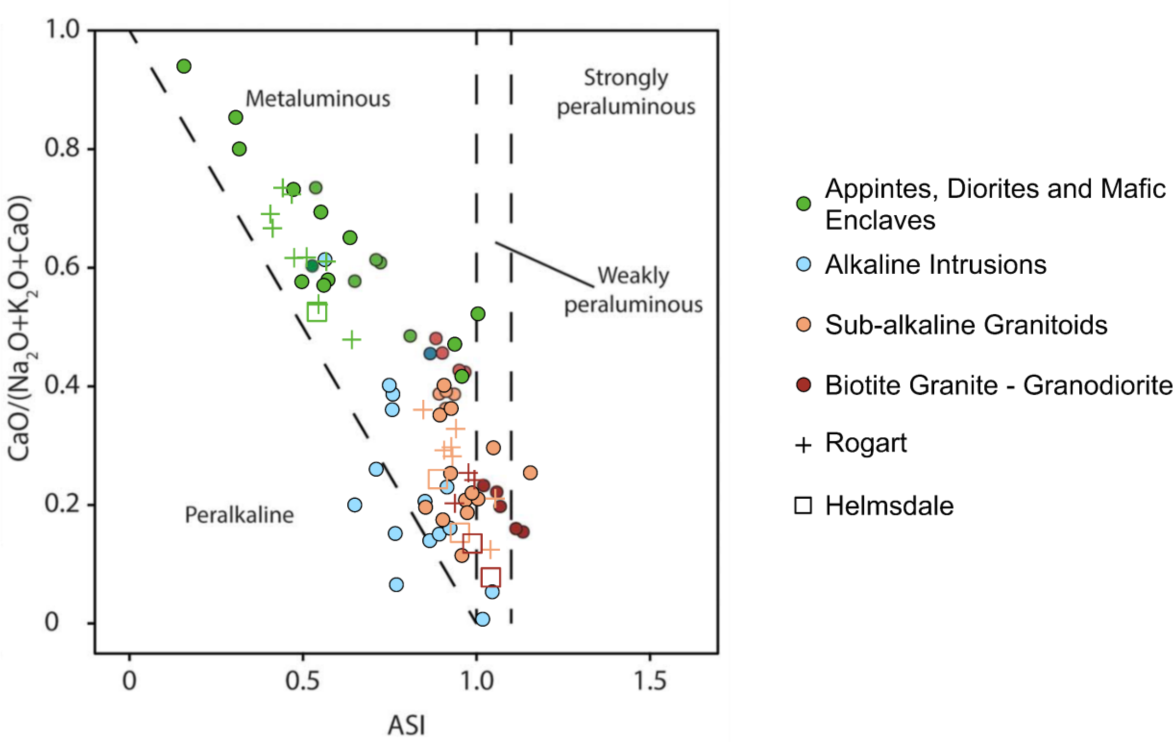

Figure 5.6 Alumina saturation diagram after Matthews et al. (2023). Molar CaO content normalised to $CaO+Na_2O+K_2O$ (C/CNK) vs aluminium saturation index (ASI, $Al_2O_3/(Al_2O_3+Na_2O+K_2O)$) for Northern Highlands Caledonian intrusions. C/CNK and ASI values were calculated using whole rock data from Fowler (1992), Fowler et al. (2008, 2001), Fowler and Henney (1996), Lundmark et al. (2019), Thirlwall and Burnard (1990) and Thompson and Fowler (1986). See Appendix G for full data summary. Late biotite granites and granodiorite highlighted are the Sanda facies at Strontian, inner Helmsdale Granite and the innermost biotite granite phase at the Rogart intrusion. Additional data points from Strontian depicted by Matthews et al. (2023) are of a quartz monzodiorite dyke (dark blue) and a shoshonitic mafic enclave (dark green).

30 Myr period of sinistral motion and could signify a more complex or punctuated fault history with possible periods of stagnation or reversal of fault motion.

If a period of dextral GGF motion is required, a change in fault nature, the distinct 'late' pulse of granitoid magmatism, and overlap in timing with the docking of peri-Gondwanan terranes with the Laurentian margin further southwest may be further evidence for the effects of Acadian orogenesis, known to have reactivated the fault (Mendum and Noble 2010; Gemmell *et al.* 2023; Law *et al.* 2023). If dextral motion is not required, the Strontian pluton may have been intruded along a fault structure such as a fault jog during sinistral motion. More systematic study of fabrics and possibly magnetic susceptibility across the whole pluton would be necessary to determine the emplacement mechanism for the Sunart and Sanda phases.

Additional support for the role of decompression, changes to upper plate stress and delamination over that of slab breakoff for the emplacement of Caledonian intrusions may be derived from the tectonic history of the Scandinavian Caledonides. The Western Gneiss Region (WGR) of Norway, considered to represent the subducted leading edge of Baltica, is shown to record a south to north propagation of collision consistent with sinistrally oblique collision and anti-clockwise rotation of Baltica (Soper *et al.* 1992; Torsvik *et al.* 2012; Bottrill *et al.* 2014). Continuation of this south to north trend is supported by typically earlier occurrence of orogenic stages in the Northern Highlands, including i) postulated collision with Baltica promontories at c. 450 Ma cf. 438 – 434 Ma (Slagstad and Kirkland 2018; Milne *et al.* 2023), ii) hard collision with Baltica c. 437 Ma cf. decrease in convergence rate and early development of continental eclogite in the WGR c. 430 Ma (Glodny *et al.* 2008; Torsvik *et al.* 2012; Slagstad and Kirkland 2018), and iii) the onset of orogenic collapse c. 415 Ma cf. c. 410 Ma (Wiest *et al.* 2021; Mako *et al.* 2024; Strachan *et al.* 2020a). Orogenic collapse in the Norwegian Caledonides involved the exhumation of the WRG, via eduction or plate divergence, for which both mechanisms have been related to slab breakoff and the loss of slab pull (Duretz *et al.* 2012; Bottrill *et al.* 2014; Butler *et al.* 2015).

Given this regional trend, slab breakoff in the Scandinavian Caledonides to the northeast c. 410 Ma, and slab breakoff in the Southern Uplands to the SW now identified at 420 – 418 Ma (Gemmell *et al.* 2023), it follows that slab breakoff beneath the Northern Highlands occurred sometime between 418 and 410 Ma. This timing is broadly after that of plutonism in the Northern Highlands and supports that slab breakoff may have aided decompression and any possible decompression melting but was likely not related to peak magmatic emplacement c. 428 – c. 423 Ma (Fig. 5.4d). This interpretation is, however, contingent on i) coupling of the upper and lower plates and the assumption that uplift and breakoff in the lower plate is indicative of uplift in the upper plate, and ii) limited thermochronological constraint on uplift in the Northern Highlands (Mako *et al.* 2019, 2024; Spencer *et al.* 2020).

5.4 Future Work

Continued use of in situ methods to fully constrain zircon growth and chemical history, combined with high precision CA-ID-TIMS dating and textural control, will enable a confident understanding of the magmatic history of plutons. Subsequent interpretations of changes in slab dynamics, upper plate stress state and late Caledonian geodynamics can thus also be made with greater confidence. While sufficient data to determine the timing of emplacement has been obtained here using quadrupole LA-ICP-MS zircon U-Pb analysis, there are some remaining uncertainties (e.g., see section 5.1.2). Increased duration of analysis, increased laser fluence and(or) use of multi-collector (MC-) LA-ICP-MS may improve precision of ages individual spot ages (cf. Lim et al., 2023; Milne et al., 2023). Improved spot precision may reduce occurrence of error overlap between spots and perhaps enable clearer distinction between emplacement and antecrystic zircon populations. Improved spot precision may also reduce the uncertainty in final ages, particularly that of the Strontian Sanda facies, Helmsdale and Abriachan (chapter 4, section 5.1). Final age uncertainties may also be improved by further concentration of laser spot selections on clear oscillatory zoning to maximise return of emplacement and antecrystic aged spots, and bypass interesting (but less relevant in this context) xenocrystic zircon (cf. Prave *et al.* 2024).

A wider range of age-constrained chemical data may be obtained, for example, by use of split stream LA-ICP-MS. Use of split stream laser ablation would remove uncertainty over whether zircon material analysed for U and Pb isotopes is the same as that measured for trace elements, as was encountered in this study (e.g., Yuan et al., 2008). Concurrent analysis with U-Pb and isotope systems such as Lu-Hf or Sm-Nd would indicate the relative contribution of crustal and mantle sources of magmatism over time (e.g., Kinny and Maas, 2003; Scherer et al., 2007). Stable isotope data including O isotope ratios may also be obtained via Secondary Ion Mass Spectrometry (SIMS) and may further detect relative crustal and mantle component and indicate magma evolution history (e.g., Appleby et al., 2008). In situ geochemistry may help distinguish between emplacement related and antecrystic zircon populations and add confidence to that determined by zircon texture and statistical measures. Distinguishing populations in this way may yet prove difficult where plutons show evidence of homogenisation during evolution as found in this study (see section 5.2.1). This approach may be more successful for plutons which have experienced a greater degree of assimilation and chemical evolution on emplacement than those studied here (e.g., Strontian, Helmsdale, cf. Rogart, Ratagain; Fowler et al., 2008).

Combination of in situ results with highly targeted CA-ID-TIMS will enable precise and confident constraint on emplacement ages. For example, initial use of in situ analysis to constrain magmatic duration and evolution, along with CL imaging, will enable selection of emplacement aged grains unaffected by Pb loss. Selected grains can then be removed from resin stubs (e.g., by microdrilling) and used for sequential dissolution CA-ID-TIMS to obtain final precise constraint on emplacement age (Gaynor *et al.* 2022). This workflow, though costly, should provide robust data on which to frame a well constrained Scandian tectono-magmatic history once scaled regionally. The workflow would be applied to both redating of intrusions with contentious ages and dating of those without ages. Redating intrusions which are recognised as key markers of geodynamic changes will be key to understanding the relative timing of e.g., thrusting (Assynt Alkaline Suite, Goodenough et al., 2011), the minimum age of sinistral motion on the Great Glen Fault (Clunes, Stewart et al., 2001) and upright folding (Strachan and Evans 2008). Intrusions which are not yet dated include the Migdale, Fearn and Orrin intrusions (Fig.1). These intrusions are evolved, each comprising biotite granite with no noted mafic enclaves (I. Neill, pers. comm. 2024). Given their evolved nature and proximity or relative proximity to the Strath Fleet-Loch Shin, Dornoch Firth and Strathglass faults it is possible these were emplaced within the same time frame and tectonic regime as the Sanda facies, Helmsdale and Abriachan intrusions c. 418 – c. 417 Ma (Fig. 2.1,5.2d; British Geological Survey, 2016; Holdsworth et al., 2015).

Detailed structural studies of plutons will constrain emplacement mechanisms and the nature and timing of any associated fault movement. Existing emplacement models (e.g., Hutton, 1988) were developed using the geochronological data available at the time and should be updated to consider new data and more developed understanding of tectonic processes. This may comprise a combination of extensive field studies, and use of techniques such as Anisotropy of Magnetic Susceptibility (AMS) (e.g., Lawrence et al., 2022; Petronis et al., 2012). AMS could prove particularly useful where plutons have been emplaced over significant periods of time, and magma batches may have been emplaced during different tectonic regimes (e.g., Strontian).

Understanding the absolute timing of events and the role of upper plate stress states are key to understanding the distribution of resource potential in a region.

For example, a transition from compression and extensive LCHZ development to transpression and rapid uplift is critical to forming porphyry deposits, and may be controlled by e.g., the rate of slab rollback or collision dynamics (Chiaradia and Caricchi 2017; Richards 2021). This is true at a regional scale, where emplacement of magma derived from different pockets of LCHZ magmas, or extracted from the LCHZ at different times, may produce plutons with slightly different chemistries and therefore resource potential (e.g., Carty et al., 2021; Wan et al., 2018). Understanding the timing of local effects of geodynamic events is also critical, for example where the timing of uplift may determine mineralisation history (Holdsworth *et al.* 2015). Thus, constraining the relative and absolute timing of regional Caledonian events in the Northern Highlands is key to providing context for future investigation into resource potential. Such research is a likely endeavour in the near future given UK targets for domestic mineral supplies (UK Government 2022; Deady *et al.* 2023), known occurrences associated with Caledonian intrusions (e.g., Garson et al., 1984; Tweedie, 1979), and renewed academic interest (Heptinstall *et al.* 2023).

Further, it is suggested above that the later c. 418 – c. 417 Ma granites are typically more peraluminous and more evolved (Fig. 5.6). Undated evolved intrusions may also be part of this 'late' suite of intrusions (see section 5.3.3). As a group these intrusions may be more likely to be high heat producing, with Helmsdale, Fearn and Abriachan already identified as such (Downing and Gray 1986; Gillespie *et al.* 2013; McCay and Younger 2017). Wider assessment of heat production and 3D models of pluton shape via field and AMS study may enable recent advances in geothermal energy technology to be better taken advantage of. Advances such as deep, closed-loop heat exchangers (e.g., that of Eavor) will enable geothermal energy production with a small surface impact and limited water usage, and eliminate the risk of induced seismicity (Toews and Holmes 2021; Beckers and Johnston 2022). Understanding the formation, structure and any chemical enrichments (e.g., U, Tweedie 1979) of these late intrusions could therefore contribute to a green UK energy transition. These next stages of application are now being undertaken at the University of Glasgow.

Chapter 6 Conclusions

New LA-ICP-MS U-Pb zircon emplacement dates have been obtained for the Strontian Sunart facies (423.5 ± 2.1 Ma), Strontian Sanda facies (418.2 ± 6.3 Ma), Helmsdale (417.0 ± 4.0 Ma) and Abriachan (418.2 ± 5.6 Ma) intrusions. The results provide further confidence in emplacement dates for the Sunart facies and inner Helmsdale intrusions (cf. Pidgeon and Aftalion, 1978; Rogers and Dunning, 1991), confirm non-peer reviewed monazite data for the Sanda facies (Paterson *et al.* 1993), and provide the only available emplacement age for the Abriachan intrusion. Emplacement of a distinct 'late' group of evolved intrusions, dominantly biotite granodiorite to monzogranite in composition, c. 418 – c. 417 Ma is defined.

The use of in situ LA-ICP-MS analysis enabled the identification of antecrystic zircon thus providing a fuller record of magmatism than ID-TIMS studies which dominate the existing record. Evidence of antecrystic zircon in each sample, with an overall maximum crystallisation age of c. 450 Ma is consistent with existing in situ zircon U-Pb data and the LCHZ zone model of Milne et al. (2023). The geochronological data obtained here thus supports the existence of an LCHZ beneath the Northern Highlands from c. 450 Ma to c. 418 - c. 417 Ma.

The lack of a definitive relationship between Sunart facies zircon heavy REE concentration and Ti-in-zircon temperature, and emplacement related and antecrystic zircon growth is compatible with a long-lived, open-system LCHZ beneath Strontian (cf. a closed, fractionation dominated system), though the limited size of this dataset is acknowledged.

Given the additional support for an LCHZ obtained and the concerns with slab breakoff models discussed in chapter 2, the following model is suggested as a plausible explanation for Scandian magmatism in the Northern Highlands:

1) Initial collision of the Laurentian margin with Baltica promontories from c. 450 Ma during the latter stages of Iapetus subduction caused compression in the Laurentian crust, and led to the initial development of an LCHZ as set out by Milne et al. (2023) and Slagstad and Kirkland (2018). Continued subduction processes input arc magmas to the LCHZ, within which fractionation, mixing and homogenisation processes occur, possibly

continuously. Limited volumes of magma escaped the LCHZ to the mid – upper crust, with those such as Glen Dessarry, Glen Loy and Cluanie emplaced into fold structures and nascent strike-slip faults within the Loch Ness and Wester Ross supergroups (Fig. 5.2a, 5.3a).

2) The switch from a thrust-dominant to strike-slip dominant tectonic regime at c. 430 Ma enabled remobilisation of crystal mushes from the LCHZ, and more significant emplacement into the mid - upper crust than previously (Fig. 5.2b). Mantle–derived melts continue to be added to the LCHZ, evidenced by the presence of mafic enclaves and mafic facies in most plutons emplaced from c. 428 – c. 423 Ma (Fig. 5.4b).

3) The plutons emplaced from c. 428 – c. 423 Ma coincide with Scandian upright folding and peak metamorphism. The association of extensive plutonism with the culmination of the Scandian Orogeny implies a major geodynamic shift occurred at this time. Mantle melting may have been driven by delamination, and associated mafic magma input to the LCHZ would have aided heating and remobilisation of magma. Delamination and remobilisation may have been further aided by enhanced mantle convection following accelerated slab rollback from c. 437 Ma due to decreasing convergence rate. Significant volumes of magma would then be available for emplacement in the mid - upper crust via contemporaneous strike slip faults which were active at this time (Fig. 5.2c, 5.4c).

4) Remobilisation and emplacement of a final batch of evolved magmas closely associated with the GGF and related faults occurs c. 418 – c. 417 Ma (Fig. 5.2d, 5.4d). Emplacement is strongly associated with changes to upper plate dynamics and a likely phase of GGF strike slip displacement, possibly driven by Acadian tectonics and under thrusting of peri-Gondwanan terranes c. 420 Ma (Soper *et al.* 1992; Brown *et al.* 2008; Gemmell *et al.* 2023). Continued uplift and decompression may have led to a more significant component of crustal melt in these magmas, and may be linked to slab breakoff and the loss of slab pull as seen in the Scandinavian Caledonides (Duretz *et al.* 2012).

Remaining key uncertainties include (i) the distance of the Northern Highlands from the arc front and from the Scandinavian Caledonides at the time of collision and arc magmatism, (ii) the absolute timing of thrust vs strike slip faulting in relation to Scandian upright folding, (iii) emplacement mechanisms and the 3D structure of intrusions, (iv) geochronological data for undated biotite granites such as Migdale, Fearn and Orrin, and (v) controls on the development of high heat production granites such as Helmsdale and Abriachan, and of intrusions bearing metal resources such as the Loch Loyal Syenites, the Assynt Alkaline Suite, and the Shin and Grudie granites (e.g., Styles *et al.* 2004; Walters *et al.* 2013; Holdsworth *et al.* 2015). Such controls might include the transition from significant compression and LCHZ development to transpression (Richards 2021), uplift (e.g., Holdsworth et al., 2015), and varying crust vs mantle contributions to magmatism (e.g., Chandrasekharam et al., 2022). Effective future exploration and use of resources associated with late Caledonian plutons relies on a full understanding of the Scandian tectonic framework, which may be achieved by addressing the above uncertainties.

Appendix A: Thin Section Photomicrographs

Representative photomicrographs for granitoid samples are presented below, with the plane polarised light images on the left and corresponding crossed polarised light images on the right. Mineral abbreviations are as per Warr (2021).

CM22/LS-01

Granodiorite with quartz, plagioclase, alkali feldspar, hornblende and titanite. Secondary mineralogy occurs as sericite alteration of feldspar.

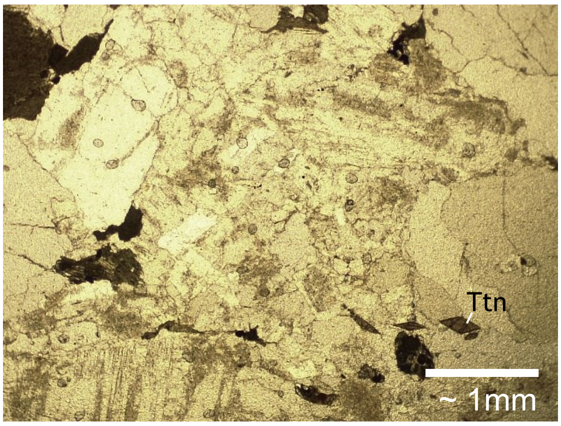

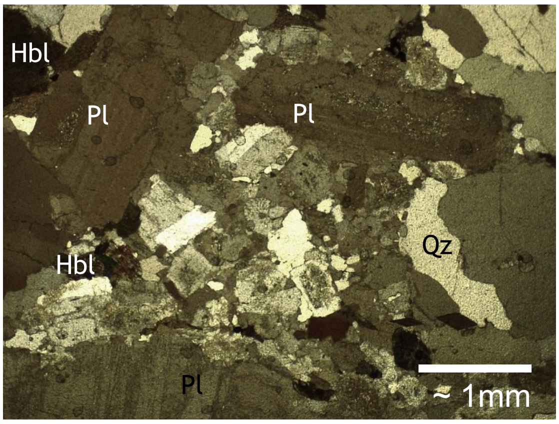

Granodiorite containing fractured alkali feldspar megacryst with feldspar inclusions.

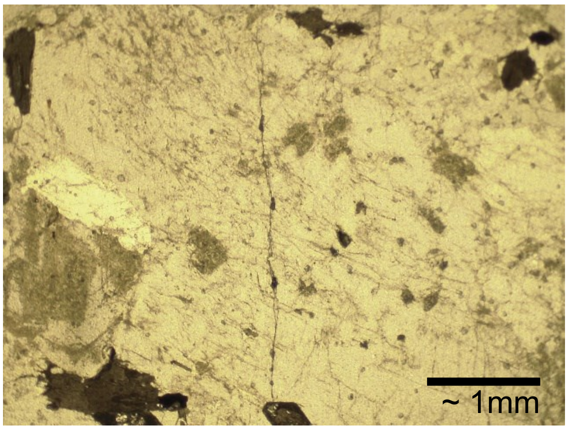

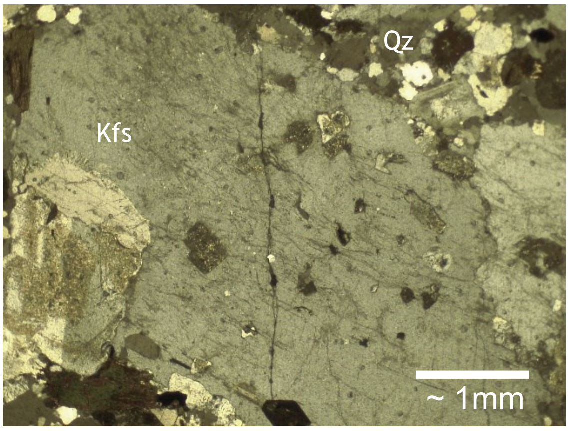

CM22/RAS-01

Granodiorite with quartz, plagioclase, alkali feldspar and biotite. Secondary mineralogy occurs as extensive haematite. Biotite often displays curved cleavage planes and undulose extinction. Quartz also displays undulose extinction.

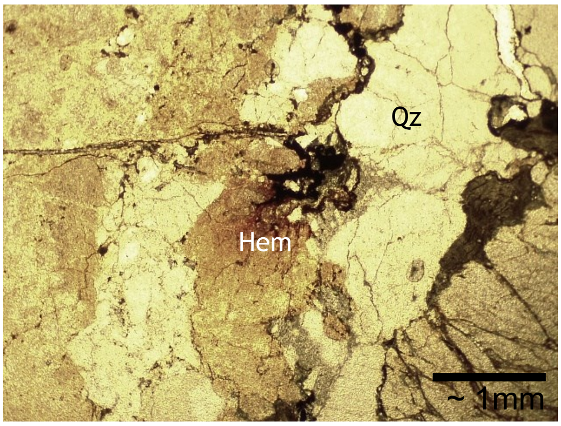

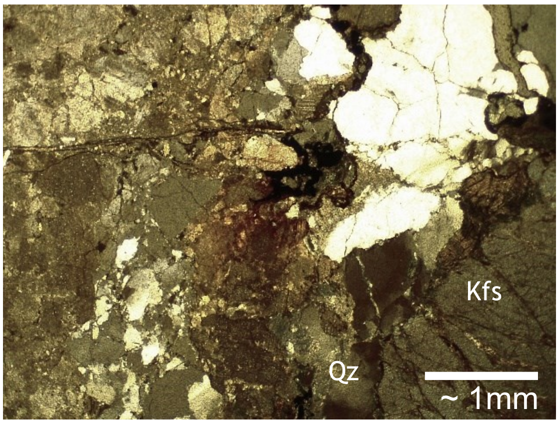

Granodiorite with curved biotite and a micro deformation zone dominated by quartz particles.

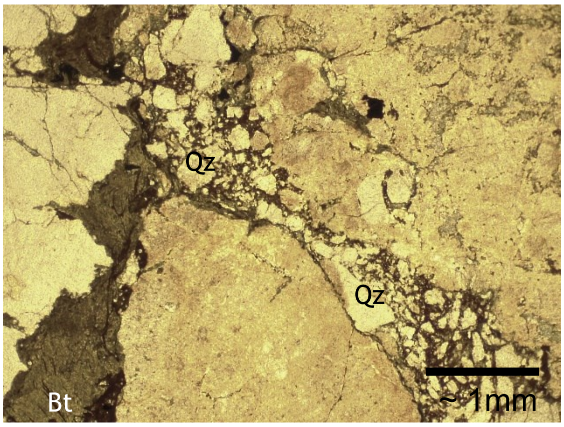

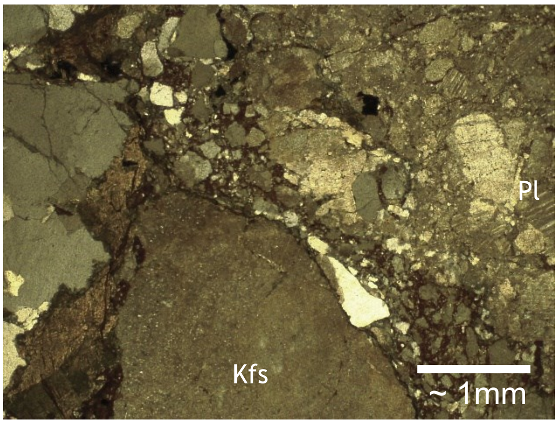

CM22/KG-01

Granodiorite with quartz, plagioclase, alkali feldspar and biotite. Feldspars are moderately sericitised, particularly in grain cores. Plagioclase is sometimes zoned.

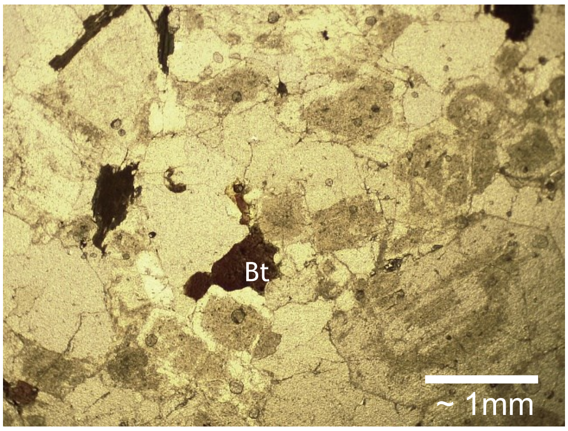

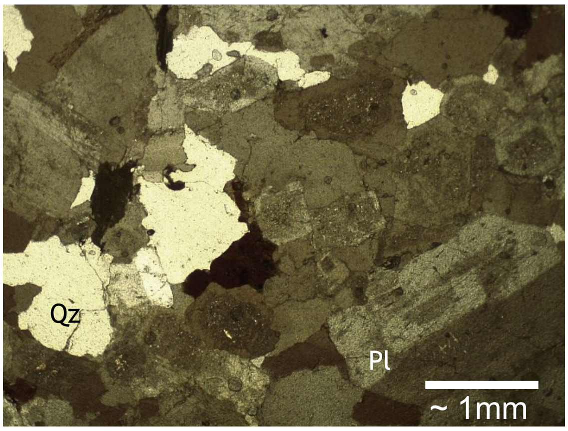

Granodiorite with alkali feldspar megacryst containing aligned feldspar inclusions.

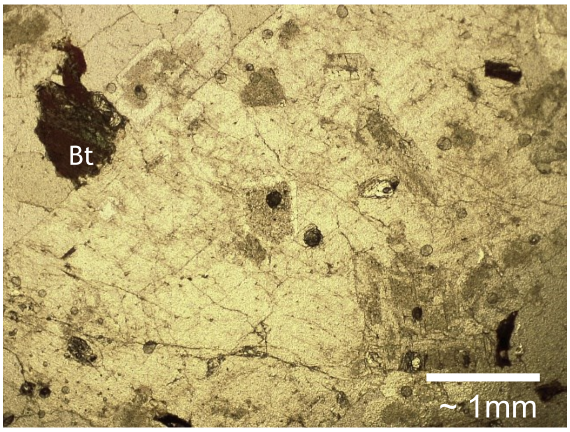

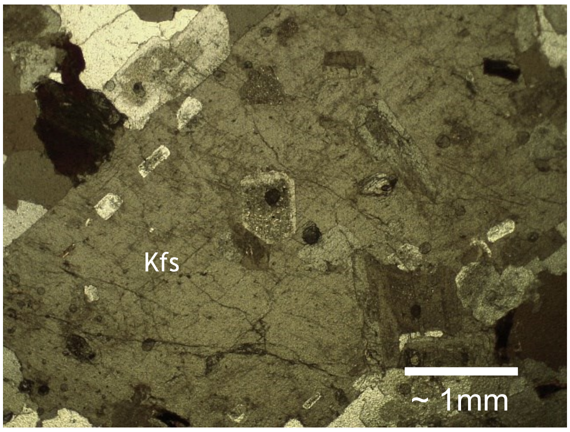

CM22/HD-01

Granite with quartz, plagioclase, alkali feldspar and biotite. Secondary mineralogy of haematite and sericite.

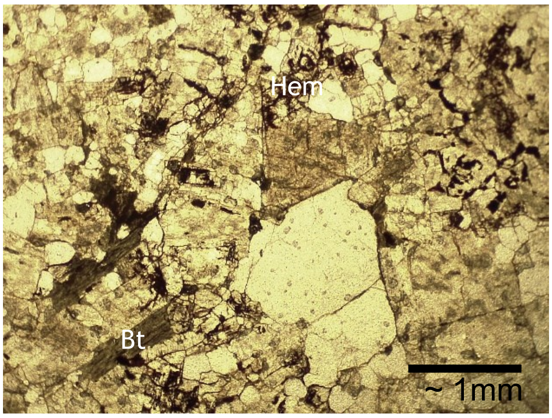

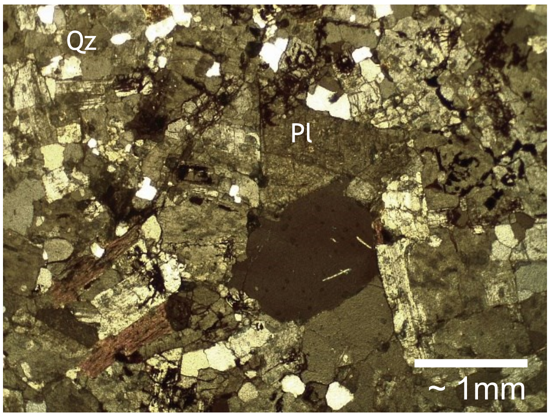

Granite containing perthitic alkali feldspar megacryst with plagioclase inclusions.

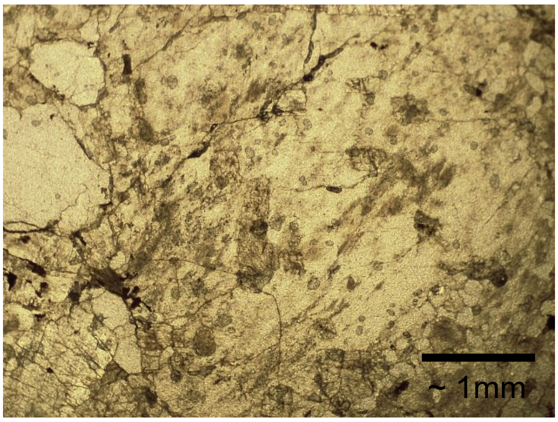

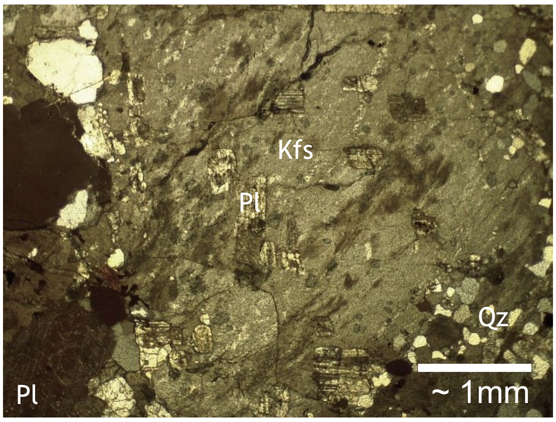

EM19/AB

Granite with quartz, plagioclase, alkali feldspar and biotite. Secondary mineralogy of haematite and sericite. Quartz displays undulose extinction.

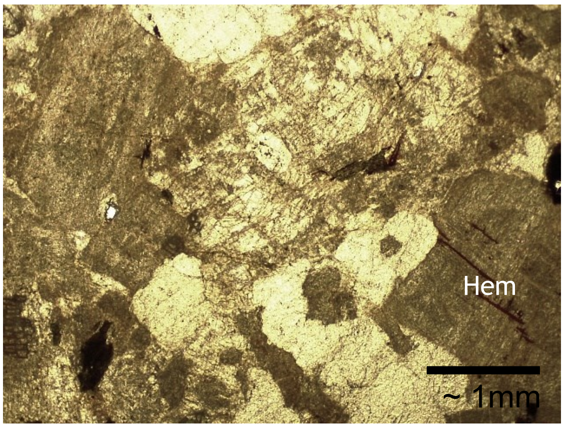

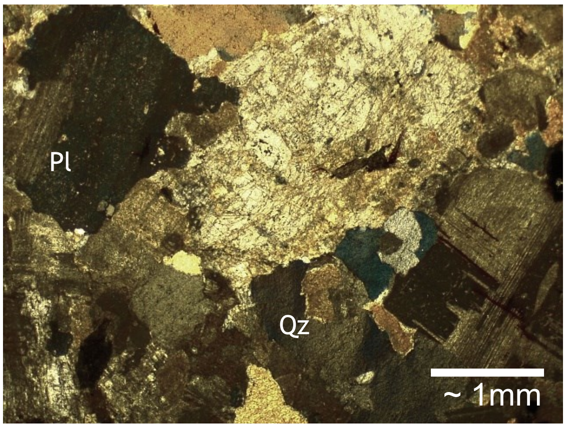

Appendix B: Zircon Cathodoluminescence Images

The full set of zircon cathodoluminescence images are available at:
https://doi.org/10.5525/gla.researchdata.1770

Images are provided for samples CM22/LS-01, CM22/RAS-01, CM22/KG-01, CM22/HD-01, EM19/AB and CM22/LB-01. Images are labelled with LA-ICP-MS spot analysis locations, colour coded as follows: light blue = emplacement related; dark blue = antecrystic,; grey = xenocrystic; black = discordant due to significant common Pb, significant Pb loss or inverted core and rim ages; yellow = concordant but rejected due to evidence of Pb loss; orange = of emplacement age but not texturally justifiable as emplacement related; red = reserved for trace element analysis. Sample CM22/LB-01 follows a different colour code: light blue = concordant spots; black = discordant spots. A key is provided in each document.

Appendix C: Zircon Textural Descriptions

Colour code as per Appendix B. Light blue = emplacement, dark blue = antecrystic, grey = xenocrystic, yellow = concordant but rejected due to evidence of Pb loss, orange = spots of emplacement age but not texturally justifiable as emplacement related. Discordant spots, spots affected by significant common Pb, significant Pb loss or with inverted core and rim ages are left uncoloured. Core-rim boundaries are defined where there is a clear change in cathodoluminescence brightness and(or) zircon texture, or where significant cross cutting relationships are observed between regions of oscillatory zoning. Textural definitions are otherwise as per (Corfu *et al*. 2003).

Ages and errors presented are uncorrected for common Pb as common Pb corrections were applied at a later stage of data presentation.

CM22/LS-01

Grain ID	Grain Shape and Texture	Spot ID and Location	Ages			
			$^{206}Pb/^{238}U$	2σ	$^{207}Pb/^{235}U$	2σ
02	Euhedral. Core and rim are of similar proportions. Both core and rim consist of complex oscillatory zoning with resorption textures between zones. Significant fracture across core and rim. Rim contains an inclusion.	002.1	345.3	10.3	450.8	20.2
03	Euhedral. Large, messy irregular core, moderately narrow rim of finely to broadly spaced oscillatory zoning.	N/A				
04	Subhedral. Fine oscillatory zoning throughout, with inclusions and a very small homogeneous core. Minor bright zone with associated homogeneous patches.	004.1	429.4	9.0	567.2	18.3
		004.2	427.5	9.8	480.0	10.8
05	Subhedral. Large core with complex oscillatory zoning, resorption textures, inclusions and minor patchy zoning and fractures. Narrow, dark oscillatory zoned rim.	005.1	419.9	8.0	531.3	15.3

06	Subhedral. Large core of fine oscillatory zoning, with a patchy, convolute zone at its margin and partially resorbed boundaries. Moderately narrow rim of oscillatory zoning with pit due to fracturing.	006.1	418.5	9.6	538.9	27.8
		006.2	419.3	9.6	421.8	10.0
		006.3	430.6	9.9	446.1	11.7
07	Euhedral. Homogeneous core with partially resorbed boundaries. Moderate to narrow rim of complex oscillatory zoning. Multiple inclusions in both core and rim, with one inclusion overlapping both.	007.1	422.7	9.3	422.8	11.4
		007.2	424.5	9.4	428.9	10.4
08	Subhedral. Complex, fine oscillatory zoning and inclusions throughout. Heavily fractured.	008.1	412.7	12.6	421.6	13.9
		008.2	428.6	9.8	500.9	14.3
		008.3	382.0	11.3	453.7	14.0
09	Anhedral. Homogeneous core with diffuse boundaries. Rim of prominent oscillatory zoning. Inclusions are situated at the core-rim boundary. Core and rim are of similar proportions.	009.1 Core	418.9	9.7	487.0	18.2
10	Subhedral. Large core with prominent oscillatory zoning, inclusions, and some patchy convolute zoning. Moderate to narrow rim of prominent oscillatory zoning and inclusions.	010.1 Core	417.5	14.1	441.2	12.3
		010.2 Core	415.7	7.7	515.9	13.5
		010.3 Rim	427.2	9.4	431.7	10.1
11	Subhedral. Small semi-homogeneous core. Wide rim of prominent, complex oscillatory zoning with inclusions and minor patchy to convolute zones.	011.1	451.3	10.2	458.0	10.6
12	Subhedral. Small, semi-homogeneous to complex, patchy zoned core. Narrow to wide rim with well-developed oscillatory zoning, inclusions and minor patchy zoning.	012.1	425.5	8.5	518.0	12.8
		012.2	413.0	8.6	469.2	9.5
13	Subhedral. Broad oscillatory zoning with inclusions, partly obscured by later complex patchy zoning. No core-rim boundary present.	013.1	431.7	9.5	433.2	10.3
14	Subhedral. Small core with moderate to wide rim, both with complex oscillatory zoning and sector zoning.	014.1	399.9	8.6	536.4	13.5
15	Subhedral. Large, mostly homogeneous core with weak sector zoning, partially resorbed. Very narrow semi-homogeneous rim with inner bright overgrowth and minor oscillatory zoning. Heavily fractured.	N/A				
16	Subhedral. Complex, oscillatory to convolute zoned core. Very narrow to wide complex oscillatory zoned rim. Inclusions occur throughout core and rim.	016.1	440.5	9.9	496.0	12.3

17	Euhedral. Semi-homogeneous core with partially resorbed boundaries, enclosed by a bright growth. Fractured rim of prominent oscillatory zoning. Core and rim are of similar proportions.	017.1	444.6	9.7	532.3	15.3
		017.2	349.5	8.8	481.5	13.7
18	Subhedral. Complex, patchy zoned core. Oscillatory zoned rim with minor patchy zoning. Core and rim are of similar proportions.	018.1	335.1	10.0	400.6	10.9
19	Euhedral. Large semi-homogeneous core with sector zoning. Very narrow semi-continuous narrow rim with feint zoning.	019.1	403.1	7.8	467.4	8.6
20	Euhedral. Very small homogeneous core. Wide rim with complex oscillatory zoning, an inclusion and minor patchy zoning.	020.1	395.6	9.5	534.8	14.1
21	Anhedral (broken). Complex oscillatory zoning with possible resorption textures. Core and rim are of similar proportions.	N/A				
22	Euhedral. Moderately small complex patchy zoned core. Narrow to wide oscillatory zoned rim with minor patchy zoning. Heavily fractured.	N/A				
23	Euhedral. Complex patchy to convolute zoned core with resorbed boundaries. Rim of oscillatory zoning. Fractured. Core and rim are of similar proportions.	N/A				
24	Anhedral (broken). Small, partially resorbed, semi-homogeneous core. Wide rim with complex oscillatory zoning with inclusions.	024.1	438.9	8.5	435.0	11.4
		024.2	433.3	8.6	470.1	13.8
		024.3	437.8	9.8	440.6	10.1
25	Subhedral. Large core with narrow rim, both consist of complex oscillatory zoning throughout with multiple large inclusions.	025.1 Core	426.5	8.9	504.3	14.5
		025.2	423.1	9.0	448.6	9.8
26	Anhedral. Moderately small, complex patchy zoned core. Moderately wide oscillatory zoned rim with convolute patchy zoning.	N/A				
27	Subhedral. Very small homogeneous core. Wide rim with oscillatory zoning, inclusions, some patchy convolute zoning and radial fractures.	027.1	504.4	15.0	1098.7	64.3
28	Subhedral. Prominent oscillatory zoning throughout with an inclusion. No clear core-rim boundary. A bright zone with convolute boundaries cross-cuts oscillatory zoning. Minor marginal fracturing occurs.	028.1	422.2	10.3	429.4	10.1
29	Subhedral. Complex oscillatory zoning throughout with some patchy zoning and inclusions. No clear core-rim boundary.	029.1	422.2	8.9	429.6	10.5
30	Subhedral. Complex oscillatory zoning with resorption textures at the core, and minor patchy zoning. No clear core-rim boundary.	030.1	416.4	9.2	571.8	25.9

31	Subhedral. Very small homogeneous core. Narrow to very wide rim with complex oscillatory zoning with inclusions. Outermost oscillatory zoning is more broadly spaced, brighter, and fractured with a ~20 μm inclusion.	031.1	472.9	10.4	659.7	42.7
		031.2	450.7	10.0	491.1	10.6
32	Subhedral. Large heterogeneous, fractured core with resorbed boundaries. Dark, moderate to narrow rim with broad zoning.	N/A				
33	Subhedral. Oscillatory zoned with homogeneous core. Heavily fractured. Core and rim are of similar priportions.	N/A				
34	Subhedral. Small homogeneous to oscillatory zoned core with partially resorbed boundaries. Wide, complex oscillatory zoned rim with radial fracturing.	034.1	418.0	10.2	635.0	24.3
		034.2	391.3	8.4	458.2	12.2
35	Subhedral (broken). Very small homogeneous to patchy zoned core with partially resorbed boundaries. Very wide rim with complex oscillatory zoning with inclusions and minor patchy zoning.	035.1	436.8	10.2	435.7	9.8
		035.2	423.8	9.1	442.7	9.2
36	Euhedral. Small patchy zoned core. Wide to very wide complex oscillatory zoned rim with multiple inclusions. Fractured.	036.1	424.5	9.7	431.6	12.9
		036.2	420.6	8.5	451.6	12.8
		036.3	422.8	8.9	428.9	9.1
37	Subhedral. Small homogeneous core, wide rim of oscillatory zoning with minor patch zoning and fracturing.	037.1	421.9	12.7	727.3	42.6
		037.2	415.9	9.2	558.6	15.1
38	Euhedral. Patchy zoned core with minor central oscillatory zoning. Oscillatory zoned rim with minor patchy zoning. Core and rim are of similar proportions.	038.1	439.9	9.2	484.0	9.6
		038.2	435.1	9.2	549.8	11.4
39	Subhedral. Oscillatory zoned with minor patchy to convolute zoning with inclusions. No clear core-rim boundary.	039.1	331.6	10.6	658.8	22.6
40	Euhedral. Complex oscillatory zoning with minor patchy to convolute zoning and many inclusions. No clear core-rim boundary.	040.1	427.1	12.8	444.8	15.9
41	Subhedral. Very large complex oscillatory zoned core with some patchy to convolute zoning and inclusions. Very narrow to moderate rim with oscillatory zoning. A fracture runs the length of the grain.	N/A				
42	Subhedral. Complex oscillatory zoning with an inclusion, minor patchy zoning and resorption textures. No clear core-rim boundary.	042.1	437.3	10.4	517.3	13.8
43	Subhedral. Patchy zoned core enclosed by complex oscillatory zoning with minor patchy zoning and inclusions. Core and rim are of similar proportions.	043.1	420.8	8.6	442.0	9.1
44		044.1	430.7	13.4	439.2	17.0

	Subhedral. Very small homogeneous core. Very wide oscillatory zoned rim with inclusions.	044.2	431.8	10.7	435.5	10.3
45	Subhedral. Complex oscillatory zoning with inclusions and resorption textures. Heavily fractured. Core and rim are of similar proportions.	045.1	425.8	10.4	436.3	10.4
46	Subhedral. Core with inner patchy zoning and outer oscillatory zoning and resorbed boundaries. Heavily fractured rim with oscillatory to convolute zoning. Core and rim are of similar proportions.	046.1	422.3	9.6	451.2	10.4
47	Subhedral. Very small semi-homogeneous core. Very wide rim with complex oscillatory zoning with minor patchy zoning and inclusions.	047.1	430.3	9.3	463.1	10.4
		047.2	356.4	7.4	403.9	8.5
48	Subhedral. Moderately large, partially resorbed core with inner homogeneous zone and outer oscillatory zoning with inclusions and marginal patchy zoning. Dark, narrow to moderate rim with oscillatory zoning and inclusions.	048.1	430.4	9.0	487.7	14.0
		048.2	440.4	9.2	448.8	10.7
		048.3	433.3	9.9	482.1	12.7
49	Euhedral. Very small partially resorbed homogeneous core. Very wide rim with complex oscillatory zoning and minor patchy zoning.	049.1	434.2	9.3	491.5	10.5
50	Subhedral. Complex oscillatory zoning with ~20 μm inclusions and some patchy zoning. No clear core-rim boundary.	050.1	421.4	12.4	431.3	14.7
51	Euhedral. Moderately large heterogeneous patchy core. Narrow to wide rim with oscillatory zoning. Fractured.	051.1	422.8	9.1	425.5	9.4
52	Subhedral. Complex oscillatory zoning with some patchy zoning and inclusions. Core and rim are likely of similar proportions, but their boundary is obscured by later bright homogeneous to convolute zoning.	N/A				
53	Euhedral. Moderately small, fractured, patchy zoned core with inclusions. Narrow to moderately wide, dark oscillatory zoned rim with an inclusion. A fracture cross-cuts the core-rim boundary.	053.1	434.9	9.6	489.6	10.8
54	Euhedral. Large complex oscillatory zoned core with some homogeneous convolute zones. Dark, narrow, oscillatory zoned rim. Inclusions and fractures occur throughout.	N/A				
55	Euhedral. Very small patchy zoned core. Very wide oscillatory zoned rim with some patchy zoning, a bright cross-cutting zone and approximately radial fractures.	055.1	436.2	9.7	461.4	9.9
56	Euhedral. Moderately small oscillatory zoned core with patchy zoning. Dark, narrow to wide oscillatory zoned rim. Inclusions in both core and rim, one is ~50 μm.	056.1	415.2	9.3	435.5	12.2
57	Euhedral. Complex oscillatory zoning with some patchy zoning, resorption textures and inclusions. No clear core-rim boundary.	057.1	428.8	8.7	434.2	9.6
		057.2	426.9	9.7	425.0	10.3

58	Subhedral. Very small homogeneous core. Very wide complex oscillatory zoned rim with inclusions, and a spatially limited cross-cutting semi-homogeneous zone.	58.1	423.2	8.8	424.9	11.1
		058.2	396.0	9.9	495.2	23.9
59	Euhedral. Very small patchy zoned core. Wide complex oscillatory zoned rim with minor patchy zoning.	059.1	428.7	12.5	440.6	11.5
60	Euhedral. Complex oscillatory zoning with inclusions and minor patchy zones. No clear core-rim boundary.	060.1	405.1	11.2	479.7	14.0
61	Subhedral. Very small homogeneous core/ Narrow to wide rim with complex oscillatory zoning, cross-cutting homogeneous to convolute zoning and inclusions.	061.1	436.2	9.3	434.9	9.3
62	Subhedral. Very large core with inner homogeneous region and outer oscillatory zoning, partially resorbed with a marginal homogeneous region with irregular boundaries. Narrow oscillatory zoned rim.	062.1	422.4	7.8	424.6	9.5
63	Euhedral. Large core with complex oscillatory zoning, some patchy convolute zoning and marginal inclusions. Narrow dark rim with oscillatory zoning.	063.1	419.0	9.0	460.3	12.4
		063.2	433.2	10.7	441.0	13.6
64	Euhedral. Very narrow zoned core. Wide rim with complex oscillatory zoning and cross-cutting patchy to convolute zones. Contains ~25-30 μm inclusions. Fractures cross-cut the width of the grain.	064.1	421.6	14.5	442.8	17.2
		064.2	440.8	9.6	442.2	9.2
65	Subhedral (broken). Complex oscillatory zoning with significant cross-cutting convolute to homogeneous regions and fracturing. Contains inclusions. No clear core-rim boundary.	065.1	425.8	8.2	423.0	9.5
66	Euhedral. Small, irregularly zoned core. Wide to very wide complex oscillatory zoned rim with minor patchy zones, fracturing, and inclusions.	066.1	438.1	11.0	486.0	14.6
67	Euhedral, elongate. Complex oscillatory zoning with cross-cutting oscillatory to convolute zoning. No clear core-rim boundary.	067.1	443.1	9.8	435.6	9.5
68	Euhedral, elongate. Ver narrow semi-homogeneous core. Wide to very wide oscillatory zoned rim, with minor patchy zones.	068.1	434.4	10.5	448.7	10.9
		068.2	417.0	9.2	724.4	27.0
69	Subhedral. Complex oscillatory zoning with very minor patchy zoning and an inclusion. Oscillatory zoning is less well developed in the core. No clear core-rim boundary.	069.1	435.2	11.0	559.7	23.7
70	Euhedral. Moderately small, oscillatory zoned, partially resorbed core with inclusions. Wide rim with complex oscillatory zoning, inclusions and fracturing.	070.1	445.9	10.3	457.8	11.0
71	Euhedral. Small, patchy zoned core with marginal homogeneous zone. Wide rim with well-developed oscillatory zoning with inclusions and marginal convolute zoning. Fractured.	071.1	438.4	9.7	475.0	11.6

72	Euhedral. Complex oscillatory zoning with inclusions, and some patchy to convolute zoning. No clear core-rim boundary.	072.1	440.4	9.7	440.3	10.2
73	Subhedral. Moderately small core with ore with broad zoning with irregular zone boundaries Narrow to wide rim with oscillatory zoning and a marginal homogeneous zone with minor convolute zoning.	073.1	412.8	8.9	474.0	12.9
		073.2	373.7	8.0	449.5	10.0
74	Subhedral. Large, partially resorbed core with complex oscillatory zoning, marginal homogeneous zone with convolute boundaries and inclusions. Moderately narrow, oscillatory zoned rim with minor homogeneous zones.	074.1	416.3	15.1	427.8	19.1
75	Subhedral. Oscillatory zoned with minor homogeneous patches, minor fractures and inclusions. No clear core-rim boundary.	075.1	428.8	8.9	423.5	9.0
		075.2	445.9	10.0	517.5	15.4
76	Subhedral. Complex oscillatory zoning with minor convolute zoning and inclusions up to ~40 µm in length. No clear core-rim boundary.	076.1	435.1	9.3	439.9	9.8
77	Subhedral. Complex oscillatory zoning with minor homogeneous zones and inclusions up to ~45 µm in length. No clear core-rim boundary.	077.1	387.9	10.3	589.5	25.1
78	Subhedral. Very small homogeneous core. Narrow to very wide rim with oscillatory zoning, minor convolute zoning, and an inclusion.	078.1	428.3	9.7	441.0	10.5
		078.2	427.4	8.8	432.0	8.9
79	Subhedral. Very small patchy zoned core. Wide to very wide rim with complex oscillatory zoning with inclusions up to ~40 µm in length. Significant fractures through core and rim.	079.1	439.8	8.2	442.5	10.9
		079.2	398.6	9.1	427.3	9.8
80	Anhedral. Small, patchy zoned core. Wide to very wide rim with complex oscillatory zoning and inclusions. Heavily fractured.	N/A				
81	Euhedral. Large patchy to convolute zoned core. Narrow to moderately narrow oscillatory zoned rim. Fractures occur across both core and rim.	081.1	416.6	10.8	471.3	11.6
82	Subhedral. Complex, feint to prominent oscillatory zoning with minor homogeneous regions, inclusions and fracturing. No clear core-rim boundary.	082.1	423.2	8.7	422.5	12.2
		082.2	439.6	9.2	446.1	11.7
83	Euhedral. Small, semi-homogeneous core. Wide, complex oscillatory zoned rim. Fractured across core and rim.	N/A				
84	Subhedral. Small, patchy zoned core. Narrow to wide complex oscillatory zoned rim. Fractures across core and rim, dominantly affecting the rim.	084.1	420.9	8.7	487.9	10.2
85	Anhedral (broken). Large, patchy zoned, fractured core and a finely oscillatory zoned rim with inclusions. Bright, convolute zoning occurs at the core-rim boundary extending into both. Core and rim are of similar proportions.	085.1	419.1	9.2	461.4	10.3

86	Euhedral. Broad oscillatory zoning cross-cut by a semi-homogeneous zone. Fracturing spatially with the semi-homogeneous zone. No clear core-rim boundary.	086.1	428.5	15.1	451.5	14.4
87	Euhedral. Small, partially resorbed, patchy zoned core. Wide to very wide complex oscillatory zoned rim.	N/A				
88	Subhedral. Complex oscillatory zoning with a homogeneous centre and inclusions. No clear core-rim boundary.	088.1	433.0	8.3	435.5	11.5
		088.2	418.7	9.7	491.5	10.1
89	Euhedral. Complex oscillatory zoning, with a homogeneous zone cross-cutting oscillatory zoning in places, minor fracture and inclusions. A marginal inclusion is ~35 µm in length. No clear core-rim boundary.	089.1	429.1	10.5	445.8	11.5
90	Subhedral. Very small homogeneous core. Very wide rim with complex oscillatory zoning and inclusions.	090.1	422.5	8.2	426.6	9.8
		090.2	387.7	8.7	424.1	10.0
91	Euhedral. Complex oscillatory zoning with minor convolute zoning, a homogeneous centre and inclusions up to ~30 µm in length. No clear core-rim boundary.	091.1	431.9	9.9	440.2	10.6
		091.2	438.3	10.6	538.0	21.1
92	Subhedral. Complex oscillatory zoning with some cross-cutting patchy to convolute zoning and inclusions. No clear core-rim boundary.	092.1	414.8	9.8	509.1	20.7
		092.2	378.3	9.7	745.2	33.2
93	Euhedral. Broad oscillatory zoned to homogeneous core with partially resorbed boundaries and inclusions. Rim is finely oscillatory zoned with inclusions and minor convolute zoning. Rim is moderately larger than the core.	093.1	423.2	9.9	443.0	11.3
		093.2	405.2	9.0	420.7	9.1
94	Subhedral. Complex oscillatory zoning with some convolute zoning adjacent to the centre, and inclusions. No clear core-rim boundary.	094.1	421.6	8.9	574.0	22.1
		094.2	419.2	9.0	464.1	10.9
95	Subhedral. Small, patchy to convolute zoned core, convolute zoning cross-cuts into the rim. Narrow to wide rim consists of fine to broad oscillatory zoning with minor slightly convolute zoning.	N/A				
96	Subhedral. Oscillatory zoning with inclusions and fractures. No clear core-rim boundary.	096.1	439.9	8.6	505.3	13.5
97	Anhedral (broken). Large, homogeneous to oscillatory zoned core with multiple inclusions up to ~30 µm, and resorbed boundaries. Narrow oscillatory zoned rim with minor convolute zoning.	N/A				
98	Subhedral. Patchy zoned core. Oscillatory zoned rim with radial fracturing from core-rim boundary to grain edge. Core and rim are of similar proportions.	N/A				
99	Subhedral. Small, partially resorbed oscillatory zoned core. Narrow to wide rim consists of broad oscillatory zoning. Fractured across both core and rim.	099.1	434.4	10.0	458.0	10.9

100	Euhedral. Complex oscillatory zoning with inclusions and minor homogeneous zones. No clear core-rim boundary.	100.1	414.8	9.7	548.5	21.5

CM22/RAS-01

Grain ID	Grain Shape and Texture	Spot ID and Location	Ages			
			$^{206}Pb/^{238}U$	2σ	$^{207}Pb/^{235}U$	2σ
01	Euhedral. Complex oscillatory zoning with a patchy zoned centre. Contains inclusions, heavily fractured. No clear core-rim boundary.	01.1	431.1	10.5	606.4	46.4
02	Subhedral. Complex oscillatory zoning with multiple inclusions and a homogeneous centre zone. Fractured. No clear core-rim boundary.	N/A				
03	Subhedral. Oscillatory zoning with multiple inclusions and a dark homogeneous marginal zone. Fractured. No clear core-rim boundary.	03.1	418.2	10.7	416.2	12.6
		03.2	441.2	11.7	444.8	11.5
		03.3	437.2	11.0	501.3	12.5
04	Anhedral. Complex oscillatory zoning with inclusions. Heavily fractured. No clear core-rim boundary.	N/A				
05	Subhedral. Large core with complex oscillatory zoning, resorbed boundaries, and a bright, cross-cutting homogeneous marginal region. Homogeneous to broad oscillatory zoned narrow rim with inclusions. Heavily fractured.	05.1	427.6	9.6	429.3	11.5
		05.2	324.9	9.8	378.3	11.7
06	Anhedral. Complex oscillatory zoning with inclusions up to ~20 μm. Heavily fractured and chipped. No clear core-rim boundary.	06.1	432.4	12.0	437.6	13.6
07	Subhedral. Small homogeneous core. Narrow to wide rim of fine oscillatory zoning with minor convolute zoning and marginal homogeneous texture.	07.1	369.8	9.3	559.8	15.9
		07.2	396.3	10.5	452.5	13.9
08	Anhedral. Complex oscillatory zoning with multiple inclusions, up to ~30 μm, and minor convolute zoning. Fractured and chipped. No clear core-rim boundary.	08.1	427.5	10.9	493.3	17.0
		08.2	439.7	13.3	473.8	15.8
09	Euhedral. Very small patchy zoned core. Very wide rim with complex, fine oscillatory zoning.	09.1	441.4	10.7	437.7	11.7
		09.2	429.4	14.5	441.0	19.3
10	Subhedral. Very small homogeneous core. Wide to very wide rim of complex oscillatory zoning with minor homogeneous zones and inclusions. Bright, cross-cutting patchy zoning occurs at one margin. Fractured.	10.1	438.7	9.4	453.8	12.1

11	Subhedral. Very large core with oscillatory zoning and a homogeneous centre zone, with cross-cutting convolute zoning. Narrow dark homogeneous rim. Fractured.	11.1	413.4	11.3	417.9	12.0
12	Subhedral. Large partially resorbed homogeneous core with possible partially annealed fractures. Narrow rim consists of fine oscillatory zoning. Fractured.	12.1	429.1	10.0	425.2	11.2
		12.2	415.9	10.8	431.4	11.0
13	Euhedral. Complex, fine oscillatory zoning with minor convolute to homogeneous zones and inclusions. No clear core-rim boundary.	13.1	440.8	10.4	432.7	11.3
		13.2	437.5	10.8	440.7	11.3
14	Anhedral (broken). Large core consists of oscillatory zoning cross-cut by homogeneous zoning, boundaries are indistinct in places. Core is cross-cut by a dark homogeneous rim with minor oscillatory and convolute boundaries. Contains multiple inclusions. Heavily fractured.	N/A				
15	Subhedral. Very large complex oscillatory zoned core, cross-cut by broad zoned rim with convolute boundaries. Contains multiple inclusions up to ~35 μm. Fractured.	15.1	423.6	10.5	422.3	10.8
16	Euhedral. Very large core with irregular patchy zoning throughout Narrow oscillatory zoned rim.	N/A				
17	Euhedral. Very large homogeneous to patchy zoned core. Wide rim with fine oscillatory zoning and a marginal dark homogeneous zone. Contains inclusions. Fractured.	17.1	428.2	10.2	433.8	11.3
18	Subhedral. Large homogeneous core with partially resorbed boundaries. Narrow to wide rim consists of complex oscillatory zoning. Fractured.	18.1	409.6	10.0	434.8	11.2
19	Subhedral. Very small semi-homogeneous core with partially resorbed boundaries. Very wide rim with complex oscillatory zoning and inclusions, cross-cut by a minor homogeneous zone. Fractured.	19.1	417.4	9.2	414.2	11.3
		19.2	432.4	10.0	427.3	10.8
20	Subhedral. Large oscillatory zoned core. Narrow dark, homogenous rim with sharp to diffuse boundaries. Fractured.	20.1	399.4	9.8	462.3	12.4
21	Subhedral. Very large complex oscillatory zoned core with a homogenous centre zone and inclusions. Very narrow homogeneous rim. A fracture cross-cuts the width of the grain.	N/A				
22	Anhedral (broken). Very large core with oscillatory zoning with inclusions, cross cut by a homogeneous to semi-homogeneous rim with convolute boundaries.	22.1	404.4	13.0	564.9	20.1
		22.2	428.0	10.3	516.1	13.0
23	Anhedral. Complex oscillatory zoning with inclusions, cross-cut by bright convolute zoning. No clear core-rim boundary.	N/A				
24	Subhedral. Complex oscillatory zoning cross-cut by a marginal homogeneous zone. Dark, narrow homogeneous rim.	N/A				

25	Anhedral (broken). Fine oscillatory zoning with a homogeneous to convolute zone and clustered inclusions. Fractured. No clear core-rim boundary.	25.1	414.2	9.6	418.4	11.0
26	Subhedral. Small patchy zoned core . Wide to very wide rim of fine oscillatory zoning with minor homogeneous to convolute zoning. Heavily fractured.	26.1	413.3	10.7	485.8	15.9
27	Subhedral. Small homogeneous to patchy zoned core. Wide rim with complex oscillatory zoning and some irregularly shaped homogeneous zones. Fractured.	N/A				
28	Euhedral. Homogeneous inner core enclosed by fine oscillatory zoned outer core with inclusions and partially resorbed boundaries. Wide rim consists of fine oscillatory zoning with frequent inclusions and minor homogeneous to convolute zoning.	28.1	447.4	12.2	653.9	43.3
		28.2	474.3	11.3	542.8	17.1
29	Subhedral. Complex oscillatory zoning cross-cut by marginal homogeneous zones. Heavily fractured, with fractures dominantly radial. No clear core-rim boundary.	N/A				
30	Subhedral. Homogeneous to patchy zoned core cross-cut by rim zonation. Rim of fine oscillatory zoning with inclusions. Heavily fractured. Core and rim are of similar proportions.	30.1	403.3	10.4	603.2	31.0
31	Subhedral. Semi-homogeneous core with marginal oscillatory zoning. Rim consists of irregular patchy zoning with some oscillatory zoning. Core and rim are of similar proportions.	31.1	427.3	9.9	421.7	11.1
32	Anhedral (broken). Small homogeneous core. Wide rim consists of oscillatory zoning with minor cross-cutting homogeneous zones.	32.1	446.3	10.7	466.2	12.7
		32.2	439.3	10.8	444.3	11.8
33	Anhedral. Homogeneous core with an elongate, zoned inclusion ~70 μm in length. Semi-enclosed by prominent oscillatory zoning, followed by weakly developed oscillatory zoning with inclusions and cross-cut by weakly developed convolute zoning. Enclosed by, and in places cross-cut by, a dark, narrow homogeneous rim.	33.1	426.1	9.7	431.5	11.3
		33.2	430.8	10.5	428.1	11.3
		33.3	415.9	12.3	421.4	11.4
34	Anhedral. Very large core with a patchy zoned centre enclosed by fine, complex oscillatory zoning cross-cut by homogeneous zonation with inclusions. Both homogeneous and oscillatory zonation are partially resorbed and cross-cut by a narrow, dark homogeneous rim. Heavily fractured.	N/A				
35	Subhedral. Very large core with fine oscillatory zoning cross-cut by marginal bright homogeneous to convolute zonation with inclusions. Dark, narrow homogeneous to oscillatory zoned rim.	35.1	429.0	10.6	425.5	10.7

36	Subhedral. Core mostly homogeneous with inclusions and partially resorbed boundaries, enclosed by a homogeneous zone. Rim consists of complex oscillatory zoning. Fractured. Core and rim are of similar proportions.	N/A				
37	Anhedral (broken). Patchy to oscillatory zoned core with multiple inclusions, enclosed by a narrow homogeneous zone. Rim is dark, narrow and homogeneous. Heavily fractured.	N/A				
38	Subhedral. Very large complex oscillatory zoned core with inclusions and minor convolute zoning. Narrow rim is dark and mostly homogeneous. Core-rim boundary is indistinct in places. Fractured.	38.1	432.2	14.5	442.0	17.1
39	Subhedral. Very small patchy zoned core enclosed by a very wide oscillatory zoned rim with inclusions at the margins. Fractured.	39.1	410.4	11.0	562.4	18.5
40	Subhedral. Homogeneous core with a wide complex oscillatory zoned rim. Fractures cross-cut the width of the grain.	40.1	408.5	10.4	522.2	19.1
41	Subhedral. Large core consists of complex patchy to oscillatory zoning with inclusions. Narrow rim is dark and largely homogeneous with some patchy zoning. Fractured.	N/A				
42	Anhedral (broken). Large core with a homogeneous centre zone enclosed by oscillatory zoning with minor convolute zoning and an inclusion. Narrow dark rim. Fractured.	42.1	404.0	9.0	418.6	10.9
43	Anhedral. Very small patchy to broad zoned core. Very wide rim with complex oscillatory zoning and multiple inclusions. Heavily fractured.	43.1	446.4	10.9	861.3	73.4
44	Euhedral. Prominent oscillatory zoning with minor bright cross-cutting homogeneous zones and inclusions. No clear core-rim boundary.	44.1	430.7	11.2	430.3	10.9
45	Subhedral. Complex oscillatory zoning with minor homogeneous to convolute zones and inclusions. No clear core-rim boundary.	45.1	434.5	10.7	665.2	35.1
46	Euhedral. Very large core with fine, complex oscillatory zoning and multiple inclusions. Very narrow, dark homogenous rim.	46.1	437.4	10.7	439.5	12.5
		46.2	424.6	12.9	424.5	14.2
47	Subhedral (broken). Very small core is partially resorbed with patchy zoning. Very wide rim consists of oscillatory zoning with minor homogeneous zones and inclusions.	47.1	438.4	11.5	439.8	12.5
48	Anhedral. Patchy zoned core with resorbed boundaries. Rim consists of fine oscillatory zoning with a very narrow, discontinuous dark outermost zone. A lathe shaped inclusion ~40 μm in length is situated within the core, but partially enclosed by the rim. Heavily fractured. Core and rim are of similar proportions.	48.1	407.0	10.4	406.8	11.0

49	Anhedral. Large oscillatory zoned core with some patchy zoning and partially resorbed boundaries. Narrow rim is mostly dark with feint zoning and a zoned, euhedral inclusion ~25 µm.	49.1	423.5	10.4	421.4	10.9
50	Subhedral. Innermost homogeneous zone enclosed by prominent to feint oscillatory zoning with inclusions. Some marginal feint patchy zoning. Fractured. No clear core-rim boundary.	50.1	422.7	13.5	429.1	13.4
51	Subhedral. Complex fine, prominent to feint, broad oscillatory zoning with inclusions. Fractured. No clear core-rim boundary.	51.1	398.4	9.6	413.0	10.3
52	Subhedral (broken). Very large core with inner homogeneous to patchy zoning and outer moderately space to broad oscillatory zoning. Narrow dark rim is somewhat convolute, and cross-cuts the core and oscillatory zoning. Fractured.	52.1	394.2	12.2	468.2	13.6
53	Anhedral (broken). Large core with inner small homogeneous zone enclosed by complex oscillatory zoning with inclusions. Dark homogeneous rim is of variable width. Heavily fractured, fractures cross-cut the width of the grain.	53.1	424.3	11.2	430.2	12.4
54	Euhedral. Homogeneous inner core with outer oscillatory zoned outer core. Zoning cross-cut by further prominent oscillatory zoning. Rim is dark, narrow and mostly homogeneous with some feint zoning. Marginal bright homogeneous to convolute zoning cross cut oscillatory zoning on one side.	54.1	423.5	9.3	424.5	11.0
		54.2	402.0	9.6	427.3	10.0
55	Subhedral. Large core with small inner homogeneous zone enclosed by complex oscillatory zoning with inclusions. Rim is dark, mostly homogeneous and narrow. Fractures cross-cut the width of the grain.	55.1	421.5	9.9	455.3	12.5
		55.2	417.4	10.7	496.3	13.0
56	Subhedral. Patchy zoned core with rim of oscillatory zoning. Both core and rim are cross-cut by bright homogeneous to convolute zoning. Core-rim boundary not clearly discernable. Heavily fractured.	N/A				
57	Anhedral (broken). Small homogeneous core with outer narrow oscillatory zoning and resorbed boundaries. Narrow to very wide rims consists of complex oscillatory zoning with inclusions.	57.1	419.6	16.3	439.6	21.0
		57.2	413.2	11.2	782.6	23.0
58	Subhedral. Core consists of patchy zoning, enclosed by a wide rim of oscillatory zoning. Both core and rim are cross-cut by further patchy zoning. Fractured.	N/A				
59	Anhedral. Large complex oscillatory zoned core with inclusions, cross-cut by bright homogeneous to convolute zoning. Rim is dark and narrow with broad zoning. Heavily fractured.	N/A				

60	Subhedral. Inner homogeneous core with outer oscillatory zoned core, cross-cut by bright homogeneous zoning. Semi-continuous dark, narrow rim. Cut by a prominent fracture across the width of the grain.	60.1	424.0	9.8	419.0	10.6
61	Subhedral. Very large core with an inner small homogeneous zone, and wide outer oscillatory zoning with inclusions. Narrow dark homogeneous rim with minor oscillatory zoning. Heavily fractured, fractures are dominantly radial.	61.1	408.4	10.1	526.6	17.5
62	Anhedral (broken). Very large core consists of homogeneous to patchy zoning with inclusions and is semi-enclosed and cross-cut by homogeneous to oscillatory convolute zoning. Rim is very narrow and dark. Fractured.	N/A				
63	Subhedral. Small patchy to oscillatory zoned core with partially resorbed boundaries. Wide rim with complex oscillatory zoning and inclusions. Fractured.	63.1 Rim	429.3	10.4	503.3	17.4
64	Subhedral. Oscillatory zoning, cross-cut in places by homogeneous zoning. Contains inclusions. No clear core-rim boundary.	64.1	442.0	10.3	443.6	11.9
65	Subhedral. Very small partially resorbed, patchy zoned core. Very wide complex oscillatory zoned rim with minor convolute zoning and inclusions. Fractured.	65.1	420.1	16.6	433.6	15.4
66	Subhedral. Complex oscillatory zoning, cross-cut in places by homogeneous to convolute zoning. No clear core-rim boundary.	N/A				
67	Anhedral. Complex oscillatory zoning, cross-cut in places by bright homogeneous zoning. No clear core-rim boundary.	N/A				
68	Anhedral (broken). Large complex patchy zoned core with inclusions. Rim consists of fine oscillatory zoning with a dark outermost zone with a possible inclusion. Heavily fractured.	68.1	409.6	10.1	687.6	40.7
69	Subhedral. Highly complex oscillatory zoning with some dark homogeneous zones, minor convolute zoning and inclusions. Cross-cut by bright homogeneous to convolute zones. Fractured. No clear core-rim boundary.	N/A				
70	Subhedral. Small patchy zoned core with inclusions. Narrow to wide complex oscillatory zoned rim with inclusions, cross-cut by bright homogeneous zones.	70.1	410.7	11.9	411.1	12.5
71	Subhedral. Very large core with complex oscillatory zoning, inclusions and some cross cutting homogeneous zones. Narrow dark rim. Fractured.	71.1	414.3	10.4	425.4	11.4
		71.2	428.1	10.3	428.4	10.4
		71.3	388.9	9.9	412.0	10.1
72		72.1	410.6	9.8	451.4	12.5

	Anhedral. Large oscillatory zoned core cross-cut by patchy to convolute zoning. Contains a ~30 µm inclusion also semi-enclosed by the rim. Dark, narrow rim with feint patchy to oscillatory zoning. Fractured.	72.2	437.5	10.7	446.9	11.7
73	Euhedral. Complex patchy zoned core. Wide oscillatory zoned rim with inclusions and an outermost dark zone of varying width. Heavily fractured, fractures are dominantly radial.	73.1	414.7	10.0	487.9	12.8
74	Subhedral. Small patchy zoned core with inclusions. Wide rim consists of complex oscillatory zoning with minor convolute zoning, inclusions and an outermost narrow dark zone. Fractured.	74.1	427.1	9.8	504.0	12.3
75	Subhedral. Complex, fine oscillatory zoning cross-cut by bright homogeneous to convolute zones. Fractured. No clear core-rim boundary.	75.1	418.1	11.4	428.0	11.9
		75.2	397.6	9.1	408.5	9.4
76	Subhedral. Very small homogeneous core. Very wide rim with complex oscillatory zoning with inclusions. Cut by a prominent fracture across the width of the grain.	76.1	427.4	11.8	435.2	13.8
77	Subhedral. Complex oscillatory zoning with inclusions up to ~35 µm in length, cross-cut by bright homogeneous to convolute zoning. Heavily fractured. No clear core-rim boundary.	N/A				
78	Subhedral. Very small homogeneous to oscillatory zoned core with partially resorbed boundaries. Very wide rim of complex oscillatory zoning with inclusions and an outermost narrow dark zone.	78.1	435.6	13.3	435.3	13.6
		78.2	382.6	9.5	400.3	9.7
79	Euhedral. Small homogeneous, with a very wide rim of complex oscillatory zoned rim with inclusions and minor homogeneous zones. Fractured.	79.1	429.3	10.0	428.9	11.1
		79.2	265.1	10.1	317.9	10.0
80	Subhedral (broken). Complex oscillatory zoning with inclusions and dark narrow outermost zone, cross-cut by minor homogeneous zoning. Fractures cross-cut the width of the grain. No clear core-rim boundary.	80.1	430.5	10.5	434.3	12.2
		80.2	428.2	10.6	446.8	13.0
81	Subhedral. Complex oscillatory zoning cross-cut by homogeneous to convolute zoning. Fractured. No clear core-rim boundary.	N/A				
82	Anhedral. Patchy to convolute zoned core. Oscillatory zoned rim cross-cut by homogeneous to convolute zoning. Fractured. Core and rim are of similar proportions.	N/A				
83	Subhedral. Complex oscillatory zoning with inclusions and a dark narrow rim, cross-cut by both bright and darker homogeneous zones. Heavily fractured.	83.1	329.6	14.6	390.0	11.4
84	Anhedral (broken). Small, complex patchy zoned core. Narrow to very wide complex oscillatory zoned rim with some convolute zoning. Heavily fractured.	84.1	423.7	11.8	420.4	13.3

85	Subhedral. Small semi-homogeneous core with feint sector zoning. Very wide complex oscillatory zoned rim. Fractured, fractures are dominantly radial.	85.1	398.1	10.8	419.1	12.1
86	Subhedral. Complex oscillatory zoning with sector zoning and minor homogeneous and convolute zoning. No clear core-rim boundary.	N/A				
87	Subhedral. Very small zoned core with resorbed boundaries. Very wide rim consists of complex oscillatory zoning with inclusions, possible annealed fractures and minor cross-cutting homogeneous zones. Heavily fractured.	87.1	426.0	13.6	425.6	12.0

CM22/KG-01

Grain ID	Grain Shape and Texture	Spot ID and Location	Ages			
			$^{206}Pb/^{238}U$	2σ	$^{207}Pb/^{235}U$	2σ
01	Euhedral. Core with feint magmatic zoning and patchy zoning. Magmatic overgrowth with broad oscillatory zoning. Core and rim are of similar proportions.	001.1	1737.8	38.5	1760.4	26.1
02	Subhedal. Very large, highly irregular and convolute zoned core. Narrow, oscillatory zoned rim.	N/A				
03	Subhedral. Large, patchy to homogeneous zoning with lath shaped inclusion. Dark, narrow feint oscillatory zoned rim. A ~40 μm prismatic inclusion is enclosed by both core and rim growth. Affected by two parallel fractures.	003.1	417.1	10.6	461.1	14.4
04	Euhedral. Very large core with inner patchy zoning and outer broad, feint zoning. Resorption texture between core and rim. Narrow rim with fine oscillatory to convolute zoning with resorption textures.	004.1	808.0	17.1	820.8	18.1
		004.2	830.5	16.8	832.4	15.8
05	Anhedral (broken). Core with inner feint patchy zoning, enclosed by feint, oscillatory zoning. Narrow rim with patchy zoning.	005.1	225.5	14.4	357.9	27.6
06	Subhedral. Small core with broad oscillatory to patchy zoning. Resorption texture between core and rim. Wide rim with fine oscillatory zoning with cross cutting relationships.	006.1	845.2	65.7	952.3	64.2
07	Subhedral. Large core with oscillatory zoning and a marginal bright irregular zone. Incomplete dark homogeneous rim.	007.1	437.5	14.3	565.8	31.1

08	Euhedral. Irregular in structure. One half contains a homogeneous core somewhat enclosed by fine oscillatory zoning. Second half contains irregular patchy to convolute zoning and is heavily fractured. A finely oscillatory zoned rim of variable width encloses the entire grain.	008.1	438.5	10.7	553.3	15.5
		008.2	450.3	11.3	471.8	11.6
09	Euhedral. Large patchy zoned, fractured core with resorbed boundaries. Dark, narrow rim with a partially resorbed inner zone and further outermost zone.	N/A				
10	Subhedral. Small core is resorbed and heavily fractured. Narrow to wide rim with feint broad zoning.	010.1	261.9	17.6	320.8	12.7
		010.2	424.2	11.4	462.2	16.3
11	Subhedral. Small irregular to feint convolute zoned core. Wide rim with fine oscillatory zoning, inclusions and a marginal homogeneous zone.	011.1	378.8	9.5	456.4	11.3
		011.2	330.7	10.5	348.6	10.3
12	Euhedral. Patchy to moderate width oscillatory zoned and fractured core with resorbed boundaries. Rim with fine oscillatory zoning. Core and rim are of similar proportions.	012.1	669.3	94.2	1738.2	170.3
13	Euhedral. Small partially resorbed core with patchy zoning. Wide rim with broad to fine oscillatory.	013.1	389.1	9.4	419.9	9.9
14	Euhedral. Large core with fine oscillatory zoning and minor patchy zoning. Rim is dark and narrow with feint oscillatory zoning.	014.1	442.6	10.9	444.5	12.1
15	Subhedral. Large, bright fractured and homogeneous to patchy core. Feint, patchy zoned dark rim.	015.1	520.0	32.5	848.4	30.4
16	Subhedral. Large, highly irregular patchy core, with irregular, angular boundaries. Dark, narrow rim with minor oscillatory zoning.	N/A				
17	Euhedral. Patchy to homogeneous core. Rim consists of fine oscillatory zoning with minor broad to patchy zoning. Core and rim are of similar proportions.	017.1	420.3	12.1	529.6	14.1
		017.2	442.3	12.4	607.9	27.8
18	Euhedral. Irregular patchy core with minor oscillatory zoning and resorbed boundaries. Rim is dark with feint oscillatory zoning. Core and rim are of similar proportions.	018.1	1583.9	36.4	1626.8	23.6
19	Euhedral. Small oscillatory zoned core with resorbed boundaries. Wide rim consists of moderate width, feint oscillatory zoning with at least one cross cutting relation present.	019.1	1420.2	29.0	1422.4	21.3
		019.2	415.7	11.5	423.8	12.0
20	Subhedral. Patchy to feint oscillatory zoned core. Dark rim with feint zoning. Core and rim are of similar proportions.	020.1	1496.7	47.6	1611.5	33.3

21	Anhedral (broken). Homogeneous with minor patchy zoning, and minor outer oscillatory zoning. At its termination there is patchy to convolute zoning with a narrow dark rim.	021.1	443.1	11.3	440.5	10.6
22	Subhedral. Broad oscillatory zoned core with resorbed boundaries. Rim is homogeneous with minor feint zoning. Core and rim are of similar proportions.	022.1	1451.1	82.4	1449.7	69.5
		022.2	437.6	25.3	677.3	24.7
23	Subhedral. Large core is dominantly homogeneous with possible sector zoning, a region of patchy convolute zoning and resorbed boundaries. Rim is finely oscillatory zoned and narrow.	023.1	1638.7	34.6	1639.2	21.6
24	Anhedral (broken). Semi-homogeneous core with resorbed boundaries. Medial zone with feint, fine oscillatory zoning. Narrow rim is finely to moderately oscillatory zoned.	024.1	405.0	12.5	661.4	30.8
		024.2	373.1	9.6	521.2	12.5
25	Subhedral. Irregular patchy to oscillatory zoned core with resorbed boundaries, partially enclosed by bright zonation. Homogeneous rim with minor feint zoning. Core and rim are of similar proportions.	N/A				
26	Subhedral. Large core with oscillatory zoning with resorbed boundaries and marginal bright zones. Fractured. Dark, narrow rim with feint zoning.	026.1	1447.7	30.6	1549.3	22.2
		026.2	989.5	25.9	1135.9	27.4
27	Subhedral. Large, homogeneous to oscillatory zoned core. Dark, narrow homogeneous rim.	N/A				
28	Subhedral. Very large core with inner patchy zoned core with resorbed edges, enclosed by outer oscillatory zoning and weak sector zoning with minor patchy zoning. Dark, narrow rim with feint zoning and resorption textures.	028.1	811.0	35.7	798.8	34.3
29	Euhedral, elongate. Patchy zoned core with regions of homogeneity. Narrow oscillatory zoned to homogeneous rim.	029.1	425.6	9.9	427.5	10.2
		029.2	427.5	11.2	497.6	24.8
		029.3	433.4	12.0	431.6	10.8
		029.4	423.9	11.0	436.2	10.7
30	Euhedral. Small sector zoned core with resorbed edges. Wide rim with oscillatory zoning, an inclusion and internal resorbed boundaries.	030.1	426.4	10.5	448.5	12.0
31	Subhedral (broken). Core with weak patchy zoning. Rim with fine oscillatory zoning. Fractures are both across the grain and radial from the core. Core and rim are of similar proportions.	031.1	435.1	11.1	432.3	10.5
		031.2	361.8	17.0	403.9	16.9

32	Subhedral. Irregular patchy zoned core with a region of homogeneity and resorbed edges. Narrow, feint oscillatory zoned rim.	032.1	1317.4	26.1	1327.3	20.3
33	Subhedral. Zoned core with irregular boundaries. Narrow to wide homogeneous to feint oscillatory zoned rim.	N/A				
34	Subhedral. Heterogeneous core with patchy and oscillatory zoning, inclusions, and resorbed edges. Narrow rim is oscillatory zoned.	034.1	435.1	13.1	442.2	13.2
35	Subhedral. Large patchy zoned core. Narrow rim with minor feint zoning and minor convolute zoning.	035.1	1489.0	39.2	1515.0	32.6
36	Subhedral. Oscillatory zoned core, with internal resorbed boundaries. Outer core also contains sector zoning. Dark, narrow rim with poorly-developed oscillatory zoning.	036.1	1548.6	32.6	1580.2	22.1
		036.2	1608.5	32.0	1600.2	22.9
37	Anhedral. Patchy zoned core. Dark rim with oscillatory zoning. Core and rim are of similar proportions.	037.1	429.9	9.2	435.2	11.5
		037.2	445.7	11.4	532.0	16.1
38	Subhedral. Small patchy zoned core with resorbed edges. Narrow to wide rim with oscillatory zoning.	038.1	1594.0	31.5	1633.8	21.6
		038.2	408.7	10.3	535.2	24.3
39	Euhedral. Homogeneous core enclosed by oscillatory zoned rim. Core and rim are of similar proportions.	039.1	421.7	10.2	528.4	15.9
		039.2	422.4	11.2	752.8	18.8
40	Euhedral. Partially resorbed patchy zoned core with outer oscillatory zoning. Enclosed by a rim of dark, feint oscillatory zoning. Core and rim are of similar proportions.	040.1	885.1	23.1	1049.1	24.3
41	Subhedral. Large patchy zoned core with bright resorbed edges. Dark, narrow homogeneous rim. Extensively fractured, one fracture is infilled and continuous with a bright homogeneous zone at the core-rim boundary.	041.1	1328.7	37.1	1329.3	37.0
42	Subhedral. Large, fractured core with inner irregular zoning with resorbed boundaries, outer oscillatory zoning with resorbed boundaries. Dark, narrow homogeneous rim.	N/A				
43	Euhedral. Small core with patchy zoning. Very narrow to wide rim with complex oscillatory zoning.	043.1	534.6	28.1	1092.0	116.9
		043.2	431.7	10.1	439.2	10.0
		043.3	438.4	11.9	865.1	65.6
44	Euhedral. Very small patchy zoned core. Wide rim with complex oscillatory to patchy zoning.	044.1	1496.5	47.9	1636.2	36.8
		044.2	1087.5	33.0	1254.1	33.9
45	Subhedral. Small, patchy zoned, fractured core with resorbed boundaries. Very narrow to wide rim with complex oscillatory zoning.	045.1	1190.7	33.1	1258.1	30.6
		045.2	430.1	10.6	457.9	10.7

46	Euhedral. Very large, patchy zoned core with broad oscillatory zoning, and partially resorbed boundaries. Dark, narrow outer rim. Fractures cross-cut the width of the grain.	046.1	1180.1	30.1	1408.0	44.1
		046.2	917.6	56.8	930.7	47.6
47	Euhedral. Smal, irregular to broad zoned core with resorbed boundaries. Wide, homogeneous rim with minor marginal zoning.	047.1	457.4	10.2	472.6	10.2
48	Subhedral. Large patchy to irregular zoned core with resorbed boundaries. Dark, narrow rim with feint oscillatory zoning.	048.1	366.2	13.0	417.0	18.9
49	Subhedral (broken). Large core, with inner irregular to convolute zoning and an outer homogeneous zone. Dark, narrow rim.	049.1	400.4	9.1	852.6	34.6
50	Subhedral (broken). Homogeneous and fractured inner core enclosed by broad oscillatory zoning. Rim is homogeneous and dark.	050.1	376.7	17.7	440.8	22.1
		050.2	230.7	13.9	460.2	40.4
51	Anhedral (broken). Large, homogeneous to patchy zoned core. Narrow, zoned rim.	N/A				
52	Euhedral. Small, patchy zoned core. Wide, complex oscillatory zoned rim. Fractures cross-cut the length and width of the grain.	N/A				
53	Subhedral. Sector zoned core. Core-rim boundary not clearly discernible. Bright sub-linear feature may be an annealed fracture.	053.1	1686.5	52.6	1693.3	28.9
54	Subhedral. Very large core with complex oscillatory zoning. Narrow dark rim with minor feint zoning.	054.1	1825.2	35.3	1850.0	21.8
		054.2	1503.9	45.9	1584.2	31.6
		054.3	546.4	39.2	995.4	69.2
2_01	Euhedral. Broad to moderate oscillatory zoning and sector zoning with inclusion. No clear core-rim boundary.	2_01.1	405.9	10.9	631.5	33.6
		2_01.2	408.9	10.6	600.4	20.0
2_02	Euhedral. Very large, sector zoned core with irregularly zoned bright margins. Dark, narrow feint zoned rim.	N/A				
2_03	Euhedral. Large, broad oscillatory zoned core with resorbed boundaries. Dark rim with feint oscillatory zoning. A bright homogeneous zone occurs at the core-rim boundary. Fractured.	2_03.1	436.3	13.3	428.2	12.6
2_04	Anhedral. Small, oscillatory zoned and fractured core which is partially resorbed. Bright zone at the core-rim boundary. Feint zoned dark rim.	N/A				
2_05	Subhedral. Very large, homogeneous to irregular zoned core with possible sector zoning, partially resorbed. Very narrow oscillatory zoned rim.	N/A				
2_06	Subhedral (broken). Large, dominantly homogeneous core. Very narrow rim with weak oscillatory zoning and inclusions.	2_06.1	433.7	9.9	667.6	39.7

2_07	Euhedral. Homogeneous core with brighter resorbed edges and possible annealed fractures. Rim fine oscillatory zoning. Core and rim are of similar proportions.	2_07.1	639.7	18.9	744.9	19.8
2_08	Subhedral (broken). Homogeneous, fractured core. Dark, feint zoned rim with an inclusion approximately at the core-rim boundary. Core and rim are of similar proportions.	2_08.1	423.1	11.3	510.5	18.9
		2_08.2	294.9	8.8	487.6	29.4
2_09	Subhedral (broken). Small, homogeneous core. Very wide rim with broad oscillatory zoning.	2_09.1	1150.9	92.1	2701.9	162.6
		2_09.2	427.9	9.4	962.1	21.6
2_10	Euhedral. Irregularly zoned core, partially resorbed. Oscillatory zoned rim. Core and rim are of similar proportions.	N/A				
1_11	Subhedral. Sector zoned with fine to moderate width oscillatory zoning. Minor convolute zoning and resorption textures. No clear core-rim boundary.	N/A				
2_12	Anhedral (broken). Irregular, patchy zoned core with resorbed boundaries. Rim is dark, mostly homogeneous with minor feint zoning, and a semi-continuous, narrow, brighter rim. Core and rim are of similar proportions.	2_12.1	992.3	26.4	1090.5	29.8
		2_12.2	418.9	10.3	437.9	11.5
2_13	Subhedral. Highly irregular, subrounded zoning. Partial rim of broad zoning.	N/A				
2_14	Euhedral. Large, fractured, partially resorbed core with inner patchy zoning and outer oscillatory zoning. Dark, narrow oscillatory zoned rim.	N/A				
2_15	Subhedral (broken). Large core with a homogeneous to patchy zoned inner core and finely oscillatory zoned outer core with resorbed boundaries. Rim consists of oscillatory zoning. A bright zone occurs at the core-rim boundary.	2_15.1	369.6	10.5	386.2	9.2
2_16	Subhedral (broken). Very small homogeneous core with resorbed boundaries. Rim consists of complex oscillatory zoning. Fractures cross-cut the width of the grain.	2_16.1	391.2	11.7	929.2	43.7
2_17	Subhedral. Homogeneous to irregularly zoned core. Dark, very narrow rim with minor convolute zoning.	N/A				
2_18	Anhedral. Patchy, convolute zoned core. Dark, narrow, mostly homogeneous rim with minor oscillatory zoning.	2_18.1	398.2	9.6	561.3	16.1
2_19	Anhedral. Homogeneous to irregularly zoned core with unclear boundaries. Dark oscillatory zoned rim with inclusion. Core and rim are of similar proportions.	N/A				
2_20	Anhedral. Large, broad to irregularly zoned core. Bright zonation at the core-rim boundary. Dark, narrow rim is dominantly homogeneous.	N/A				

2_21	Subhedral. Very small homogeneous core with resorbed boundaries. Rim consists of complex oscillatory zoning textures and an inclusion.	2_21.1	417.1	12.1	461.5	12.8
2_22	Euhedral. Small homogeneous core with minor patchy zoning and resorbed boundaries. Wide rim consists of feint oscillatory zoning.	2_22.1	1531.4	30.1	1547.6	22.5
		2_22.2	400.0	17.5	598.5	37.9
2_23	Subhedral. Highly irregular core. Very narrow rim with minor convolute zoning.	N/A				
2_24	Subhedral. Homogeneous core with marginal patchy to convolute zoning and an inclusion. Rim consists of complex oscillatory zoning. Core and rim are of similar proportions.	2_24.1	409.9	11.4	568.5	22.2
2_25	Euhedral. Small core is dominantly homogeneous. Wide rim consists of oscillatory zoning. Core-rim boundary is indistinct in places.	2_25.1	404.2	10.6	474.4	12.8
		2_25.2	402.9	9.2	429.0	9.1
2_26	Anhedral (broken). Core is highly fractured with inner patchy zoning and outer oscillatory zoning. Narrow complex oscillatory zoned rim.	N/A				
2_27	Subhedral. Patchy zoned core with resorbed boundaries. Narrow, dark rim of feint oscillatory zoning.	2_27.1	608.0	28.2	696.0	41.4
2_28	Subhedral. Core is dominantly homogeneous and partially resorbed. A discontinuous bright zone occurs at the core-rim boundary. Narrow to very narrow complex oscillatory zoned rim.	N/A				
2_29	Subhedral (broken). Semi-homogeneous core with resorption textures. Narrow, semi-continuous dark rim. Heavily fractured.	N/A				
2_30	Euhedral. Small, feint patchy zoned core. Very narrow to wide rim consists of oscillatory zoning with minor convolute zoning.	2_30.1	421.5	10.6	428.1	10.2
2_31	Subhedral. Very small, patchy zoned, fractured core. Narrow to wide rim of weakly developed oscillatory zoning.	N/A				
2_32	Subhedral (broken). Large, homogeneous to convolute, patchy zoned core. Dark, narrow rim with feint oscillatory zoning.	2_32.1	425.8	10.8	418.6	11.8
2_33	Subhedral (broken). Semi-homogeneous, fractured core with inclusion. Very narrow, dark homogeneous rim.	N/A				
2_34	Subhedral. Very small homogeneous core. Wide rim consists of complex oscillatory zoning and minor patchy zoning.	2_34.1	417.8	10.9	417.1	11.7
2_35	Subhedral. Patchy zoned and fractured core. Very narrow to wide rim consists of feint complex oscillatory zoning, minor patchy zoning with an inclusion.	2_35.1	375.8	9.5	570.1	22.1

2_36	Euhedral. Large semi-homogeneous and partially resorbed core with a significant inclusion. A bright homogeneous zone occurs at the core-rim boundary. Narrow homogeneous rim.	N/A				
2_37	Anhedral. Large, dominantly homogeneous, and highly fractured core. Semi-continuous dark, narrow rim.	N/A				
2_38	Euhedral. Homogeneous core, with a rim of feint oscillatory zoning with an inclusion.	2_38.1	433.4	10.7	468.6	13.1
2_39	Euhedral. Large, fractured core with minor oscillatory zoning and resorbed boundaries. Dark, narrow rim with limited oscillatory zoning.	N/A				
2_40	Subhedral. Very large homogeneous to patchy zoned core. Very narrow rim with minor oscillatory zoning.	N/A				
2_41	Euhedral. Large, fractured core with resorbed boundaries, inner oscillatory to patchy zoning and outer complex oscillatory zoning. Dark, narrow oscillatory zoned rim.	2_41.1	1605.1	37.1	1626.1	26.6
2_42	Euhedral. Homogeneous to irregularly zoned core. Dark rim with complex oscillatory zoning. Core and rim are of similar proportions.	N/A				
2_43	Euhedral. Heterogeneous core, with an oscillatory zoned rim. Core and rim are of similar proportions.	2_43.1	430.4	9.9	426.2	10.1
2_44	Subhedral. Large, heterogeneous core with resorbed boundaries and possible sector zoning. Dark, very narrow to wide rim with weakly developed oscillatory zoning.	N/A				
2_45	Subhedral. Broad to fine, feint to distinct oscillatory zoning with minor patchy zoning and possible resorption textures. Heavily fractured. No clear core-rim boundary.	2_45.1	401.6	11.3	539.6	26.5
2_46	Subhedral (broken). Large, semi-homogeneous, fractured core. Dark, narrow oscillatory zoned rim.	2_46.1	323.9	7.9	337.6	7.8

CM22/HD-01

Grain ID	Grain Shape and Texture	Spot ID and Location	Ages			
			$^{206}Pb/^{238}U$	2σ	$^{207}Pb/^{235}U$	2σ
01	Euhedral. Medium size, fine oscillatory zoned and sector zoned core with resorbed boundaries cross-cut by a minor homogeneous zone with convolute boundaries. Wide, fine oscillatory zoned rim. Fractured.	01.1	413.3	13.1	411.4	12.9
		01.2	412.0	9.5	417.9	9.1
		01.3	394.8	7.9	411.1	8.1
02	Anhedral. Small semi-homogeneous core with resorbed boundaries. Narrow to wide semi-homogeneous rim. Fractured.	N/A				
03	Subhedral. Large broad oscillatory to patchy zoned core with resorbed boundaries. Narrow broad oscillatory zoned rim, zoning cross-cut by a minor homogeneous zone. Rim does not fully enclose the core. Heavily fractured.	N/A				
04	Euhedral. Large core comprises homogeneous zones, convolute patchy and broad oscillatory zoning. Moderate width, complex oscillatory zoned rim. Minor fractures.	04.1	1600.7	31.9	1600.7	22.6
05	Subhedral (broken). Large patchy to convolute zoned core with inclusions. Wide to narrow oscillatory zoned rim. Fractured.	05.1	1262.7	22.1	1261.4	16.9
06	Subhedral. Large oscillatory zoned to homogeneous core with marginal patchy zoning. Narrow oscillatory zoned rim.	06.1	567.7	55.7	656.2	49.0
07	Subhedral. Small, patchy zoned core. Wide oscillatory zoned rim. Fractured.	N/A				
08	Euhedral. Large core with fine, complex oscillatory zoning, a large inclusion and partially resorbed boundaries. Narrow dark rim with minor zoning.	08.1	1726.3	31.1	1716.2	20.4
09	Subhedral. Large complex oscillatory zoned core. Narrow dark, semi-homogeneous rim. Fractured.	09.1	369.9	19.4	382.0	18.0
10	Euhedral. Fine oscillatory zoning throughout with minor homogeneous patches. Fractured.	10.1	414.9	9.1	415.6	9.3
		10.2	399.0	8.8	425.0	9.2
11	Subhedral (broken). Oscillatory to patchy zoned core with marginal convolute zoning. Narrow to wide, oscillatory zoned to homogeneous dark rim.	N/A				
12	Subhedral. Large core with irregular patchy zoning and homogeneous zones. Very narrow oscillatory zoned dark rim. Fractured.	N/A				

13	Subhedral. Oscillatory zoned core with resorbed boundaries, marginal homogeneous zones. Feint oscillatory zoned rim. Core and rim are approximately proportionate.	13.1	1314.3	45.0	1429.6	32.0
		13.2	340.2	10.4	362.7	13.0
14	Anhedral. Complex oscillatory zoning throughout with resorption textures and poorly developed sector zoning.	14.1	429.0	10.3	434.2	10.3
		14.2	420.9	12.9	423.0	13.0
15	Subhedral. Very large complex core with an innermost homogeneous zone, feint to prominent oscillatory zoning and outermost patchy zoning. Very narrow dark rim. Fractured.	15.1	1093.3	22.5	1092.5	18.3
		15.2	1110.3	19.7	1116.3	15.8
16	Euhedral. Large core with complex oscillatory zoning. Wide to narrow rim with complex oscillatory zoning. Fractured.	16.1	1292.5	25.1	1339.6	19.2
		16.2	862.9	23.8	914.3	27.0
		16.3	486.4	16.8	493.1	18.2
17	Subhedral. Small patchy to broad oscillatory zoned core with resorbed boundaries. Wide rim with feint oscillatory zoning. Fractured.	17.1	335.9	8.2	370.2	8.5
18	Subhedral. Large core with complex oscillatory zoning, marginal homogeneous zone, and resorbed boundaries. Narrow rim with feint oscillatory zoning.	N/A				
19	Euhedral. Large heterogeneous core with patchy zoning and feint oscillatory zoning. Oscillatory zoned rim.	N/A				
20	Subhedral. Large semi-homogeneous core with marginal bright zones and resorbed boundaries. Narrow rim with feint oscillatory zoning. Fractured.	20.1	828.9	51.0	911.6	46.2
21	Subhedral (broken). Very small semi-homogeneous core with indistinct boundaries. Very wide rim with fine oscillatory zoning. Fractured.	21.1	387.7	9.0	401.8	9.4
		21.2	425.0	9.1	426.7	8.9
22	Subhedral. Small semi-homogeneous core. Wide rim with broad oscillatory zoning and sector zoning, radially fractured.	22.1	439.0	9.0	443.2	10.0
		22.2	416.3	9.9	416.9	10.2
23	Subhedral. Fine oscillatory zoning throughout, with some patchy to convolute zoning, sometimes approximately parallel to oscillatory zoning.	23.1	396.2	9.3	405.1	9.2
24	Subhedral. Very large core with complex, oscillatory zoning and minor convolute zoning. Very narrow dark rim.	24.1	1624.0	30.7	1631.6	21.9
25	Anhedral. Very large core, approximately 50 % is semi-homogeneous, 50 % comprises oscillatory zoning. Narrow dark rim with an inner bright convolute zone, sometimes cross-cutting the core.	25.1	1782.9	30.6	1787.5	20.4
		25.2	1427.1	27.1	1535.0	22.1

26	Subhedral. Large homogeneous core with marginal complex zoning. Very narrow dark rim.	26.1	1469.4	25.3	1466.8	19.5
27	Euhedral. Very large core with complex oscillatory zoning cross-cut by homogeneous zones. Narrow dark rim with feint zoning. Heavily fractured.	N/A				
28	Anhedral. Heterogeneous, with patchy oscillatory and convolute zoning.	N/A				
29	Subhedral. Very small core with oscillatory and patchy zoning, resorbed boundaries. Wide homogeneous rim with and outermost narrow dark zone. Fractured.	N/A				
30	Euhedral. Small core with patchy zoning. Narrow to wide rim with oscillatory zoning, radially fractured.	30.1	358.4	10.9	379.5	10.6
31	Subhedral. Small core with patchy zoning. Wide oscillatory zoned rim with minor homogeneous zones.	31.1	385.3	9.6	400.3	9.3
32	Subhedral (broken). Oscillatory to patchy zoned core. Wide to narrow rim with oscillatory zoning. Heavily fractured.	N/A				
33	Euhedral. Large core with convolute, patchy zoning. Narrow homogeneous rim. Heavily fractured,	N/A				
34	Euhedral. Very small homogeneous core. Wide rim with oscillatory and sector zoning.	34.1	407.4	8.9	410.6	8.9
35	Anhedral. Very large core with complex oscillatory zoning and a homogeneous centre. Very narrow dark homogeneous rim. Fractured.	N/A				
36	Anhedral. Patchy zoned core and an oscillatory zoned rim.	N/A				
37	Euhedral. Complex semi-homogeneous to homogeneous core with resorbed boundaries. Dark narrow rim with some oscillatory zoning. Fractured.	N/A				
38	Subhedral. Large core with patchy zoning and a marginal irregular bright zone, resorbed boundaries. Narrow semi-homogeneous to zoned rim. Heavily fractured.	N/A				
39	Anhedral (broken). Semi-homogeneous with a significant open fracture and multiple narrow annealed fractures.	N/A				
40	Subhedral. Very small semi-homogeneous core with partially resorbed boundaries. Very wide rim with complex oscillatory zoning,	40.1	335.9	7.3	358.5	8.7
41	Subhedral. Very large homogeneous to zoned core with significant bright convolute to patchy zones sometimes cross-cutting earlier zoning. Fractured.	41.1	1492.6	32.1	1495.8	22.8

42	Subhedral. Homogeneous to oscillatory zoned core with partially resorbed boundaries. Wide to moderate rim with feint, complex oscillatory zoning. Heavily fractured.	42.1	337.6	8.0	370.4	8.1
43	Anhedral. Large homogeneous to patchy zoned core and resorbed boundaries. Narrow to very narrow dark homogeneous rim.	N/A				
44	Subhedral. Small semi-homogeneous core. Wide to narrow rim with fine oscillatory zoning.	44.1	330.7	10.8	456.6	14.5
		44.2	392.7	9.2	393.8	9.3
45	Euhedral. Semi-homogeneous core with an oscillatory zoned rim. Core-rim boundary is indistinct.	45.1	365.2	8.0	375.1	8.7
		45.2	370.9	8.2	380.7	8.3
		45.3	339.4	8.0	356.8	8.6
46	Subhedral. Irregular patch zoning throughout.	N/A				
47	Anhedral. Very large semi-homogeneous core with some feint zoning and resorbed boundaries. Narrow dark rim with some feint zoning.	47.1	926.9	17.8	941.4	20.4
48	Euhedral. Very small homogeneous core with and inclusion. Very wide, complex oscillatory zoned rim.	48.1	378.0	12.2	387.3	11.2
		48.2	414.6	8.9	417.7	9.0
49	Anhedral. Very large heterogeneous core with some zoning. Dominantly very narrow rim with complex oscillatory zoning. Heavily fractured.	N/A				
50	Anhedral (broken). Very large core, homogeneous with a single bright zone approximately parallel to the grin edges. Very narrow dark rim with feint oscillatory zoning. Heavily fractured.	N/A				
51	Subhedral (broken). Small homogeneous core wit partially resorbed boundaries. Wide rim with complex oscillatory zoning.	51.1	417.2	8.8	418.0	8.7
		51.2	411.4	9.5	414.7	8.7
52	Subhedral. Very large core, heterogeneous with minor oscillatory zoning and a prominent bright convolute marginal zone, and resorbed boundaries. Narrow dark homogeneous rim. Core-rim boundaries is highly irregular.	52.1	992.4	19.0	992.2	18.8
53	Euhedral. Large heterogeneous core with minor oscillatory zoning and prominent bright convolute marginal zone. Wide dark rim with minor feint zoning. Heavily fractured.	53.1	875.7	24.2	940.0	19.9
54	Anhedral (broken). Large patchy to convolute zoned core. Narrow to very narrow rim with complex oscillatory zoning. Fractured.	N/A				
55	Subhedral. Oscillatory zoning throughout, with minor homogeneity. Fractured.	55.1	210.3	11.6	274.0	15.4

56	Subhedral (broken). Small, semi-homogeneous core with marginal oscillatory zoning and partially resorbed boundaries. Wide, heavily fractured rim with moderately well-developed complex oscillatory zoning.	56.1	304.8	6.6	523.5	16.8
57	Euhedral. Large core with oscillatory zoning, a bright, narrow marginal zone and resorbed boundaries. Narrow to moderate rim comprises oscillatory zoning.	57.1	1486.5	27.8	1494.2	19.4
		57.2	367.6	10.4	411.9	10.9
58	Subhedral. Large core with patchy zoning, a very narrow bright marginal zone and resorbed boundaries. Narrow rim with complex oscillatory zoning. Fractured.	58.1	461.5	14.7	529.0	16.3
59	Subhedral. Large core with patchy zoning, with narrow bright zones at the margins and cross-cutting the core. Narrow rim with oscillatory zoning. Fractured.	N/A				
60	Anhedral. Very large core with patchy zoning and minor oscillatory zoning. Narrow discontinuous dark rim with oscillatory zoning.	N/A				
61	Subhedral. Very small semi-homogeneous core. Very wide rim with oscillatory zoning and minor homogeneous patches. Fractured.	61.1	396.7	9.2	406.8	9.2
		61.2	425.6	9.4	427.8	9.1
62	Subhedral. Small semi-homogeneous core. Wide rim with feint oscillatory zoning and minor homogeneous patches. Core-rim boundary is indistinct.	62.1	389.0	10.0	397.6	9.6
		62.2	385.8	10.3	408.9	9.6
63	Subhedral. Very large heterogeneous core with an inner semi-homogeneous zone, outer oscillatory zoning and a marginal narrow bright zone. Core boundaries are partially resorbed. Rim is very narrow and dark.	N/A				
64	Anhedral (broken). Small semi-homogeneous core with marginal oscillatory zoning and partially resorbed boundaries. Wide to narrow rim with poorly-developed broad oscillatory zoning.	64.1	1473.5	51.3	1585.5	34.1
65	Subhedral (broken). Complex oscillatory zoning throughout. Fractured.	65.1	406.9	8.9	424.3	9.8
66	Subhedral (broken). Large, semi-homogeneous, heavily fractured core. Narrow dark rim with feint oscillatory zoning.					
67	Anhedral (broken). Very small semi-homogeneous core. Very wide rim with complex oscillatory zoning.	67.1	425.1	10.8	425.1	10.7
		67.2	374.3	8.1	388.7	9.1
68	Euhedral. Large core with an inner semi-homogeneous zone with some approximately parallel bright zones, and outer oscillatory zoning with resorbed boundaries. Narrow to very narrow oscillatory zoned rim.	68.1	1439.8	33.8	1526.8	23.2
69	Anhedral (broken). Bright, patchy zoned core with irregular boundaries. Wide rim with moderately well-developed oscillatory zoning.	69.1	299.9	7.2	378.9	9.6

70	Subhedral. Partially resorbed, complex oscillatory zoned core. Wide to narrow rim with complex zoning.	70.1	474.4	10.3	475.7	10.9
71	Subhedral. Large core with inner patchy zoning, outer complex oscillatory zoning, and radial fracturing. Narrow dark rim with feint oscillatory zoning.	71.1	898.0	46.3	949.3	48.7
72	Subhedral. Small semi-homogeneous core with resorbed boundaries. Wide to narrow rim with broad, complex oscillatory zoning. Fractured.	72.1	966.8	47.2	1069.3	42.2
73	Subhedral. Very large heterogeneous core with an inner homogeneous zone, and outer oscillatory and patchy zoning. Narrow dark rim. Heavily fractured.	N/A				
74	Anhedral. Small core with patchy zoning. Narrow to very wide oscillatory zoned rim, radially fractured.	74.1	334.2	10.0	352.7	10.2
75	Anhedral (broken). Very large semi-homogeneous core with some patchy zoning and a very narrow marginal bright zone. Very narrow dark rim. Fractured.	75.1	1487.8	30.9	1514.5	27.9
76	Subhedral. Very large patchy zoned core. Very narrow dark rim with feint zoning.	N/A				
77	Subhedral. Partially resorbed core with patchy and oscillatory zoning. Narrow to moderate rim with broad zoning and an inner bright zone with irregular boundaries.	77.1	1535.9	26.7	1539.9	18.4
78	Subhedral. Very large heterogeneous core with patchy and broad oscillatory zoning, resorbed boundaries, and a marginal bright zone. Very narrow dark rim with minor zoning.	78.1	1620.3	31.5	1616.8	20.6
79	Subhedral. Small, irregular shaped patchy zoned core. Wide to narrow rim with fine to broad oscillatory zoning.	79.1	391.2	10.6	392.2	11.5
80	Euhedral. Large semi-homogeneous to patchy zoned core. Narrow oscillatory zoned rim.	80.1	750.0	55.6	809.8	56.6
81	Subhedral. Very small semi-homogeneous core. Very wide oscillatory and sector zoned rim with minor homogeneous patches.	81.1	370.5	11.6	381.2	10.3
		81.2	365.5	9.6	391.4	9.7
82	Anhedral. Very large bright core with parallel to patchy zoning and resorbed boundaries. Very narrow dark semi-homogeneous rim. Fractured.	82.1	405.2	36.7	464.4	37.9
83	Subhedral. Patchy zoned core. Wide to narrow rim with complex oscillatory zoning. Fractured.	83.1	936.7	21.3	992.2	21.1
		83.2	434.9	9.2	433.1	9.2
84	Subhedral. Very large heterogeneous core with patchy and oscillatory zoning, and a marginal narrow bright zone. Very narrow dark rim with feint complex oscillatory zoning.	84.1	1393.5	39.0	1476.7	27.3

85	Euhedral. Very large, partially resorbed, complex oscillatory zoned core with minor homogeneous zones and a discontinuous marginal bright zone. Narrow oscillatory zoned rim.	85.1	1459.3	25.0	1459.6	18.1
		85.2	1487.7	25.2	1489.9	18.0
		85.3	1335.9	27.7	1377.8	20.4
86	Subhedral. Small homogeneous core. Narrow to very wide heterogeneous rim with oscillatory and patchy zoning, and homogeneous zones. Heavily fractured.	N/A				
87	Subhedral. Very large oscillatory zoned, heavily fractured, core with marginal homogeneity. Narrow dark rim with poorly developed zoning.	87.1	1660.3	29.0	1675.4	19.8
88	Subhedral. Very large heterogeneous core, dominantly patchy zoned with some homogeneity and oscillatory zoning. Narrow heterogeneous and sometimes convolute rim. Heavily fractured.	88.1	471.8	9.1	467.4	10.5
89	Euhedral. Very large oscillatory zoned core with marginal bright zones. Narrow dark oscillatory zoned rim.	89.1	365.2	11.7	388.0	11.4
		89.2	292.4	9.1	349.0	8.8
90	Subhedral. Very small patchy zoned core. Very wide rim with oscillatory zoning. Grain margins are heavily fractured.	90.1	300.4	7.4	333.0	8.0
		90.2	312.5	7.6	348.9	8.6
91	Anhedral. Complex oscillatory zoning cross-cut by semi-homogeneous to convolute zonation. Heavily fractured.	N/A				

EM19/AB

Grain ID	Grain Shape and Texture	Spot ID and Location	Ages			
			$^{206}Pb/^{238}U$	2σ	$^{207}Pb/^{235}U$	2σ
01	Subhedral. Large heterogeneous core with poorly developed complex oscillatory zoning and resorbed boundaries. Narrow rim with complex oscillatory zoning and a cross-cutting homogeneous zone. Fractured.	N/A				
02	Subhedral. Large heterogeneous core with resorbed boundaries. Narrow rim with broad zoning.	02.1	673.2	21.0	689.6	19.8
04	Large core with inner feint oscillatory zoning, an outer homogeneous zone with minor patchy zoning, and resorbed boundaries. Narrow oscillatory zoned rim. Fractured, particularly radial fracturing in the rim.	04.1	965.4	37.8	1005.8	30.4

05	Subhedral. Very large complex oscillatory to patchy zoned cores. Very narrow dark rim. Fractures cross-cut the width of the grain.	N/A				
06	Euhedral. Large core with broad, feint oscillatory zoning and patchy zoning, a very narrow bright marginal zone, resorbed boundaries and fractures. Narrow dark, oscillatory zoned rim.	6.1	830.5	30.8	882.4	34.2
07	Subhedral. Very patchy and heterogeneous zoning with some oscillatory zoning.	N/A				
08	Anhedral (broken). Very small homogeneous core. Very wide to moderate rim with complex oscillatory zoning, inclusions, and a narrow discontinuous marginal bright zone. Fractured, core and innermost rim particularly affected.	08.1	1416.6	27.5	1437.1	20.2
09	Subhedral. Core with an inner semi-homogeneous zone, outer complex oscillatory zoning, a discontinuous bright marginal zone and resorbed boundaries.	N/A				
10	Subhedral. Very large, partially resorbed core with inner oscillatory zoning and an outer semi-homogeneous one with marginal oscillatory zoning. Narrow to very narrow heterogenous rim. Fractured.	10.1	1289.0	102.4	1324.6	103.0
		10.2	1666.8	35.2	1766.8	22.6
11	Anhedral. Very large heterogeneous core with oscillatory zoning. Very narrow, semi-continuous dark rim.	11.1	1746.7	37.7	1744.8	24.7
12	Subhedral. Very large oscillatory zoned core with marginal patchy zoning and resorbed boundaries. Very narrow dark rim with feint complex oscillatory zoning.	12.1	733.8	30.2	779.3	29.0
13	Subhedral. Small semi-homogeneous core with resorbed boundaries. Narrow to wide oscillatory zoned rim. Fractured, rim particularly affected.	13.1	1392.9	34.4	1488.2	23.5
		13.2	341.8	18.6	515.1	16.9
14	Anhedral. Heterogeneous patchy zoning with marginal poorly developed oscillatory zoning. Fractured.	N/A				
15	Euhedral. Smal heterogeneous core with resorbed boundaries. Very narrow to wide rim with complex oscillatory zoning.	15.1	422.6	10.4	476.0	18.6
16	Subhedral. Very large semi-homogeneous core with marginal convolute zoning. Very narrow, dark, oscillatory zoned rim. Fractured, core particularly affected.	N/A				
17	Euhedral. Large core with inner patchy zoning and outer oscillatory and sector zoning with radial fractures and resorbed boundaries. Narrow to moderate dark rim with complex oscillatory zoning.	17.1	401.2	9.6	412.3	10.0
18	Subhedral. Large core with complex patchy zoning and resorbed boundaries. Narrow to moderate rim with complex oscillatory to convolute zoning. Heavily fractured.	N/A				

19	Subhedral. Small homogeneous core with resorbed boundaries. Very wide rim with oscillatory zoning cross-cut by homogeneous to convolute zones. Fractured.	19.1	383.7	9.7	459.6	18.4
20	Subhedral. Very large partially resorbed core with complex, broad oscillatory zoning, heavily affected by open and some possible filled fractures. Very narrow complex zoned rim.	20.1	1046.3	28.5	1193.1	26.1
21	Anhedral (broken). Very large, complex patchy zoned core. Narrow oscillatory zoned rim cross cut by homogeneous zonation. Heavily fractured throughout.	N/A				
22	Anhedral. Very large semi-homogeneous core heavily affected by open and filled fractures. Very narrow dark rim with a semi-continuous bright zone.	N/A				
23	Euhedral. Heterogeneous core with some oscillatory zoning and partially resorbed boundaries. Narrow core with poorly developed oscillatory zoning cross-cut by minor homogeneous zones.	23.1	1392.2	29.2	1430.2	20.1
24	Subhedral. Very large complex oscillatory and sector zoned core, with marginal homogeneous zones with convolute boundaries and a possible lath-shaped inclusion, and cross-cut by a filled fracture. Very narrow dark rim with a discontinuous bright narrow zone.	24.1	1540.1	31.6	1514.7	24.6
25	Subhedral. Large core with broad zoning and resorbed boundaries. Complex oscillatory zoned rim with inclusions. Affected by open and some filled fractures.	N/A				
26	Euhedral. Large semi-homogeneous to patchy zoned core. Narrow to wide oscillatory zoned rom cross-cut by minor homogeneous zones. Heavily fractured.	N/A				
27	Subhedral (broken). Large semi-homogeneous core. Oscillatory zoned rim with minor homogeneous and convolute zoning. Fractured.	N/A				
28	Euhedral. Large complex oscillatory zoned core with resorbed boundaries. Very narrow to moderate complex oscillatory zoned rim.	N/A				
29	Large broad zoned core with resorbed boundaries, and inclusion and a bright cross-cutting marginal zone. Narrow, dark oscillatory zoned rim.	29.1	1364.1	28.5	1361.2	20.6
		29.2	422.1	10.3	425.6	10.2
30	Euhedral. Small patchy zoned core. Rim with well developed oscillatory zoning.	30.1	434.3	13.2	564.5	38.3
31	Subhedral. Large semi-homogeneous to patchy zoned core. Wide, dark, complex oscillatory zoned rim. Fractured, core particularly affected.	N/A				
32	Subhedral. Very large semi-homogeneous core. Narrow semi-homogeneous rim. Heavily fractured.	N/A				
33	Very large heterogeneous core with resorbed boundaries. Dark homogeneous rim.	N/A				

34	Subhedral. Large core with oscillatory zoning cross-cut by homogeneous zones, and resorbed boundaries. Narrow, dark oscillatory zoned rim.	34.1	700.3	24.0	734.0	24.6
		34.2	1017.7	20.8	1017.9	20.5
35	Anhedral. Dark homogeneous core. Oscillatory zoned to semi-homogeneous rim.	N/A				
36	Euhedral. Fine, prominent oscillatory zoning cross-cut by bright convolute zoning, sometimes approximately parallel to oscillatory zoning.	36.1	422.6	10.3	419.1	9.9
		36.2	400.9	10.4	428.8	14.5
37	Euhedral. Large heterogeneous core with resorbed boundaries. Narrow to wide rim with complex oscillatory zoning. Heavily fractured.	37.1	1746.8	36.4	1740.6	21.1
38	Euhedral. Large core with complex, feint oscillatory zoning. Narrow to wide rim oscillatory zoning. Heavily fractured, rim particularly affected.	38.1	729.3	39.3	844.1	40.9
40	Anhedral. Dark homogeneous core with resorbed boundaries. Narrow to wide broad zoned rim with radial fracturing.	40.1	1019.8	23.6	1023.9	17.7
41	Euhedral. Larger homogeneous core with marginal oscillatory zoning and resorbed boudaries. Narrow dark rim with oscillatory zoning.	41.1	416.1	9.1	406.9	12.7
42	Subhedral. Complex oscillatory zoned core with open and filled fractures, and partially resorbed boundaries. Narrow to wide heterogeneous rim.	N/A				
43	Subhedral (broken). Small, partially resorbed complex oscillatory zoned core with a marginal, very narrow bright zone. Narrow to very wide, dark, complex oscillatory zoned rim. Fractured.	43.1	1756.9	35.3	1750.2	22.1
44	Subhedral. Complex oscillatory zoning throughout, with minor homogeneous zones, and a marginal bright zone which cross-cuts oscillatory zoning. Heavily fractured.	N/A				
45	Anhedral (broken). Elongate patchy zoned core. Narrow to wide, dark homogeneous rim.	45.1	402.3	10.5	536.3	21.2
46	Subhedral. Oscillatory zoning throughout, with some marginal homogeneous zones which cross-cut oscillatory zoning. Fractured.	46.1	369.5	15.6	413.3	14.4
47	Subhedral. Small, patchy zoned core with open fractures. Narrow to very wide complex oscillatory zoned rim with minor homogeneous zones, contains some filled fractures.	47.1	361.8	10.5	442.0	11.1
48	Euhedral. Small, semi-homogeneous core. Narrow to wide complex oscillatory zoned rim with some homogeneous zones, minor convolute zoning and a possible inclusion.	N/A				
49	Subhedral. Semi-homogeneous core with some parallel zoning. Very narrow to wide heterogeneous rim. Heavily fractured.	N/A				
50		50.1	428.8	11.3	432.8	14.5

	Euhedral. Small, lighter complex oscillatory zoned core. Narrow to wide dark oscillatory zoned rim, affected by open fractures.	50.2	408.3	9.8	411.8	10.0
51	Euhedral. Large, partially resorbed, complex oscillatory zoned core with an inner homogeneous zone. Narrow, dark homogeneous rim with minor oscillatory zoning and an innermost bright zone with irregular boundaries.	N/A				
52	Subhedral. Very large semi-homogeneous core with a central bright zone oblique to grain edges, and resorbed boundaries. Narrow dark homogeneous rim with an innermost narrow bright zone.	52.1	477.0	12.3	477.6	12.1
53	Subhedral. Very large heterogeneous core with minor oscillatory zoning. Very narrow rim with minor oscillatory zoning.	53.1	1305.3	29.7	1394.1	22.5
54	Subhedral. Very large semi-homogeneous to patchy core cross-cut by open fractures. Narrow, dark homogeneous rim with a very narrow, discontinuous bright zone.	N/A				
55	Euhedral. Semi homogeneous core with an outer homogeneous zone, possible filled fractures and resorbed boundaries. Narrow to moderate heterogeneous rim. Heavily fractured.	55.1	1574.1	35.3	1617.3	21.7
56	Euhedral. Very large, semi-homogeneous core with resorbed boundaries, Narrow, dark complex oscillatory zoned rim with minor cross-cutting homogeneous zones.	56.1	421.6	9.1	416.7	11.6
57	Subhedral. Large, semi-homogeneous to homogeneous core. Narrow to wide broad oscillatory zoned rim. Fractured.	N/A				
58	Euhedral. Semi-homogeneous core. Narrow to moderate complex oscillatory zoned rim with minor homogeneous zones.	58.1	407.6	9.8	409.4	11.4
59	Anhedral (broken). Large, homogeneous to patchy zoned core with resorbed boundaries. Narrow complex oscillatory zoned rim.	N/A				
60	Subhedral. Large semi-homogeneous to complex oscillatory zoned core. Narrow complex oscillatory zoned rim with minor convolute zoning. Heavily fractured, rim and a limited region of the core are particularly affected.	60.1	982.1	22.4	984.9	28.3
		60.2	604.3	15.9	1293.7	28.2
61	Subhedral. Large semi-homogeneous to patchy zoned core with resorbed boundaries. Narrow to moderate rim with poorly developed oscillatory zoning and some patchy zoning. Heavily fractured.	N/A				
62	Subhedral. Large, partially resorbed complex oscillatory zoned core. Very narrow to wide complex oscillatory zoned rim. Fractured.	62.1	1413.2	39.8	1438.5	26.0
		62.2	470.2	14.8	510.6	16.2

63	Subhedral. Large core with homogeneous zones, complex oscillatory zoning, and possible inclusions. Narrow zoned rim with a possible large inclusion. Heavily fractured, fractures dominantly parallel.	N/A				
64	Subhedral. Large core with broad homogeneous zones. Narrow dark homogeneous rim. Heavily fractured.	64.1	1640.3	36.2	1620.4	31.3
65	Subhedral. Semi-homogeneous core, fractured. Narrow to wide complex oscillatory zoned rim.	65.1	271.1	8.0	384.2	9.7
66	Euhedral. Small, partially resorbed core with oscillatory zoning and minor homogeneous zones. Narrow to very wide complex oscillatory zoned rim, with inclusions and an innermost very narrow bright zone.	66.1	1460.4	27.8	1479.2	20.0
		66.2	418.9	16.4	425.2	19.5
67	Subhedral. Large semi-homogeneous core with resorbed boundaries, fractured. Narrow to wide, complex oscillatory zoned rim.	67.1	749.7	24.3	833.9	26.0
68	Subhedral. Complex zoning, each zone comprised of complex oscillatory zoning and inner zones have resorbed to partially resorbed boundaries. Heavily fractured.	N/A				
69	Subhedral. Semi-homogeneous to patchy zoning with inclusions and minor, marginal oscillatory zoning. Heavily fractured.	N/A				
70	Subhedral. Large core with inner sector zoning, outer oscillatory zoning and resorbed boundaries. Narrow, dark rim with feint broad zoning.	70.1	413.2	9.2	414.5	10.7
71	Anhedral. Heterogeneous with marginal broad oscillatory zoning.	N/A				
72	Euhedral. Semi-homogeneous core with resorbed boundaries. Wide complex oscillatory zoned rim with small inclusions, a discontinuous bright homogeneous zone with convolute boundaries which cross-cut oscillatory zoning, and a further cross cutting homogeneous zone.	N/A				
73	Anhedral (broken). Very large semi-homogeneous core with resorbed boundaries, heavily fractured by open fractures, and one filled fracture which is continuous with a bright marginal zone. Narrow, dark homogeneous rim.	N/A				
74	Subhedral. Moderately well-developed complex oscillatory zoning cross-cut by marginal semi-homogeneous zoning.	N/A				
75	Subhedral. Patchy zoned core with resorbed boundaries. Narrow to moderate complex oscillatory zoned rim. Heavily fractured.	N/A				
76	Euhedral. Complex zoned, elongate core with a marginal bright zone and resorbed boundaries. Narrow oscillatory zoned rim.	76.1	408.9	10.7	423.9	10.4

77	Euhedral. Semi-homogeneous core with feint oscillatory and sector zoning, a very narrow bright marginal zone, and resorbed boundaries. Very narrow, dark oscillatory zoned rim.	77.1	1634.2	31.4	1644.0	20.9
78	Subhedral. Very large heterogeneous core. Narrow rim with feint oscillatory zoning. Core-rim boundary is at times indistinct. Heavily fractured.	N/A				
79	Subhedral. Very small homogeneous core. Very wide, complex oscillatory zoned rim with minor homogeneous zones. Heavily fractured throughout, some are filled.	79.1	1649.4	31.2	1737.1	21.9
80	Euhedral. Homogeneous core with a bright, narrow, marginal zone and resorbed boundaries. Narrow, semi-homogeneous dark rim.	80.1	415.7	10.5	415.9	11.1
81	Anhedral (broken). Very large, patchy zoned core. Narrow rim with some poorly developed oscillatory zoning and some convolute boundaries cross-cutting the core.	N/A				
82	Subhedral. Patchy zoned core with a bright, narrow marginal zone and resorbed boundaries. Narrow to wide rim with fine oscillatory zoning, and some homogeneous to convolute zoning.	N/A				
83	Euhedral. Partially resorbed core with indistinct patchy zoning. Narrow to moderate rim with oscillatory zoning and an inclusion. Fractured.	N/A				
84	Subhedral. Very large, partially resorbed core with complex oscillatory zoning and a very narrow marginal bright zone. Narrow rim with complex oscillatory zoning.	84.1	1036.3	75.8	1151.2	81.1
		84.2	1160.9	108.0	1213.2	111.4
85	Euhedral. Semi-homogeneous to patchy zoned core, affected by dominantly parallel fractures and with resorbed boundaries. Narrow, dark rim with oscillatory zoning.	N/A				
86	Anhedral. Heterogeneous with minor feint oscillatory zoning and a discontinuous marginal bright zone.	N/A				
87	Euhedal. Large, patchy zoned core with resorbed boundaries. Narrow to wide rim with oscillatory zoning and radial fractures.	87.1	399.2	13.6	482.4	13.5
88	Anhedral. Semi-homogeneous core with resorbed boundaries. Very narrow to wide rim with complex oscillatory zoning.	88.1	418.2	10.0	430.2	10.0
89	Subhedral. Highly patchy core with resorbed boundaries, fractured. Very narrow to very wide rim with complex oscillatory zoning.	89.1	424.4	10.1	428.5	10.2
90	Anhedral. Heterogeneous core with broad oscillatory zoning. Narrow to moderate dark rim with feint zoning.	90.1	1617.7	34.1	1622.2	22.4
91	Euhedral. Heterogeneous core with minor, marginal bright convolute zoning. Narrow dark oscillatory zoned rim.	91.1	342.6	14.0	743.9	49.6

92	Subhedral. Very large oscillatory and sector zoned core. Semi-continuous, dark, homogeneous rim.	92.1	278.9	10.7	304.9	12.0
93	Subhedral. Partially resorbed core with semi-homogeneous zones and an inclusion. Narrow to very wide rim with complex oscillatory zoning. Fractures cross-cut the core and rim.	93.1	1013.2	20.4	1018.3	18.6
		93.2	583.2	28.5	694.5	31.9

Appendix D: U-Pb Zircon and Apatite Data

The full suite of U-Pb LA-ICP-MS data obtained for zircon and apatite samples is available at: https://doi.org/10.5525/gla.researchdata.1770

The dataset includes Pb/U, Pb/Th, Pb/Pb and U/Pb ratios and ages with 2 sigma propagated errors, approximated Th, U and Pb concentrations in ppm and Th/U ratios.

Data presented in Appendix D is as exported from Iolite v.4 software following data reduction and prior to common Pb correction as common Pb correction was applied at a later stage of data presentation (see chapter 3).

Appendix E: Trace Element Data and Ti-in-zircon Results

Mean trace element isotope concentrations (ppm) for samples CM22/LS-01 and CM22/RAS-01 and the Mt Dromedary reference material are presented below with 2σ absolute and 1σ percentage errors.

CM22/LS-01

Isotope	Trace Element Spot			
	TE_35.1	TE_67.1	TE_76.1	TE_79.1
Ti49_ppm_mean	4.98	2.68	17.32	4.12
Ti49_ppm_2SE(int)	1.30	0.90	1.67	0.70
% err	13%	17%	5%	8%
V51_ppm_mean	0.25	0.14	2.84	
V51_ppm_2SE(int)	0.14	0.10	0.40	
% err	27%	33%	7%	
Fe57_ppm_mean	5.38		81.77	
Fe57_ppm_2SE(int)	4.22		6.91	
% err	39%		4%	
Cu63_ppm_mean	0.34	0.22	2.05	0.10
Cu63_ppm_2SE(int)	0.32	0.12	0.42	0.07

% err	47%	27%	10%	36%
Zn66_ppm_mean		0.48	1.03	0.29
Zn66_ppm_2SE(int)		0.27	0.35	0.18
% err		28%	17%	31%
Sr88_ppm_mean	0.56	0.49	15.69	0.51
Sr88_ppm_2SE(int)	0.06	0.07	1.91	0.08
% err	6%	7%	6%	8%
Nb93_ppm_mean	3.42	2.25	3.35	2.29
Nb93_ppm_2SE(int)	0.30	0.24	0.25	0.17
% err	4%	5%	4%	4%
Ag109_ppm_mean	16.21	14.26	15.02	11.55
Ag109_ppm_2SE(int)	0.94	0.91	0.86	0.72
% err	3%	3%	3%	3%
Sn118_ppm_mean	0.23	0.26	0.25	0.11
Sn118_ppm_2SE(int)	0.14	0.10	0.09	0.05
% err	30%	19%	17%	25%
La139_ppm_mean	0.25	0.47	23.22	0.04
La139_ppm_2SE(int)	0.06	0.06	4.46	0.02
% err	12%	6%	10%	22%
Ce140_ppm_mean	56.89	27.56	191.09	39.08

Ce140_ppm_2SE(int)	1.56	2.35	19.29	2.49
% err	1%	4%	5%	3%
Pr141_ppm_mean	0.17	0.23	16.44	0.08
Pr141_ppm_2SE(int)	0.04	0.04	2.68	0.02
% err	12%	9%	8%	14%
Nd146_ppm_mean	1.41	1.29	80.55	1.09
Nd146_ppm_2SE(int)	0.33	0.25	11.87	0.14
% err	12%	10%	7%	7%
Sm147_ppm_mean	2.49	0.89	23.25	1.82
Sm147_ppm_2SE(int)	0.47	0.25	2.81	0.22
% err	9%	14%	6%	6%
Eu153_ppm_mean	1.03	0.44	11.14	0.73
Eu153_ppm_2SE(int)	0.16	0.07	1.75	0.07
% err	8%	8%	8%	5%
Gd157_ppm_mean	12.31	5.80	29.57	9.19
Gd157_ppm_2SE(int)	0.92	0.82	2.47	0.71
% err	4%	7%	4%	4%
Y89_ppm_mean	686.48	452.09	685.80	446.30
Y89_ppm_2SE(int)	37.47	49.10	28.82	29.62
% err	3%	5%	2%	3%

Tb159_ppm_mean	4.02	1.84	5.58	2.99
Tb159_ppm_2SE(int)	0.22	0.25	0.19	0.20
% err	3%	7%	2%	3%
Dy163_ppm_mean	51.86	25.95	55.97	35.89
Dy163_ppm_2SE(int)	2.59	3.19	1.91	2.41
% err	2%	6%	2%	3%
Ho165_ppm_mean	20.11	11.99	19.84	13.60
Ho165_ppm_2SE(int)	1.04	1.37	0.77	0.94
% err	3%	6%	2%	3%
Er166_ppm_mean	108.98	70.03	99.47	70.04
Er166_ppm_2SE(int)	6.63	8.40	5.55	4.72
% err	3%	6%	3%	3%
Tm169_ppm_mean	25.25	17.96	22.91	15.72
Tm169_ppm_2SE(int)	1.44	2.00	1.46	1.07
% err	3%	6%	3%	3%
Yb172_ppm_mean	263.15	206.21	236.23	153.94
Yb172_ppm_2SE(int)	15.91	21.75	15.04	10.64
% err	3%	5%	3%	3%
Lu175_ppm_mean	63.82	56.83	59.75	34.51
Lu175_ppm_2SE(int)	4.72	5.65	3.92	2.45

% err	4%	5%	3%	4%
Hf178_ppm_mean	9500.48	10182.28	9863.15	8932.80
Hf178_ppm_2SE(int)	303.51	397.63	430.04	293.15
% err	2%	2%	2%	2%
Ta181_ppm_mean	1.16	0.63	0.99	1.07
Ta181_ppm_2SE(int)	0.11	0.08	0.07	0.09
% err	5%	7%	3%	4%
W182_ppm_mean	14.40	3.16	19.19	0.12
W182_ppm_2SE(int)	1.32	0.33	2.29	0.03
% err	5%	5%	6%	14%

CM22/RAS-01

Isotope	**Trace Element Spot**							
	TE_09.1	**TE_13.1**	**TE_46.2**	**TE_47.1**	**TE_50.1**	**TE_60.1**	**TE_64.1**	**TE_76.1**
Ti49_ppm_mean	3.07	5.50	4.65	30.42	4.38	4.19	4.05	6.12
Ti49_ppm_2SE(int)	0.83	1.42	2.26	14.62	0.91	0.95	0.97	1.55
% err	14%	13%	24%	24%	10%	11%	12%	13%
V51_ppm_mean	0.10	0.17	0.25	2.43	0.92	0.12	1.06	

V51_ppm_2SE(int)	0.08	0.10	0.13	0.38	0.14	0.08	0.25	
% err	43%	29%	27%	8%	8%	32%	12%	
Fe57_ppm_mean	4.47	43.34		384.42	113.81		39.28	4.98
Fe57_ppm_2SE(int)	2.73	14.01		81.76	23.36		9.57	3.58
% err	31%	16%		11%	10%		12%	36%
Cu63_ppm_mean	0.12			3.57	0.25		0.75	
Cu63_ppm_2SE(int)	0.16			2.22	0.13		0.16	
% err	67%			31%	25%		11%	
Zn66_ppm_mean	0.41	0.57		0.63	1.45		0.46	
Zn66_ppm_2SE(int)	0.26	0.27		0.34	0.49		0.31	
% err	32%	24%		26%	17%		34%	
Sr88_ppm_mean	1.64	0.89	0.49	21.43	5.90	0.39	2.45	0.85
Sr88_ppm_2SE(int)	0.74	0.13	0.11	3.56	1.57	0.05	0.38	0.15
% err	22%	7%	11%	8%	13%	6%	8%	9%
Nb93_ppm_mean	2.17	5.86	3.79	3.20	2.24	3.68	2.97	3.09
Nb93_ppm_2SE(int)	0.16	0.30	0.26	0.20	0.15	0.31	0.20	0.27
% err	4%	3%	3%	3%	3%	4%	3%	4%
Ag109_ppm_mean	14.50	16.73	17.52	15.53	15.36	13.81	15.63	15.69
Ag109_ppm_2SE(int)	0.78	0.89	1.12	0.87	0.80	0.77	0.79	1.08
% err	3%	3%	3%	3%	3%	3%	3%	3%

Sn118_ppm_mean	0.21	0.41	0.37	0.18	0.25	0.20	0.21	0.13
Sn118_ppm_2SE(int)	0.06	0.10	0.15	0.09	0.07	0.08	0.09	0.09
% err	14%	13%	20%	24%	15%	19%	22%	33%
La139_ppm_mean	2.09	0.28		75.05	1.54	0.03	1.20	0.11
La139_ppm_2SE(int)	1.41	0.06		14.18	0.24	0.01	0.18	0.05
% err	34%	11%		9%	8%	26%	8%	20%
Ce140_ppm_mean	54.02	75.06	50.31	156.35	62.02	46.98	48.94	54.58
Ce140_ppm_2SE(int)	4.40	2.39	1.61	16.51	3.97	3.06	1.86	2.57
% err	4%	2%	2%	5%	3%	3%	2%	2%
Pr141_ppm_mean	0.85	0.39	0.08	11.15	2.20	0.08	1.30	0.18
Pr141_ppm_2SE(int)	0.36	0.07	0.03	1.59	0.42	0.02	0.20	0.04
% err	21%	9%	19%	7%	9%	11%	8%	10%
Nd146_ppm_mean	7.30	3.71	1.75	43.29	14.66	1.41	8.42	1.86
Nd146_ppm_2SE(int)	1.76	0.50	0.33	5.45	1.89	0.15	1.25	0.32
% err	12%	7%	9%	6%	6%	5%	7%	8%
Sm147_ppm_mean	7.97	4.62	2.43	15.33	12.67	2.60	7.19	2.57
Sm147_ppm_2SE(int)	0.56	0.51	0.42	1.42	1.39	0.33	0.67	0.54
% err	4%	6%	9%	5%	5%	6%	5%	11%
Eu153_ppm_mean	2.85	1.78	1.00	5.70	5.06	0.95	2.82	1.05
Eu153_ppm_2SE(int)	0.21	0.16	0.13	0.57	0.44	0.10	0.28	0.13

% err	4%	4%	6%	5%	4%	5%	5%	6%
Gd157_ppm_mean	32.41	20.90	13.96	31.46	38.04	13.45	21.04	13.73
Gd157_ppm_2SE(int)	1.60	0.91	1.03	2.13	1.83	0.90	1.08	0.85
% err	2%	2%	4%	3%	2%	3%	3%	3%
Y89_ppm_mean	1156.76	1080.93	764.08	956.68	1333.24	691.68	859.55	609.71
Y89_ppm_2SE(int)	46.04	23.38	26.05	20.77	56.89	40.83	23.55	14.17
% err	2%	1%	2%	1%	2%	3%	1%	1%
Tb159_ppm_mean	9.26	6.62	4.54	9.19	10.98	4.09	6.34	4.06
Tb159_ppm_2SE(int)	0.43	0.25	0.32	0.62	0.37	0.22	0.36	0.30
% err	2%	2%	4%	3%	2%	3%	3%	4%
Dy163_ppm_mean	102.37	83.71	57.30	95.78	119.22	52.83	75.74	49.21
Dy163_ppm_2SE(int)	4.36	2.33	1.73	4.49	4.87	2.89	2.80	2.49
% err	2%	1%	2%	2%	2%	3%	2%	3%
Ho165_ppm_mean	36.29	32.68	22.76	29.69	41.92	20.86	26.37	18.16
Ho165_ppm_2SE(int)	1.55	0.67	0.73	1.17	1.72	1.21	0.72	0.68
% err	2%	1%	2%	2%	2%	3%	1%	2%
Er166_ppm_mean	175.10	170.72	121.34	138.17	199.21	109.55	129.45	93.28
Er166_ppm_2SE(int)	7.12	3.82	3.71	3.97	9.05	6.35	3.51	3.98
% err	2%	1%	2%	1%	2%	3%	1%	2%
Tm169_ppm_mean	37.08	39.08	28.13	27.70	42.86	24.96	28.68	20.54

Tm169_ppm_2SE(int)	1.61	1.16	0.87	0.64	2.01	1.58	0.84	0.83
Yb172_ppm_mean	348.83	393.08	286.08	260.47	430.55	249.14	282.86	209.03
Yb172_ppm_2SE(int)	14.45	10.45	6.47	6.12	26.29	15.36	7.48	5.03
% err	2%	1%	1%	1%	3%	3%	1%	1%
Lu175_ppm_mean	75.13	88.69	64.56	57.73	104.48	56.48	67.94	45.05
Lu175_ppm_2SE(int)	3.05	2.92	1.96	1.97	7.74	3.47	1.99	1.41
% err	2%	2%	2%	2%	4%	3%	1%	2%
Hf178_ppm_mean	9482.61	9496.91	8917.78	9352.32	10447.57	9468.02	9968.72	9222.66
Hf178_ppm_2SE(int)	291.39	397.30	247.40	382.96	539.16	320.82	358.52	325.59
% err	2%	2%	1%	2%	3%	2%	2%	2%
Ta181_ppm_mean	1.01	2.25	1.69	1.15	0.84	1.51	1.23	1.44
Ta181_ppm_2SE(int)	0.07	0.15	0.17	0.06	0.07	0.12	0.10	0.09
% err	3%	3%	5%	3%	4%	4%	4%	3%
W182_ppm_mean	0.32	13.46	0.23	145.44	200.20		14.57	1.10
W182_ppm_2SE(int)	0.08	3.07	0.11	8.94	37.25		3.03	0.21
% err	12%	11%	23%	3%	9%		10%	10%

Ti-in-Zircon Temperature

Ti-in-zircon calculations as per Watson et al. (2006) are summarised below (i) for measured Ti concentration, presented in chapter 4 and (ii) maximum possible temperature accounting for analytical error and error induced by the equation of Watson et al. (2006). Final errors presented in chapter 4 are the difference between (i) and (ii) in degrees Celsius.

Trace element spot	**Ti (ppm)**	**Temperature for measured Ti concentration**				**Maximum possible temperature**				**Difference to calculated T in zircon (°C); Final 1 sigma error**
		Log (Ti ppm)	T (K)	T (°C)	1 sigma Ti error	Max amount (=T ((°C) + 1 sigma error)	Log max amount	T(K) max	T (°C) max	
LS01_TE_35.1	4.98	0.697	956.144	683.144	0.651	5.63	0.750	966.039	693.039	9.894
LS01_TE_67.1	2.68	0.428	910.109	637.109	0.448	3.13	0.495	921.618	648.618	11.509
LS01_TE_76.1	17.32	1.239	1064.682	791.682	0.836	18.16	1.259	1068.832	795.832	4.150
LS01_TE_79.1	4.12	0.615	941.664	668.664	0.349	4.47	0.651	948.150	675.150	6.486
RAS01_TE_09.1	3.07	0.487	919.855	646.855	0.415	3.49	0.542	929.497	656.497	9.642
RAS01_TE_13.2	5.50	0.741	964.063	691.063	0.708	6.21	0.793	973.920	700.920	9.856
RAS01_TE_46.2	4.65	0.667	950.783	677.783	1.131	5.78	0.762	968.104	695.104	17.321
RAS01_TE_47.1	30.42	1.483	1122.203	849.203	7.308	37.73	1.577	1144.889	871.889	22.686
RAS01_TE_50.1	4.38	0.642	946.262	673.262	0.457	4.84	0.685	954.175	681.175	7.913
RAS01_TE_60.1	4.19	0.622	942.847	669.847	0.477	4.67	0.669	951.385	678.385	8.538
RAS01_TE_64.1	4.05	0.608	940.349	667.349	0.485	4.54	0.657	949.262	676.262	8.913
RAS01_TE_76.1	6.12	0.786	972.513	699.513	0.775	6.89	0.838	982.361	709.361	9.849

Appendix F: CM22/LB-01 Apatite and Zircon Data Summary

CL Images and Laser Spot Locations

Cathodoluminescence images are presented here for grains which produced concordant ages, the full set of CL images for CM22/LB-01 are presented in Appendix B. Locations of concordant spots are outlined in light blue and discordant spots in black.

Grain 002

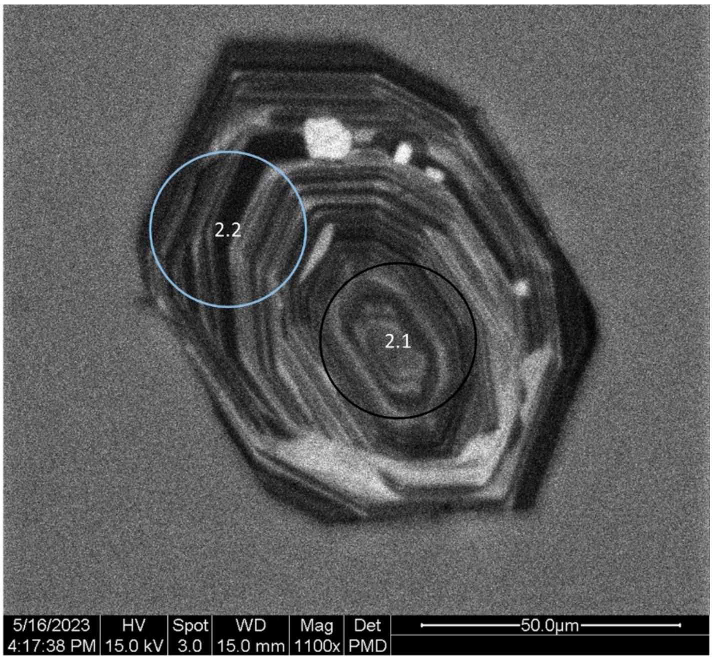

Grain 005

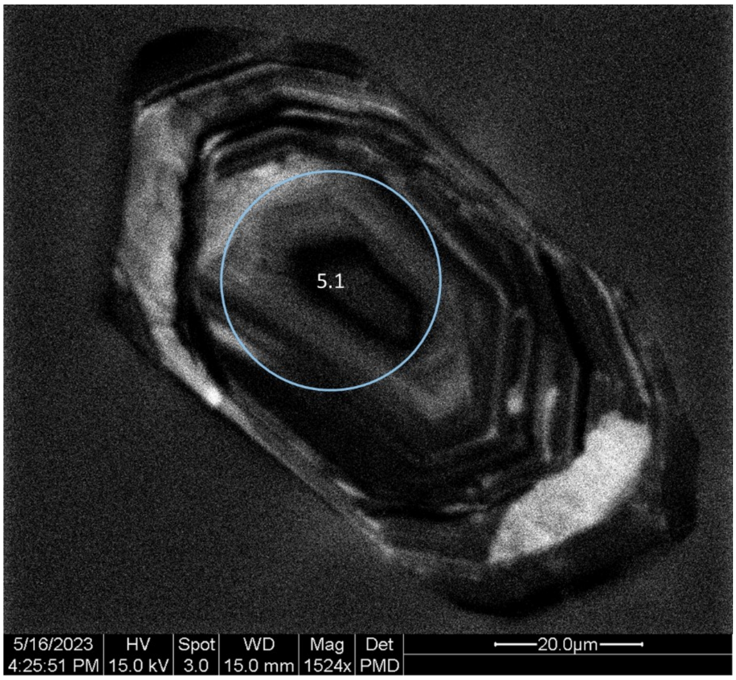

Zircon Textural Descriptions

Spots highlighted in light blue are concordant, those which are discordant or show evidence of Pb loss are left uncoloured. Core-rim boundaries are defined where there is a clear change in cathodoluminescence brightness and(or) zircon texture, or where significant cross cutting relationships are observed between regions of oscillatory zoning. Ages and errors presented are uncorrected for common Pb as common Pb correction was carried out at a later stage of data presentation.

It should be noted that the uncorrected age presented here for spot 02.2 was obtained by integrating only the final ~ 8 seconds of the ablation during data reduction, and may not correspond to the texture observed in CL. Not enough concordant data was obtained to determine if either concordant spot (2.2 or 5.1) is emplacement related or older. The full suite of LA-ICP-MS zircon data obtained for this sample is presented in Appendix D.

Grain ID	Grain Shape and Texture	Spot ID and Location	Ages			
			$^{206}Pb/^{238}U$	2σ	$^{207}Pb/^{235}U$	2σ
1	Subhedral (broken). Sector and oscillatory zoned with minor right homogeneous zones.	01.1	260.8	20.0	414.2	13.2
2	Euhedral. Complex oscillatory zoning with inclusions, and minor bright homogeneous zones with convolute boundaries.	02.1	411.2	9.7	450.0	12.2
		02.2 (final 8s)	420.2	12.8	421.2	13.4
3	Subhedral. Homogeneous core. Narrow oscillatory zoned rim. Heavily fractured.	N/A				
4	Anhedral. Very large core with complex oscillatory zoning. Very narrow to narrow homogeneous dark rim.	N/A				
5	Subhedral. Very large core with complex oscillatory zoning with cross-cutting bright	05.1	420.7	14.6	429.4	18.3

	homogeneous zones and partially resorbed boundaries. Dark, narrow homogeneous rim.					
6	Euhedral. Complex oscillatory zoning with minor cross-cutting homogeneous zones. Fractures spatially limited to the innermost zones.	N/A				
7	Subhedral. Large, patchy zoned core with resorbed boundaries. Narrow, light semi-homogeneous rim. Fractured.	N/A				
8	Subhedral. Complex oscillatory zoning with inclusions and cross-cutting homogeneous zones.	N/A				
9	Euhedral. Complex oscillatory zoning with marginal sector zoning and homogeneous zones.	09.1	387.2	12.8	400.3	16.0

Apatite Data and Discordia Age

CM22/LB-01 apatite data and discordia age (concordia lower intercept) are presented below on a Tera-Wasserburg concordia plot, followed by a summary of U-Pb data with spots included in the intercept age highlighted. The full suite of data obtained by LA-ICP-MS for CM22/LB-01 apatite is presented in Appendix D.

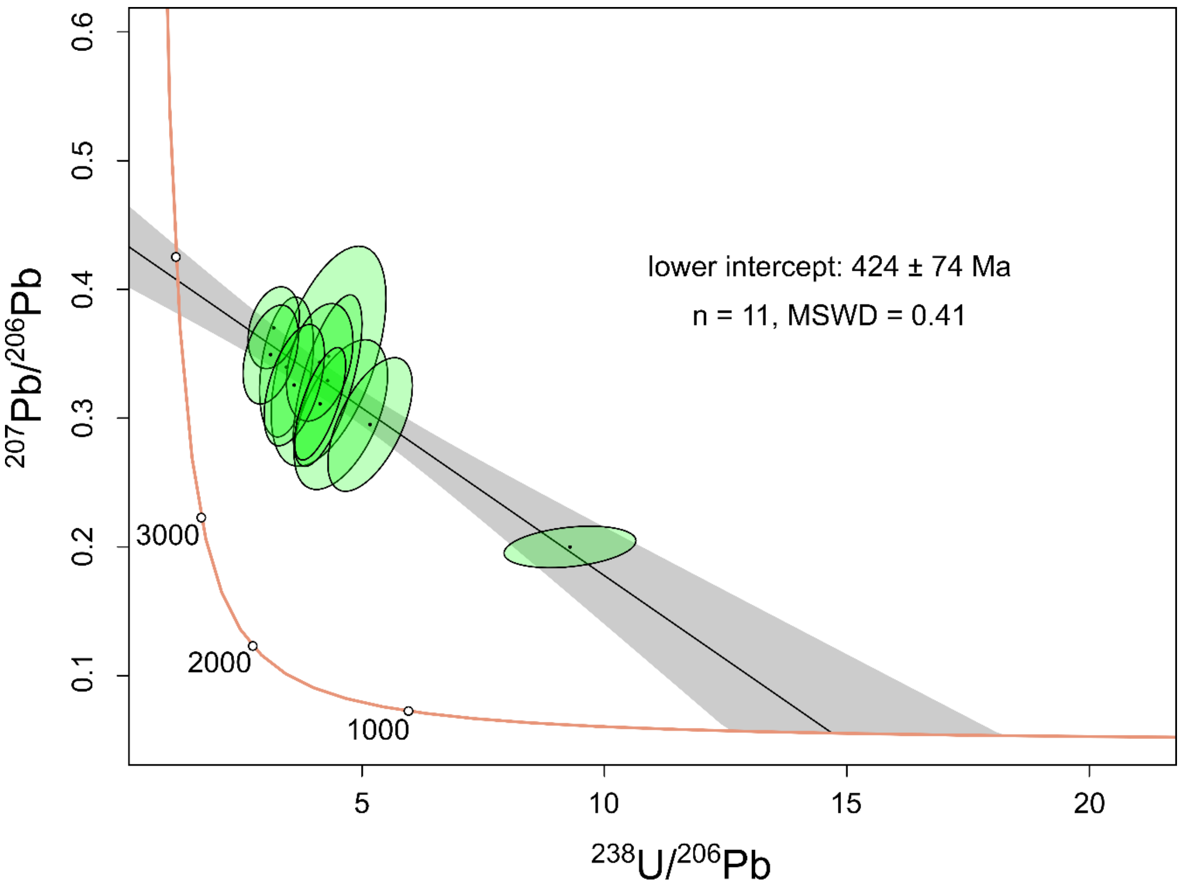

Laser Spot	$^{238}U/^{206}Pb$ (mean)	2σ error (propagated)	$^{207}Pb/^{206}Pb$ (mean)	2σ error (propagated)	Rho $^{238}U/^{206}Pb$ vs $^{207}Pb/^{206}Pb$
LB01_01	4.31170	0.95384	0.34807	0.06883	0.52475
LB01_02	-0.20107	0.72141	-0.06425	0.82781	0.24607
LB01_03	3.44353	0.44745	0.33974	0.04379	0.33295
LB01_04	0.18383	0.24764	0.36989	0.19837	0.16558
LB01_05	-0.05535	0.25264	0.55545	1.29042	-0.33927
LB01_06	0.06024	0.19016	0.34162	0.16588	0.39396
LB01_07	0.05404	0.12499	0.39148	0.20252	0.01207
LB01_08	4.56478	0.77553	0.30278	0.04685	0.52253
LB01_09	-0.03293	0.28155	0.08276	0.73065	0.01115

LB01_10	0.20027	0.89165	-0.14333	0.57425	0.14535
LB01_11	-0.10765	0.56100	-0.07650	0.61546	-0.14013
LB01_12	4.29232	0.56932	0.32915	0.05363	0.66018
LB01_13	5.16810	0.70238	0.29507	0.04178	0.58266
LB01_2_01	3.18001	0.42601	0.37024	0.02558	0.28703
LB01_2_02	4.12854	0.55225	0.34334	0.03676	0.35656
LB01_2_03	-0.37280	0.91356	0.07971	0.57796	0.46563
LB01_2_04	9.28959	1.09590	0.19996	0.01299	0.30099
LB01_2_05	3.11744	0.45971	0.34940	0.03093	0.38606
LB01_2_05_2	3.60364	0.50050	0.32569	0.03793	0.51302
LB01_2_06	-0.34359	0.71761	-0.06668	0.40485	0.20737
LB01_2_07	4.13712	0.42343	0.31117	0.03521	0.68541
LB01_2_08	4.13712	0.42343	0.31117	0.03521	0.68541

Appendix G: Literature Whole Rock Data

The table below (with legend) presents the whole rock data retrieved from existing literature to determine alumina saturation of Caledonian intrusions. Data from Matthews et al. (2023) was already presented on the figure adapted to create Fig. 5.6 and is included here for completeness. Samples with an aluminium saturation index of approximately or greater than 1 are highlighted in bold.

Values presented in Fig. 5.6 were determined using the following equations:

Aluminium saturation index = $(Al_2O_3/101.9613)/(((CaO/56.0774)-3.33*(P_2O_5/141.9445))+(Na_2O/61.9789)+(K_2O/94.196))$

CaO normalised to CaO + N_2O + K_2O = $((CaO/56.0774)-3.33*(P_2O_5/141.9445))/((CaO/56.0774)-3.33*(P_2O_5/141.9445)+(Na_2O/61.9789)+(K_2O/94.196))$

Legend:

(green)	Appinites, diorites
(light blue)	Alkaline Granitoids
(orange)	Sub alkaline Granitoids
(red)	Late Biotite Granite - Granodiorite

Intrusion	Sample Number	Sample Type (As described in data source)	Data Source	Whole Rock Chemistry (wt%)						Ratios	
				SiO_2	Al_2O_3	CaO	Na_2O	K_2O	P_2O5	**ASI**	**C/CNK**
Loch Loyal	BL1	Syenite	Fowler et al. 2008	63.6	13.1	2.83	6.32	5.29	0.44	0.647995	0.202466
	BL4	Syenite	Fowler et al. 2008	62.75	15.45	2.03	6.41	5.99	0.24	0.76691	0.154718
	BL9	Syenite	Fowler et al. 2008	64.55	16.59	1.91	6.13	5.86	0.31	0.86592	0.14256
	BLSE	Syenite	Fowler et al. 2008	65.04	15.13	0.96	6.95	6.38	0.17	0.76887	0.068037
	MS390	Leucosyenite	Thompson and Fowler 1986	63.76	16.6	2.03	6.04	5.35	0.35	0.893375	0.153585
Glenelg-Ratagain	MS405	Syenite	Thompson and Fowler 1986	61.49	17.13	2.65	6.62	4.79	0.35	0.854087	0.198494
	SRR652	Syenite	Fowler et al. 2008	61.85	17.61	2.27	6.38	5.08	0.28	0.9053	0.17775
	MS434	Granite	Fowler et al. 2008	69.05	15.2	1.31	5.36	4.76	0.22	0.96046	0.117254
	DRR206	Diorite - Monzodiorite	Fowler et al. 2008	50.3	7.53	11.13	1.81	1.72	0.4	0.312196	0.799356
	DRR207	Diorite - Monzodiorite	Fowler et al. 2008	45.28	16.97	6.86	3.48	3.54	1.65	0.938451	0.471505
	DRR213	Diorite - Monzodiorite	Fowler et al. 2008	50.42	11.77	7.63	3.02	3.42	0.8	0.57054	0.579723
Loch Borralan	**27639**	**Quartz syenite**	**Thirlwall and Burnard 1990**	**71.01**	**16.35**	**0.51**	**6.71**	**3.41**	**0.02**	**1.047461**	**0.056342**
	3/6	Mafic syenite	Thirlwall and Burnard 1990	54.23	20.19	4.23	6.6	9.33	0.1	0.710698	0.26231
	3/7	Mafic syenite	Thirlwall and Burnard 1990	49.99	16.67	10.36	1.31	8.57	0.27	0.562747	0.614092
	37563	**Quartz syenite**	**Thirlwall and Burnard 1990**	**68.1**	**18.54**	**0.13**	**7.57**	**5.11**	**0.02**	**1.020185**	**0.010374**
	932	Appinite	Thirlwall and Burnard 1990	46.48	13.16	12.53	3.79	1.17	0.97	0.470614	0.731744
Glen Dessarry	GD27	Melasyenite	Fowler 1992	56.7	15.36	5.14	3.71	5.81	0.62	0.758335	0.388184
	GD28	Melasyenite	Fowler 1992	57.24	15.34	4.77	3.05	7.28	0.56	0.758238	0.362482
	GD44	Melasyenite	Fowler 1992	52.6	14.81	5.58	4.02	4.81	0.91	0.748404	0.402701

	MJ001	Leucosyenite	Fowler 1992	59.8	17.63	2.93	4.59	6.65	0.36	0.917489	0.232431
	MJ005	Leucosyenite	Fowler 1992	61.14	17.68	2.7	5.85	6.27	0.25	0.853203	0.208051
	MJ006	Leucosyenite	Fowler 1992	61.99	18.35	2.05	5.88	6.4	0.2	0.924446	0.163678
Cluanie	CL1	Appinite/diorite	Fowler et al. 2008	50.92	11.17	8.59	2.03	2.67	0.64	0.549777	0.693382
	CL4	Porphyritic granite	Fowler et al. 2008	69.12	16.03	2.55	6.07	2.68	0.09	0.926169	0.255444
	Cl6	Porphyritic granite	Fowler et al. 2008	67.86	16.08	2.01	4.82	4.75	0.07	0.971124	0.210603
	CL9	Porphyritic granite	Fowler et al. 2008	70.61	15.92	1.73	5.98	3.13	0.02	0.975287	0.18977
Strath Halladale	**SHG 90B**	**Granite**	**Fowler et al. 2008**	**71.28**	**16.16**	**2.52**	**5.45**	**1.68**	**0**	**1.051659**	**0.298182**
	SHG 97	Granite	Fowler et al. 2008	73.05	15.2	1.76	5.07	3.29	0	1.006493	0.211898
	SHG C	**Granodiorite**	**Fowler et al. 2008**	**69.69**	**16.27**	**1.98**	**4.17**	**3.3**	**0**	**1.159477**	**0.256559**
	SHG 132	**Granodiorite**	**Fowler et al. 2008**	**71**	**14.96**	**1.85**	**5.12**	**3.09**	**0**	**0.988676**	**0.222301**
	SHG 65	Ultramafic	Fowler et al. 2008	49	7.69	12.77	1.32	1.47	0.63	0.301871	0.852295
	SHG 450	Ultramafic	Fowler et al. 2008	49.8	3.91	14.1	0.54	0.63	0.63	0.152138	0.9389
	SHG 403	Diorite - enclave	Fowler et al. 2008	54.77	19.28	5.19	5.18	2.93	0.44	0.960291	0.417592
	RD1	Diorite - Reay Diorite	Fowler et al. 2008	46.19	20.22	7.08	3.88	2.94	0.99	1.007459	0.523408
Helmsdale	**iHG317**	**Quartz monzoite - biotite bearing**	**Fowler et al. 2008**	**72.37**	**14.89**	**1.14**	**4.92**	**4.5**	**0.01**	**0.991761**	**0.136466**
	iHG837	**Quartz monzoite - biotite bearing**	**Fowler et al. 2008**	**72.3**	**15.08**	**0.65**	**4.88**	**4.83**	**0.01**	**1.046193**	**0.080332**
	oHG159	Granodiorite - porphyritic	Fowler et al. 2008	70.05	14.16	2.24	4.25	4.63	0.08	0.891418	0.244351
	oHG810	Granodiorite - porphyritic	Fowler et al. 2008	73.36	13.99	1.26	4.51	4.57	0.01	0.956047	0.154925
	HG159As	Appinite/diorite	Fowler et al. 2008	54.12	13.01	7.41	2.46	6.82	0.35	0.540619	0.525071
Ach'Uaine	CCB2	Monzogabbro/monzo diorite	Fowler and Henney 1996	48.56	12.24	10.75	2.98	4.16	2.93	0.557817	0.571368
	LYD1	Monzogabbro/monzo diorite	Fowler and Henney 1996	46.62	10.98	10.9	2.98	4.16	2.93	0.494251	0.576631
Rogart	**RG1**	**Biotite Granite**	**Fowler et al. 2001**	**67.16**	**14.89**	**2.48**	**5.15**	**2.63**	**0.26**	**0.979197**	**0.255635**
	RHG1	Biotite Granite	Fowler et al. 2001	69.24	14.7	1.96	5	3.89	0.15	0.939832	0.204904
	R5	**Biotite Granite**	**Fowler et al. 2001**	**73.2**	**14.64**	**1.98**	**5.25**	**2.29**	**0.009**	**0.996318**	**0.243537**

	RG2	Granodiorite	Fowler et al. 2001	65.63	15.05	3.06	4.96	3.27	0.29	0.908304	0.293922
	RHG2	Granodiorite	Fowler et al. 2001	67.04	15.3	3.06	4.89	3.23	0.27	0.929598	0.298804
	RT1	Tonalite/Quartz Monzodiorite	Fowler et al. 2001	62.98	15.4	4.09	4.88	3.29	0.36	0.847798	0.361989
	R1	Tonalite/Quartz Monzodiorite	Fowler et al. 2001	66.68	14.88	3.24	4.83	2.43	0.29	0.943354	0.3295
	R2	Tonalite/Quartz Monzodiorite	Fowler et al. 2001	71.2	14.02	2.56	5.13	2.15	0.16	0.932272	0.284066
	R3A(H)	**Tonalite/Quartz Monzodiorite**	**Fowler et al. 2001**	**71.73**	**15.83**	**1.9**	**5.18**	**3.01**	**0.11**	**1.05736**	**0.213176**
	R3A(P)	**Tonalite/Quartz Monzodiorite**	**Fowler et al. 2001**	**72.69**	**14.96**	**1.05**	**4.25**	**5.11**	**0.04**	**1.0435**	**0.126493**
	RA1	Appinite	Fowler et al. 2001	47.57	12.41	9.22	3.41	2.69	1.42	0.566953	0.610692
	PJH215	Appinite	Fowler et al. 2001	48.92	9.67	9.2	1.78	2.61	0.72	0.465825	0.722844
	PJH192	Appinite	Fowler et al. 2001	48.97	9.77	10.12	2.12	4.12	1.06	0.410295	0.666253
	LPR	Appinite	Fowler et al. 2001	49.05	11.56	9.11	2.87	3.68	1.06	0.508505	0.61709
	PJH213	Appinite	Fowler et al. 2001	49.22	11.86	8.35	3.14	4.54	1.44	0.543599	0.537993
	PJH196	Appinite	Fowler et al. 2001	49.76	9.54	9.83	2.49	2.97	0.65	0.403733	0.690593
	PJH191	Appinite	Fowler et al. 2001	50.92	14.17	7.28	4.27	4.14	1.11	0.641542	0.479076
	PJH194	Appinite	Fowler et al. 2001	55.02	10.1	7.97	2.63	3.59	0.55	0.472223	0.616024
	RA2	Appinite	Fowler et al. 2001	57.2	10.03	9.7	2.96	1.1	0.36	0.439222	0.73462
Strontian - Sunart	SR1	Granodiorite - hornblende and biotite bearing	Fowler et al. 2008	62.81	15.46	3.65	4.33	3.74	0.23	0.895819	0.35267
	SR2	Appinite	Fowler et al. 2008	48.34	12.89	8.17	2.57	2.65	0.68	0.634204	0.65085
	SR3	Granodiorite - hornblende and biotite bearing	Fowler et al. 2008	63.23	15.9	3.77	4.78	2.79	0.26	0.928936	0.364142
	SR4	Granodiorite - hornblende and biotite bearing	Fowler et al. 2008	63.83	15.94	4.2	4.68	2.57	0.23	0.907368	0.403385
	SG18MB01	Quartz Monzodiorite	Matthews et al 2023	60.53	17.07	4.75	4.99	1.93	0.32	0.939499	0.433211

	SG18MB02	Quartz Monzodiorite	Matthews et al 2023	64.12	15.9	3.93	4.42	2.14	0.26	0.986876	0.404911
	SG18MB05	Quartz Monzodiorite	Matthews et al 2023	62.36	16.58	4	4.56	2.2	0.28	1.005693	0.400527
	SG18MB03	Quartz Monzodiorite	Matthews et al 2023	61.52	16.42	3.73	4.67	2.84	0.34	0.981739	0.356864
	SG18MB04	Quartz Monzodiorite	Matthews et al 2023	61.91	16.36	3.86	4.61	3.07	0.34	0.956052	0.362614
	SG18MB10	Quartz Monzodiorite	Matthews et al 2023	64.64	15.59	3.41	4.46	3.29	0.29	0.950331	0.335661
	SG18MB19	Quartz Monzodiorite	Matthews et al 2023	61.63	16.26	3.88	4.64	3.26	0.31	0.930462	0.361266
	SG18MB15	Quartz Monzodiorite Dyke	Matthews et al 2023	61.47	15.44	4.46	4.21	2.57	0.3	0.902955	0.432277
Strontian - Mafic Enclaves	SG18MB06	Mafic Enclave	Matthews et al 2023	48.09	11.74	8.84	2.05	2.24	0.41	0.562005	0.722487
	SG18MB07	Mafic Enclave	Matthews et al 2023	51.24	14.75	7	3.08	2.73	0.44	0.748843	0.592733
	SG18MB08	Mafic Enclave	Matthews et al 2023	52.53	15.08	6.98	3.35	2.45	0.46	0.763392	0.586763
	SG18MB20	Mafic Enclave	Matthews et al 2023	55.25	16.98	5.6	5.26	1.99	0.4	0.847622	0.460514
	SG18MB21	Mafic Enclave	Matthews et al 2023	54.62	11.88	5.81	2.53	3.3	0.7	0.714646	0.53475
	SG18MB16	Mafic Enclave - shoshonite	Matthews et al 2023	51.06	11.62	7.32	2.5	4.29	1.1	0.597903	0.549443
Strontian - Sanda Facies	SG18MB12	Granodiorite	Matthews et al 2023	71.44	14.67	1.69	4.3	3.43	0.1	1.077071	0.208043
	SG18MB13	Granodiorite	Matthews et al 2023	71.57	14.12	1.77	3.77	4.08	0.13	1.043942	0.214947
	SG18MB14	Granodiorite	Matthews et al 2023	71.51	14.76	1.5	4.26	3.77	0.1	1.087129	0.183261
	SG18MB17	Granodiorite	Matthews et al 2023	72.11	14.68	1.16	4.4	3.54	0.09	1.132356	0.146085
	SG18MB18	Granodiorite	Matthews et al 2023	71.58	14.94	1.12	4.37	3.65	0.1	1.154811	0.138918

References

Allen, C.M. and Campbell, I.H. 2012. Identification and elimination of a matrix-induced systematic error in LA–ICP–MS 206Pb/238U dating of zircon. *Chemical Geology*, **332–333**, 157–165, https://doi.org/10.1016/j.chemgeo.2012.09.038.

Allen, M.B., Kheirkhah, M., Neill, I., Emami, M.H. and Mcleod, C.L. 2013. Generation of Arc and Within-plate Chemical Signatures in Collision Zone Magmatism: Quaternary Lavas from Kurdistan Province, Iran. *Journal of Petrology*, **54**, 887–911, https://doi.org/10.1093/petrology/egs090.

Alonso-Perez, R., Müntener, O. and Ulmer, P. 2009. Igneous garnet and amphibole fractionation in the roots of island arcs: experimental constraints on andesitic liquids. *Contributions to Mineralogy and Petrology*, **157**, 541–558, https://doi.org/10.1007/s00410-008-0351-8.

Annen, C., Blundy, J.D. and Sparks, R.S.J. 2006. The Genesis of Intermediate and Silicic Magmas in Deep Crustal Hot Zones. *Journal of Petrology*, **47**, 505–539, https://doi.org/10.1093/petrology/egi084.

Ansberque, C., Mark, C., Caulfield, J.T. and Chew, D.M. 2019. Combined in-situ determination of halogen (F, Cl) content in igneous and detrital apatite by SEM-EDS and LA-Q-ICPMS: A potential new provenance tool. *Chemical Geology*, **524**, 406–420, https://doi.org/10.1016/j.chemgeo.2019.07.012.

Apen, F.E., Gaynor, S.P., Schoene, B. and Cottle, J.M. 2024. Evaluating reference materials and common-Pb corrections for high-resolution apatite UPb geochronology. *Chemical Geology*, **661**, 122191, https://doi.org/10.1016/j.chemgeo.2024.122191.

Appleby, S.K., Graham, C.M., Gillespie, M.R., Hinton, R.W., Oliver, G.J.H., and Eimf. 2008. A cryptic record of magma mixing in diorites revealed by high-precision SIMS oxygen isotope analysis of zircons. *Earth and Planetary Science Letters*, **269**, 105–117, https://doi.org/10.1016/j.epsl.2008.02.006.

Archibald, D.B. and Murphy, J.B. 2021. A slab failure origin for the Donegal composite batholith, Ireland as indicated by trace-element geochemistry. *Geological Society, London, Special Publications*, **503**, 347–370, https://doi.org/10.1144/SP503-2020-6.

Archibald, D.B., Macquarrie, L.M.G., et al. 2021. The construction of the Donegal composite batholith, Irish Caledonides: Temporal constraints from U-Pb dating of zircon and titanite. *GSA Bulletin*, **133**, 2335–2354, https://doi.org/10.1130/B35856.1.

Archibald, D.B., Murphy, J.B., Fowler, M., Strachan, R.A. and Hildebrand, R.S. 2022. Testing petrogenetic models for contemporaneous mafic and felsic to intermediate magmatism within the 'Newer Granite' suite of the Scottish and Irish Caledonides. *In*: *New Developments in the Appalachian-Caledonian_Variscan Orogen*. Special Paper**554**.

Armitage, T.B., Watts, L.M., Holdsworth, R.E. and Strachan, R.A. 2021. Late Carboniferous dextral transpressional reactivation of the crustal-scale Walls Boundary Fault, Shetland: the role of pre-existing structures and lithological heterogeneities. *Journal of the Geological Society*, **178**, jgs2020-078, https://doi.org/10.1144/jgs2020-078.

Armitage, T.B., Holdsworth, R.E., Strachan, R.A., Dempsey, E.D., Walker, R.J., Alvarez-Ruiz, D.T. and Lloyd, G.E. 2024. Overprinting orogenic events, ductile extrusion and strain partitioning during Caledonian transpression, NW Mainland Shetland. *Journal of Structural Geology*, **180**, 105088, https://doi.org/10.1016/j.jsg.2024.105088.

Artemieva, I.M. and Shulgin, A. 2019. Geodynamics of Anatolia: Lithosphere Thermal Structure and Thickness. *Tectonics*, **38**, 4465–4487, https://doi.org/10.1029/2019TC005594.

Ashley, K.T., Thigpen, J.R. and Law, R.D. 2015. Prograde evolution of the Scottish Caledonides and tectonic implications. *Lithos*, **224–225**, 160–178, https://doi.org/10.1016/j.lithos.2015.03.011.

Ashworth, J.R. and Tyler, I.M. 1983. The distribution of metamorphic temperatures around the Strontian Granodiorite. *Geological Magazine*, **120**, 281–290, https://doi.org/10.1017/S0016756800025462.

Atherton, M.P. and Ghani, A.A. 2002. Slab breakoff: a model for Caledonian, Late Granite syn-collisional magmatism in the orthotectonic (metamorphic) zone of Scotland and Donegal, Ireland. *Lithos*, **62**, 65–85, https://doi.org/10.1016/S0024-4937(02)00111-1.

Badenszki, E., Daly, J.S., Whitehouse, M.J., Kronz, A., Upton, B.G.J. and Horstwood, M.S.A. 2019. Age and Origin of Deep Crustal Meta-igneous Xenoliths from the Scottish Midland Valley: Vestiges of an Early Palaeozoic Arc and 'Newer Granite' Magmatism. *Journal of Petrology*, **60**, 1543–1574, https://doi.org/10.1093/petrology/egz039.

Bardelli, L., Lucci, F., et al. 2023. The rise and fate of a long-lived deep crustal 'hot zone' beneath the neogene-quaternary Cordillera de San Buenaventura in the Southern Puna Plateau (NW Argentina). *International Geology Review*, **65**, 2447–2478, https://doi.org/10.1080/00206814.2022.2145511.

Barnes, C.J., Majka, J., Callegari, R., Walczak, K., Ziemniak, G. and Bukała, M. 2023. Ordovician–Silurian deformation of the Neoproterozoic upper gneiss unit in the northern Seve Nappe Complex: implications for subduction of the Baltican margin. *Journal of the Geological Society*, **180**, jgs2022-161, https://doi.org/10.1144/jgs2022-161.

Barr, D., Roberts, A.M., Highton, A.J., Parson, L.M. and Harrisg, A.L. 1985. Structural setting and geochronological significance of the West Highland Granitic Gneiss, a deformed early granite within Proterozoic, Moine rocks of NW Scotland. *Journal of the Geological Society*, **142**, 663–675, https://doi.org/10.1144/gsjgs.142.4.0663.

Barth, A.P. and Wooden, J.L. 2010. Coupled elemental and isotopic analyses of polygenetic zircons from granitic rocks by ion microprobe, with implications for melt evolution and the sources of granitic magmas. *Chemical Geology*, **277**, 149–159, https://doi.org/10.1016/j.chemgeo.2010.07.017.

Baxter, E.F., Ague, J.J. and Depaolo, D.J. 2002. Prograde temperature–time evolution in the Barrovian type–locality constrained by Sm/Nd garnet ages from Glen Clova, Scotland. *Journal of the Geological Society*, **159**, 71–82, https://doi.org/10.1144/0016-76901013.

Beall, A.P., Moresi, L. and Stern, T. 2017. Dripping or delamination? A range of mechanisms for removing the lower crust or lithosphere. *Geophysical Journal International*, **210**, 671–692, https://doi.org/10.1093/gji/ggx202.

Beckers, K.F. and Johnston, H.E. 2022. Techno-Economic Performance of Eavor-Loop 2.0. *In*: *Proceedings 47th Workshop on Geothermal Reservoir Engineering*.

Bird, A., Cutts, K., Strachan, R., Thirlwall, M.F. and Hand, M. 2018. First evidence of Renlandian (c. 950–940 Ma) orogeny in mainland Scotland: Implications for the status of the Moine Supergroup and circum-North Atlantic correlations. *Precambrian Research*, **305**, 283–294, https://doi.org/10.1016/j.precamres.2017.12.019.

Bird, A., Thirlwall, M., Strachan, R.A., Millar, I.L., Dempsey, E.D. and Hardman, K. 2023. Eclogites and basement terrane tectonics in the northern arm of the Grenville orogen, NW Scotland. *Geoscience Frontiers*, **14**, 101668, https://doi.org/10.1016/j.gsf.2023.101668.

Bird, A.F., Thirlwall, M.F., Strachan, R.A. and Manning, C.J. 2013. Lu-Hf and Sm-Nd dating of metamorphic garnet: evidence for multiple accretion events during the Caledonian orogeny in Scotland. *Journal of the Geological Society*, **170**, 301–317, https://doi.org/10.1144/jgs2012-083.

Black, L.P., Kamo, S.L., et al. 2004. Improved 206Pb/238U microprobe geochronology by the monitoring of a trace-element-related matrix effect; SHRIMP, ID–TIMS, ELA–ICP–MS and oxygen isotope documentation for a series of zircon standards. *Chemical Geology*, **205**, 115–140, https://doi.org/10.1016/j.chemgeo.2004.01.003.

Bottrill, A.D., van Hunen, J., Cuthbert, S.J., Brueckner, H.K. and Allen, M.B. 2014. Plate rotation during continental collision and its relationship with the exhumation of UHP metamorphic terranes: Application to the Norwegian Caledonides. *Geochemistry, Geophysics, Geosystems*, **15**, 1766–1782, https://doi.org/10.1002/2014GC005253.

Brewer, T.S., Storey, C.D., Parrish, R.R., Temperley, S. and Windley, B.F. 2003. Grenvillian age decompression of eclogites in the Glenelg-Attadale Inlier, NW Scotland. *Journal of the Geological Society*, **160**, 565–574, https://doi.org/10.1144/0016-764902-061.

British Geological Survey. 2016. DiGMapGB-50, using Digimap Geology Collection, https://digimap.edina.ac.uk.

Brown, M. 2007. Crustal melting and melt extraction, ascent and emplacement in orogens: mechanisms and consequences. *Journal of the Geological Society*, **164**, 709–730, https://doi.org/10.1144/0016-76492006-171.

Brown, P.E., Ryan, P.D., Soper, N.J. and Woodcock, N.H. 2008. The Newer Granite problem revisited: a transtensional origin for the Early Devonian Trans-Suture Suite. *Geological Magazine*, **145**, 235–256, https://doi.org/10.1017/S0016756807004219.

Bruand, E., Storey, C. and Fowler, M. 2014. Accessory Mineral Chemistry of High Ba–Sr Granites from Northern Scotland: Constraints on Petrogenesis and Records of Whole-rock Signature. *Journal of Petrology*, **55**, 1619–1651, https://doi.org/10.1093/petrology/egu037.

Bullock, L., Parnell, J., Perez, M. and Feldmann, J. 2017. Tellurium Enrichment in Jurassic Coal, Brora, Scotland. *Minerals*, **7**, 231, https://doi.org/10.3390/min7120231.

Burnham, A.D. 2020. Key concepts in interpreting the concentrations of the rare earth elements in zircon. *Chemical Geology*, **551**, 119765, https://doi.org/10.1016/j.chemgeo.2020.119765.

Butler, J.P., Beaumont, C. and Jamieson, R.A. 2015. Paradigm lost: Buoyancy thwarted by the strength of the Western Gneiss Region (ultra)high-pressure terrane, Norway. *Lithosphere*, **7**, 379–407, https://doi.org/10.1130/L426.1.

Carty, K., Schwartz, J.J., Wiesenfeld, J., Klepeis, K.A., Stowell, H.H., Tulloch, A.J. and Barnes, C.G. 2021. The Generation of Arc Andesites and Dacites in the Lower Crust of a Cordilleran Arc, Fiordland, New Zealand. *Journal of Petrology*, **62**, egab043, https://doi.org/10.1093/petrology/egab043.

Cashman, K.V., Sparks, R.S.J. and Blundy, J.D. 2017. Vertically extensive and unstable magmatic systems: A unified view of igneous processes. *Science*, **355**, eaag3055, https://doi.org/10.1126/science.aag3055.

Castro, A. and Stephens, W.E. 1992. Amphibole-rich polycrystalline clots in calc-alkaline granites and their enclaves.pdf. *The Canadian Mineralogist*, **30**, 1093–1112.

Cawood, P.A., Nemchin, A.A., Strachan, R.A., Kinny, P.D. and Staci Loewy. 2004. Laurentian provenance and an intracratonic tectonic setting for the Moine Supergroup, Scotland, constrained by detrital zircons from the Loch Eil and Glen Urquhart successions. *Journal of the Geological Society*, **161**, 861–874, https://doi.org/10.1144/16-764903-117.

Cawood, P.A., Strachan, R.A., et al. 2015. Neoproterozoic to early Paleozoic extensional and compressional history of East Laurentian margin sequences: The Moine Supergroup, Scottish Caledonides. *GSA Bulletin*, **127**, 349–371, https://doi.org/10.1130/B31068.1.

Chandrasekharam, D., Baba, A., Ayzit, T. and Singh, H.K. 2022. Geothermal potential of granites: Case study- Kaymaz and Sivrihisar (Eskisehir region)

Western Anatolia. *Renewable Energy*, **196**, 870–882, https://doi.org/10.1016/j.renene.2022.07.035.

Chappell, B.W., Bryant, C.J. and Wyborn, D. 2012. Peraluminous I-type granites. *Lithos*, **153**, 142–153, https://doi.org/10.1016/j.lithos.2012.07.008.

Chaussard, E. and Amelung, F. 2014. Regional controls on magma ascent and storage in volcanic arcs. *Geochemistry, Geophysics, Geosystems*, **15**, 1407–1418, https://doi.org/10.1002/2013GC005216.

Cherniak, D.J. and Watson, E.B. 2001. Pb diffusion in zircon. *Chemical Geology*, **172**, 5–24, https://doi.org/10.1016/S0009-2541(00)00233-3.

Chew, D.M. and Strachan, R.A. 2014. The Laurentian Caledonides of Scotland and Ireland. *Geological Society, London, Special Publications*, **390**, 45–91, https://doi.org/10.1144/SP390.16.

Chew, D.M., Daly, J.S., Magna, T., Page, L.M., Kirkland, C.L., Whitehouse, M.J. and Lam, R. 2010. Timing of ophiolite obduction in the Grampian orogen. *GSA Bulletin*, **122**, 1787–1799, https://doi.org/10.1130/B30139.1.

Chew, D.M., Petrus, J.A. and Kamber, B.S. 2014. U–Pb LA–ICPMS dating using accessory mineral standards with variable common Pb. *Chemical Geology*, **363**, 185–199, https://doi.org/10.1016/j.chemgeo.2013.11.006.

Chiaradia, M. 2015. Crustal thickness control on Sr/Y signatures of recent arc magmas: an Earth scale perspective. *Scientific Reports*, **5**, 8115, https://doi.org/10.1038/srep08115.

Chiaradia, M. 2020. How Much Water in Basaltic Melts Parental to Porphyry Copper Deposits? *Frontiers in Earth Science*, **8**.

Chiaradia, M. 2022. Distinct magma evolution processes control the formation of porphyry Cu–Au deposits in thin and thick arcs. *Earth and Planetary Science Letters*, **599**, 117864, https://doi.org/10.1016/j.epsl.2022.117864.

Chiaradia, M. and Caricchi, L. 2017. Stochastic modelling of deep magmatic controls on porphyry copper deposit endowment. *Scientific Reports*, **7**, 44523, https://doi.org/10.1038/srep44523.

Chiaradia, M., Müntener, O., Beate, B. and Fontignie, D. 2009. Adakite-like volcanism of Ecuador: lower crust magmatic evolution and recycling. *Contributions to Mineralogy and Petrology*, **158**, 563–588, https://doi.org/10.1007/s00410-009-0397-2.

Chiaradia, M., Müntener, O. and Beate, B. 2020. Effects of aseismic ridge subduction on the geochemistry of frontal arc magmas. *Earth and Planetary Science Letters*, **531**, 115984, https://doi.org/10.1016/j.epsl.2019.115984.

Claiborne, L.L., Miller, C.F., Gualda, G.A.R., Carley, T.L., Covey, A.K., Wooden, J.L. and Fleming, M.A. 2018. Zircon as Magma Monitor: Robust,Temperature-Dependent Partition Coefficients from Glass and Zircon Surface and Rim Measurements from Natural Systems. *In*: *Microstructural Geochronology*. 1–33., https://doi.org/10.1002/9781119227250.ch1.

Clemens, J.D., Darbyshire, D.P.F. and Flinders, J. 2009. Sources of post-orogenic calcalkaline magmas: The Arrochar and Garabal Hill–Glen Fyne complexes, Scotland. *Lithos*, **112**, 524–542, https://doi.org/10.1016/j.lithos.2009.03.026.

Cogné, N., Derycke, A., and Gallagher, K. 2024. The McClure Mountain Syenite Apatite as a Potential Age Control Reference Material for LA-ICP-MS AFT and U-Pb Double Dating. Geostandards and Geoanalytical Research, 48, 381-391, https://doi.org/10.1111/ggr.12545.

Condon, D., Schoene, B., et al. 2024. Recommendations for the reporting and interpretation of isotope dilution U-Pb geochronological information. *GSA Bulletin*, https://doi.org/10.1130/B37321.1.

Corfu, F., Hanchar, J.M., Hoskin, P.W.O. and Kinny, P. 2003. Atlas of Zircon Textures. *Reviews in Mineralogy and Geochemistry*, **53**, 469–500, https://doi.org/10.2113/0530469.

Couzinié, S., Laurent, O., Moyen, J.-F., Zeh, A., Bouilhol, P. and Villaros, A. 2016. Post-collisional magmatism: Crustal growth not identified by zircon Hf–O isotopes. *Earth and Planetary Science Letters*, **456**, 182–195, https://doi.org/10.1016/j.epsl.2016.09.033.

Crisp, L.J., Berry, A.J., Burnham, A.D., Miller, L.A. and Newville, M. 2023. The Ti-in-zircon thermometer revised: The effect of pressure on the Ti site in zircon. *Geochimica et Cosmochimica Acta*, **360**, 241–258, https://doi.org/10.1016/j.gca.2023.04.031.

Crowley, J.L., Brown, R.L., Gervais, F. and Gibson, H.D. 2008. Assessing Inheritance of Zircon and Monazite in Granitic Rocks from the Monashee Complex, Canadian Cordillera. *Journal of Petrology*, **49**, 1915–1929, https://doi.org/10.1093/petrology/egn047.

Crowley, Q.G. and Strachan, R.A. 2015. U–Pb zircon constraints on obduction initiation of the Unst Ophiolite: an oceanic core complex in the Scottish Caledonides? *Journal of the Geological Society*, **172**, 279–282, https://doi.org/10.1144/jgs2014-125.

Cutts, K.A., Kinny, P.D., et al. 2010. Three metamorphic events recorded in a single garnet: Integrated phase modelling, in situ LA-ICPMS and SIMS geochronology from the Moine Supergroup, NW Scotland. *Journal of Metamorphic Geology*, **28**, 249–267, https://doi.org/10.1111/j.1525-1314.2009.00863.x.

Cutts, K.A., Hand, M., Kelsey, D.E. and Strachan, R.A. 2011. P–T constraints and timing of Barrovian metamorphism in the Shetland Islands, Scottish Caledonides: implications for the structural setting of the Unst ophiolite. *Journal of the Geological Society*, **168**, 1265–1284, https://doi.org/10.1144/0016-76492010-165.

Dallmeyer, R.D., Strachan, R.A., Rogers, G., Watt, G.R. and Friend, C.R.L. 2001. Dating deformation and cooling in the Caledonian thrust nappes of north Sutherland, Scotland: insights from 40Ar/39Ar and Rb-Sr chronology. *Journal of the Geological Society*, **158**, 501–512, https://doi.org/10.1144/jgs.158.3.501.

Davies, J.H. and von Blanckenburg, F. 1995. Slab breakoff: A model of lithosphere detachment and its test in the magmatism and deformation of collisional orogens. *Earth and Planetary Science Letters*, **129**, 85–102, https://doi.org/10.1016/0012-821X(94)00237-S.

de Saint Blanquat, M., Tikoff, B., Teyssier, C. and Vigneresse, J.L. 1998. Transpressional kinematics and magmatic arcs. *Geological Society, London, Special Publications*, **135**, 327–340, https://doi.org/10.1144/GSL.SP.1998.135.01.21.

Deady, E., Goodenough, K.M., et al. 2023. *Potential for Critical Raw Material Prospectivity in the UK*. **CR/23/024**Decarbonisation and Resource Management Programme.

Deans, T., Garson, M.S. and Coats, J.S. 1971. Fenite-type Soda Metasomatism in the Great Glen, Scotland. *Nature Physical Science*, **234**, 145–147, https://doi.org/10.1038/physci234145a0.

Dewey, J.F. 2005. Orogeny can be very short. *Proceedings of the National Academy of Sciences*, **102**, 15286–15293, https://doi.org/10.1073/pnas.0505516102.

Dewey, J.F. and Shackleton, R.M. 1984. A model for the evolution of the Grampian tract in the early Caledonides and Appalachians. *Nature*, **312**, 115–121, https://doi.org/10.1038/312115a0.

Dewey, J.F. and Strachan, R.A. 2003. Changing Silurian-Devonian relative plate motion in the Caledonides: sinistral transpression to sinistral transtension. *Journal of the Geological Society*, **160**, 219–229, https://doi.org/10.1144/0016-764902-085.

Dewey, J.F., Dalziel, I.W.D., Reavy, R.J. and Strachan, R.A. 2015. The Neoproterozoic to Mid-Devonian evolution of Scotland: a review and unresolved issues. *Scottish Journal of Geology*, **51**, 5–30, https://doi.org/10.1144/sjg2014-007.

Dichiarante, A.M., Holdsworth, R.E., et al. 2016. New structural and Re–Os geochronological evidence constraining the age of faulting and associated mineralization in the Devonian Orcadian Basin, Scotland. *Journal of the Geological Society*, **173**, 457–473, https://doi.org/10.1144/jgs2015-118.

D'Lemos, R.S., Brown, M. and Strachan, R.A. 1992. Granite magma generation, ascent and emplacement within a transpressional orogen. *Journal of the Geological Society*, **149**, 487–490, https://doi.org/10.1144/gsjgs.149.4.0487.

Domeier, M. 2016. A plate tectonic scenario for the Iapetus and Rheic oceans. *Gondwana Research*, **36**, 275–295, https://doi.org/10.1016/j.gr.2015.08.003.

Downing, R.A. and Gray, D.A. (eds). 1986. *Geothermal Energy: The Potential in the United Kingdom*. **WZ/86/003**.

Ducea, M.N., Seclaman, A.C., Murray, K.E., Jianu, D. and Schoenbohm, L.M. 2013. Mantle-drip magmatism beneath the Altiplano-Puna plateau, central Andes. *Geology*, **41**, 915–918, https://doi.org/10.1130/G34509.1.

Dunk, M., Strachan, R.A., et al. 2019. Evidence for a late Cambrian juvenile arc and a buried suture within the Laurentian Caledonides of Scotland: Comparisons with hyperextended Iapetan margins in the Appalachian Mountains (North America) and Norway. *Geology*, **47**, 734–738, https://doi.org/10.1130/G46180.1.

Duretz, T., Gerya, T.V., Kaus, B.J.P. and Andersen, T.B. 2012. Thermomechanical modeling of slab eduction. *Journal of Geophysical Research: Solid Earth*, **117**, https://doi.org/10.1029/2012JB009137.

Elkins-Tanton, L.T. 2007. Continental magmatism, volatile recycling, and a heterogeneous mantle caused by lithospheric gravitational instabilities. *Journal of Geophysical Research: Solid Earth*, **112**, https://doi.org/10.1029/2005JB004072.

Elkins-Tanton, L.T. and Grove, T.L. 2003. Evidence for deep melting of hydrous metasomatized mantle: Pliocene high-potassium magmas from the Sierra Nevadas. *Journal of Geophysical Research: Solid Earth*, **108**, https://doi.org/10.1029/2002JB002168.

Elliott, D. and Johnson, M.R.W. 1980. Structural evolution in the northern part of the Moine thrust belt, NW Scotland. *Transactions of the Royal Society of Edinburgh: Earth Sciences*, **71**, 69–96, https://doi.org/10.1017/S0263593300013523.

England, P.C. and Thompson, A. 1986. Some thermal and tectonic models for crustal melting in continental collision zones. *Geological Society, London, Special Publications*, **19**, 83–94, https://doi.org/10.1144/GSL.SP.1986.019.01.05.

England, P.C. and Thompson, A.B. 1984. Pressure—Temperature—Time Paths of Regional Metamorphism I. Heat Transfer during the Evolution of Regions of Thickened Continental Crust. *Journal of Petrology*, **25**, 894–928, https://doi.org/10.1093/petrology/25.4.894.

European Commission. 2020. Critical raw materials resilience: charting a path towards greater security and sustainability.

Ferriss, E.D.A., Essene, E.J. and Becker, U. 2008. Computational study of the effect of pressure on the Ti-in-zircon geothermometer. *European Journal of Mineralogy*, **20**, 745–755, https://doi.org/10.1127/0935-1221/2008/0020-1860.

Fettes, D. and Macdonald, R. 1978. Glen Garry vein complex. *Scottish Journal of Geology*, **14**, 335–358, https://doi.org/10.1144/sjg14040335.

Fowler, M.B. 1988. Ach'uaine hybrid appinite pipes: Evidence for mantle-derived shoshonitic parent magmas in Caledonian granite genesis. *Geology*, **16**, 1026–1030, https://doi.org/10.1130/0091-7613(1988)016<1026:AUHAPE>2.3.CO;2.

Fowler, M.B. 1992. Elemental and O-Sr-Nd isotope geochemistry of the Glen Dessarry syenite, NW Scotland. *Journal of the Geological Society*, **149**, 209–220, https://doi.org/10.1144/gsjgs.149.2.0209.

Fowler, M.B. and Henney, P.J. 1996. Mixed Caledonian appinite magmas: implications for lamprophyre fractionation and high Ba-Sr granite genesis. *Contributions to Mineralogy and Petrology*, **126**, 199–215, https://doi.org/10.1007/s004100050244.

Fowler, M.B., Henney, P.J., Darbyshire, D.P.F. and Greenwood, P.B. 2001. Petrogenesis of high Ba-Sr granites: the Rogart pluton, Sutherland. *Journal of the Geological Society*, **158**, 521–534, https://doi.org/10.1144/jgs.158.3.521.

Fowler, M.B., Kocks, H., Darbyshire, D.P.F. and Greenwood, P.B. 2008. Petrogenesis of high Ba-Sr plutons from the Northern Highlands Terrane of the British Caledonian Province. *Lithos*, **105**, 129–148, https://doi.org/10.1016/j.lithos.2008.03.003.

Freeburn, R., Bouilhol, P., Maunder, B., Magni, V. and van Hunen, J. 2017. Numerical models of the magmatic processes induced by slab breakoff. *Earth and Planetary Science Letters*, **478**, 203–213, https://doi.org/10.1016/j.epsl.2017.09.008.

Freeman, S.R., Butler, R.W.H., Cliff, R.A. and Rex, D.C. 1998. Direct dating of mylonite evolution: a multi-disciplinary geochronological study from the Moine Thrust Zone, NW Scotland. *Journal of the Geological Society*, **155**, 745–758, https://doi.org/10.1144/gsjgs.155.5.0745.

Friend, C.R.L., Jones, K.A. and Burns, I.M. 2000a. New high-pressure granulite event in the Moine Supergroup, northern Scotland: Implications for Taconic (early Caledonian) crustal evolution. *Geology*, **28**, 543–546, https://doi.org/10.1130/0091-7613(2000)28<543:NHGEIT>2.0.CO;2.

Friend, C.R.L., Strachan, R.A. and Kinny, P.D. 2008. U-Pb zircon dating of basement inliers within the Moine Supergroup, Scottish Caledonides: implications of Archaean protolith ages. *Journal of the Geological Society*, **165**, 807–815, https://doi.org/10.1144/0016-76492007-125.

Friend, P.F., Williams, B.P.J., Ford, M. and Williams, E.A. 2000b. Kinematics and dynamics of Old Red Sandstone basins. *Geological Society, London, Special Publications*, **180**, 29–60, https://doi.org/10.1144/GSL.SP.2000.180.01.04.

Fritschle, T., Daly, J.S., Whitehouse, M.J., McConnell, B. and Buhre, S. 2018. Multiple intrusive phases in the Leinster Batholith, Ireland:

geochronology, isotope geochemistry and constraints on the deformation history. *Journal of the Geological Society*, **175**, 229–246, https://doi.org/10.1144/jgs2017-034.

Gallagher, M.J. 1958. *The Petrography of the Mineralised Dykes of W. Scotland*. PhD Thesis, Durham University.

Gallagher, M.J. 1963. Lamprophyre dykes from Argyll. *Mineralogical magazine and journal of the Mineralogical Society*, **33**, 415–430, https://doi.org/10.1180/minmag.1963.033.260.07.

Gardiner, N.J., Hawkesworth, C.J., Robb, L.J., Mulder, J.A., Wainwright, A.N. and Cawood, P.A. 2021. Metal anomalies in zircon as a record of granite-hosted mineralization. *Chemical Geology*, **585**, 120580, https://doi.org/10.1016/j.chemgeo.2021.120580.

Garson, M.S., Coats, J.S., Rock, N.M.S. and Deans, T. 1984. Fenites, breccia dykes, albitites, and carbonatitic veins near the Great Glen Fault, Inverness, Scotland. *Journal of the Geological Society*, **141**, 711–732, https://doi.org/10.1144/gsjgs.141.4.0711.

Garzanti, E., Radeff, G. and Malusà, M.G. 2018. Slab breakoff: A critical appraisal of a geological theory as applied in space and time. *Earth-Science Reviews*, **177**, 303–319, https://doi.org/10.1016/j.earscirev.2017.11.012.

Gasser, D., Majka, J., Jakob, J. and J. Barnes, C. 2024. A review of the Caledonian Wilson cycle from a North Atlantic perspective. *Journal of the Geological Society*, **181**, https://doi.org/10.1144/jgs2023-211.

Gaynor, S.P., Ruiz, M. and Schaltegger, U. 2022. The importance of high precision in the evaluation of U-Pb zircon age spectra. *Chemical Geology*, **603**, 120913, https://doi.org/10.1016/j.chemgeo.2022.120913.

Gemmell, C., Neill, I., Currie, D., Wildman, M., Spruzeniece, L., MacRae, C. and Einsle, J. 2023. Geochronology and geodynamics of collision magmatism in the Southern Uplands-Down-Longford Terrane in Scotland and Ireland.

Geological Society of London. 2015. Reporting standards for 40Ar–39Ar and U–Pb geochronometric data.

Gillespie, M.R., Crane, E.J. and Barron, H.F. 2013. *Deep Geothermal Energy Potential in Scotland*. **British Geological Survey Comissioned Report, CR/12/131. 129.**

Glazner, A.F. 1991. Plutonism, oblique subduction, and continental growth: An example from the Mesozoic of California. *Geology*, **19**, 784–786, https://doi.org/10.1130/0091-7613(1991)019<0784:POSACG>2.3.CO;2.

Glodny, J., Kühn, A. and Austrheim, H. 2008. Geochronology of fluid-induced eclogite and amphibolite facies metamorphic reactions in a subduction-collision system, Bergen Arcs, Norway. *Contributions to Mineralogy and Petrology*, **156**, 27–48, https://doi.org/10.1007/s00410-007-0272-y.

Gómez Frutos, D. and Castro, A. 2023. *Mafic Microgranular Enclaves Trace the Origin of Post-Collisional Magmatism*. **EGU23-7430**, https://doi.org/10.5194/egusphere-egu23-7430.

Goodenough, K.M., Young, B.N. and Parsons, I. 2004. The minor intrusions of Assynt, NW Scotland: early development of magmatism along the Caledonian Front. *Mineralogical Magazine*, **68**, 541–559, https://doi.org/10.1180/0026461046840207.

Goodenough, K.M., Millar, I., Strachan, R.A., Krabbendam, M. and Evans, J.A. 2011. Timing of regional deformation and development of the Moine Thrust Zone in the Scottish Caledonides: constraints from the U–Pb geochronology of alkaline intrusions. *Journal of the Geological Society*, **168**, 99–114, https://doi.org/10.1144/0016-76492010-020.

Gorczyk, W., Hobbs, B. and Gerya, T. 2012. Initiation of Rayleigh–Taylor instabilities in intra-cratonic settings. *Tectonophysics*, **514–517**, 146–155, https://doi.org/10.1016/j.tecto.2011.10.016.

Goscombe, B., Foster, D.A., et al. 2022. Episodic intra-continental reactivation during collapse of a collisional orogen: The Damara Belt, Namibia. *Gondwana Research*, **109**, 285–375, https://doi.org/10.1016/j.gr.2022.05.003.

Guo, Z. and Wilson, M. 2019. Late Oligocene–early Miocene transformation of postcollisional magmatism in Tibet. *Geology*, **47**, 776–780, https://doi.org/10.1130/G46147.1.

Hall, J., Brewer, J.A., Matthews, D.H. and Warner, M.R. 1984. Crustal structure across the Caledonides from the 'WINCH' seismic profile: influences on the evolution of the Midland Valley of Scotland. *Transactions of the Royal Society of Edinburgh: Earth Sciences*, **75**, 97–109, https://doi.org/10.1017/S0263593300013766.

Halliday, A.N., Aftalion, M., van Breemen, O. and Jocelyn, J. 1979. Petrogenetic significance of Rb-Sr and U-Pb isotopic systems in the 400 Ma old British Isles granitoids and their hosts. *Geological Society, London, Special Publications*, **8**, 653–661, https://doi.org/10.1144/GSL.SP.1979.008.01.79.

Halliday, A.N., Aftalion, M., Parsons, I., Dickin, A.P. and Johnson, M.R.W. 1987. Syn-orogenic alkaline magmatism and its relationship to the Moine Thrust Zone and the thermal state of the Lithosphere in NW Scotland. *Journal of the Geological Society*, **144**, 611–617, https://doi.org/10.1144/gsjgs.144.4.0611.

Hanchar, J.M. and Van Westrenen, W. 2007. Rare Earth Element Behavior in Zircon-Melt Systems. *Elements*, **3**, 37–42, https://doi.org/10.2113/gselements.3.1.37.

Harig, C., Molnar, P. and Houseman, G.A. 2010. Lithospheric thinning and localization of deformation during Rayleigh-Taylor instability with nonlinear rheology and implications for intracontinental magmatism.

Journal of Geophysical Research: Solid Earth, **115**, https://doi.org/10.1029/2009JB006422.

Harmon, R.S., Halliday, A.N., Clayburn, J. a. P., Stephens, W.E., Moorbath, S.E., Thompson, R.N. and Oxburgh, E.R. 1984. Chemical and isotopic systematics of the Caledonian intrusions of Scotland and Northern England: a guide to magma source region and magma-crust interaction. *Philosophical Transactions of the Royal Society of London. Series A, Mathematical and Physical Sciences*, **310**, 709–742, https://doi.org/doi.org/10.1098/rsta.1984.0016.

He, J.J.Y. and Kapp, P. 2023. Basin record of a Miocene lithosphere drip beneath the Colorado Plateau. *Nature Communications*, **14**, 4433, https://doi.org/10.1038/s41467-023-40147-7.

Heptinstall, E.A., Parnell, J., Boyce, A.J. and Still, J.W. 2023. Trace element minerals from carbonatite-related fluids, The Aird, Scotland. *Scottish Journal of Geology*, **59**, sjg2021-015, https://doi.org/10.1144/sjg2021-015.

Highton, A.J., Hyslop, E.K. and Noble, S.R. 1999. U-Pb zircon geochronology of migmatization in the northern Central Highlands: evidence for pre-Caledonian (Neoproterozoic) tectonometamorphism in the Grampian block, Scotland. *Journal of the Geological Society*, **156**, 1195–1204, https://doi.org/10.1144/gsjgs.156.6.1195.

Hildebrand, R.S., Whalen, J.B. and Bowring, S.A. 2018. Resolving the crustal composition paradox by 3.8 billion years of slab failure magmatism and collisional recycling of continental crust. *Tectonophysics*, **734–735**, 69–88, https://doi.org/10.1016/j.tecto.2018.04.001.

Hildreth, W. and Moorbath, S. 1988. Crustal contributions to arc magmatism in the Andes of Central Chile. *Contributions to Mineralogy and Petrology*, **98**, 455–489, https://doi.org/10.1007/BF00372365.

Hines, R., Paterson, S.R., Memeti, V. and Chambers, J.A. 2018. Nested Incremental Growth of Zoned Upper Crustal Plutons in the Southern Uplands Terrane, UK: Fractionating, Mixing, and Contaminated Magma Fingers. *Journal of Petrology*, **59**, 483–516, https://doi.org/10.1093/petrology/egy034.

Holden, P., Halliday, A.N. and Stephens, W.E. 1987. Neodymium and strontium isotope content of microdiorite enclaves points to mantle input to granitoid production. *Nature*, **330**, 53–56, https://doi.org/10.1038/330053a0.

Holden, P., Halliday, A.N., Ed Stephens, W. and Henney, P.J. 1991. Chemical and isotopic evidence for major mass transfer between mafic enclaves and felsic magma. *Chemical Geology*, **92**, 135–152, https://doi.org/10.1016/0009-2541(91)90053-T.

Holdsworth, R.E. 1989. The geology and structural evolution of a Caledonian fold and ductile thrust zone, Kyle of Tongue region, Sutherland, northern

Scotland. *Journal of the Geological Society*, **146**, 809–823, https://doi.org/10.1144/gsjgs.146.5.0809.

Holdsworth, R.E. and Roberts, A.M. 1984. Early curvilinear fold structures and strain in the Moine of the Glen Garry region, Inverness-shire. *Journal of the Geological Society*, **141**, 327–338, https://doi.org/10.1144/gsjgs.141.2.0327.

Holdsworth, R.E., McErlean, M.A. and Strachan, R.A. 1999. The influence of country rock structural architecture during pluton emplacement: the Loch Loyal syenites, Scotland. *Journal of the Geological Society*, **156**, 163–175, https://doi.org/10.1144/gsjgs.156.1.0163.

Holdsworth, R.E., Dempsey, E., et al. 2015. Silurian–Devonian magmatism, mineralization, regional exhumation and brittle strike-slip deformation along the Loch Shin Line, NW Scotland. *Journal of the Geological Society*, **172**, 748–762, https://doi.org/10.1144/jgs2015-058.

Hollister, L.S. and Andronicos, C.L. 2006. Formation of new continental crust in Western British Columbia during transpression and transtension. *Earth and Planetary Science Letters*, **249**, 29–38, https://doi.org/10.1016/j.epsl.2006.06.042.

Horstwood, M.S.A., L. Foster, G., R. Parrish, R., R. Noble, S. and M. Nowell, G. 2003. Common-Pb corrected in situ U–Pb accessory mineral geochronology by LA-MC-ICP-MS. *Journal of Analytical Atomic Spectrometry*, **18**, 837–846, https://doi.org/10.1039/B304365G.

Houseman, G.A. and Molnar, P. 1997. Gravitational (Rayleigh-Taylor) instability of a layer with non-linear viscosity and convective thinning of continental lithosphere. *Geophysical Journal International*, **128**, 125–150, https://doi.org/10.1111/j.1365-246X.1997.tb04075.x.

Houseman, G.A., McKenzie, D.P. and Molnar, P. 1981. Convective instability of a thickened boundary layer and its relevance for the thermal evolution of continental convergent belts. *Journal of Geophysical Research: Solid Earth*, **86**, 6115–6132, https://doi.org/10.1029/JB086iB07p06115.

Hutton, D.H.W. 1988. Igneous emplacement in a shear-zone termination: The biotite granite at Strontian, Scotland. *Geological Society of America Bulletin*, **100**, 1392–1399, https://doi.org/10.1130/0016-7606(1988)100<1392:IEIASZ>2.3.CO;2.

Hutton, D.H.W. and McErlean, M. 1991. Silurian and Early Devonian sinistral deformation of the Ratagain granite, Scotland: constraints on the age of Caledonian movements on the Great Glen fault system. *Journal of the Geological Society*, **148**, 1–4, https://doi.org/10.1144/gsjgs.148.1.0001.

Johnson, T.E., Kirkland, C.L., Viete, D.R., Fischer, S., Reddy, S.M., Evans, N.J. and McDonald, B.J. 2017. Zircon geochronology reveals polyphase magmatism and crustal anatexis in the Buchan Block, NE Scotland: Implications for the Grampian Orogeny. *Geoscience Frontiers*, **8**, 1469–1478, https://doi.org/10.1016/j.gsf.2017.02.002.

Johnstone, G.S. 1975. The Moine Succession. *In*: Harris, A. L., Shackleton, R. M., Watson, J. V., Downie, C., Harland, W. B. and Moorbath, S. (eds) *A Correlation of Precambrian Rocks in the British Isles*. Geological Society of London Special Reports.

Johnstone, G.S. and Mykura, W. 1989. *British Regional Geology: The Northern Highlands of Scotland*, Fourth.

Kaislaniemi, L., van Hunen, J., Allen, M.B. and Neill, I. 2014. Sublithospheric small-scale convection—A mechanism for collision zone magmatism. *Geology*, **42**, 291–294, https://doi.org/10.1130/G35193.1.

Kaislaniemi, L., van Hunen, J. and Bouilhol, P. 2018. Lithosphere Destabilization by Melt Weakening and Crust-Mantle Interactions: Implications for Generation of Granite-Migmatite Belts. *Tectonics*, **37**, 3102–3116, https://doi.org/10.1029/2018TC005014.

Kay, R.W. and Kay, S.M. 1993. Delamination and delamination magmatism. *Tectonophysics*, **219**, 177–189, https://doi.org/10.1016/0040-1951(93)90295-U.

Kennedy, W.Q. 1946. The Great Glen Fault. *Quarterly Journal of the Geological Society*, **102**, 41–76, https://doi.org/10.1144/GSL.JGS.1946.102.01-04.04.

Keskin, M. 2003. Magma generation by slab steepening and breakoff beneath a subduction-accretion complex: An alternative model for collision-related volcanism in Eastern Anatolia, Turkey. *Geophysical Research Letters*, **30**, https://doi.org/10.1029/2003GL018019.

Kimbell, G.S. 1986. *Geophysical Surveys Near Strontian, Highland Region*. **85**Mineral Reconnaissance Programme Report.

Kinny, P.D. and Maas, R. 2003. Lu–Hf and Sm–Nd isotope systems in zircon. *In*: Hanchar, J. M. and Hoskin, P. W. O. (eds) *Zircon*. Reviews in Mineralogy and Geochemistry, 327–342.

Kinny, P.D., riend, C.R.L., Strachan, R.A., Watt, G.R. and Burns, I.M. 1999. U-Pb geochronology of regional migmatites in East Sutherland, Scotland: evidence for crustal melting during the Caledonian orogeny. *Journal of the Geological Society*, **156**, 1143–1152, https://doi.org/10.1144/gsjgs.156.6.1143.

Kinny, P.D., Strachan, R.A., Friend, C.R.L., Kocks, H., Rogers, G. and Paterson, B.A. 2003. U-Pb geochronology of deformed metagranites in central Sutherland, Scotland: evidence for widespread late Silurian metamorphism and ductile deformation of the Moine Supergroup during the Caledonian orogeny. *Journal of the Geological Society*, **160**, 259–269, https://doi.org/10.1144/0016-764901-087.

Kirkland, C.L., Strachan, R.A. and Prave, A.R. 2008. Detrital zircon signature of the Moine Supergroup, Scotland: Contrasts and comparisons with other Neoproterozoic successions within the circum-North Atlantic region. *Precambrian Research*, **163**, 332–350, https://doi.org/10.1016/j.precamres.2008.01.003.

Kocks, H. 2002. *Structural Setting and Petrogenesis of Silurian Granites in the Caledonides of Northern Scotland*. Ph.D., Oxford Brookes University.

Kocks, H., Strachan, R.A. and Evans, J.A. 2006. Heterogeneous reworking of Grampian metamorphic complexes during Scandian thrusting in the Scottish Caledonides: insights from the structural setting and U–Pb geochronology of the Strath Halladale Granite. *Journal of the Geological Society*, **163**, 525–538, https://doi.org/10.1144/0016-764905-008.

Kocks, H., Strachan, R.A., Evans, J.A. and Fowler, M. 2014. Contrasting magma emplacement mechanisms within the Rogart igneous complex, NW Scotland, record the switch from regional contraction to strike-slip during the Caledonian orogeny. *Geological Magazine*, **151**, 899–915, https://doi.org/10.1017/S0016756813000940.

Kohn, M.J. 2017. Titanite Petrochronology. *In*: Kohn, M. J., Engi, M. and Lanari, P. (eds) *Petrchronology: Methods and Applications*. Reviews in Mineralogy and Geochemistry, 419–441.

Krabbendam, M., Prave, T. and Cheer, D. 2008. A fluvial origin for the Neoproterozoic Morar Group, NW Scotland; implications for Torridon-Morar Group correlation and the Grenville Orogen foreland basin. *Journal of the Geological Society*, **165**, 379–394, https://doi.org/10.1144/0016-76492007-076.

Krabbendam, M., Strachan, R.A., Leslie, A.G., Goodenough, K.M. and Bonsor, H.C. 2011. The internal structure of the Moine Nappe Complex and the stratigraphy of the Morar Group in the Fannichs–Beinn Dearg area, NW Highlands. *Scottish Journal of Geology*, **47**, 1–20, https://doi.org/10.1144/0036-9276/01-419.

Krabbendam, M., Leslie, A.G. and Goodenough, K.M. 2014. Structure and stratigraphy of the Morar Group in Knoydart, NW Highlands: implications for the history of the Moine Nappe and stratigraphic links between the Moine and Torridonian successions. *Scottish Journal of Geology*, **50**, 125–142, https://doi.org/10.1144/sjg2014-002.

Krabbendam, M., Ramsay, J.G., Leslie, A.G., Tanner, P.W.G., Dietrich, D. and Goodenough, K.M. 2018. Caledonian and Knoydartian overprinting of a Grenvillian inlier and the enclosing Morar Group rocks: structural evolution of the Precambrian Proto-Moine Nappe, Glenelg, NW Scotland. *Scottish Journal of Geology*, **54**, 13–35, https://doi.org/10.1144/sjg2017-006.

Krabbendam, M., Strachan, R. and Prave, T. 2022. A new stratigraphic framework for the early Neoproterozoic successions of Scotland. *Journal of the Geological Society*, **179**, jgs2021-054, https://doi.org/10.1144/jgs2021-054.

Lancaster, P.J., Strachan, R.A., Bullen, D., Fowler, M., Jaramillo, M. and Saldarriaga, A.M. 2017. U–Pb zircon geochronology and geodynamic significance of 'Newer Granite' plutons in Shetland, northernmost Scottish Caledonides. *Journal of the Geological Society*, **174**, 486–497, https://doi.org/10.1144/jgs2016-106.

Law, R., Thigpen, R., Mako, C., Kylander-Clark, A., Caddick, M. and Moore, L.R. 2023. Metasedimentary rocks of the Rosemarkie Inlier, Great Glen Fault Zone, Scotland: Monazite-xenotime petrochronology and shear sense/deformation temperatures indicated by quartz c-axis fabrics. *In*: *Geological Society of America, Abtracts with Programs* – GSA Connects 2023 Meeting, https://doi.org/10.1130/abs/2023AM-392106.

Law, R.D., Thigpen, J.R., et al. 2021. Tectonic Transport Directions, Shear Senses and Deformation Temperatures Indicated by Quartz c-Axis Fabrics and Microstructures in a NW-SE Transect across the Moine and Sgurr Beag Thrust Sheets, Caledonian Orogen of Northern Scotland. *Geosciences*, **11**, 411, https://doi.org/10.3390/geosciences11100411.

Lawrence, A., Maffione, M. and Stevenson, C.T.E. 2022. Mush ado about the Ratagain Complex, NW Scotland: insights into Caledonian granitic magmatism and emplacement from magnetic fabric analyses. *Scottish Journal of Geology*, **58**, sjg2021-018, https://doi.org/10.1144/sjg2021-018.

Lawrence, A., Fowler, M., Kingsbury, C.G., Knott, T., Mark, D. and Stevenson, C.T.E. 2023. Slab-failure or Slab-success? Examining the contributions of crust and mantle to post-subduction magmatism in the Ratagain Complex, NW Scotland. *Lithos*, **448–449**, 107139, https://doi.org/10.1016/j.lithos.2023.107139.

Le Bas, M.J. and Streckeisen, A.L. 1991. The IUGS systematics of igneous rocks. *Journal of the Geological Society*, **148**, 825–833, https://doi.org/10.1144/gsjgs.148.5.0825.

Le Breton, E., Cobbold, P.R. and Zanella, A. 2013. Cenozoic reactivation of the Great Glen Fault, Scotland: additional evidence and possible causes. *Journal of the Geological Society*, **170**, 403–415, https://doi.org/10.1144/jgs2012-067.

Lebedev, V.A., Goltsman, Yu.V., Oleinikova, T.I., Parfenov, A.V. and Yakushev, A.I. 2021. The Pliocene Post-Collisional Volcanism of Central Armenia: Isotope-Geochronology and Geochemical Evolution of Magmatic Melts. *Petrology*, **29**, 627–656, https://doi.org/10.1134/S0869591121060059.

Lim, H., Nebel, O., et al. 2023. Lower crustal hot zones as zircon incubators: Inherited zircon antecryts in diorites from a mafic mush reservoir. *Geological Society, London, Special Publications*, **537**, SP537-2021–2195, https://doi.org/10.1144/SP537-2021-195.

Liu, B. and Lee, C.-T. 2020. Large Silicic Eruptions, Episodic Recharge, and the Transcrustal Magmatic System. *Geochemistry, Geophysics, Geosystems*, **21**, e2020GC009220, https://doi.org/10.1029/2020GC009220.

Loader, M.A., Nathwani, C.L., Wilkinson, J.J. and Armstrong, R.N. 2022. Controls on the magnitude of Ce anomalies in zircon. *Geochimica et Cosmochimica Acta*, **328**, 242–257, https://doi.org/10.1016/j.gca.2022.03.024.

Lundmark, A.M., Augland, L.E. and Bjerga, A.D. 2019. Timing of strain partitioning and magmatism in the Scottish Scandian collision, evidence from the high Ba-Sr Orkney granite complex. *Scottish Journal of Geology*, **55**, 21–34, https://doi.org/10.1144/sjg2018-001.

Magni, V. and Király, Á. 2020. Delamination. *In*: *Reference Module in Earth Systems and Environmental Sciences*. B9780124095489095154., https://doi.org/10.1016/B978-0-12-409548-9.09515-4.

Mako, C.A. 2019. *The Thermal and Metamorphic Evolution of the Northern Highlands Terrane, Scotland*. PhD, Virginia Polytechnic Institute and State University.

Mako, C.A., Law, R.D., Caddick, M.J., Ryan Thigpen, J., Ashley, K.T., Cottle, J. and Kylander-Clark, A. 2019. Thermal evolution of the Scandian hinterland, Naver nappe, northern Scotland. *Journal of the Geological Society*, **176**, 669–688, https://doi.org/10.1144/jgs2018-224.

Mako, C.A., Caddick, M.J., Law, R.D. and Thigpen, J.R. 2024. Monazite–xenotime thermometry: a review of best practices and an example from the Caledonides of northern Scotland. *Geological Society, London, Special Publications*, **537**, 185–208, https://doi.org/10.1144/SP537-2022-246.

Mark, D.F., Rice, C.M., Hole, M. and Condon, D. 2020. Multi-chronometer dating of the Souter Head complex: rapid exhumation terminates the Grampian Event of the Caledonian Orogeny. *Earth and Environmental Science Transactions of The Royal Society of Edinburgh*, **111**, 95–108, https://doi.org/10.1017/S1755691020000043.

Marston, R.J. 1967. Newer Granites of Foyers and Strontian and the Great Glen Fault. *Nature*, **214**, 159–161, https://doi.org/10.1038/214159b0.

Matthews, T.J., Loader, M.A., Wilkinson, J.J., Buret, Y., Large, S.J.E. and Birt, E.A. 2023. The Strontian Intrusive Complex: Petrography, Thermobarometry and the Influence of Titanite on Residual Melt Chemistry. *Journal of Petrology*, **64**, egad059, https://doi.org/10.1093/petrology/egad059.

Mattinson, J.M. 2005. Zircon U–Pb chemical abrasion (“CA-TIMS”) method: Combined annealing and multi-step partial dissolution analysis for improved precision and accuracy of zircon ages. *Chemical Geology*, **220**, 47–66, https://doi.org/10.1016/j.chemgeo.2005.03.011.

Mazza, S.E., Mako, C., Law, R.D., Caddick, M.J., Krabbendam, M. and Cottle, J. 2018. Thermobarometry of the Moine and Sgurr Beag thrust sheets, northern Scotland. *Journal of Structural Geology*, **113**, 10–32, https://doi.org/10.1016/j.jsg.2018.05.002.

McAteer, C.A., Daly, J.S., Flowerdew, M.J., Whitehouse, M.J. and Monaghan, N.M. 2014. Sedimentary provenance, age and possible correlation of the Iona Group SW Scotland. *Scottish Journal of Geology*, **50**, 143–158, https://doi.org/10.1144/sjg2013-019.

McCay, A.T. and Younger, P.L. 2017. Ranking the geothermal potential of radiothermal granites in Scotland: are any others as hot as the Cairngorms? *Scottish Journal of Geology*, **53**, 1-11, https://doi.org/10.1144/sjg2016-008.

McDonough, W.F. and Sun, S. -s. 1995. The composition of the Earth. *Chemical Geology*, **120**, 223–253, https://doi.org/10.1016/0009-2541(94)00140-4.

McKay, L., Kemp, S.J., Leslie, G.A., Todd, A., Shipton, Z.K., Lunn, R.J. and Booth, J. 2024. Unravelling multiple thermotectonic events accommodated by the Highland Boundary Fault: Insights from K–Ar dating. *Journal of Structural Geology*, **179**, 105030, https://doi.org/10.1016/j.jsg.2023.105030.

McKerrow, W.S., Mac Niocaill, C. and Dewey, J.F. 2000. The Caledonian Orogeny redefined. *Journal of the Geological Society*, **157**, 1149–1154, https://doi.org/10.1144/jgs.157.6.1149.

McLeod, G.W., Dempster, T.J. and Faithfull, J.W. 2011. Deciphering Magma-Mixing Processes Using Zoned Titanite from the Ross of Mull Granite, Scotland. *Journal of Petrology*, **52**, 55–82, https://doi.org/10.1093/petrology/egq071.

Meissner, R. and Mooney, W. 1998. Weakness of the lower continental crust: a condition for delamination, uplift, and escape. *Tectonophysics*, **296**, 47–60, https://doi.org/10.1016/S0040-1951(98)00136-X.

Mendum, J.R. and Noble, S.R. 2010. Mid-Devonian sinistral transpressional movements on the Great Glen Fault: the rise of the Rosemarkie Inlier and the Acadian Event in Scotland. *Geological Society, London, Special Publications*, **335**, 161–187, https://doi.org/10.1144/SP335.8.

Miles, A., Graham, C., Hawkesworth, C., Gillespie, M., Dhuime, B. and Hinton, R. 2014. Using Zircon Isotope Compositions to Constrain Crustal Structure and Pluton Evolution: the Iapetus Suture Zone Granites in Northern Britain. *Journal of Petrology*, **55**, 181–207, https://doi.org/10.1093/petrology/egt065.

Miles, A.J. 2013. *Genesis of Zoned Granite Plutons in the Iapetus Suture Zone : New Constraints from High-Precision Micro-Analysis of Accessory Minerals*. Ph.D., University of Edinburgh.

Miles, A.J., Woodcock, N.H. and Hawkesworth, C.J. 2016. Tectonic controls on post-subduction granite genesis and emplacement: The late Caledonian suite of Britain and Ireland. *Gondwana Research*, **39**, 250–260, https://doi.org/10.1016/j.gr.2016.02.006.

Miller, J.A. and Brown, P.E. 1965. Potassium–Argon Age Studies in Scotland. *Geological Magazine*, **102**, 106–134, https://doi.org/10.1017/S0016756800057459.

Miller, J.S., Matzel, J.E.P., Miller, C.F., Burgess, S.D. and Miller, R.B. 2007. Zircon growth and recycling during the assembly of large, composite arc plutons. *Journal of Volcanology and Geothermal Research*, **167**, 282–299, https://doi.org/10.1016/j.jvolgeores.2007.04.019.

Milne, E.J.M. 2019. *The Great Glen Caledonian Igneous Suite: New Geochemical and Geochronological Insights into the Final Stages of the Caledonian Orogeny*. MSc by Research, University of Glasgow.

Milne, E.J.M., Neill, I., et al. 2023. Caledonian hot zone magmatism in the 'Newer Granites': insight from the Cluanie and Clunes plutons, Northern Scottish Highlands. *Journal of the Geological Society*, **180**, jgs2022-076, https://doi.org/10.1144/jgs2022-076.

Milne, E.J.M., Neill, I., et al. 2023b. Caledonian hot zone magmatism in the "Newer Granites": insight from the Cluanie and Clunes plutons, Northern Scottish Highlands. *Journal of the Geological Society*, **0**, jgs2022-076, https://doi.org/10.1144/jgs2022-076.

Missenard, Y. and Cadoux, A. 2012. Can Moroccan Atlas lithospheric thinning and volcanism be induced by Edge-Driven Convection? *Terra Nova*, **24**, 27–33, https://doi.org/10.1111/j.1365-3121.2011.01033.x.

Möller, C., Cai, Y., Brueckner, H.K., Szilas, K. and Whitehouse, M.J. 2024. An Iapetus origin for a layered eclogite complex in the northern Western Gneiss Region, Scandinavian Caledonides. *Journal of Metamorphic Geology*, **42**, 319–354, https://doi.org/10.1111/jmg.12757.

Muir, R.J. and Vaughan, A.P.M. 2017. Digital Mapping and Three-Dimensional Model Building of the Ben Nevis Igneous Complex, Southwest Highlands, Scotland: New Insights into the Emplacement and Preservation of Postorogenic Magmatism. *The Journal of Geology*, **125**, 607–636, https://doi.org/10.1086/693858.

Munro, M. 1965. Some structural features of the Caledonian granitic complex at Strontian, Argyllshire. *Scottish Journal of Geology*, **1**, 152–175, https://doi.org/10.1144/sjg01020152.

Nabelek, P.I. 2020. Petrogenesis of leucogranites in collisional orogens. *Geological Society, London, Special Publications*, **491**, 179–207, https://doi.org/10.1144/SP491-2018-181.

Neill, I. and Stephens, W.E. 2009. The Cluanie granodiorite, NW Highlands of Scotland: a late Caledonian pluton of trondhjemitic affinity. *Scottish Journal of Geology*, **45**, 117–130, https://doi.org/10.1144/0036-9276/01-373.

Neill, I., Meliksetian, K., Allen, M.B., Navasardyan, G. and Kuiper, K. 2015. Petrogenesis of mafic collision zone magmatism: The Armenian sector of the Turkish-Iranian Plateau. *Chemical Geology*, **403**, 24–41, https://doi.org/10.1016/j.chemgeo.2015.03.013.

Neilson, J.C., Kokelaar, B.P. and Crowley, Q.G. 2009. Timing, relations and cause of plutonic and volcanic activity of the Siluro-Devonian post-collision magmatic episode in the Grampian Terrane, Scotland. *Journal of* *the Geological Society*, **166**, 545–561, https://doi.org/10.1144/0016-76492008-069.

Noble, S.R., Hyslop, E.K. and Highton, A.J. 1996. High-precision U–Pb monazite geochronology of the c. 806 Ma Grampian Shear Zone and the implications for the evolution of the Central Highlands of Scotland. *Journal of the Geological Society*, **153**, 511–514, https://doi.org/10.1144/gsjgs.153.4.0511.

Oliver, G.J.H., Chen, F., Buchwaldt, R. and Hegner, E. 2000. Fast tectonometamorphism and exhumation in the type area of the Barrovian and Buchan zones. *Geology*, **28**, 459–462, https://doi.org/10.1130/0091-7613(2000)28<459:FTAEIT>2.0.CO;2.

Oliver, G.J.H., Wilde, S.A. and Wan, Y. 2008. Geochronology and geodynamics of Scottish granitoids from the late Neoproterozoic break-up of Rodinia to Palaeozoic collision. *Journal of the Geological Society*, **165**, 661–674, https://doi.org/10.1144/0016-76492007-105.

Padrón-Navarta, J.A., López Sánchez-Vizcaíno, V., Menzel, M.D., Gómez-Pugnaire, M.T. and Garrido, C.J. 2023. Mantle wedge oxidation from deserpentinization modulated by sediment-derived fluids. *Nature Geoscience*, **16**, 268–275, https://doi.org/10.1038/s41561-023-01127-0.

Pamukçu, O.A., Akçığ, Z., Demirbaş, Ş. and Zor, E. 2007. Investigation of Crustal Thickness in Eastern Anatolia Using Gravity, Magnetic and Topographic Data. *Pure and Applied Geophysics*, **164**, 2345–2358, https://doi.org/10.1007/s00024-007-0267-7.

Pankhurst, R.J. 1969. Strontium Isotope Studies related to Petrogenesis in the Caledonian Basic Igneous Province of NE. Scotland. *Journal of Petrology*, **10**, 115–143, https://doi.org/10.1093/petrology/10.1.115.

Pankhurst, R.J. and Sutherland, D.S. 1982. Caledonian granites and diorites of Scotland and Ireland. *In*: *Igneous Rocks of the British Isles*. 149–214.

Parnell, J. 1988. Migration of biogenic hydrocarbons into granites: a review of hydrocarbons in British plutons. *Marine and Petroleum Geology*, **5**, 385–396, https://doi.org/10.1016/0264-8172(88)90032-3.

Parrish, R.R. 1990. U–Pb dating of monazite and its application to geological problems. *Canadian Journal of Earth Sciences*, **27**, 1431–1450, https://doi.org/10.1139/e90-152.

Paterson, B.A., Rogers, G., Stephens, W.E. and Hinton, R.W. 1993. The longevity of acid-basic magmatism associated with a major transcurrent fault. *In*: *Geological Society of America, Abstracts with Programs*. A42.

Paterson, B.A., Stephens, W.E., Rogers, G., Williams, I.S., Hinton, R.W. and Herd, D.A. 1992a. The nature of zircon inheritance in two granite plutons. *Earth and Environmental Science Transactions of the Royal Society of Edinburgh*, **83**, 459–471, https://doi.org/10.1017/S0263593300008130.

Paterson, B.A., Rogers, G. and Stephens, W.E. 1992b. Evidence for inherited Sm–Nd isotopes in granitoid zircons. *Contributions to Mineralogy and Petrology*, **111**, 378–390, https://doi.org/10.1007/BF00311198.

Paton, C., Woodhead, J.D., Hellstrom, J.C., Hergt, J.M., Greig, A. and Maas, R. 2010. Improved laser ablation U-Pb zircon geochronology through robust downhole fractionation correction. *Geochemistry, Geophysics, Geosystems*, **11**, https://doi.org/10.1029/2009GC002618.

Paton, C., Hellstrom, J., Paul, B., Woodhead, J. and Hergt, J. 2011. Iolite: Freeware for the visualisation and processing of mass spectrometric data. *Journal of Analytical Atomic Spectrometry*, **26**, 2508–2518, https://doi.org/10.1039/C1JA10172B.

Pattison, D.R.M. and Goldsmith, S.A. 2022. Metamorphism of the Buchan type-area, NE Scotland and its relation to the adjacent Barrovian domain. *Journal of the Geological Society*, **179**, jgs2021-040, https://doi.org/10.1144/jgs2021-040.

Paul, A.N., Spikings, R.A. and Gaynor, S.P. 2021. U-Pb ID-TIMS reference ages and initial Pb isotope compositions for Durango and Wilberforce apatites. *Chemical Geology*, **586**, 120604, https://doi.org/10.1016/j.chemgeo.2021.120604.

Paul, B., Petrus, J., et al. 2023. Time resolved trace element calibration strategies for LA-ICP-MS. *Journal of Analytical Atomic Spectrometry*, **38**, 1995–2006, https://doi.org/10.1039/D3JA00037K.

Pearce, J.A., Bender, J.F., et al. 1990. Genesis of collision volcanism in Eastern Anatolia, Turkey. *Journal of Volcanology and Geothermal Research*, **44**, 189–229, https://doi.org/10.1016/0377-0273(90)90018-B.

Petronis, M.S., O'Driscoll, B., Stevenson, C.T.E. and Reavy, R.J. 2012. Controls on emplacement of the Caledonian Ross of Mull Granite, NW Scotland: Anisotropy of magnetic susceptibility and magmatic and regional structures. *GSA Bulletin*, **124**, 906–927, https://doi.org/10.1130/B30362.1.

Petrus, J.A. and Kamber, B.S. 2012. VizualAge: A Novel Approach to Laser Ablation ICP-MS U-Pb Geochronology Data Reduction. *Geostandards and Geoanalytical Research*, **36**, 247–270, https://doi.org/10.1111/j.1751-908X.2012.00158.x.

Pidgeon, R.T. and Aftalion, M. 1978. Cogenetic and inherited zircons U-Pb systems in granites: Palaeozoic granites of Scotland and England. *In*: *Crustal Evolution in Northwestern Britain and Adjacent Regions*. Geological Journal Special Issue**10**, 183–220.

Pointer, C.M., Ashworth, J.R. and Simpson, P.R. 1989. Genesis of coffinite and the U-Ti association in lower old red sandstone sediments, Ousdale, Caithness, Scotland. *Mineralium Deposita*, **24**, 117–123, https://doi.org/10.1007/BF00206313.

Powell, D. and Friend, C. 2010. Moine geology from Glenfinnan to Morar - an excursion. *In*: Strachan, R. A., Friend, C., Alsop, I. and Miller, S. (eds) *A Geological Excursion Guide to the Moine Geology of the Northern Highlands of Scotland.*

Prave, A.R., Stephens, W.E., Fallick, A.E., Williams, I. and Kirsimäe, K. 2024. How great is the Great Glen Fault? *Journal of the Geological Society*, jgs2024-085, https://doi.org/10.1144/jgs2024-085.

Read, H.H. 1961. Aspects of Caledonian magmatism in Britain. *Geological Journal*, **2**, 653–683, https://doi.org/10.1002/gj.3350020408.

Richards, J.P. 2009. Postsubduction porphyry Cu-Au and epithermal Au deposits: Products of remelting of subduction-modified lithosphere. *Geology*, **37**, 247–250, https://doi.org/10.1130/G25451A.1.

Richards, J.P. 2021. Porphyry copper deposit formation in arcs: What are the odds? *Geosphere*, **18**, 130–155, https://doi.org/10.1130/GES02086.1.

Richardson, S.W. 1968. The petrology of the metamorphosed syenite in Glen Dessarry, Inverness-shire. *Quarterly Journal of the Geological Society of London*, **124**, 9–49, https://doi.org/10.1144/gsjgs.124.1.0009.

Robert, B., Domeier, M. and Jakob, J. 2021. On the origins of the Iapetus Ocean. *Earth-Science Reviews*, **221**, 103791, https://doi.org/10.1016/j.earscirev.2021.103791.

Rock, N.M.S. and Hunter, R.H. 1987. Late Caledonian dyke-swarms of northern Britain: Spatial and temporal intimacy between lamprophyric and granitic magmatism around the Ross of Mull pluton, Inner Hebrides. *Geologische Rundschau*, **76**, 805–826, https://doi.org/10.1007/BF01821065.

Rock, N.M.S., Gaskarth, J.W., Henney, P.J. and Shand, P. 1988. Late Caledonian dyke-swarms of northern Britain: some preliminary petrogenetic and tectonix implications of their province-wide distribution and chemical variation. *Canadian Mineralogist*, **26**, 3–22.

Rogers, D.A., Marshall, J.E.A. and Astin, T.R. 1989. Short Paper: Devonian and later movements on the Great Glen fault system, Scotland. *Journal of the Geological Society*, **146**, 369–372, https://doi.org/10.1144/gsjgs.146.3.0369.

Rogers, G. and Dunning, G.R. 1991. Geochronology of appinitic and related granitic magmatism in the W Highlands of Scotland: constraints on the timing of transcurrent fault movement. *Journal of the Geological Society*, **148**, 17–27, https://doi.org/10.1144/gsjgs.148.1.0017.

Rogers, G., Hyslop, E.K., Strachan, R.A., Paterson, B.A. and Holdsworth, R.E. 1998. The structural setting and U–Pb geochronology of Knoydartian pegmatites in W Inverness-shire: evidence for Neoproterozoic tectonothermal events in the Moineof NW Scotland. *Journal of the Geological Society*, **155**, 685–696, https://doi.org/10.1144/gsjgs.155.4.0685.

Rogers, G., Kinny, P.D., Strachan, R.A., Friend, C.R.L. and Paterson, B.A. 2001. U-Pb geochronology of the Fort Augustus granite gneiss: constraints on the timing of Neoproterozoic and Palaeozoic tectonothermal events in the NW Highlands of Scotland. *Journal of the Geological Society*, **158**, 7–14, https://doi.org/10.1144/jgs.158.1.7.

Ryan, P.D. and Dewey, J.F. 2004. The South Connemara Group reinterpreted: a subduction-accretion complex in the Caledonides of Galway Bay, western Ireland. *Journal of Geodynamics*, **37**, 513–529, https://doi.org/10.1016/j.jog.2004.02.018.

Ryder, G. and Gillis, J. 1994. The petrogenetic interpretation of tiny fragments of evolved lunar rocks: An analog analysis of the Abriachan Granite, Scotland. *Abstracts of the 25th Lunar and Planetary Science Conference*, 1179.

Sabine, P.A. 1963. The Strontian Granite, Complex Argyllshire. *Bulletin of the Geological Survey of Great Britain*, 6–41.

Scaillet, B. and MacDonald, R. 2001. Phase Relations of Peralkaline Silicic Magmas and Petrogenetic Implications. *Journal of Petrology*, **42**, 825–845, https://doi.org/10.1093/petrology/42.4.825.

Scaillet, B., Holtz, F. and Pichavant, M. 2016. Experimental Constraints on the Formation of Silicic Magmas. *Elements*, **12**, 109–114, https://doi.org/10.2113/gselements.12.2.109.

Schärer, U. 1984. The effect of initial230Th disequilibrium on young UPb ages: the Makalu case, Himalaya. *Earth and Planetary Science Letters*, **67**, 191–204, https://doi.org/10.1016/0012-821X(84)90114-6.

Scherer, E.E., Whitehouse, M.J. and Münker, C. 2007. Zircon as a Monitor of Crustal Growth. *Elements*, **3**, 19–24, https://doi.org/10.2113/gselements.3.1.19.

Schiller, D. and Finger, F. 2019. Application of Ti-in-zircon thermometry to granite studies: problems and possible solutions. *Contributions to Mineralogy and Petrology*, **174**, 51, https://doi.org/10.1007/s00410-019-1585-3.

Schoene, B. and Bowring, S.A. 2006. U-Pb systematics of the McClure Mountain syenite: thermochronological constraints on the age of the 40Ar/39Ar standard MMhb. *Contributions to Mineralogy and Petrology*, **151**, 615–630, https://doi.org/10.1007/s00410-006-0077-4.

Searle, M.P. 2021. Tectonic evolution of the Caledonian orogeny in Scotland: a review based on the timing of magmatism, metamorphism and deformation. *Geological Magazine*, **159**, 124–152, https://doi.org/10.1017/S0016756821000947.

Siégel, C., Bryan, S.E., Allen, C.M. and Gust, D.A. 2018. Use and abuse of zircon-based thermometers: A critical review and a recommended approach to identify antecrystic zircons. *Earth-Science Reviews*, **176**, 87–116, https://doi.org/10.1016/j.earscirev.2017.08.011.

Simpson, P.R., Brown, G.C., et al. 1997. Uranium mineralization and granite magmatism in the British Isles. *Philosophical Transactions of the Royal Society of London. Series A, Mathematical and Physical Sciences*, **291**, 385–412, https://doi.org/10.1098/rsta.1979.0034.

Slagstad, T. and Kirkland, C.L. 2018. Timing of collision initiation and location of the Scandian orogenic suture in the Scandinavian Caledonides. *Terra Nova*, **30**, 179–188, https://doi.org/10.1111/ter.12324.

Sláma, J., Košler, J., et al. 2008. Plešovice zircon — A new natural reference material for U–Pb and Hf isotopic microanalysis. *Chemical Geology*, **249**, 1–35, https://doi.org/10.1016/j.chemgeo.2007.11.005.

Smith, A.G. and Briden, J.C. 1977. *Mesozoic and Cenozoic Paleocontinental Maps*.

Smith, D.I. 1979. Caledonian minor intrusions of the N Highlands of Scotland. *Geological Society, London, Special Publications*, **8**, 683–697, https://doi.org/10.1144/GSL.SP.1979.008.01.83.

Smith, D.I. and Watson, J. 1983. Scale and timing of movements on the Great Glen fault, Scotland. *Geology*, **11**, 523–526, https://doi.org/10.1130/0091-7613(1983)11<523:SATOMO>2.0.CO;2.

Snyder, D.B. and Flack, C.A. 1990. A Caledonian age for reflectors within the mantle lithosphere north and west of Scotland. *Tectonics*, **9**, 903–922, https://doi.org/10.1029/TC009i004p00903.

Soper, N.J. 1986. The Newer Granite problem: a geotectonic view. *Geological Magazine*, **123**, 227–236, https://doi.org/10.1017/S0016756800034725.

Soper, N.J., Strachan, R.A., Holdsworth, R.E., Gayer, R.A. and Greiling, R.O. 1992. Sinistral transpression and the Silurian closure of Iapetus. *Journal of the Geological Society*, **149**, 871–880, https://doi.org/10.1144/gsjgs.149.6.0871.

Spencer, B.M., Thigpen, J.R., Law, R.D., Mako, C.A., McDonald, C.S., Hodges, K.V. and Ashley, K.T. 2020. Rapid cooling during late-stage orogenesis and implications for the collapse of the Scandian retrowedge, northern Scotland. *Journal of the Geological Society*, **178**, jgs2020-022, https://doi.org/10.1144/jgs2020-022.

Spencer, B.M., Thigpen, J.R., Gallen, S.F., Dortch, J.M., Hodges, K.V., Law, R.D. and Mako, C.A. 2021. An Evaluation of Erosional-Geodynamic Thresholds for Rapid Orogenic Denudation. *Journal of Geophysical Research: Solid Earth*, **126**, e2021JB022353, https://doi.org/10.1029/2021JB022353.

Spencer, C., Kirkland, C. and Taylor, R. 2016. Strategies towards statistically robust interpretations of in situ U–Pb zircon geochronology. *Geoscience Frontiers*, **7**, 581–589, https://doi.org/10.1016/j.gsf.2015.11.006.

Spencer, C.J., Cawood, P.A., Hawkesworth, C.J., Prave, A.R., Roberts, N.M.W., Horstwood, M.S.A. and Whitehouse, M.J. 2015. Generation and preservation of continental crust in the Grenville Orogeny. *Geoscience Frontiers*, **6**, 357–372, https://doi.org/10.1016/j.gsf.2014.12.001.

Stacey, J.S. and Kramers, J.D. 1975. Approximation of terrestrial lead isotope evolution by a two-stage model. *Earth and Planetary Science Letters*, **26**, 207–221, https://doi.org/10.1016/0012-821X(75)90088-6.

Stein, C., Comeau, M.J., Becken, M. and Hansen, U. 2022. Numerical study on the style of delamination. *Tectonophysics*, **827**, 229276, https://doi.org/10.1016/j.tecto.2022.229276.

Steinhoefel, G., Hegner, E. and Oliver, G.J.H. 2008. Chemical and Nd isotope constraints on granitoid sources involved in the Caledonian Orogeny in Scotland. *Journal of the Geological Society*, **165**, 817–827, https://doi.org/10.1144/0016-76492007-107.

Stephens, W.E. and Halliday, A.N. 1984. Geochemical contrasts between late Caledonian granitoid plutons of northern, central and southern Scotland. *Transactions of the Royal Society of Edinburgh: Earth Sciences*, **75**, 259–273.

Stewart, E.M., Baxter, E.F. and Ague, J.J. 2017. Initiation and duration of Grampian orogenesis constrained by refined Sm–Nd garnet geochronology of the Ballantrae ophiolite, Scotland. *Journal of the Geological Society*, **174**, 968–978, https://doi.org/10.1144/jgs2017-010.

Stewart, M., Strachan, R.A. and Holdsworth, R.E. 1999. Structure and early kinematic history of the Great Glen Fault Zone, Scotland. *Tectonics*, **18**, 326–342, https://doi.org/10.1029/1998TC900033.

Stewart, M., Strachan, R.A., Martin, M.W. and Holdsworth, R.E. 2001. Constraints on early sinistral displacements along the Great Glen Fault Zone, Scotland: structural setting, U-Pb geochronology and emplacement of the syn-tectonic Clunes tonalite. *Journal of the Geological Society*, **158**, 821–830, https://doi.org/10.1144/jgs.158.5.821.

Stone, P. 2014. The Southern Uplands Terrane in Scotland – a notional controversy revisited. *Scottish Journal of Geology*, **50**, 97–123, https://doi.org/10.1144/sjg2014-001.

Stone, P. and Rushton, A.W.A. 2018. On the age of the Ballantrae Complex, SW Scotland. *Scottish Journal of Geology*, **54**, 77–86, https://doi.org/10.1144/sjg2017-012.

Storey, C.D., Brewer, T.S., Anczkiewicz, R., Parrish, R.R. and Thirlwall, M.F. 2010. Multiple high-pressure metamorphic events and crustal telescoping in the NW Highlands of Scotland. *Journal of the Geological Society*, **167**, 455–468, https://doi.org/10.1144/0016-76492009-024.

Strachan, R.A. and Evans, J.A. 2008. Structural setting and U–Pb zircon geochronology of the Glen Scaddle Metagabbro: evidence for polyphase Scandian ductile deformation in the Caledonides of northern Scotland. *Geological Magazine*, **145**, 361–371, https://doi.org/10.1017/S0016756808004500.

Strachan, R.A., Smith, M., Harris, A.L. and Fettes, D.J. 2002. The Northern Highland and Grampian terranes. *In*: Trewin, N. H. (ed.) *The Geology of Scotland*. 0., https://doi.org/10.1144/GOS4P.4.

Strachan, R.A., Friend, C., Alsop, I. and Miller, S. (eds). 2010. *Excursion Guide to the Moine Geology of the Northern Highlands of Scotland*.

Strachan, R.A., Alsop, G.I., Ramezani, J., Frazer, R.E., Burns, I.M. and Holdsworth, R.E. 2020a. Patterns of Silurian deformation and magmatism during sinistral oblique convergence, northern Scottish Caledonides. *Journal of the Geological Society*, **177**, 893–910, https://doi.org/10.1144/jgs2020-039.

Strachan, R.A., Johnson, T.E., Kirkland, C.L., Kinny, P.D. and Kusky, T. 2020b. A Baltic heritage in Scotland: Basement terrane transfer during the Grenvillian orogeny. *Geology*, **48**, 1094–1098, https://doi.org/10.1130/G47615.1.

Styles, M.T., Gunn, A.G. and Rollin, K.E. 2004. A preliminary study of PGE in the Late Caledonian Loch Borralan and Loch Ailsh alkaline pyroxenite-syenite complexes, north-west Scotland. *Mineralium Deposita*, **39**, 240–255, https://doi.org/10.1007/s00126-003-0404-x.

Tang, M., Ji, W.-Q., Chu, X., Wu, A. and Chen, C. 2020. Reconstructing crustal thickness evolution from europium anomalies in detrital zircons. *Geology*, **49**, 76–80, https://doi.org/10.1130/G47745.1.

Tanner, P.W.G. 1970. The Sgurr Beag Slide–a major tectonic break within the Moinian of the Western Highlands of Scotland. *Quarterly Journal of the Geological Society of London*, **126**, 435–463, https://doi.org/10.1144/gsjgs.126.1.0435.

Tanner, P.W.G. 2014. A kinematic model for the Grampian Orogeny, Scotland. *Geological Society, London, Special Publications*, **390**, 467–511, https://doi.org/10.1144/SP390.23.

Thigpen, J.R., Ashley, K.T., Mako, C., Law, R.D. and Spencer, B. 2021. Interplay Between Crustal-Scale Thrusting, High Metamorphic Heating Rates, and the Development of Inverted Thermal-Metamorphic Gradients: Numerical Models and Examples From the Caledonides of Northern Scotland. *Tectonics*, **40**, e2021TC006716, https://doi.org/10.1029/2021TC006716.

Thirlwall, M.F. 1988. Geochronology of Late Caledonian magmatism in northern Britain. *Journal of the Geological Society*, **145**, 951–967, https://doi.org/10.1144/gsjgs.145.6.0951.

Thirlwall, M.F. and Burnard, P. 1990a. Pb-Sr-Nd isotope and chemical study of the origin of undersaturated and oversaturated shoshonitic magmas from the Borralan pluton, Assynt, NW Scotland. *Journal of the Geological Society*, **147**, 259–269, https://doi.org/10.1144/gsjgs.147.2.0259.

Thirlwall, M.F. and Burnard, P. 1990b. Pb-Sr-Nd isotope and chemical study of the origin of undersaturated and oversaturated shoshonitic magmas from the Borralan pluton, Assynt, NW Scotland. *Journal of the Geological Society*, **147**, 259–269, https://doi.org/10.1144/gsjgs.147.2.0259.

Thompson, R.N. and Fowler, M.B. 1986. Subduction-related shoshonitic and ultrapotassic magmatism: a study of Siluro-Ordovician syenites from the Scottish Caledonides. *Contributions to Mineralogy and Petrology*, **94**, 507–522, https://doi.org/10.1007/BF00376342.

Thomson, K., Underhill, J.R., Green, P.F., Bray, R.J. and Gibson, H.J. 1999. Evidence from apatite fission track analysis for the post-Devonian burial and exhumation history of the northern Highlands, Scotland. *Marine and Petroleum Geology*, **16**, 27–39, https://doi.org/10.1016/S0264-8172(98)00064-6.

Tibaldi, A. 2008. Contractional tectonics and magma paths in volcanoes. *Journal of Volcanology and Geothermal Research*, **176**, 291–301, https://doi.org/10.1016/j.jvolgeores.2008.04.008.

Toews, M. and Holmes, M. 2021. Eavor-Lite Performance Update and Extrapolation to Commercial Projects. *Geothermal Resources Council Transactions*, **45**, 86–103.

Torsvik, T.H. 1984. Palaeomagnetism of the Foyers and Strontian granites, Scotland. *Physics of the Earth and Planetary Interiors*, **36**, 163–177, https://doi.org/10.1016/0031-9201(84)90017-7.

Torsvik, T.H., Eide, E.A. and Rehnström, E.F. 2003. Palaeomagnetism and geochronology of four Laurentian (Scottish) granites with implications for Iapetus Ocean closure models. *In*: *Abstracts from the Meeting Held in Nice, France* – EGS - AGU - EUG Joint Assembly. 2183.

Torsvik, T.H., Van der Voo, R., et al. 2012. Phanerozoic polar wander, palaeogeography and dynamics. *Earth-Science Reviews*, **114**, 325–368, https://doi.org/10.1016/j.earscirev.2012.06.007.

Trail, D., Bruce Watson, E. and Tailby, N.D. 2012. Ce and Eu anomalies in zircon as proxies for the oxidation state of magmas. *Geochimica et Cosmochimica Acta*, **97**, 70–87, https://doi.org/10.1016/j.gca.2012.08.032.

Trewin, N.H. and Thirlwall, M.F. 2002. Old Red Sandstone. *In*: Trewin, N. H. (ed.) *The Geology of Scotland*. 0., https://doi.org/10.1144/GOS4P.8.

Tulstrup, J. 1980. *An Interpretation of Gravity and Magnetic Anomalies Associated with the Helmsdale Fault Line*. **WB/MG/80/108**Marine Geology: Marine Geophysics.

Turner, S., Sandiford, M. and Foden, J. 1992. Some geodynamic and compositional constraints on ‘postorogenic’ magmatism. *Geology*, **20**, 931–934, https://doi.org/10.1130/0091-7613(1992)020<0931:SGACCO>2.3.CO;2.

Tweedie, J.R. 1979. Origin of uranium and other metal enrichments in the Helmsdale Granite, eastern Sutherland, Scotland. *Transaction of the*

Institution of Mining and Metallurgy. Section B, Applied Earth Science, **88**, B145–B153.

Tyler, I.M. and Ashworth, J.R. 1982. Sillimanite-potash feldspar assemblages in graphitic pelites, Strontian area, Scotland. *Contributions to Mineralogy and Petrology*, **81**, 18–29, https://doi.org/10.1007/BF00371155.

UK Government. 2022. Resilience for the Future: The United Kingdom's Critical Minerals Strategy.

Upton, B.G.J., Stephenson, D., Smedley, P.M., Wallis, S.M. and Fitton, J.G. 2004. Carboniferous and Permian magmatism in Scotland. *Geological Society, London, Special Publications*, **223**, 195–218, https://doi.org/10.1144/GSL.SP.2004.223.01.09.

van Staal, C.R. and Zagorevski, A. 2023. Paleozoic tectonic evolution of the rifted margins of Laurentia. *In*: Whitmeyer, S. J., Williams, M. L., Kellett, D. A. and Tikoff, B. (eds) *Laurentia: Turning Points in the Evolution of a Continent*. 0., https://doi.org/10.1130/2022.1220(24).

Van Staal, C.R., Dewey, J.F., Niocaill, C.M. and McKerrow, W.S. 1998. The Cambrian-Silurian tectonic evolution of the northern Appalachians and British Caledonides: history of a complex, west and southwest Pacific-type segment of Iapetus. *Geological Society, London, Special Publications*, **143**, 197–242, https://doi.org/10.1144/GSL.SP.1998.143.01.17.

van Staal, C.R., Whalen, J.B., Valverde-Vaquero, P., Zagorevski, A. and Rogers, N. 2009. Pre-Carboniferous, episodic accretion-related, orogenesis along the Laurentian margin of the northern Appalachians. *Geological Society, London, Special Publications*, **327**, 271–316, https://doi.org/10.1144/SP327.13.

van Staal, C.R., Barr, S.M., Waldron, J.W.F., Schofield, D.I., Zagorevski, A. and White, C.E. 2021. Provenance and Paleozoic tectonic evolution of Ganderia and its relationships with Avalonia and Megumia in the Appalachian-Caledonide orogen. *Gondwana Research*, **98**, 212–243, https://doi.org/10.1016/j.gr.2021.05.025.

Vermeesch, P. 2018. IsoplotR: A free and open toolbox for geochronology. *Geoscience Frontiers*, **9**, 1479–1493, https://doi.org/10.1016/j.gsf.2018.04.001.

Viete, D.R., Richards, S.W., Lister, G.S., Oliver, G.J.H. and Banks, G.J. 2010. Lithospheric-scale extension during Grampian orogenesis in Scotland. *Geological Society, London, Special Publications*, **335**, 121–160, https://doi.org/10.1144/SP335.7.

Walker, S., Thirlwall, M.F., Strachan, R.A. and Bird, A.F. 2016. Evidence from Rb-Sr mineral ages for multiple orogenic events in the Caledonides of Shetland, Scotland. *Journal of the Geological Society*, **173**, 489–503, https://doi.org/10.1144/jgs2015-034.

Walker, S., Bird, A.F., Thirlwall, M.F. and Strachan, R.A. 2021. Caledonian and Pre-Caledonian orogenic events in Shetland, Scotland: evidence from garnet Lu–Hf and Sm–Nd geochronology. *In*: Murphy, J. B., Strachan, R. A. and Quesada, C. (eds) *Pannotia to Pangaea: Neoproterozoic and Paleozoic Orogenic Cycles in the Circum-Atlantic Region*. 0., https://doi.org/10.1144/SP503-2020-32.

Walters, A.S., Goodenough, K.M., Hughes, H.S.R., Roberts, N.M.W., Gunn, A.G., Rushton, J. and Lacinska, A. 2013. Enrichment of Rare Earth Elements during magmatic and post-magmatic processes: a case study from the Loch Loyal Syenite Complex, northern Scotland. *Contributions to Mineralogy and Petrology*, **166**, 1177–1202, https://doi.org/10.1007/s00410-013-0916-z.

Wan, B., Deng, C., et al. 2018. Fertilizing porphyry Cu deposits through deep crustal hot zone melting. *Gondwana Research*, **60**, 179–185, https://doi.org/10.1016/j.gr.2018.04.006.

Wang, D., Wang, X.-L., Cai, Y., Chen, X., Zhang, F.-R. and Zhang, F.-F. 2017. Heterogeneous Conservation of Zircon Xenocrysts in Late Jurassic Granitic Intrusions within the Neoproterozoic Jiuling Batholith, South China: a Magma Chamber Growth Model in Deep Crustal Hot Zones. *Journal of Petrology*, **58**, 1781–1810, https://doi.org/10.1093/petrology/egx074.

Warr, L.N. 2021. IMA-CNMNC approved mineral symbols. Mineralogical Magazine, **85**, 291-320, https:// doi:10.1180/mgm.2021.43.

Watson, E.B., Wark, D.A. and Thomas, J.B. 2006. Crystallization thermometers for zircon and rutile. *Contributions to Mineralogy and Petrology*, **151**, 413–433, https://doi.org/10.1007/s00410-006-0068-5.

Watson, J. 1984. The ending of the Caledonian orogeny in Scotland. *Journal of the Geological Society*, **141**, 193–214, https://doi.org/10.1144/gsjgs.141.2.0193.

Watson, J.V. and Plant, J. 1997. Regional geochemistry of uranium as a guide to deposit formation. *Philosophical Transactions of the Royal Society of London. Series A, Mathematical and Physical Sciences*, **291**, 321–338, https://doi.org/10.1098/rsta.1979.0030.

Whitehouse, M.J. and Kamber, B.S. 2002. On the overabundance of light rare earth elements in terrestrial zircons and its implication for Earth's earliest magmatic differentiation. *Earth and Planetary Science Letters*, **204**, 333–346, https://doi.org/10.1016/S0012-821X(02)01000-2.

Wiedenbeck, M., Allé, P., et al. 1995. Three Natural Zircon Standards for U-Th-Pb, Lu-Hf, Trace Element and REE Analyses. *Geostandards Newsletter*, **19**, 1–23, https://doi.org/10.1111/j.1751-908X.1995.tb00147.x.

Wiest, J.D., Jacobs, J., Fossen, H., Ganerød, M. and Osmundsen, P.T. 2021. Segmentation of the Caledonian orogenic infrastructure and exhumation of the Western Gneiss Region during transtensional collapse. *Journal of the Geological Society*, **178**, jgs2020-199, https://doi.org/10.1144/jgs2020-199.

Woodcock, N.H. and Strachan, R.A. (eds). 2012. *Geological History of Britain and Ireland*, 2nd ed.

Yakymchuk, C., Kirkland, C.L. and Clark, C. 2018. Th/U ratios in metamorphic zircon. *Journal of Metamorphic Geology*, **36**, 715–737, https://doi.org/10.1111/jmg.12307.

Yakymchuk, C., Holder, R.M., Kendrick, J. and Moyen, J.-F. 2023. Europium anomalies in zircon: A signal of crustal depth? *Earth and Planetary Science Letters*, **622**, 118405, https://doi.org/10.1016/j.epsl.2023.118405.

Yuan, H.-L., Gao, S., et al. 2008. Simultaneous determinations of U–Pb age, Hf isotopes and trace element compositions of zircon by excimer laser-ablation quadrupole and multiple-collector ICP-MS. *Chemical Geology*, **247**, 100–118, https://doi.org/10.1016/j.chemgeo.2007.10.003.

Zhao, Z.-F., Dai, L.-Q. and Zheng, Y.-F. 2013. Postcollisional mafic igneous rocks record crust-mantle interaction during continental deep subduction. *Scientific Reports*, **3**, 3413, https://doi.org/10.1038/srep03413.

Zhong, S., Feng, C., Seltmann, R., Li, D. and Qu, H. 2018. Can magmatic zircon be distinguished from hydrothermal zircon by trace element composition? The effect of mineral inclusions on zircon trace element composition. *Lithos*, **314–315**, 646–657, https://doi.org/10.1016/j.lithos.2018.06.029.

Zhong, S., Seltmann, R., Qu, H. and Song, Y. 2019. Characterization of the zircon Ce anomaly for estimation of oxidation state of magmas: a revised Ce/Ce* method. *Mineralogy and Petrology*, **113**, 755–763, https://doi.org/10.1007/s00710-019-00682-y.

Zou, X., Qin, K., Han, X., Li, G., Evans, N.J., Li, Z. and Yang, W. 2019. Insight into zircon REE oxy-barometers: A lattice strain model perspective. *Earth and Planetary Science Letters*, **506**, 87–96, https://doi.org/10.1016/j.epsl.2018.10.031.